

NASA CR-

160662

Axiomatix

(NASA-CR-160662) SHUTTLE Ku-BAND AND S-BAND
COMMUNICATIONS IMPLEMENTATION STUDY Final
Report (Axiomatix, Los Angeles, Calif.)
274 p HC A12/MF A01

N80-25522

CSSL 17B

Unclass

G3/32 22960



SHUTTLE KU-BAND AND S-BAND
COMMUNICATIONS IMPLEMENTATION STUDY

FINAL REPORT

Contracts NAS 9-15240E and NAS 9-15240F

Prepared for

NASA Lyndon B. Johnson Space Center
Houston, Texas 77058

Prepared by

James G. Dodds
Gaylord K. Huth
Peter W. Nilsen
Andreas Polydoros
Marvin K. Simon
Charles L. Weber

Axiomatix

9841 Airport Blvd., Suite 912
Los Angeles, California 90045

Axiomatix Report No. R8005-3
May 21, 1980

TABLE OF CONTENTS

	<u>Page</u>
LIST OF TABLES	iii
LIST OF FIGURES	iv
1.0 EXECUTIVE SUMMARY	1
2.0 INTRODUCTION	2
3.0 S-BAND NETWORK COMMUNICATION ANTENNA CALIBRATION STUDY . . .	3
3.1 General Technical Approach	5
3.2 Data Gathering Procedure	10
3.3 Processing Algorithm Considerations	14
3.3.1 Summary of Kalman-Bucy Filtering	15
3.3.2 Basic Signal Model	15
3.3.3 Basic Kalman-Bucy Estimation Algorithms	17
3.3.4 Properties and Advantages of the Kalman Filter.	20
3.3.5 Application of Optimal Linear Filtering to the Antenna Calibration Problem	22
3.3.6 Variable and Parameter Assignments for the Antenna Model	24
3.3.7 Variable and Parameter Assignments for the Observations	28
3.3.8 Basic Flow Diagram for Antenna Calibration Estimation	29
3.4 STDN Calibration Considerations	31
4.0 KU-BAND COMMUNICATION SYSTEM STUDY	34
4.1 Analysis of TDRS Ku-Band Pointing Accuracy	35
4.1.1 TDRS Calibration Errors	35
4.1.2 Open-Loop Pointing Budget	39
4.1.3 Results of Revised Pointing Budget Analysis	40
4.1.4 Conclusions	43
4.2 Performance Characteristics of the Ku-Band Channel 3 Convolutional Code with G_2 Inversion	44
4.2.1 Run Length of the Convolutional Code with G_2 Inversion	45
4.2.2 Code Behavior with DC Input	48
4.2.3 Summary of Performance	54
4.3 Effects Due To Specific TDRSS User Constraint Parameters	55
4.3.1 Ku-Band Bit Synchronizer BER Degradation due to Data Bit Clock Jitter	55
4.3.2 Effect of Data Asymmetry on Unbalanced QPSK Signals with Noisy Phase Reference	56

5.0 S-BAND PAYLOAD COMMUNICATION SYSTEM STUDY	61
5.1 Bent-Pipe Performance with the Current PI/KuSP RMS Regulator Capability	61
5.2 Sweep Acquisition of Deep-Space (DS) Payloads by the PI .	63
5.3 Two-Way Phase Noise Performance for PI and Coherent Payload Transponders	63
REFERENCES	65

APPENDICES:

I	Ku-Band Synchronizer BER Degradation due to Data Bit Clock Jitter
II	Effect of Data Asymmetry on Unbalanced QPSK Signals with Noisy Phase Reference
III	Peak Regulator Design and Breadboard Evaluation
IV	Acquisition Sweep Rate Viewgraphs
V	Maximum Sweep Frequency for Phase-Locked Loops with Large Damping Factors
VI	The Theory of Mean-Square Phase Noise Performance of One/Two-Way Coherent Communication Links
VII	Mean-Square Error Approximation to Phase Noise Spectra
VIII	Calculations and Final Results on the Phase Noise Error Variance for the S-Band PI and Transponder for SGLS and STDN

LIST OF TABLES

	<u>Page</u>
1. Absolute Flux Density and Antenna Temperatures at 2295 MHz. . .	31
2. Summary of Error Models - A/T Null	36
3. TDRS/Shuttle Transmit Pointing Budget, 0.06° Null-to-Boresight Error	38
4. TDRS/Shuttle Transmit Pointing Budget, 0.92° Null-to-Boresight Error	41
5. TDRS/Atmospheric Explorer Pointing Budget, Worst Case	42
6. Degradation for the Three Bit Synchronizer Classes and the Two Jitter Specifications [(a) and (b)] for Sine Wave Jitter (Uncoded Data)	57
7. Degradation for the Three Bit Synchronizer Classes and the Two Jitter Specifications [(a) and (b)] Random Noise Jitter (Uncoded Data)	57
8. Bent-Pipe FM Transmitter Mean Deviations (MHz).	61

LIST OF FIGURES

	<u>Page</u>
1. Link Relationships for Determination of Shuttle Antenna Gain During OFT	8
2. Information Flow for Gain Pattern Determination of Shuttle Antenna During STS	11
3. Unprocessed Gain Matrix	12
4. Basic Signal Model, a Finite-Dimensional Linear System	16
5. Basic Structure of One-Step Predictor Version of the Kalman-Bucy Estimator	19
6. Kalman Estimator Redrawn to Emphasize its Structure as a Copy of the Original System Driven by the Estimation Error	21
7. Specification of the Angles for Antenna Calibration	23
8. Conversion of AGC Voltage to Received Average Power Signal Strength	25
9. Antenna Measurements Taken versus Time Assignments, k	27
10. Basic Flow Diagram for Antenna Calibration Estimation	30
11. Flow Chart for Calibrating Arbitrary DSN Station	32
12. Master Station Block Diagram Gain Transfer Calibration System	33
13. Rate One-Half Encoder Representation, Ku-Band Return Link, Mode 1	46
14. The Rate One-Half, Constraint Length 7 NASA Planetary Standard Code	47
15. Effect of Zero Input Data on Decoder Output	49
16. (a) Source Model for Ambiguous Check Symbol Sequence (b) K = 7 Encoder	53

1.0 EXECUTIVE SUMMARY

Various aspects of the Shuttle Orbiter S-band network communication system, the S-band payload communication system, and the Ku-band communication system are included in this final report.

The first topic, Section 3.0, deals with a proposed method of obtaining more accurate S-band antenna patterns of the actual Shuttle Orbiter vehicle during flight. The preliminary antenna patterns using mock-ups are not realistic since they do not include the effects of additional appendages such as wings and tail structures.

Section 4.0 discusses the Ku-band communication system, especially the TDRS antenna pointing accuracy with respect to the Orbiter and the modifications required and resulting performance characteristics of the convolutionally encoded high data rate return link to maintain bit synchronizer lock on the ground. Also included is the TDRS user constraints on data bit clock jitter and data asymmetry on unbalanced QPSK with noisy phase references.

Section 5.0 outlines the S-band payload communication system study, including the advantages and experimental results of a peak regulator design built and evaluated by Axiomatix for the bent-pipe link versus the existing RMS-type regulator. Also discussed is the selection of the nominal sweep rate for the deep-space transponder of 250 Hz/s, justifying this conclusion with a phase-plane analysis which incorporates the transponder operating conditions and tolerances. And finally, the effects of phase noise on the performance of a communication system is analyzed in great detail. The phase noise spectra is characterized using experimental results and included into models of the carrier tracking loops to determine the phase noise system errors of the overall system. Different types of two-way links are considered, including the phase noise effects of multiple internal control loops which are equivalent to three- and four-way links. Both in-band and out-of-band noise sources are also included.

Eight appendices are included at the end of this final report which describe in detail the models used, the derivations and the conclusions of the studies for those who are interested in the technical aspects of the investigations.

2.0 INTRODUCTION

This final report summarizes the system implementation studies of the S-Band Network Communication System, the Ku-Band Communication System, and the S-Band Payload Communication System. The specific areas of study are covered under Contracts NAS 9-15240E and NAS 9-15240F; however, in the interests of continuity of conciseness, the results of the study will be reported as a unit.

3.0 S-BAND NETWORK COMMUNICATION ANTENNA CALIBRATION STUDY

This section presents the results of the investigation to date of an approach to calibrate the Orbiter S-band antennas (and UHF antenna also) during STS flights. The actual gain patterns of the flush-mounted S-band quadratures (PM, two on each side of the Orbiter) and the S-band hemi antennas (FM) are difficult, at best, to predict from the customary ground antenna range pattern measurements. This is because, for flush-mounted antennas, the Orbiter structure itself has a significant influence on the pattern. Consequently, the adjacent sections of the Orbiter structure in which the antennas are mounted have been mocked-up and, along with the antenna(s) mounted in them, used for pattern tests on the JSC antenna range. This technique typically yields fairly accurate gain measurements near the boresight of the antenna, i.e., normal to the surface of the structure. However, as the angle off boresight increases, the accuracy in the gain pattern decreases due to edge effects of the limited structural mock-up and the missing influence of the more remote parts of the structure, such as the wings.

Even though the operation of these antennas is expected to take place primarily in the central portion of the main beam, it is important to have accurate knowledge of the natural antenna gain pattern throughout the entire main beam and the sidelobes. This is the case for the following reasons:

(1) During the ascent and descent portions of flight, the range to the ground stations will be relatively short. As a result, the signal strength will be quite high. The configuration of the Orbiter and the ground station, however, may be such that communication will be via the low gain portion of the main beam or even a sidelobe.

During lift-off, the present geometric configuration is such that a weak portion of the S-band pattern will be in use. As a result, more precise information about the gain patterns is necessary in these regions. At such short ranges, even in the low gain portions of the pattern, the SNR should be very adequate, but the extent of such coverage is not really known.

(2) The long-term plan is to replace the S-band quadratures with two-position switched beam phase-array antennas mounted in the same physical location. The S-band quadratures are presently planned for the first six to nine STS flights. The main problem of appendage blockage is reduced by the use of phased-array antennas. This would not be necessary, however, if by chance the S-band quadratures operated satisfactorily in the fringe areas (i.e., in the vicinity of -1 to +1 dB).

(3) The long-term plan is also to transfer communication to the Shuttle/TDRSS links via the S-band quadratures or S-band phased arrays as soon as possible into the STS mission. Because of the predicted narrow design margins for some of the S-band Shuttle/TDRSS links, it is important to show how large the spatial region is in which acceptable link performance can be expected. This can be determined with accurate knowledge of the S-band antenna patterns in the "fringe areas." A prime opportunity to accomplish this finer calibration exists during the STS phase because, during STS, communication with the Shuttle will be via STDN stations. While in orbit, the actual performance of the Shuttle antennas will be free of all the ground effects present on conventional antenna ranges. Thus, with appropriate link calibration and data processing, the STS Orbiter/STDN link can function in the same manner as an antenna range.

The remainder of this section describes a technical approach to be used during STS to obtain the finer gain calibration. The results described are preliminary, and further refinement of the approach is expected to continue on a subsequent contract. The emphasis is placed on the main problem, namely, the changes in the S-band quadrature patterns due to appendages.

3.1 General Technical Approach

The RF link information which will be available during STS for purposes of Shuttle antenna calibration will fall into two general categories. First, there is the link information which will be obtained during communication while the Orbiter is in an "as flown" mission. The other category of link information is that which is obtained while the Orbiter's attitude is determined and controlled specifically to support antenna calibration. The FTR (Flight Test Requirement) for this category is to determine antenna coverage that cannot be verified on the ground. The only objective in these "special antenna-pattern tests" is to utilize specific antenna coordinate profiles, or "passes," to obtain gain information for that portion of the antenna(s) pattern. This would be implemented by having the Orbiter perform suitable roll maneuvers for two or three ground-station passes. The present plan is to perform a 720° roll at 2°/sec, requiring approximately six minutes. During such a maneuver, only one of the S-band quadrature antennas would be operating, thereby providing low gain and sidelobe information. The 720° roll would be performed twice, once for one of the lower quadrant S-band antennas and once for one of the upper quadrant antennas.

The type of measurement information obtained from the programmed attitude profile will be superior to the "as flown" category. This is because the portion of the pattern used in the "as flown" flights will necessarily concentrate on the main beam of one of the S-band quadratures. The antenna in use will be chosen so that the best signal strength is obtained. The flights programmed for antenna measurements will provide broader pattern coverage and will come closest to conventional antenna pattern measurement techniques; however, the "as flown" measurements will be the predominantly available information due to the pressure of numerous mission requirements for STS flights. The signal processing and data reduction developed for the antenna measurements will be the same, however, for both categories.

The general approach to updating the calibration of the Orbiter S-band antennas from the measurements described above is as follows:

- (1) Calibrate the STDN stations and Orbiter RF systems

The best information we have at this time is:

(a) The Shuttle transmitter power can be determined to within ± 0.1 dB.

(b) NASA Goddard presently plans to accurately calibrate one of the ground stations. At this time, it is not known whether this calibration will produce values that are known to within ± 1 dB.

(2) Record uplink and downlink received signal strength versus Orbiter structure.

(3) JSC will provide BET (Best Estimate Trajectories) and attitudes of the flights. These will be sufficiently accurate that they can be assumed to be deterministic.

(4) The data will be filtered to provide estimates of the actual antenna gain in the immediate vicinity of the location where the measurements were taken. The estimates can be updated as more STS flights are taken. For example, data from STS-1 may be replaced with actual measured points from STS-2 or used in addition to those from STS-2 and succeeding flights. Part of the filtering process will consist of a "data good" algorithm to determine when data should be accepted or rejected.

(5) In those regions where the orbital antenna measurements were not made and where the antenna pattern is relatively smooth, an interpolation algorithm will be developed to provide updated values of the antenna gain. For the sidelobes and/or in those regions where the antenna gain variation is very large with respect to either elevation or azimuth, little if any interpolation is likely. In these regions, the average antenna pattern gain may be adjustable (biased) from that of the ground measurements. The overall antenna gain measurement process is enhanced because the gain of the main beam near boresight is expected to have no appreciable change due to the appendages.

All aspects of the filtering algorithm will be fundamental in determining actual antenna coverage capability that could not be verified on the ground. All aspects of the filtering and interpolation process will also continuously compare measured orbital values with those obtained from the ground test-range patterns, particularly when confidence in the orbital measurements is low.

Figure 1 illustrates the basic mathematical link relationship for determination of antenna gain from received signal power. From this figure, it is seen that, in addition to Orbiter attitude, the key parameters which must be known or measured are received signal power, calibrated STDN gain and circuit losses, Orbiter transmitted power and circuit losses, line-of-sight range, and carrier frequency. This calculation is not normally encountered in conventional antenna measurement procedures because, in conventional procedures, a standard gain horn is substituted for the antenna being measured and the received signal power is measured. Thereafter, the dB difference in received signal power with the measured antenna indicates the gain relative to the standard gain horn.

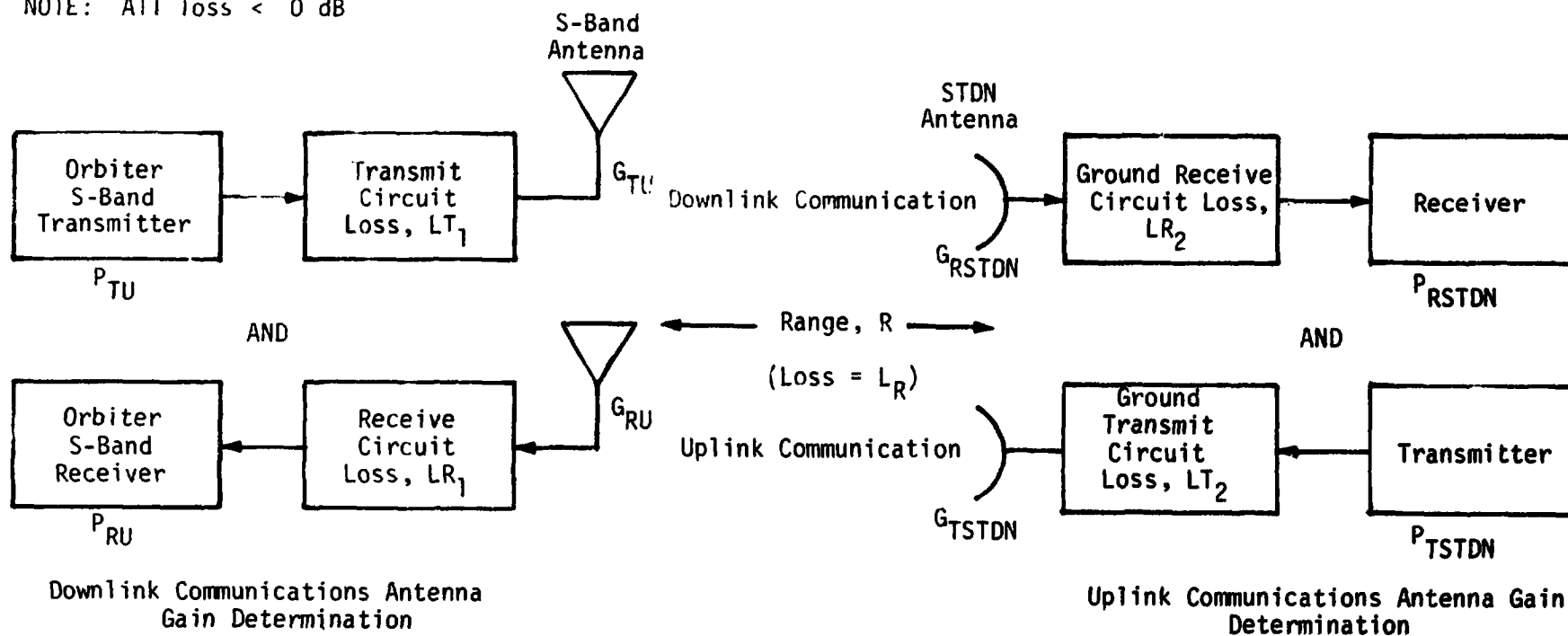
Ideally, a completely calibrated STDN consists of precise knowledge of all gains in the power budget computation, including antenna feed circuit losses, preamp gain and receiver gains. The signal strength is determined by monitoring the AGC levels. The relationship between AGC level and signal strength must therefore also be determined (calibrated). In addition, since it may be desirable to measure received signal power on the Orbiter, the STDN gains and losses and power in the transmit mode would ideally be accurately known. Similarly, the Orbiter transmit power and circuit losses in the transmit and receive modes would ideally be accurately measured.

However, an error budget analysis will be carried out on all of the parameters necessary to normalize the raw data (AGC output) into a raw estimate of antenna gain.

Parameter	Bias	RMS Error
Range		
Attitude		
Circuit Losses		
Frequency		
Transmitter Power		
STDN Gain		
Gain Uncertainty		
AGC Quality		
AGC Nonlinearity Curve (dBm versus volts)		

Both bias and RMS error need to be estimated, as indicated in the above table. With these estimates, the errors of the raw antenna gain data can be estimated. The range data is expected to be very accurate, based on Best Estimate Trajectory (BET).

NOTE: All loss < 0 dB



$$P_{RSTDN} = P_{TU} + LT_1 + G_{TU} + L_R - G_{RSTDN} + LR_2$$

$$G_{TU} = P_{RSTDN} - P_{TU} - LT_1 - L_R - G_{RSTDN} - LR_2$$

where

- G_{TU} = Shuttle transmit antenna gain
- G_{RU} = Shuttle receive antenna gain
- P_{TU} = Shuttle transmitter output power
- P_{RU} = Shuttle received power at receiver
- LT_1 = Shuttle transmit circuit loss
- LR_1 = Shuttle receive circuit loss

$$P_{RU} = P_{TSTDN} + LT_2 + G_{TSTDN} + L_R + G_{RU} - LR_1$$

$$G_{RU} = P_{RU} - P_{TSTDN} - LT_2 - G_{TSTDN} - L_R - LR_1$$

- G_{RSTDN} = STDN transmit antenna gain
- G_{TSTDN} = STDN transmit antenna gain
- P_{RSTDN} = STDN receive power
- P_{TSTDN} = STDN transmitter power
- LR_2 = STDN receive circuit loss
- LT_2 = STDN transmit circuit loss

L_R = path loss

Figure 1. Link Relationships for Determination of Shuttle Antenna Gain During OFT

Both uplink and downlink data will be available during the flights. The weighting of the uplink and downlink data needs to be determined. The SNR in each link can be estimated via the previous table for each link. One simplification of the overall data reduction process is obtained by consolidating each uplink and downlink data point into one data point.

The STDN stations, however, have heretofore had abundant design margins so that such accuracies have not been necessary. Therefore, most parameters in the power budget computations at most STDN stations are not accurately known. The most economical approach to circumvent this is proposed as follows:

(1) Accurately calibrate one STDN station and use this station to make absolute gain measurements over a portion of the S-band antenna patterns. A high degree of confidence would then exist for the absolute gain in these portions of the patterns.

(2) Use the information in (1) above to calibrate the STDN stations when the Orbiter passes by. Measurements over the remainder of the patterns would then provide antenna gain values relative to those which are known absolutely.

The best portion of the pattern in which to make these absolute measurements is the region of boresight. This has the additional advantage that the pattern in the main beam should closely agree with the measurements made in the antenna ground test range. It is expected that the appendages will not appreciably affect the antenna pattern in the high-gain portion of the main beam.

An alternate method of obtaining the absolute antenna gain measurements is by way of a calibrated standard gain horn at one STDN site. Whether or not this approach involves fewer calibration difficulties is yet to be determined.

3.2 Data Gathering Procedure

The basic information gathering and processing procedure to obtain the gain pattern is shown in Figure 2. Provisions for gain calculations from both uplink and downlink communications are shown. The majority of Figure 2 depicts the information flow necessary to evaluate the equations shown in Figure 1. The box labeled "Unprocessed Gain Matrix" represents the three-dimensional matrix of measured antenna gain samples. This matrix is depicted in Figure 3. The X and Y coordinates correspond to the quantized θ, ϕ look angle coordinates of the Orbiter antenna. The Z coordinate corresponds to the measured gain samples. There may be more than one sample for a given coordinate, resulting from the several passes by the same station or samples of the gain at that coordinate for several stations. In general, the elements of the three-dimensional gain matrix are identified by $G_{N\theta,\phi}$

where

$G_{N\theta,\phi}$ = gain sample which is a function of station, Orbiter antenna, station elevation angle, Orbiter look angle, and Orbiter transmit circuit

N = number of gain samples for the particular θ, ϕ cell

The matrix of $G_{N\theta,\phi}$ will, in general, have many θ, ϕ cells for which there will be no values and others for which there will be several values. Thus, to arrive at the final antenna pattern, it is necessary to pass this matrix through an appropriate filter/estimator.

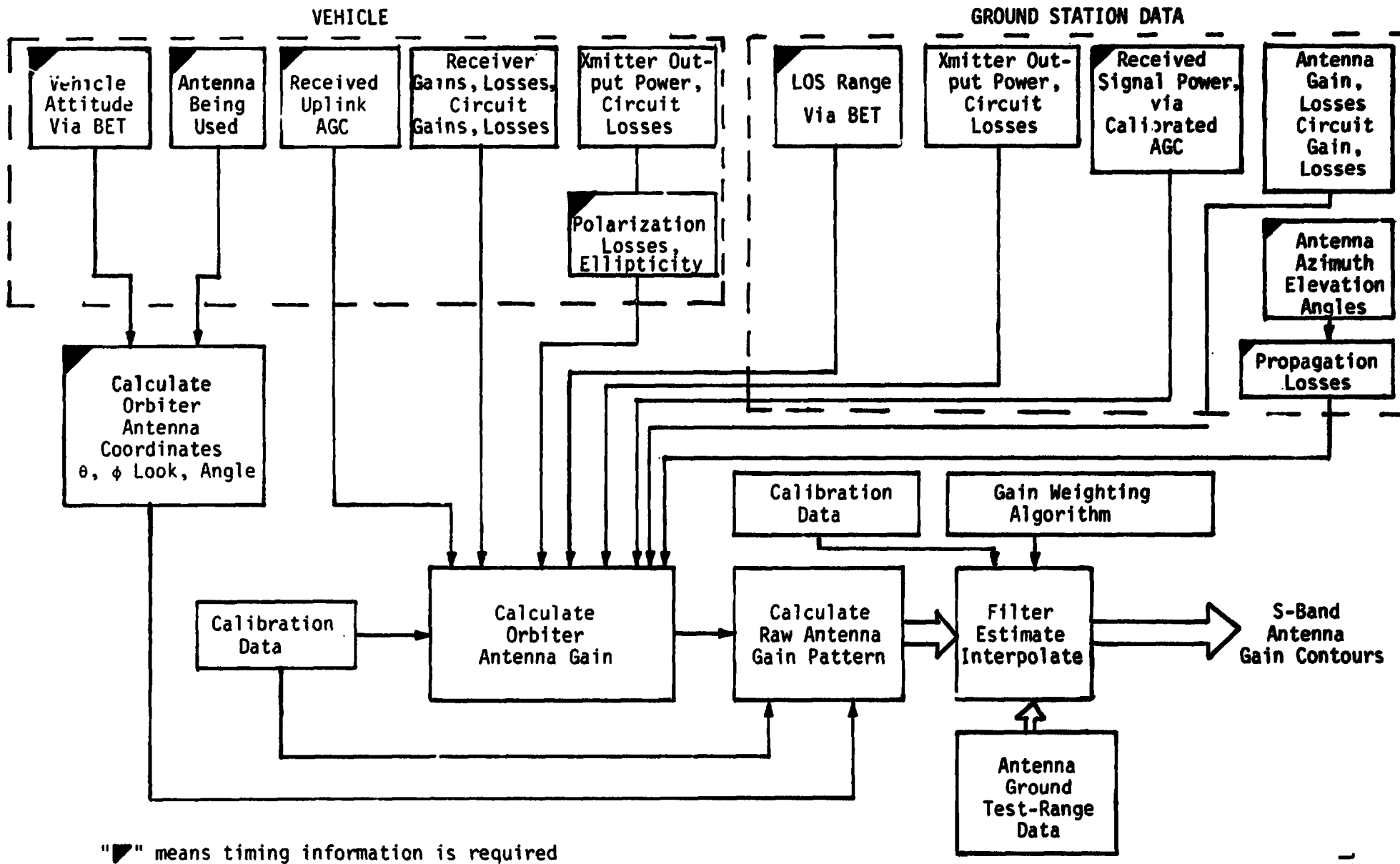
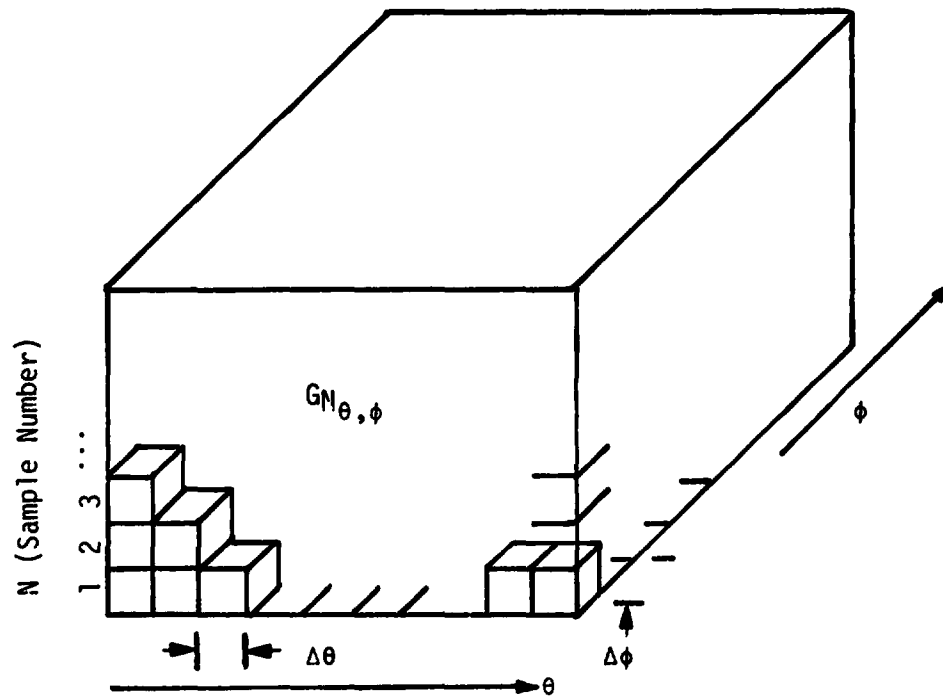


Figure 2. Information Flow for Gain Pattern Determination of Shuttle Antenna During STS



$G_{N_{\theta, \phi}} = f(\text{station, station elevation angle, time, Orbiter attitude, Orbiter transmitter})$

$N = \text{number of gain samples for the particular } \theta, \phi \text{ cell}$

Figure 3. Unprocessed Gain Matrix

The drawing in Figure 3 should not lead to the conclusion that all samples are separated by $\Delta\theta$ and $\Delta\phi$ in θ and ϕ , respectively. The actual locations of the measurements are not now presently known. It can be safely assumed that the measurement locations will be irregularly spaced. The present plan for the "special antenna-pattern tests" is to sample the AGC at 20 samples/sec during the roll maneuvers described above. This corresponds to 10 samples/degree, which is quite adequate.

After the signal processing has been completed, the desired output is a grid of estimated antenna gain values. A satisfactory grid size appears to be $2^\circ \times 2^\circ$. This is certainly adequate over the main beam of the S-band quadratures. However, the size of the computational problem needs to be determined. The array of values for each of the quadrature antennas is 90×45 based on the 2° -by- 2° grid. This is also assuming that each antenna pattern is evaluated only over the region where it is the primary antenna. This evaluation will be performed during the next phase of the investigation.

3.3 Processing Algorithm Considerations

The signal processing for Shuttle antenna measurements can be partitioned into two parts, as follows:

(1) Preprocessing. The effects of range, frequency, circuit losses, biases, etc. are taken into account. In addition, the necessary bookkeeping, such as which antenna is in use, look angle, data source, etc., is carried out. The result is a set of normalized antenna measurements which are used to update the appropriate antenna pattern.

(2) The algorithm. The computational procedure employed to update the antenna gain pattern using the normalized antenna measurements described above.

A recursive Kalman-Bucy type estimation algorithm is discussed below as a candidate suggested by Prof. B. Tranter, which has received extensive attention in the recent literature on signal processing, is the Maximum Entropy approach. This method has been shown to have excellent performance in the estimation of power spectral densities when only sparse data is available. The limitation appears to be that highly reliable data is necessary or, equivalently, that the observations are at very high signal-to-noise ratios (SNR). This signal-processing technique will be examined to see if it can be extended to spatial filtering at intermediate values of SNR. In this case, the dominant noise is the calibration error variance.

If these techniques do not prove to be adequate, the class of the nearest neighbor algorithms will also be examined in the next phase of the investigation.

We cannot determine which of these algorithms is optimum since essentially no statistical information is available. The real issue is which of the candidate algorithms will do the most satisfactory job.

3.3.1 Summary of Kalman-Bucy Filtering

In this section, the basic ideas of the discrete time Kalman-Bucy filter are presented. Restriction is made to discrete time processing since that is most amenable to digital computation and the raw data is also expected to come to us in discrete time.

The Kalman-Bucy filtering algorithm determines the best linear mean-square estimate of a signal immersed in additive noise when the signal and noise can be modeled in a certain manner. This basic signal model is quite general and can be made to fit a wide variety of signal statistics.

3.3.2 Basic Signal Model

The basic signal model presented is not the most general but is more than adequate for the antenna calibration problem. The basic signal model is diagrammed in Figure 4 and is described analytically by the following equations:

$$X_{k+1} = F_k X_k + G_k W_k \quad (1)$$

$$Y_k = H'_k X_k + N_k \quad (2)$$

where:

X_k = a stochastic signal vector which is modeled in (1) as a first-order Markov process

N_k = measurement noise

W_k = input noise process which makes the signal stochastic

$Y_k = S_k + N_k$ is the measurement or observed process

$S_k = H'_k X_k$ is the system input process, a weighted value of the desired signal, X_k . It is the observed signal when there is no measurement noise. The notation ' means transpose.

k represents a discrete time argument, $k \geq 0$, and without loss of generality, k takes on integer values only.

We shall make the following assumptions with regard to the noise processes:

1. $\{N_k\}$ and $\{W_k\}$ are individual white processes. By white in discrete time, we mean that, for any k and ℓ , $k \neq \ell$, N_k and N_ℓ are independently random vectors and W_k and W_ℓ are independent random vectors.

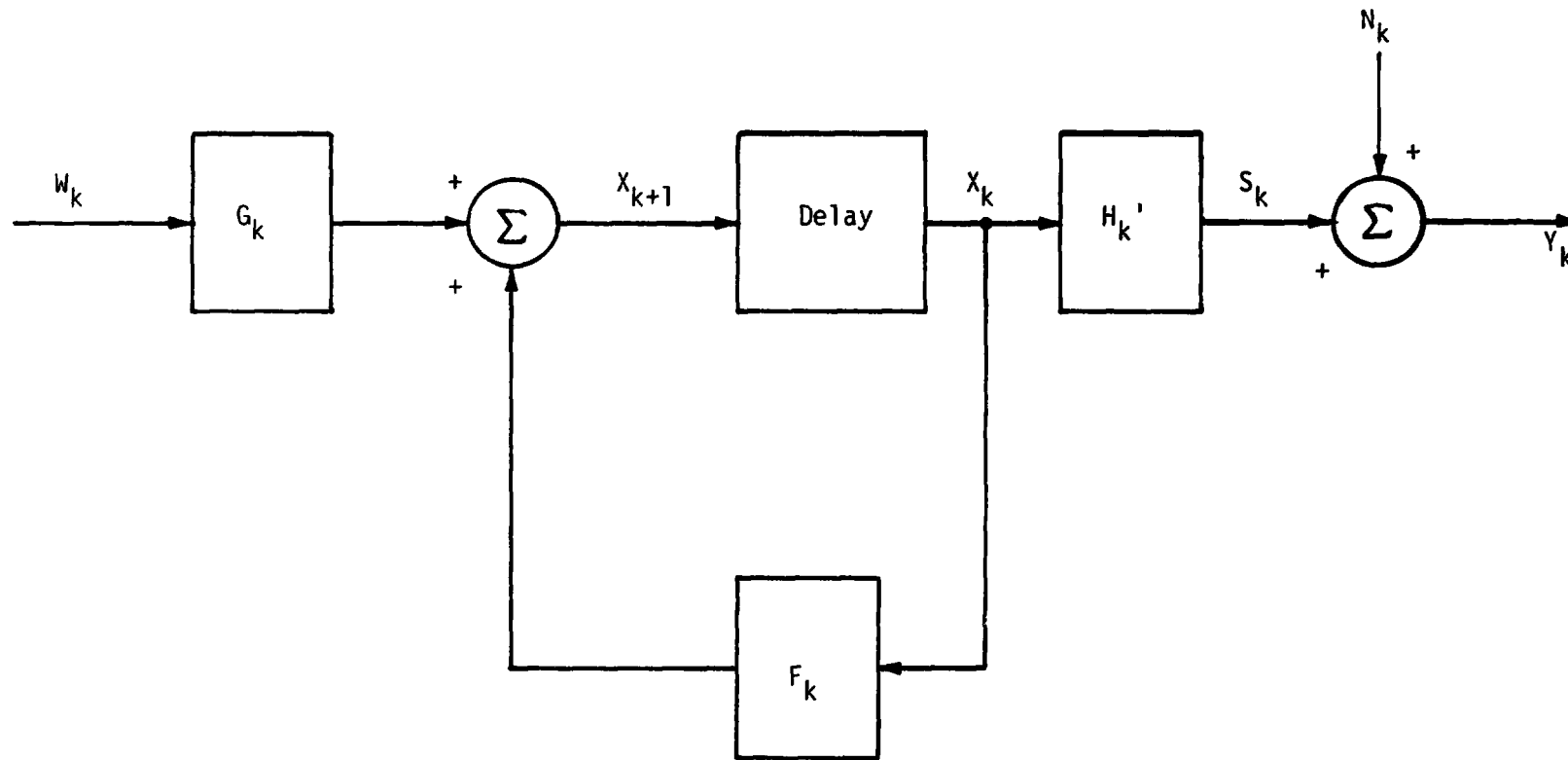


Figure 4. Basic Signal Model, a Finite-Dimensional Linear System

2. $\{N_k\}$ and $\{W_k\}$ are individual zero mean, Gaussian random vector processes with known covariance matrices, namely,

$$E \begin{bmatrix} N_k & N_\ell' \end{bmatrix} = R_k \delta_{k\ell} \quad (3a)$$

$$E \begin{bmatrix} W_k & W_\ell' \end{bmatrix} = Q_k \delta_{k\ell} \quad (3b)$$

where $\delta_{k\ell}$ is the Kronecker delta.

3. $\{N_k\}$ and $\{W_k\}$ are independent random vector processes.

In equations (1) and (2), $\{F_k\}$, $\{G_k\}$, and $\{H_k\}$ are sequences of deterministic (generally known) matrices which are chosen so that the first-order and second-order statistics of $\{X_k\}$ and $\{Y_k\}$ agree as closely as possible with those of the real world system being modeled.

3.3.3 Basic Kalman-Bucy Estimation Algorithms

Given the basic signal model in equations (1) and (2) and in Figure 4, the Kalman filter determines the best mean-square estimate of the process $\{X_k\}$, given the sequence of observations $\{Y_k\}$. The basic discrete time Kalman filtering problem can equivalently be stated as follows:

Suppose that the initial state vector, X_0 , of the desired signal is a Gaussian random vector with mean, $E(X_0) = \bar{X}_0$ and covariance matrix P_0 , and independent of the noise processes $\{N_k\}$ and $\{W_k\}$.

Then determine:

$$\hat{X}_{k/k-1} \triangleq E \left[X_k | Y_\ell, \ell \leq k-1 \right] \quad (4a)$$

and

$$\hat{X}_{k/k} \triangleq E \left[X_k | Y_\ell, \ell \leq k \right] \quad (4b)$$

and the associated error covariance matrices, $\Sigma_{k/k-1}$ and $\Sigma_{k/k}$, respectively. In (4a), the best estimate is denoted by $\hat{X}_{k/k-1}$ and represents a one-step predictor in that the estimate of $\{X_k\}$ is determined for time k given all of the observations up to time $k-1$, namely, $\{Y_0, Y_1, \dots, Y_{k-1}\}$. In (4b), the estimate is $\hat{X}_{k/k}$ and represents a filter estimate in that $\{X_k\}$ is determined for time k given all observations up to and including time k , namely, $\{Y_0, Y_1, \dots, Y_k\}$.

We distinguish between the one-step predictor and the filter versions of the Kalman algorithm since the one-step predictor is significantly simpler than the filtering algorithm. At this stage of the antenna calibration problem development, it is enough to consider only the one-step predictor version of the Kalman algorithm.

Referring again to (4), the notation on the right side represents the conditional expectations (ensemble average) of what is to be estimated given what has been observed. Under very general conditions, this is the best mean-square estimate.

Without proof, we now present the one-step predictor version of the class of Kalman estimators.

The Kalman one-step predictor comprises the system depicted in Figure 5 and is described for $k \geq 0$ by the equations

$$\hat{X}_{k+1/k} = \left[F_k - K_k H_k' \right] \hat{X}_{k/k-1} + K_k Y_k \quad (5)$$

with

$$\hat{X}_{0/-1} = X_0 \quad (6)$$

The gain matrix K_k is determined from the error covariance matrix by

$$K_k = F_k \Sigma_{k/k-1} H_k \left[H_k' \Sigma_{k/k-1} H_k + R_k \right]^{-1} \quad (7)$$

assuming the inverse exists (which is normally the case). The conditional error covariance matrix associated with the estimate $\hat{X}_{k/k-1}$ is defined as

$$\Sigma_{k/k-1} = E \left[\begin{pmatrix} X_k - \hat{X}_{k/k-1} & X_k - \hat{X}_{k/k-1} \end{pmatrix}' \middle| Y_1, \dots, Y_{k-1} \right] \quad (8)$$

and is minimized by the estimate defined in (4a). This conditional error covariance matrix can be computed recursively by the discrete time Riccati equation, namely,

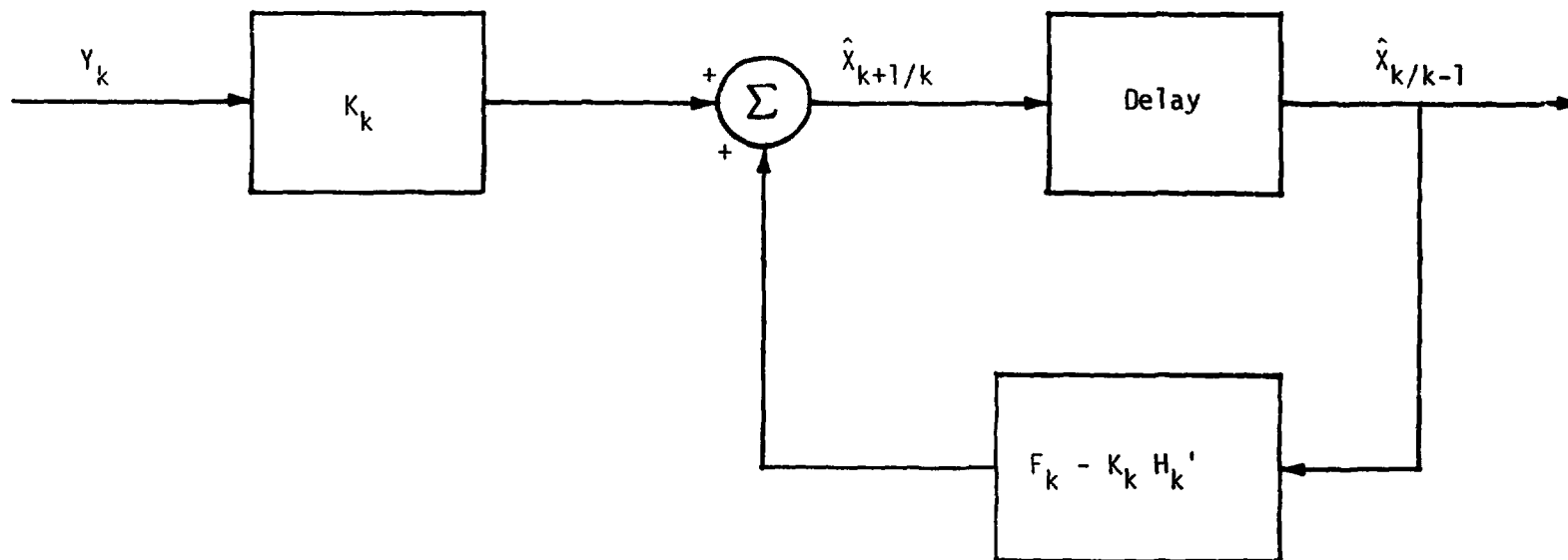


Figure 5. Basic Structure of One-Step Predictor Version of the Kalman-Bucy Estimator

$$\begin{aligned} \Sigma_{k+1/k} = & F_k \left[\Sigma_{k/k-1} - \Sigma_{k/k-1} H_k \left(H_k' \Sigma_{k/k-1} H_k + R_k \right)^{-1} \right. \\ & \left. \times H_k' \Sigma_{k/k-1} \right] F_k' + G_k Q_k G_k' \end{aligned} \quad (9)$$

This equation is initialized by

$$\Sigma_{0/-1} = P_0$$

3.3.4 Properties and Advantages of the Kalman Filter

We hereby enumerate certain properties and advantages of the Kalman algorithm:

1. The Kalman filter is a linear, finite-dimensional, discrete-time system. This is most advantageous in that it could have been nonlinear and/or infinite dimensional.

2. The output of the system $\{\hat{X}_{k/k-1}\}$ is dependent, of course, on the input $\{Y_k\}$. The conditional error covariance matrix, on the other hand, is independent of the input sequence $\{Y_k\}$. As a result, the error covariance matrix sequence $\{\Sigma_{k/k-1}\}$ and the gain matrix sequence $\{K_k\}$ can be computed before the filter is actually run.

3. The conditional covariance matrix definition in (8) identifies $\Sigma_{k/k-1}$ as the covariance matrix associated with a particular estimate. Since $\Sigma_{k/k-1}$ is independent of $\{Y_k\}$, however, we may take the expectation of both sides of (8) over all possible $\{Y_k\}$ to conclude that

$$\Sigma_{k/k-1} = E \left[\left(X_k - \hat{X}_{k/k-1} \right) \left(X_k - \hat{X}_{k/k-1} \right)' \right] \quad (10)$$

This means that $\Sigma_{k/k-1}$ is also an unconditional error covariance matrix associated with the Kalman filter, i.e., $\Sigma_{k/k-1}$ is the covariance matrix associated with the estimator.

4. The Kalman estimator is redrawn in Figure 6 to further emphasize its structure as a copy of the original signal model driven by the estimation error. The Kalman estimator can also be interpreted as developing an estimate of the observation at time k given all observations up to time $k-1$, namely $(\hat{Y}_{k/k-1})$, as shown in Figure 6. The error $(Y_k - \hat{Y}_{k/k-1})$,

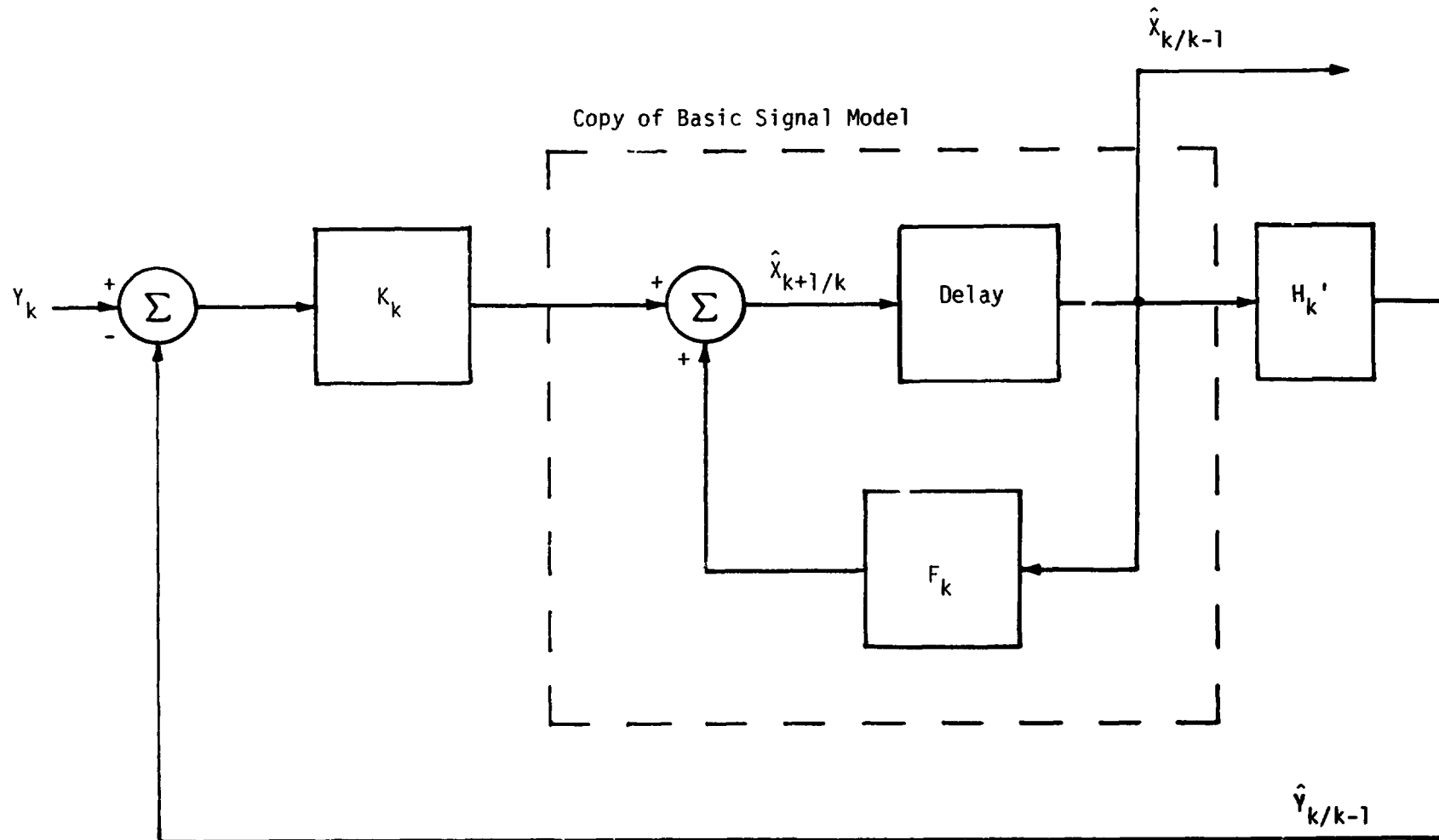


Figure 7. Kalman Estimator Redrawn to Emphasize its Structure as a Copy of the Original System Driven by the Estimation Error

is the input to the gain matrix K_k and is, essentially, what drives the estimator. If the error is zero, the copy of the basic signal model present in the estimator runs by itself and continues to generate additional estimates.

5. Suppose the underlying signal model is time invariant and the input and output noise processes are stationary. Then, F_k , G_k , H_k , Q_k , and R_k are all constant (independent of k). In general, however, $\Sigma_{k/k-1}$ and therefore K_k will not be constant, so the Kalman estimator will normally still be time-varying despite time invariance and stationarity in the signal model.

3.3.5 Application of Optimal Linear Filtering to the Antenna Calibration Problem

In this final section, we present the first version of tailoring the Kalman-Bucy estimation algorithm to the antenna gain calibration problem. As updated information is obtained about the accuracy of the various ground station and Shuttle parameters, the filtering algorithm will also be appropriately updated. We begin by making various observations:

1. For the present, we restrict attention to the S-band quads. The desired output is an updated antenna pattern which has a grid size of 2° -by- 2° . That is, the value for each 2° -by- 2° component of the entire pattern will be an estimate of the average gain in that region or the gain at the center. There is no way to distinguish between which of the two values are being represented by the desired output.

The specification of the angles for antenna pattern specification is shown in Figure 7. Based on a grid size of 2° -by- 2° , there are 4050 values necessary to specify the pattern for all four S-band quads.

The antenna pattern will be specified by the vector X_k at time k . Therefore, X_k is a 4050-dimensional vector. This is too large. We reduce it by a factor of four by considering S-band quad antennas separately. The dimensionality of X_k is therefore reduced to 1012, which is still quite large. The dimensionality can be further reduced substantially by considering only those positions of the patterns which have a reasonable chance of being used. At the present time, it is not clear how much reduction in dimensionality is appropriate.

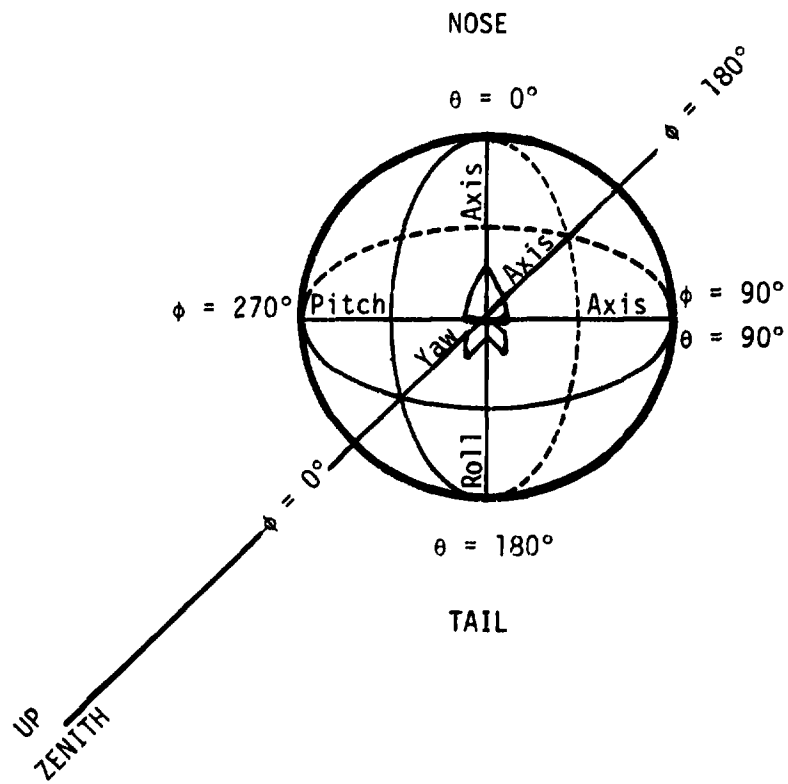


Figure 7. Specification of the Angles for Antenna Calibration

For each of the four S-band quads, there are three Shuttle configurations [1]:

- a. Solid Rocket Boosters (SRB) + External Tanks (ET) + Orbiter. (This configuration lasts from liftoff to the first approximately 120 seconds.)
- b. ET + Orbiter (first approximately 500 seconds)
- c. Orbiter only.

Ideally, therefore, there will be 12 distinct antenna patterns and each data point which is collected applies to only one of the patterns.

2. The raw data that is collected are AGC voltage measurements onboard the Orbiter and in the various ground stations, as shown in Figure 8. This data must be transformed into average received power at the various locations. As shown in Figure 8, signal strength will be simultaneously available from the Orbiter receiver and one of the ground stations. To perform this transformation requires calibration of the AGC on the Orbiter and at the various ground stations. At present, we assume that this transformation is carried out external to the filtering program so that the inputs to the antenna calibration program consist of signal strength.

3.3.6 Variable and Parameter Assignments for the Antenna Model

The basic signal model in Figure 4 is tailored to represent the antenna pattern as a function of time. As indicated above, X_k represents the vector of components which constitute the antenna pattern for one of the S-band quads in one of the configurations. To be specific, we assume that the Orbiter is in orbit since most of the data generated will be for that configuration. We make the following assignments:

X_0 represents the antenna pattern measured in the antenna ground range and is assumed known

X_k , $k \geq 1$ represents the antenna pattern for the antenna mounted onboard the Orbiter at the k th time period. More will be said subsequently about how k represents time.

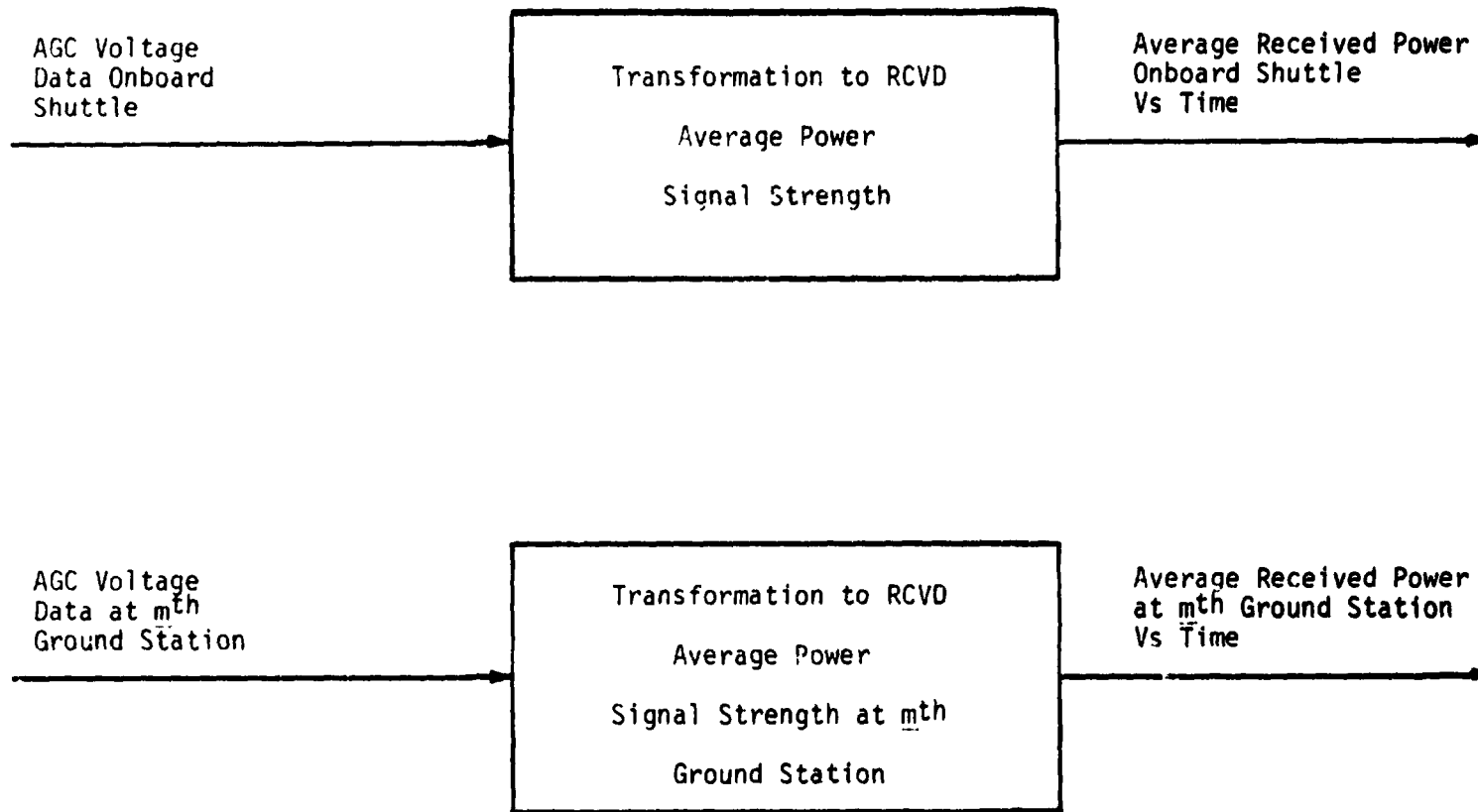


Figure 8. Conversion of AGC Voltage to Received Average Power Signal Strength

Each integer value of k represents that portion of one flight when communication is with one ground station. This is best seen by inspection of Figure 9, where an example is presented. The time $k = 1$, for example, corresponds to the Orbiter communicating with ground station BDA (see [1]) for designations, locations, etc.) during which measurements were taken at those antenna component indices across from the vertical bar above $k = 1$ in Figure 9.

The antenna pattern associated with X_1 is the modified version of X_0 due to the appendages on the Shuttle and due to being mounted on the Orbiter itself. What we are after is an estimate of X_1 . It is assumed that the antenna pattern remains constant throughout a given mission. Therefore,

$$X_1 = X_2 = \dots = X_k = \dots = X_{K_1} \quad (11)$$

where K_1 represents the last time period of the first mission. The antenna pattern X_1 is related to X_0 by

$$X_1 = F_0 X_0 \quad (12)$$

where the matrix F_0 is unknown. Of course, our problem can be equivalently stated as finding F_0 . We assume that F_0 is diagonal, unknown and constant. The values of F_k are

$$F_k = 0 \quad , \quad 1 \leq k \leq K_1 - 1 \quad (13)$$

Equivalently stated, the matrix F_k remains zero throughout the remainder of the first mission.

Since the antenna pattern is assumed to remain constant, then

$$G_k = 0 \quad , \quad Q_k = 0 \quad \text{for all } k. \quad (14)$$

At the beginning of the second mission, we assume that the antenna pattern is uniformly attenuated by the factor "a." This is modeled by

$$X_{K_1+1} = a X_{K_1} \quad (15)$$

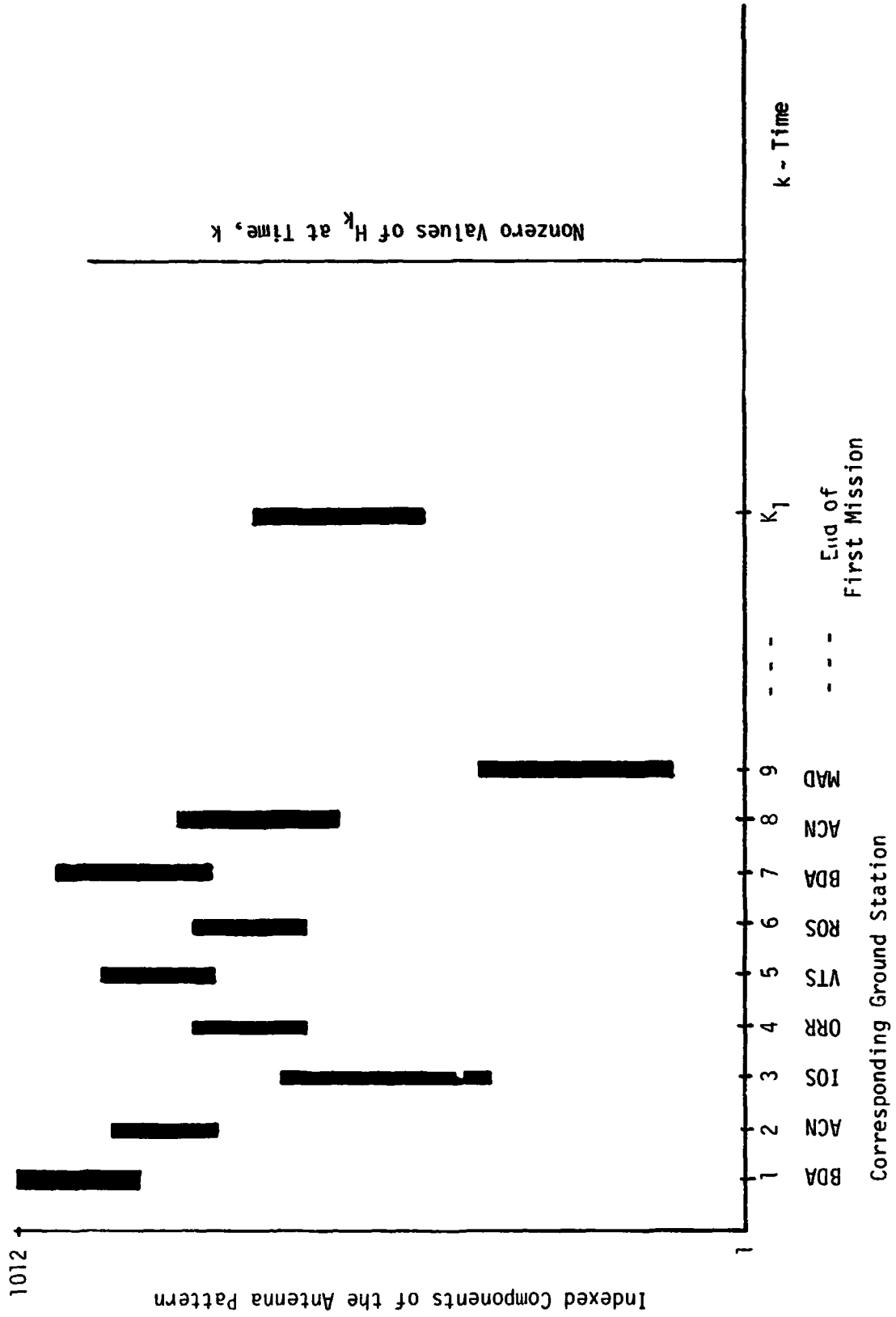


Figure 9. Antenna Measurements Taken versus Time Assignments, k

which is equivalent to saying

$$F_{K_1} = a I \quad (16)$$

where I is an identity matrix. The attenuation factor "a" is initially unknown and results from the TPS tiles being charred during reentry. The attenuation parameter "a" can be estimated, however, from signal strength measurement variations from one mission to the next.

3.3.7 Variable and Parameter Assignments for the Observations

The weighting between the value of antenna gain and the signal strength observation is performed by the matrix H_k . This matrix is also diagonal. For a particular value of k , it has nonzero values only for those indices which correspond to antenna positions where measurements were obtained, as indicated in Figure 9.

The nonzero values of H_k convert the antenna gain to signal strength. This is accomplished by the communication link equation

$$P_R = \frac{P_T G_T G_R \lambda^2}{(4\pi)^2 R^2} \quad (17)$$

For the downlink, the parameters in (17) are as follows:

P_T = Orbiter transmitted power

G_T = antenna gain of Orbiter, at some designated angular coordinates (θ, ϕ)

G_R = Ground station antenna gain

λ = wavelength

R = range between Orbiter and designated ground station.

All measurements taken at a given ground station associated with a particular orbital pass will be associated with a particular value of k .

For the downlink, each component of H_k will contain

$$\frac{P_T G_R \lambda^2}{(4\pi)^2 R^2},$$

which relates the antenna gain onboard the Orbiter to the signal strength in the ground station receiver.

3.3.8 Basic Flow Diagram for Antenna Calibration Estimation

A basic flow diagram for antenna calibration estimation is shown in Figure 10. The Kalman estimation algorithm is shown in Figure 6, where all necessary matrices are assumed known. In Figure 10 and the previous sections, we have described the inputs required to compute the matrices in Figure 6.

As more specific information is obtained regarding the availability and accuracy of the necessary parameters, the basic flow diagram will be developed in further detail.

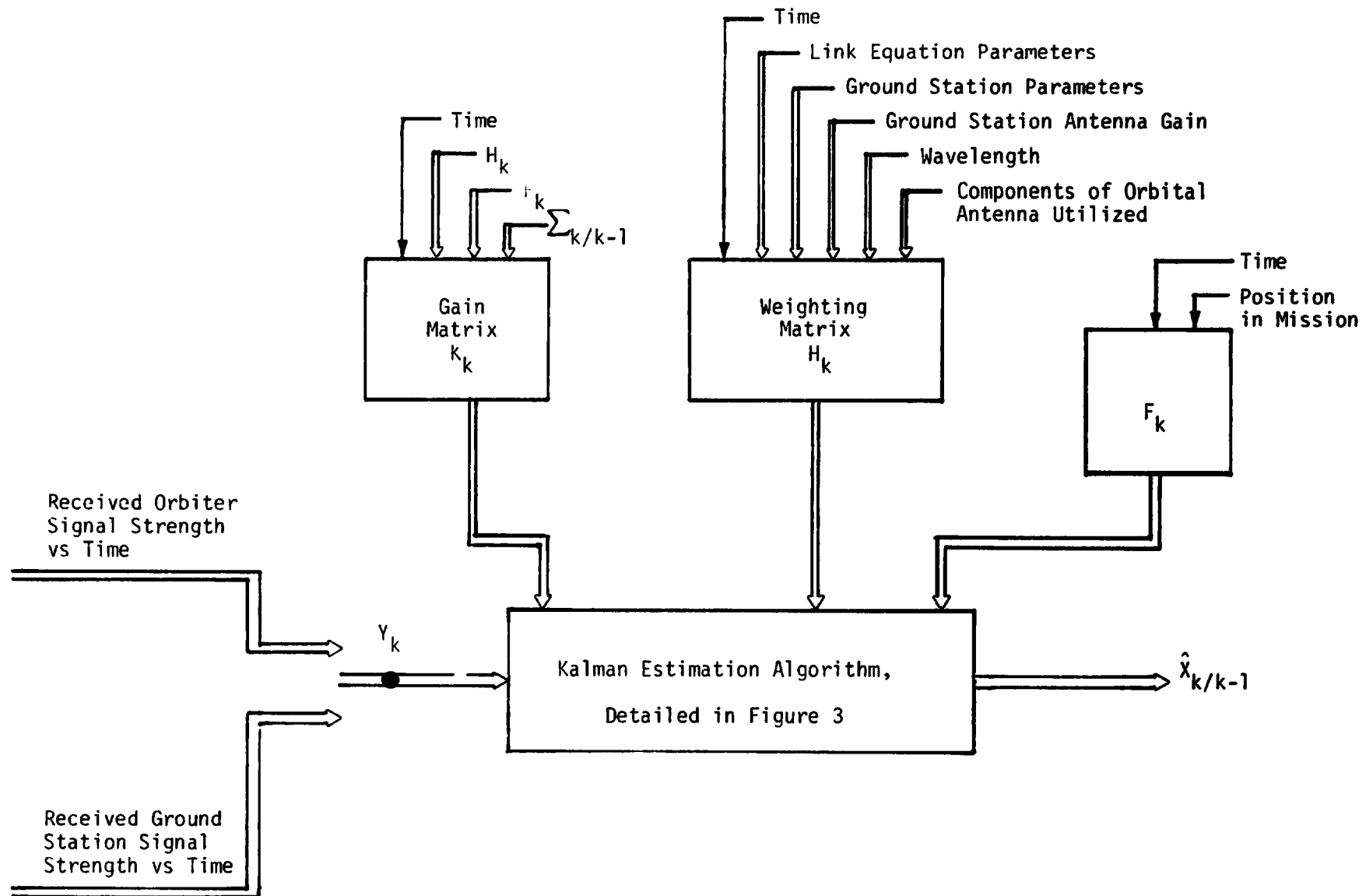


Figure 10. Basic Flow Diagram for Antenna Calibration Estimation

3.4 STDN Calibration Considerations

In order to assess the magnitude of the problem of accurately calibrating the gain of the STDN stations, a preliminary investigation of the techniques utilized by DSN to calibrate DSN stations at S-band has been undertaken. The investigation has found that the DSN has the capability of calibrating station antenna gain to a 3σ accuracy of ± 0.1 dB or better. This accuracy is achieved as a result of making a series of very exact measurements and utilizing averaging techniques on the data. On a one-shot basis, wherein one or very few measurements are used, a 3σ accuracy of ± 0.3 dB can be expected.

The technique utilized by DSN essentially utilizes accurately measured radio stars as RF sources. The flux density of several selected stars, listed in Table 1, was determined by means of an accurately calibrated DSN station, DSS-13 (Goldstone 26M). This station was calibrated by means of a gain calibration transfer technique. The ultimate source of calibrated antenna gain was an S-band Standard Gain Horn developed and accurately calibrated by JPL specifically for this purpose. The major steps for calibrating DSN stations, via the radio star, beginning with the Standard Gain Horn, are shown in Figure 11. A block diagram of the DSN gain transfer system is shown in Figure 12. The complexity and problems associated with implementing these types of calibration techniques at selected STDN stations will be investigated in the next phase of the study.

Table 1. Absolute Flux Density and Antenna Temperatures at 2295 MHz

Source	Flux Density $S \pm 1\sigma$, JY	100% Efficient Antenna T_S , K		
		26 m	34 m	64 m
3C123	31.0 ± 0.61	5.92	10.2	36.2
3C218 (Hydra A)	26.7 ± 0.51	5.10	8.78	31.2
3C274 (Virgo A)	136 ± 2.6	25.9	44.6	158
3C405 (Cygnus A)	887 ± 15	169	292	1034
3C461 (Cassiopeia A)*	1525 ± 27	291	502	1777

* Flux density known to decrease approximately 1% per year (observation epoch 1972.6)

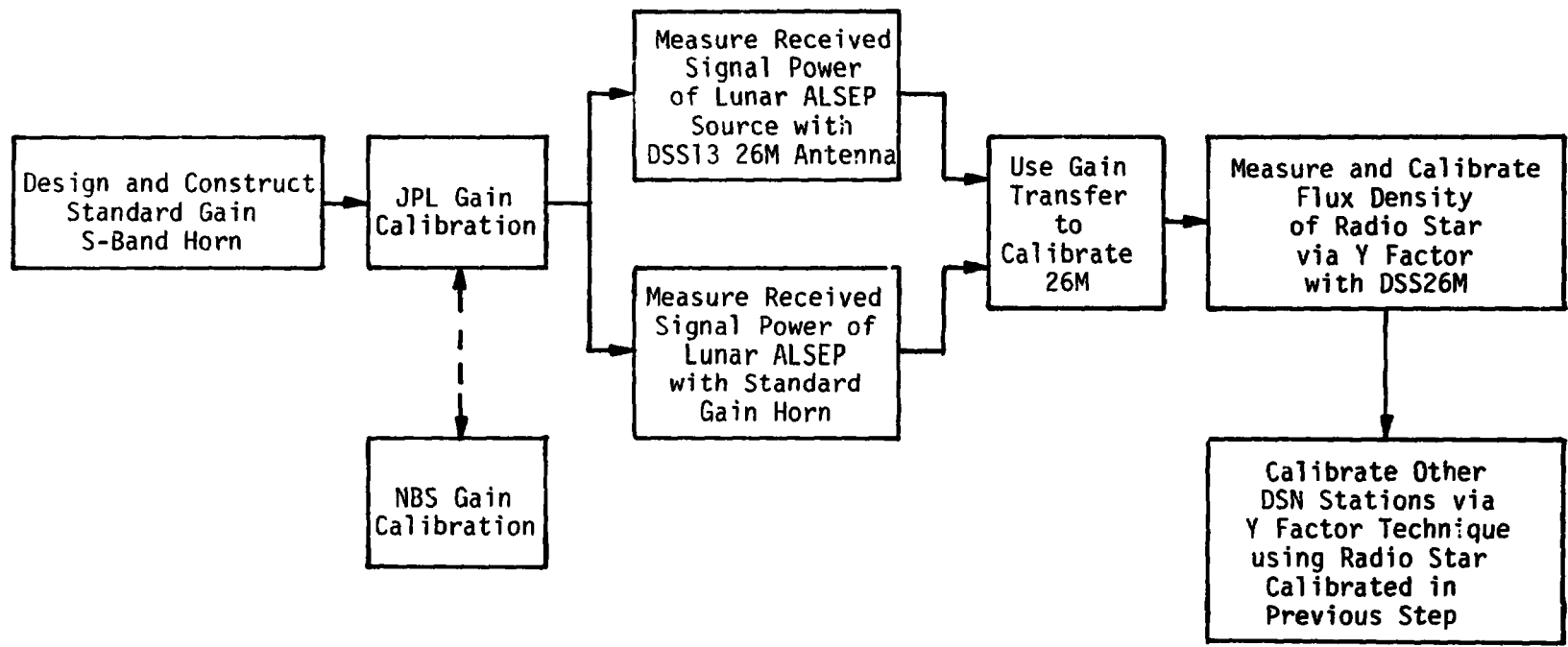


Figure 11. Flow Chart for Calibrating Arbitrary DSN Station

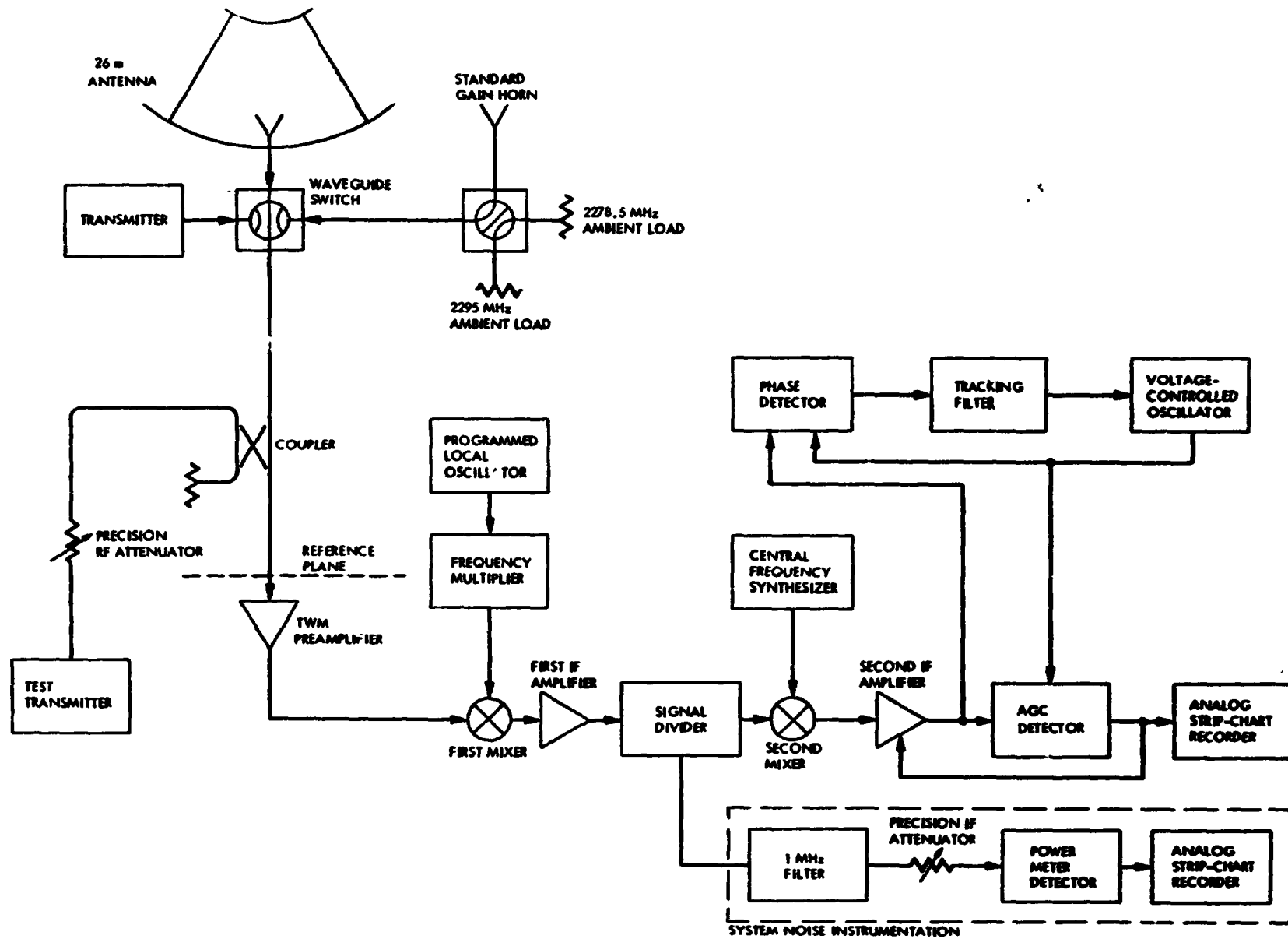


Figure 12. Master Station Block Diagram Gain Transfer Calibration System

4.0 KU-BAND COMMUNICATION SYSTEM STUDY

The Ku-band communication system study investigated the accuracy with which the TDRS Ku-band antenna could be pointed at the Orbiter Ku-band antenna, as discussed in Section 4.1. The Orbiter Ku-band system high data rate convolutionally coded return link was modified to eliminate the need for a minimum transition density to keep the bit synchronizer on the ground in lock. Section 4.2 presents the performance characteristics of the modification to the convolutional encoder. The performance effects due to TDRSS user constraints of data bit clock jitter and data asymmetry on unbalanced QPSK with noisy phase reference are discussed in Section 4.3.

4.1 Analysis of TDRS Ku-Band Pointing Accuracy

In order to meet EIRP specifications, the TDRS must point its high-gain Ku-band antenna to within 0.24° of the user. TRW has done extensive analysis and simulation of the open-loop pointing budget and has concluded [6] that the TDRS is capable of meeting the requirements under worst-case conditions. This report is a review of the TRW analysis, with emphasis on the Space Shuttle as a user. Certain parameters considered by TRW improve with respect to the Shuttle, and others degrade. The net effect, if the TRW analysis were flawless, would be that the TDRS could easily service the Shuttle with the specified pointing accuracy. However, TRW assumptions as to residual errors after calibration appear to be optimistic. As a result, the ability of the TDRS to point to the Shuttle to within 0.24° is marginal with more realistic assumptions as to residual calibration errors.

In subsequent sections, we discuss the various parameters used to estimate the pointing accuracy, with emphasis on the more critical parameters. Error budgets are given using our best estimates of attainable measurement errors. We consider errors with the Shuttle at 100-mile and 200-mile orbits and the TRW worst-case atmospheric explorer orbit.

4.1.1 TDRS Calibration Errors

Item 17 of the attached pointing budgets appears to be the most controversial in the pointing budget. On orbit, the TDRS high-gain Ku-band antennas will be calibrated using the White Sands terminal. Specifically, the autotrack null will be calibrated using the autotrack error signal [7]. Prior to calibration, the autotrack null to mechanical bore-sight uncertainty is greater than 1° .

During calibration, the antenna is swept past the White Sands terminal and the autotrack error signal is used to estimate the position of the null relative to the gimbal angle readout. Errors introduced by lags in the system are first calibrated out by offsetting the null and sweeping a fixed pattern. Local maxima and minima are correlated with gimbal angle readouts to estimate the system time lag.

Table 2 of [6] is a list of the errors involved in the calibration procedure. Due to the complicated nature of the model, the resultant

Parameter	True Value	Error (difference between true and nominal values)
a. WSGT look angles	$\theta_u = 7^\circ, \phi_u = 5^\circ$	$\Delta\theta_u, \Delta\phi_u = B_1 + B_2$ $B_1 \sim 0.01^\circ \sin\left(\frac{2\pi t}{24} + \theta\right)$ $B_2 \sim N(0, 1.1 \times 10^{-4})$
b. Electrical Boresight Angles	$[\theta_{BS}^2 + \phi_{BS}^2]^{\frac{1}{2}} \sim \text{Unif}(\pm 0.1^\circ)$	$\Delta\theta_{BS} = 0.006 + 0.015 \sin\left(\frac{2\pi t}{24} + \theta\right)$ $+ \sqrt{u_1} \cdot N_1$ $\Delta\phi_{BS} = \pm \sqrt{1-u_1} \cdot N_1$ $u_1 \sim \text{Unif}(0, 1)$ $N_1 \sim N(0, 1.1 \times 10^{-4})$
c. Attitude Angles	$\theta_a \sim N(u_\theta, 0.0025)$ $\phi_a \sim N(u_\phi, 0.0025)$ $\psi_a \sim N(0, 0.1111)$ $u_\theta = \begin{cases} 0 & \text{during calib.} \\ \text{Unif}(\pm 2.0) & \text{after calib.} \end{cases}$ $u_\phi = \begin{cases} 0 & \text{during calib.} \\ \text{Unif}(\pm 0.5) & \text{after calib.} \end{cases}$	$\Delta\theta_a, \Delta\phi_a \sim N(0, 4.131 \times 10^{-4})$ $\Delta\psi_a = E_1 + E_2 + E_3$ $E_1 \sim 0.191^\circ \sin\left(\frac{2\pi t}{12} + \theta\right)$ $E_2 \sim 0.14^\circ \sin\left(\frac{2\pi t}{0.5} + \theta\right)$ $E_3 \sim N(0, 7.291 \times 10^{-4})$
d. Gimbal Misalignment Angles	$[\theta_D^2 + \phi_D^2 + \psi_D^2]^{\frac{1}{2}}$ $\sim N(0, 0.134)$	$[\Delta\theta_D^2 + \Delta\phi_D^2 + \Delta\psi_D^2]^{\frac{1}{2}}$ $\sim N(0, 4.841 \times 10^{-4})$
e. Time-tagging Errors	-	$\text{CBET}, \text{CBE}^2 = A_1 + A_2 + A_3 + A_4 + A_5$ $A_1 \sim 0.0075^\circ \text{Int}(\pm 1)$ $A_2 \sim \text{Unif}(\pm 0.05^\circ)$ $A_3 \sim 0.01^\circ \sin(2\pi t + \theta)$ $A_4 \sim N(0, 2.951 \times 10^{-7})$ $A_5 \sim 0.0075^\circ \text{Int}(\pm 2)$

Notation: $\text{Unif}(\pm C)$ = random variable uniform on the interval $[-C, C]$.

$N(0, \sigma^2)$ = normal random variable with 0 mean, variance σ^2 .

$\text{Int}(\pm N)$ = discrete random variable taking on the values $(-N, \dots, N)$

B 's = uniform $(0, 2\pi)$ random variables.

Table 2. Summary of Error Models - A/T Null

residual calibration error has been determined by TRW using a Monte Carlo simulation. The fixed error after calibration, item 17 of Table 3, is estimated at 0.0418° N-S and 0.0471° E-W. The autotrack noise (item A₄ of Table 2) used in the simulation is based on the worst-case minimum autotrack scale factor of 0.041 V/V/°. We feel that it is probable that the null can be measured to the accuracy claimed by TRW since worst-case estimates of the error terms were used in the model and the slope of the autotrack null is steep.

TRW has used the same technique to estimate the residual calibration errors of the transmit peak (boresight). The intent is to calibrate out the null-to-transmit boresight misalignment. This misalignment is composed of two parts: an electrical boresight term and a boresight null shift term. The electrical boresight term is specified at 0.06° and the null shift term is specified at 0.032° , for a possible worst-case misalignment of 0.092° . TRW, however, has chosen to optimistically use an electrical misalignment of 0.013° and a null shift misalignment of 0.012° . Inasmuch as the contractor building the antenna will sign up to only the specified values (0.06° and 0.032°), we feel that the more optimistic assumptions by TRW are not valid; consequently, we use the specification values in the estimates of the residual errors. In addition, these are not random errors--they are fixed quantities. Hence, they are added directly, not RSS'ed, to the worst-case E-W residual error of the autotrack null. This would not pose a problem if the transmit boresight could be calibrated; the misalignment error could be removed.

The transmit boresight misalignment is calibrated by observing the output of a Hewlett-Packard Model 436A digital power meter, as the beam is swept past the ground station. The peak is tagged and correlated with the gimbal position readout. TRW has calculated that, at a received C/N of 45.5 dB, the peak can be read to an accuracy of 1.22×10^{-4} dB, equivalent to $8.94 \times 10^{-4}^\circ$. Two problems arise: the power meter has a specified accuracy of ± 0.02 dB and a least count (resolution) of 0.01 dB, and the fast variations (item 19 of Table 3) have a peak of 0.0876° , equivalent to a variation of 1.1 dB. Either item will preclude the claimed accuracy. The fast errors, consisting of quantization noise and mechanical noise, will appear in the power meter. Even in the absence of the fast variations, the time constant of the power meter will prevent the measurement to even 0.01 dB.

	One-Dimensional Errors				Fast Variations (deg)
	Fixed (Max) (deg)	Slow Variations (3σ)			
		N-S (deg)	E-W (deg)	Yaw (deg)	
1. Software					0.026
<u>Antenna/Boom</u>					
2. Thermal (Boom)		-	0.021	0.013	
3. Thermal (Antenna)		0.0	0.06	-	
4. Elect/Mech Alignment Spacecraft Z to Z _{SA} Misalignment	1.0				
Spacecraft Z to Z _{SA} Measurement Uncertainty	0.066				
Z _{SA} (Mech) to A/T Elect Earth Sensor	0.2				
5. Null Loc Alignment	0.05				
6. Mech Alignment	0.05				
7. Bias Errors		0.0500	0.0494	-	
8. Power Supply		0.0100	0.0099	-	
9. Radiance Uncertainty		0.0150	0.0148	-	
10. Noise and Quantization					0.03 (0.04)*
<u>Control System</u>					
11. Step Size & Dynamic Oscillations					0.06 (0.08)**
12. GDA Position Error					0.04
13. Drive Axis Wobble					0.03
14. Yaw Coupling Errors		-	-	0.0382	
15. User Ephemeris		-	-	0.113	
16. TDRS Position Determination		0.014	0.014	-	
17. Fixed Error After Calibration		N-S 0.0418 E-W 0.107			
18. RSS of the Slow Varying Errors			0.0550	0.0836	0.120
19. PSS of the Fast Varying Errors					0.0876
20. Uncertainty Ellipse Major Axis (3σ)	0.170				
21. Uncertainty Ellipse Minor Axis (3σ)	0.103				
22. Probability of Pointing within 0.24 degree	0.986				
23. Pointing Loss to KSA Forward EIRP (dB) at 0.24 degree	9.6				

* Exceeds 0.03 degrees for 20 sec following slew start or stop of other SA antenna.

** Exceeds 0.06 degrees for 15 sec following slew start or stop of other SA antenna.

Table 3. TDRS/Shuttle Transmit Pointing Budget, 0.06° Null-to-Boresight Error

In the next section, we discuss revised pointing budgets based on null-to-boresight misalignments of 0.06° and 0.092° . The 0.06° misalignment is used as a likely value to be encountered with the actual antenna, and the 0.092° is the worst-case specification. These are added directly to the null E-W calibration error to form the mean of the probability ellipse used in the calculation of the probability of pointing within 0.24° of the Shuttle.

4.1.2 Open-Loop Pointing Budget

Tables 3 and 4 are the open-loop pointing budgets, TDRS-to-Shuttle. Items 1-6 are taken directly from [6]. Items 1, 2 and 3 are beyond the scope of this analysis and are taken at face value. The values given are not unreasonable; however, verification would require extensive analysis of the software algorithms and the mechanical model of the system. Items 4, 5 and 6 are calibrated out by the procedure described earlier, with residual errors given in item 17. Items 7, 8 and 9 remain unchanged in the N-S direction but, for the Shuttle, increase to 0.0494° , 0.0099° and 0.0148° , respectively, in the E-W direction. They are given as the pitch error allocation (0.05° , 0.01° and 0.015°) times \cos (target elevation), with target elevation equal to 8.9° for the Shuttle.

Items 10-13 are also taken directly from [6]. Again, verification of these quantities would require extensive analysis of the system hardware and structural design.

Item 14, yaw coupling, is decreased from worst-case 0.129° for the atmospheric explorer to 0.0382° for the Shuttle. This error is given as $0.25^\circ \sin$ (target elevation).

Item 15, user ephemeris, is given as the 9-second uncertainty times the relative user angular velocity, $\dot{\theta}$. With h the altitude of the user in miles,

$$= \frac{1.1436 \times 10^{12}}{(6.371 \times 10^8 + h \times 1.609 \times 10^5)^{3/2}} \times \frac{(h + 3959)}{(22284 - h)} .$$

Thus, for $h = 100$ miles, $\dot{\theta} = 1.25 \times 10^{-2} \text{ }^\circ/\text{sec}$ and the uncertainty is 0.113° . For $h = 200$ miles, $\dot{\theta} = 1.24 \times 10^{-2} \text{ }^\circ/\text{sec}$ and the uncertainty is 0.112° . We use the worst-case value of 0.113° in the revised pointing budgets.

Item 16, TDRS position determination, is taken directly from [6]. The N-S error of item 17 (0.0418°), fixed error after calibration, is taken from [6] and is a result of TRW simulation of the effect of all anticipated error sources, as discussed in a prior paragraph. The E-W residual error is the direct sum of the transmit peak-to-null boresight misalignment and the residual null calibration error (0.0471°).

Items 18 and 19 are the RSS of the error in the respective columns. Item 20 is the RSS of items 18 E-W, 18 yaw and 19. Item 21 is the RSS of item 18 N-S and item 19. Items 20 and 21 are termed the peak values of the errors and used as 3σ values for probability calculations, with item 17 N-S used as the mean of the minor axis and item 17 E-W used as the mean of the major axis of a bivariate Gaussian distribution.

Item 22 is the integral of the bivariate Gaussian over a circle of 0.24° , which gives a pointing loss of 9.6 dB.

4.1.3 Results of Revised Pointing Budget Analysis

Two cases of null-to-boresight misalignment were analyzed for the Shuttle orbit. A nominal 0.06° misalignment is used to represent a compromise between the optimistic 0.03° used by TRW and the worst-case 0.092° in the specification. The results of this analysis are presented in Table 3. The 0.06° case is equivalent to a pointing loss of 0.5 dB during calibration of the transmit boresight. This is well above the accuracy of the power meter, and may be attainable if not masked by the fast variations extant in the hardware. The probability of pointing to within 0.24° (item 22) is 0.986 for this case.

As a worst-case, a null-to-boresight misalignment of 0.092° is used. From Table 4, the probability of pointing to within 0.24° is 0.954.

For purposes of comparison with the TRW worst-case (atmospheric explorer) budget, Table 5 gives the pointing budget based on the 0.137° E-W worst-case residual error. TRW calculates a probability of pointing within 0.24° of 0.993, while the worst-case estimate gives a probability of 0.898.

	One-Dimensional Errors				
	Fixed (Max) (deg)	Slow Variations (3σ)			Fast Variations (deg)
		N-S (deg)	E-W (deg)	Yaw (deg)	
1. Software					0.026
<u>Antenna/Boom</u>					
2. Thermal (Boom)		-	0.021	0.013	
3. Thermal (Antenna)		0.0	0.06	-	
4. Elect/Mech Alignment Spacecraft Z to Z_{SA} Misalignment	1.0				
Spacecraft Z to Z_{SA} Measurement Uncertainty	0.066				
Z_{SA} (Mech) to A/T Elect Earth Sensor	0.2				
5. Null Loc Alignment	0.05				
6. Mech Alignment	0.05				
7. Bias Errors		0.0500	0.0494	-	
8. Power Supply		0.0100	0.0099	-	
9. Radiance Uncertainty		0.0150	0.0148	-	
10. Noise and Quantization					0.03 (0.04)*
<u>Control System</u>					
11. Step Size & Dynamic Oscillations					0.06 (0.08)**
12. GDA Position Error					0.04
13. Drive Axis Wobble					0.03
14. Yaw Coupling Errors		-	-	0.0382	
15. User Ephemeris		-	-	0.113	
16. TDRS Position Determination		0.014	0.014	-	
17. Fixed Error After Calibration		N-S 0.0418 E-W 0.137			
18. RSS of the Slow Varying Errors			0.0550	0.0836	0.120
19. RSS of the Fast Varying Errors					0.0876
20. Uncertainty Ellipse Major Axis (3σ)	0.178				
21. Uncertainty Ellipse Minor Axis (3σ)	0.103				
22. Probability of Pointing within 0.24 degree	0.954				
23. Pointing Loss to KSA Forward EIRP (dB) at 0.24 degree	9.6				

* Exceeds 0.03 degrees for 20 sec following slew start or stop of other SA antenna.

** Exceeds 0.06 degrees for 15 sec following slew start or stop of other SA antenna.

Table 4. TDRS/Shuttle Transmit Pointing Budget, 0.092° Null-to-Boresight Error

	One-Dimensional Errors				Fast Variations (deg)
	Fixed (Max) (deg)	Slow Variations (3σ)			
		N-S (deg)	E-W (deg)	Yaw (deg)	
1. Software					0.026
<u>Antenna/Boom</u>					
2. Thermal (Boom)		-	0.021	0.013	
3. Thermal (Antenna)		0.0	0.06	-	
4. Elect/Mech Alignment Spacecraft Z to Z_{SA} Misalignment	1.0				
Spacecraft Z to Z_{SA} Measurement Uncertainty	0.066				
Z_{SA} (Mech) to A/T Elect	0.2				
<u>Earth Sensor</u>					
5. Null Loc Alignment	0.05				
6. Mech Alignment	0.05				
7. Bias Errors		0.0500	0.0429	-	
8. Power Supply		0.0100	0.0086	-	
9. Radiance Uncertainty		0.0150	0.0129	-	
10. Noise and Quantization					0.03 (0.04)*
<u>Control System</u>					
11. Step Size & Dynamic Oscillations					0.06 (0.08)**
12. GDA Position Error					0.04
13. Drive Axis Wobble					0.03
14. Yaw Coupling Errors		-	-	0.129	
15. User Ephemeris		-	-	0.122	
16. TDRS Position Determination		0.014	0.014	-	
17. Fixed Error After Calibration	{ N-S 0.0418 E-W 0.137				
18. RSS of the Slow Varying Errors		0.0550	0.795	0.1776	
19. RSS of the Fast Varying Errors					0.0876
20. Uncertainty Ellipse Major Axis (3σ)	0.213				
21. Uncertainty Ellipse Minor Axis (3σ)	0.103				
22. Probability of Pointing within 0.24 degree	0.898				
23. Pointing Loss to KSA Forward EIRP (dB) at 0.24 degree	9.6				

* Exceeds 0.03 degrees for 20 sec following slew start or stop of other SA antenna.

** Exceeds 0.06 degrees for 15 sec following slew start or stop of other SA antenna.

Table 5. TDRS/Atmospheric Explorer Pointing Budget, Worst-Case

4.1.4 Conclusions

A significant loophole has been found in the TRW analysis of the transmit pointing budget. While the pointing loss may be marginally acceptable for the Shuttle, other users could experience difficulty in acquisition. These results are predicated on the other errors being within budget. It should be emphasized that the remaining error budget items are TRW engineering estimates rather than hard specifications. Errors greater than the TRW estimates due to mechanical noise, quantization effects, thermal effects or larger than anticipated Earth sensor errors will adversely affect the ability of the Shuttle to acquire TDRS.

Should the null-to-boresight error, however, be larger than the worst-case 0.092° , it could probably be calibrated to this value using the techniques proposed by TRW. This error is equivalent to an error of 1.25 dB at the power meter, and should be discernible if the other errors are within bounds.

4.2 Performance Characteristics of the Ku-Band Channel 3 Convolutional Code with G_2 Inversion

The present implementation of the high data rate (mode 1, channel 3) error-correcting code can engender system performance degradation under certain input conditions. The data-derived clock at the receiver requires a minimum transition density, e.g., a transition-free string of data exceeding the maximum specified value of 64 symbols can cause loss of lock at the bit synchronizer. Uncoded input data consisting of all zeros (not necessarily an unlikely event) will result in a coded output of all zeros and loss of bit synchronizer lock. In order to preclude this event, the code is being modified by inversion of the second encoded check bit (G_2) out of the encoder. This check bit is reinverted after demodulation and prior to decoding.

Users should be made aware of two minor problems with the proposed method of G_2 inversion. The encoded symbol stream can slightly exceed the maximum transition-free length under certain pathological (low probability) conditions and, with high probability, the decoder will output meaningless data if the uncoded input data is all zeros or all ones. The first problem is probably of no concern since the input data giving rise to the long transition-free run of coded symbols has a low probability of occurrence. The second problem may be of some concern since input data consisting of all zeros may be valid if the user ignores the constraints of at least 64 transitions in 512 bits and no more than 64 bits without a transition.

4.2.1 Run Length Performance of the Convolutional Code with G_2 Inversion

Figure 13 is a representation of the return link encoder with G_2 inversion. This code is derived from the NASA Planetary Standard rate one-half constraint length 7 code shown in Figure 14 by replacing $g(x)$ with $g(x^5)$. The resultant code is an interleaved version of five constraint length 7 codes and is decoded with five parallel Viterbi decoders. The run length properties of the $K = 7$ code have been investigated by Simon and Smith [8] who have shown that an input sequence of 10101001011001 (read left to right) will result in an output sequence of 1000000000000001 with G_2 inversion. That is, the maximum run length is 14. The results of Simon and Smith can easily be extended to the modified $K = 31$ code by repeating each input symbol five times. Referring to Figure 1, by alternately concatenating five check symbols from the first mod 2 adder and five from the second, each symbol in the original $K = 7$ code will be replaced by five symbols. Thus, if each input bit is repeated five times, each check symbol will be repeated five times and the maximum run length is extended to 70 symbols. Note, however, that a unique 62-bit input data stream (or its complement) is required. Assuming "random" input data at 50 Mbps, this event should occur once every several thousand years.

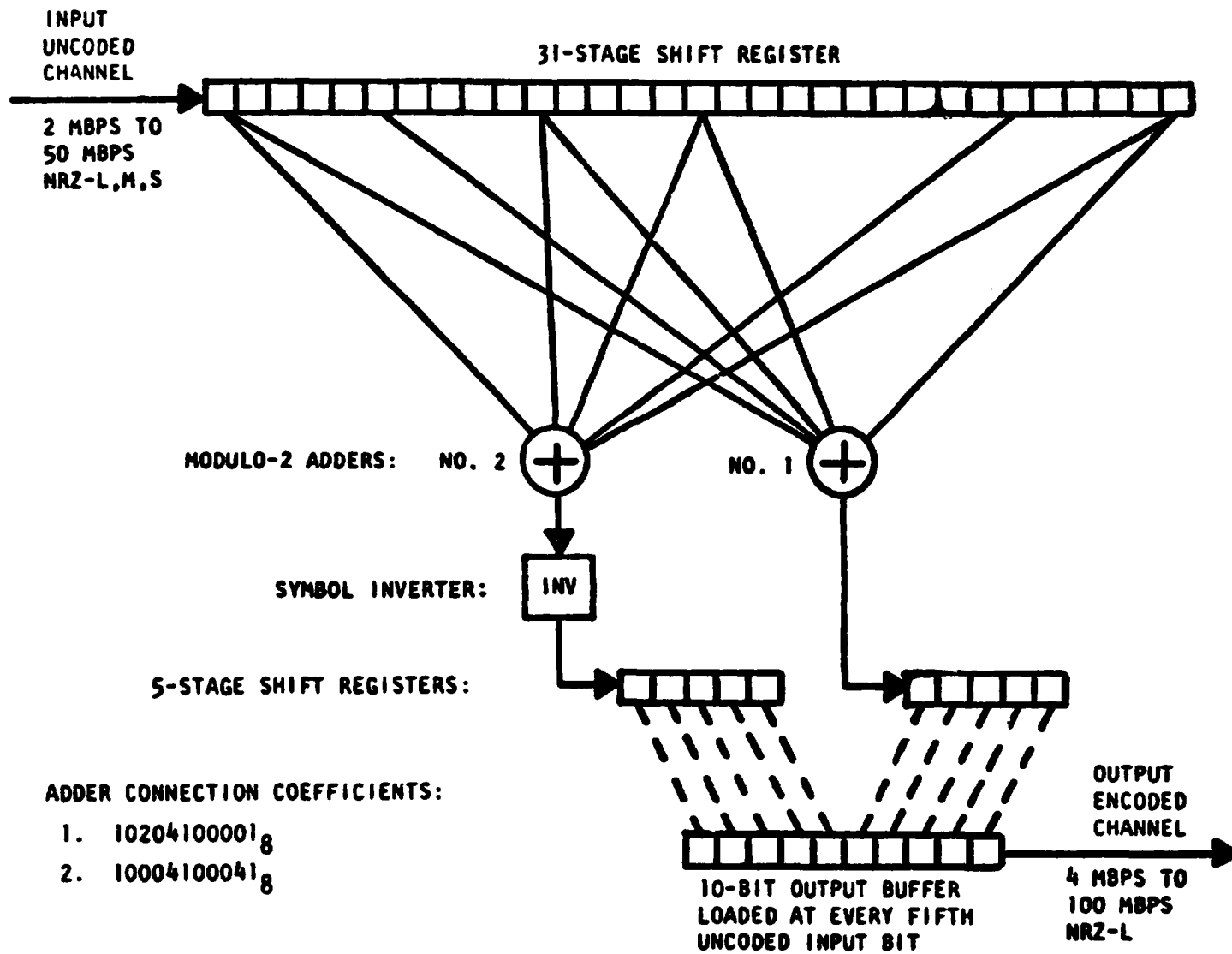


Figure 13. Rate One-Half Encoder Representation, Ku-Band Return Link, Mode 1

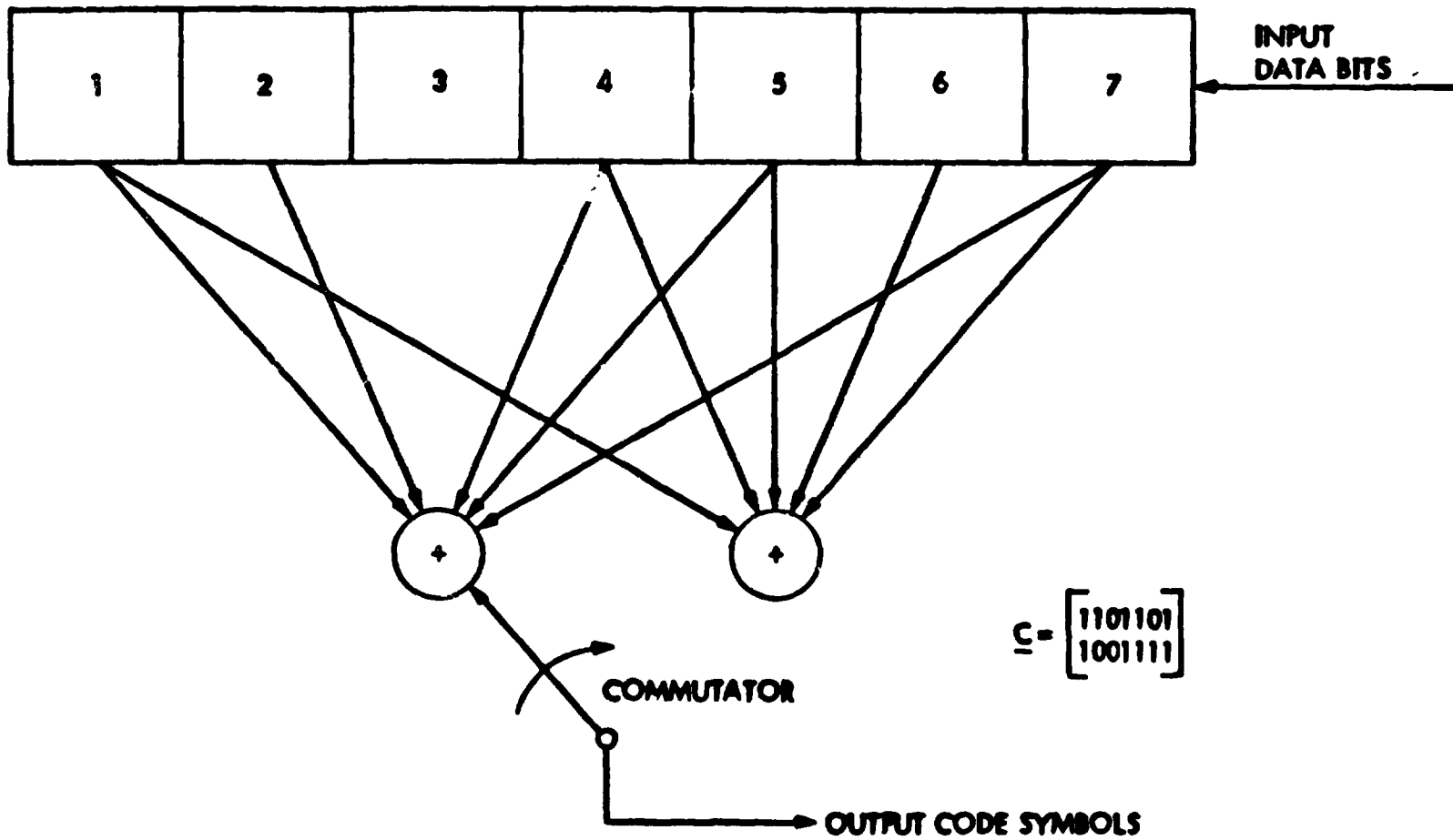
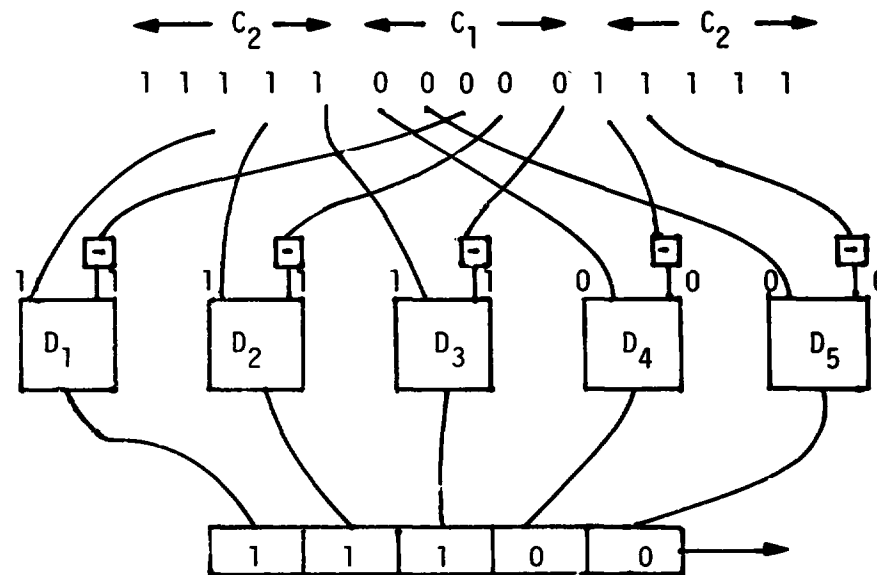


Figure 14. The Rate One-Half, Constraint Length 7 NASA Planetary Standard Code

4.2.2 Code Behavior with DC Input

With all zeros (or all ones) as input to the encoder, the resultant coded sequence will consist of alternating strings of five zeros and five ones, e.g., ...111110000011111..., which is the whole point of implementing G_2 inversion. In the event that the five decoders are not synchronized to the correct phase of the check bit pairs by prior transmission of nonzero data, each decoder will arbitrarily get alternating ones and zeros as input. After reinversion, a decoder will attempt to decode either all zeros or all ones. Since this is a transparent code, the all ones "encoded" sequence will produce a valid output data stream of all ones. This output sequence will be interleaved with the output of the other decoders, producing a cyclic string of ones and zeros. This is because a decoder cannot acquire branch synchronization on all ones or all zeros. In fact, under these conditions, the decoder will output erroneous "data" 90% of the time. This can be illustrated by examining Figure 15. The relative origin time of the alternating sequence can take on one of 10 values with respect to the first of the five decoders. In this example, decoder 1 (D_1) takes as input check bit 2, number 3 inverted at the transmitter and check bit 1, number 3 as the receive. Thus, decoder 1 sees a string of all ones, a valid code word, and outputs all ones. By contrast, decoder 4 sees all zeros and outputs all zeros. The only case wherein all zeros will be output is when decoder 1 starts decoding check bit 1, number 1 and check bit 2, number 1, reinverted at the decoder. Assuming that the decoder starts up at a random point on the encoder sequence, this will happen 10% of the time. One of the remaining nine incorrect decoded sequences is the all-one sequence, an inverted version of the actual data. This, too, presumably could be acceptable to the user by virtue of the inverted frame synchronization. It should be pointed out that periodic frame synchronization bits in the all-zero sequence will appear as noise to a decoder which is not correctly branch synchronized. On the average, each decoder will see five "noise" symbols--not enough to effect branch synchronization.

The question arises as to the number, if any, of additional sequences which have the property that branch synchronization is ambiguous. This can be analyzed formally by examining the response of one constraint length 7 encoder. The bit inversion can be ignored since this



Input Data: 0 0 0 0 0

Encoded Symbols (with inversion): 0 0 0 0 0 1 1 1 1 1 0 0 0 0 0 1 1

Decoded Data: 1 1 1 0 0 1 1 1 0 0 1 1 1 0 0

Figure 15. Effect of Zero Input Data on Decoder Output

has the effect of complementing the encoded symbol sequence if the phase of the check bits is slipped by one symbol and the complement of a code word is also a code word. Let $C_1(x)$ and $C_2(x)$ be the polynomial representation of the encoder output, e.g.,

$$C_1(x) = C_{10} + C_{11}x + C_{12}x^2 + \dots = g_1(x) I(x),$$

$$C_2(x) = C_{20} + C_{21}x + C_{22}x^2 + \dots = g_2(x) I(x),$$

with $g_1(x)$ the generator polynomial for the first check symbol and $I(x)$ the polynomial representation of the information sequence. If the branch synchronization is ambiguous, the symbol pairs $C_{20} C_{11}, C_{21} C_{12}, C_{22} C_{13}, \dots$ will form a code word. This can be written in polynomial form as:

$$C_{20} + C_{21}x + C_{22}x^2 + \dots = g_1(x) I^*(x),$$

$$C_{11} + C_{12}x + C_{13}x^2 + \dots = g_2(x) I^*(x),$$

with $I^*(x)$ the alternate information sequence. Thus,

$$g_2(x) I(x) = g_1(x) I^*(x), \text{ and}$$

$$\frac{g_1(x) I(x)}{x} = g_2(x) I^*(x).$$

This pair of equations can be solved to determine the input conditions under which branch synchronization is ambiguous; e.g., if $C_1 C_2$ represents a code word, so does $C_2 C_1$.

Solving for $I(x)$ and $I^*(x)$, we find that

$$I(x) \left[xg_2^2(x) + g_1^2(x) \right] = 0$$

and

$$I^*(x) \left[xg_2^2(x) + g_1^2(x) \right] = 0.$$

For the NASA constraint length 7 code,

$$g_1(x) = 1 + x^2 + x^3 + x^5 + x^6,$$

and

$$g_1^2(x) = 1 + x + x^2 + x^3 + x^6.$$

Thus,

$$\begin{aligned} xg_2^2(x) + g_1^2(x) &= x^{13} + x^{12} + x^{10} + x^7 + x^6 + x^5 + x^4 + x^3 + 1 \\ &= (x+1)(x^{12} + x^9 + x^8 + x^7 + x^5 + x^3 + 1) \\ &= p_1(x)p_2(x) \end{aligned}$$

factored into irreducible polynomials $p_1(x)$ and $p_2(x)$.

If

$$I(x) = I_0 + I_1x + I_2x^2 + \dots + I_{13}x^{13} + \dots,$$

the criterion that $I(x)p_1(x)p_2(x) = 0$ implies that

$$I_0 + I_1 + I_3 + I_6 + I_7 + I_8 + I_9 + I_{10} + I_{12} + I_{13} = 0 \pmod{2},$$

or

$$I_{13} = I_0 + I_1 + I_3 + I_6 + I_7 + I_8 + I_9 + I_{10} + I_{12}.$$

That is, given 13 specific input bits as initial conditions, if the fourteenth bit (I_{13}) satisfies the above equation, the output sequence is ambiguous. Note, however, in order for this sequence to sustain itself, each subsequent input bit must also satisfy the relationship. That is,

$$I_{14} = I_1 + I_2 + I_4 + I_7 + I_8 + I_9 + I_{10} + I_{11} + I_{13}, \text{ etc.}$$

The sequence can be modeled as the output of a linear feedback shift register, as shown in Figure 16, with taps appropriate to $p_1(x)p_2(x)$. The properties of these sequences are well known. $p_1(x) = 1 + x$ corresponds to the all-one sequence and its complement, the all-zero sequence, which we know are ambiguous. From [9], we find that $p_2(x)$ is primitive, and the shift register model of the sequence will have period $2^{12} - 1$. Depending on the initial conditions of the register, the sequence generated will be all zeros, all ones, or one of two complementary periodic sequences, each with period $2^{12} - 1$. The probability of any data source generating this specific "infinite" sequence with period 4095 is presumably rather low; hence, we have shown that branch synchronization with this code will not be a problem with real data. In any case, if $I(x)p_1(x)p_2(x) = 0$, then $I^*(x)p_1(x)p_2(x) = 0$, and the decoded $I^*(x)$ will merely be a delayed version of $I(x)$. This would certainly not be a problem with a single decoder; the only problem is in conjunction with the five interleaved decoders, which is shown to be a result of pathological input data.

The only remaining caveat is that the input data to the encoder should not have a period of five, as this would result in each of the five decoders seeing a constant string of ones or zeros.

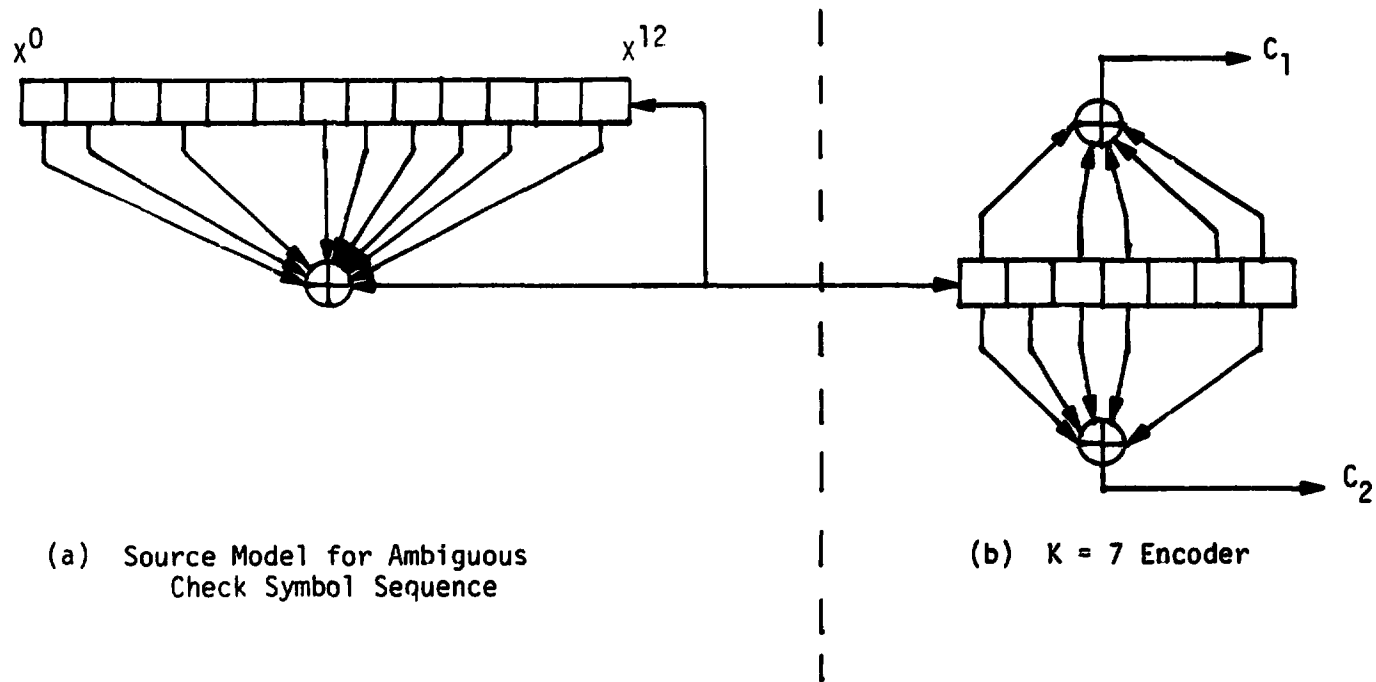


Figure 16.

4.2.3 Summary of Performance

With certain input data, the mode 1, channel 3, encoder/decoder with G_2 inversion will not perform as specified. These conditions are delineated below.

- With very low probability, the encoded symbol stream will have transition-free runs longer than 64 symbols.
- With high probability, the decoder will not attain branch synchronization if the user constraints are ignored and all zeros are input.
- With high probability, the decoder will not attain branch synchronization if the input data is cyclic with a period of five bits.
- No aperiodic data stream exists which will preclude branch synchronization.

Problem area 1, the possible output of transition-free runs of encoded symbols greater than 64, is a result of unique input data and should not be of concern. Problem area 2, the inability of the decoder to synchronize on all-zero data, will be of concern only if a user attempts to initiate transmission with data consisting of all zeros (or all ones) in violation of the user constraints or if the input data is cyclic with a five-bit period.

4.3 Effects Due To Specific TDRSS User Constraint Parameters

In the previous study (NAS 9-15240E [10]), all but two Ku-band TDRSS user constraints were evaluated and compared to Hughes Aircraft Company specifications. The cumulative performance degradation effects of the TDRSS user constraints were analyzed and summarized. In this section, the performance degradation of the remaining two user constraints, data bit clock jitter and data asymmetry on unbalanced QPSK, are presented.

4.3.1 Ku-Band Bit Synchronizer BER Degradation due to Data Bit Clock Jitter

Appendix I determines the timing error variance and resulting bit error rate degradation in a Ku-band Shuttle-compatible second-order bit synchronizer due to input data clock jitter modeled as either a sinusoidal signal or a spectrally flat random process. Both NRZ and Manchester data are considered.

Results are obtained for the bit synchronizer tracking error for both the sinusoidal and random jitter cases. Next, the bit error probability for both sinusoidal and Gaussian data clock jitter is derived and plotted. Using the timing variance, it is then possible to compute the bit error probability and the associated degradation from the jitter-free case.

Finally, the three bit synchronizer types used with Ku-band data are evaluated to determine their respective bit error rate degradation. Depending on which specification, modulation format and synchronizer are considered, bit error rate degradations vary from less than 0.1 dB to over 10 dB. The degradations tend to be small (0.1 dB) when the frequency deviation and deviation rate are specified at 0.10% R_s but quite large when specified at 0.1% R_s , where R_s is the symbol rate.

To evaluate the BER degradation, it is necessary to know the bit synchronizer loop bandwidths. Based on a telephone conversation with John Roach of Harris Corporation (Melbourne, Florida), the following bit synchronizer specifications were obtained:

1. Ultra-High Data Rate Bit Synchronizer (UHDR)

$$R_s = 75-150 \text{ Msps}$$

$$f_n \cong 60 \text{ kHz } (B_L = 200 \text{ Hz})$$

Manufacturer: Motorola

Jitter problems comments: Yes, since they could not make the loop bandwidth narrow enough due to internal delays

2. High Rate Bit Synchronizer (HDR)

$R_S = 10-75$ Msps (will operate down to 4 Msps)

$f_n \approx 0.08\% R_S$ ($B_L = 0.267\% R_S$)

Manufacturer: Harris Corporation

Jitter problem: No.

3. Low-Medium Data Bit Synchronizer (LMDR)

$R_S = 1$ kbps to 10 Msps

$f_n = 0.1\% R_S, 0.3\% R_S, 1\% R_S$ and $2\% R_S$

Manufacturer: Aydin Monitor

Jitter problem: No.

First we consider the sinusoidal jitter case. We consider two subcases; the first is for $\Delta f = 0.01\% R_S$ and $f_m = 0.01\% R_S$, we call this case (a). The second is for $\Delta f = 0.1\% R_S$ and $f_m = 0.1\% R_S$, which we call case (b). The BER degradations are shown in Table 6.

For the random case using the same two subcases, we obtain the results for BER degradation which are shown in Table 7.

In conclusion, we see that, when the frequency deviation and the deviation rate are specified at $0.01\% R_S$, the degradation does not exceed 0.2 dB but, with the specifications at $0.1\% R_S$, the degradation can be over 10 dB. Also from Tables 6 and 7, it can be seen that Manchester data causes more degradation than NRZ data, as is well known. Finally, sine wave jitter and flat random noise jitter cause roughly the same level of degradation based on the Ku-band Shutter jitter specification.

4.3.2 Effect of Data Asymmetry on Unbalanced QPSK Signals with Noisy Phase Reference

In Appendix II, an analysis of the impact of data asymmetry on the bit error rate performance of a QPSK signaling scheme used to transmit two data streams with different rates and different powers is

Table 6. Degradation for the Three Bit Synchronizer Classes and the Two Jitter Specifications [(a) and (b)] for Sine Wave Jitter (Uncoded Data)

Bit Synchronizer Class	Degradation		f_m/f_n
	NRZ Data	Bi- ϕ -L Data	
UHDR (a)	0.1 dB	0.2 dB	0.25
UHDR (b)	2.5 dB	\approx 10.0 dB	2.5
HDR (a)	\leq 0.1 dB	\leq 0.1 dB	0.125
HDR (b)	2.0 dB	\approx 8.0 dB	1.25
LMDR (a)	\leq 0.1 dB	\leq 0.1 dB	0.1
LMDR (b)	1.7 dB	4.5 dB	1.0

Table 7. Degradation for the Three Bit Synchronizer Classes and the Two Jitter Specifications [(a) and (b)] Random Noise Jitter (Uncoded Data)

Bit Synchronizer Class	Degradation		f_m/f_n
	NRZ Data	Bi- ϕ -L Data	
UHDR (a)	0.03 dB	0.08 dB	0.25
UHDR (b)	2.6 dB	\geq 10.0 dB	2.5
HDR (a)	\leq 0.1 dB	\leq 0.1 dB	0.125
HDR (b)	1.6 dB	9.0 dB	1.25
LMDR (a)	\leq 0.1 dB	\leq 0.1 dB	0.1
LMDR (b)	0.7 dB	2.3 dB	1.0

presented. Such a model arises, for example, in the QDSB system employed in the Shuttle Ku-band Mode 1 return link [11], which is essentially a cascade of two such unbalanced QPSK systems. Of primary interest here will be the subcarrier QPSK system and, in particular, the version implemented via a digital phase-shift-modulated square-wave subcarrier [12].

The performance of the recently popular unbalanced QPSK (UQPSK) systems in the presence of reference phase noise has been examined by a number of authors (see [13] to [17] and references therein). The general approach is to evaluate the bit error probability conditioned on the data and the value ϕ of the phase error, then average over these variables. The marginal probability density function (pdf) of ϕ strongly depends on the employed tracking loop and is, in general, difficult to accurately evaluate for sophisticated receivers. Here we follow a truncated Taylor series expansion approach, indicated in [15], which provides credible results, assuming high loop signal-to-noise ratio (SNR). Regardless of the particular method used, the bit error probability (BEP) depends on the powers and data rates of the individual channels.

The ϕ -conditioned BEP (which is a reasonable estimate of BEP for very high SNR) is an increasing function of ϕ , the reason being that an imperfect phase lock loop attenuates the demodulated signal power and at the same time increases interchannel cross talk.

Data asymmetry is a potential source of performance degradation in any digital transmission system. It arises whenever the modulator spends more time at one amplitude state than the other as a result of the misalignment of a threshold device. It is usually defined as the difference between the elongated pulse length and the shortened pulse length normalized by the nominal length. References [18] and [19] pertain to previous work on the issue of determining the effect of data asymmetry on the BEP of BPSK signaling ([18] for a variety of coded and uncoded data) and UQPSK with equal data rates [19]. Since no cross talk was considered in [19], the two QPSK channels are essentially two independent identical BPSK channels with different power allocations.

Appendix II addresses the problem of evaluating the performance degradation of a UQPSK system due to both data asymmetry and noisy reference. As we shall see, the degradation of each channel can qualitatively be perceived as consisting of a "self-degradation" term plus a

"cross-degradation" term. The former is the superposition of a power attenuation (due to noisy reference) along with the impairment caused by asymmetry. The latter (which is actually the interchannel interference) exists because of the presence of noisy reference and also depends on the asymmetry of the companion channel data stream. Hence, the results to be derived here should coincide with those in [18] and [19], if the phase error is assumed to be zero.

The parameter of interest here is the additional signal-to-noise ratio ΔSNR (dB) required to compensate for the losses due to asymmetry and phase noise for each channel. It is defined as the difference between the SNR required to achieve a BEP of 10^{-5} under the aforementioned conditions and the nominal value of 9.6 dB for an ideal BPSK system without impairments other than Gaussian noise.

We have assumed a power ratio of 4 and a data rate ratio of 10 for the two channels. These are typical values for the I and Q components of the subcarrier QPSK system of the Orbiter's Ku-band, which operate at 2 Mbps and 0.2 Mbps, respectively.

According to the approach taken in Appendix II, the phase error impact is sufficiently characterized by the mean m_ϕ and the variance σ_ϕ^2 of the tracking jitter ϕ . When a biphase Costas tracking loop is employed at the receiver, references [20] and [21] provide some (although complicated) analytic results for σ_ϕ . We felt that an extension of these results in the presence of asymmetry is a prohibitively complicated task; therefore, we can only postulate some values for m_ϕ and σ_ϕ . However, it is intuitively appealing to assume that, in the presence of small asymmetry, typical values for σ_ϕ will be slightly higher than what appears in the figures of [20] and [21]. As such, we have selected to examine the cases of $m_\phi = 0^\circ, 3^\circ, 5^\circ$ and $\sigma_\phi^2 = 0, 4, 9$ (degrees)².

Before commenting on the computer results, let us focus on the assumptions made in the course of the analysis. First, we consider NRZ-L data for both channels. An analysis for biphase-L data would follow on the same lines. Second, we have assumed perfect symbol synchronization for each individual channel. Third, we have assumed that the data rate ratio N is much greater than one, in general (for the specific application where $N=10$, such an assumption is well justified). The above assumptions suffice in order to derive a good estimate of the bit error

probability of the high data rate channel. For the low data rate channel, two more assumptions are involved: first, that N is an integer and, second, that the two channels are aligned, i.e., no epoch difference exists. Although the second assumption is perhaps rarely met in practice (since there are two different data clocks for the two channels, they most likely are independent, therefore not aligned), one can argue that the significance of the epoch difference diminishes as N increases. Similarly, if N is not an integer, one can consider the integer part of it and still get credible results. In summary, the cardinal assumptions for the analysis to be reasonably precise are that (1) each channel is perfectly synchronized, and (2) N is sufficiently greater than one. The low data rate

The low data rate channel (Q) is found to be more sensitive to parameter variation than the high data rate channel (I). In general, the SNR losses increase exponentially with the amount of asymmetry present for both channels. For the values considered, Figure 7 in Appendix II shows the range from 0 dB to 1.4 dB for the I channel and from 0 dB to 1.9 dB for the Q channel. As shown in Figure 8 of Appendix II, the effects of phase mean and phase variance are effectively decoupled. However, as expected, as σ_ϕ increases, the effect of phase offset becomes more and more drastic.

5.0 S-BAND PAYLOAD COMMUNICATION SYSTEM STUDY

Three major system interface issues in the payload communication system required a detailed investigation. These interfaces are the payload interrogator (PI) and Ku-band signal processor (KuSP), the sweep acquisition of the payload by the PI, and two-way phase noise generated in the PI and turned around by a coherent transponder.

5.1 Bent-Pipe Performance with the Current PI/KuSP RMS Regulator Capability

The maximum allowable deviation of the Ku-band FM transmitter is ± 11 MHz. Optimum bent-pipe performance is obtained whenever the modulating waveform is allowed to produce this maximum deviation in accord with its peak values. For this reason, Axiomatix has proposed that a peak type rather than an RMS type of AGC regulating loop be employed. A comparison between the RMS and peak regulator performance, as measured by FM transmitter mean deviation, is summarized in Table 8.

Table 8. Bent-Pipe FM Transmitter Mean Deviations (MHz)

Waveform	RMS Regulator	Peak Regulator
One Sinusoid	3.7	7.8
Two Sinusoids	3.7	5.5
Three Sinusoids	3.7	4.4
Four Sinusoids	3.7	3.9
Square	3.7	11.0
Gaussian	3.7	3.7

The peak regulator optimizes the FM deviation for all waveforms, providing maximum bent-pipe SNR performance for all waveform conditions. The RMS regulator, on the other hand, may have its output scaled to provide optimum deviation for any chosen waveform, but the deviation for all other waveforms will be suboptimum. If, for example, the RMS regulator output is optimized for the Gaussian waveform (characteristic of

PI low SNR conditions), the FM transmitter will be underdeviated for all other waveforms. As part of the development and specification of the PI/KuSP bent-pipe interface, Axiomatix undertook the design and evaluation of a signal waveform peak regulator. A final report on the entire activity appears in Appendix III.

Now suppose that the RMS regulator is used and its output is scaled to provide optimum deviation for a single-sinusoidal waveform. From Table 8, the mean deviation will be 7.8 MHz. If a Gaussian waveform rather than the single sinusoid then appears at the input to the RMS regulator, the RMS regulator will automatically scale the Gaussian waveform to cause a mean deviation of 7.8 MHz. But the peak-to-RMS ratio of a Gaussian waveform is on the order of 3:1; therefore, the peak deviation will be 23.4 MHz, or more than two times larger than the maximum deviation limit.

To prevent overdeviation, an amplitude clipper is usually employed at the input to the FM transmitter. Thus, for the Gaussian waveform example just cited, it will be clipped at its 1.4σ level, causing extreme distortion and SNR loss.

For the bent-pipe, the waveform condition for which the RMS regulator output should be scaled to provide optimum deviation is an open issue. The final choice will have to be a value judgment. An expedient solution may be to optimize the bent-pipe performance for the two-sinusoid case (as this may be the most likely bent-pipe signal). Thus, the mean deviation would be set at 5.5 MHz and amplitude clipping would keep any other waveform, such as the Gaussian, from exceeding the 11 MHz limit. The peak-to-RMS ratio would therefore become 2. Underdeviation would occur for single-sinusoid and square waveforms, while the Gaussian waveform would be clipped at its 2σ level. It is interesting that the current TRW RMS regulator and output circuit design provides for a 1.5:1 peak clipping-to-RMS ratio. TRW, however, would like to change the maximum to 8V peak-to-peak, achieving the 2:1 ratio.

SNR performance estimates for the underdeviation cases may be easily calculated. The peak clipping cases, however, are not readily amenable to analysis (although performance bounds may be obtained by analysis). Simulation or actual hardware measurements must therefore be used to obtain quantitative figures for the clipping cases.

5.2 Sweep Acquisition of Deep-Space (DS) Payloads by the PI

On June 22, Axiomatix completed the effort to assess the proper sweep rate for the DS transponder. A formal viewgraph presentation was subsequently prepared and presented at RI on June 26. This meeting was attended by RI, NASA and Axiomatix personnel.

The viewgraphs used at the June 26 meeting appear as Appendix IV to this report. It is noted, however, that an error appeared on the last page of the presentation, resulting in a too-fast sweep rate of 400 Hz/s being agreed upon at the June 26 meeting. As a part of the resolution process, it was decided by all present that the DS transponder would never be operated in conjunction with the PI transmitter +4 dBm power level at a range of 10 nmi. Thus, the sweep rate corresponding to the +27 dBm level was selected.

At the TRW monthly program review on July 12, Axiomatix corrected the aforementioned error. TRW also estimated that, within the neighborhood of the proper sweep rate, a tolerance as large as $\pm 30\%$ (rather than $\pm 20\%$, as assumed on June 26) of the nominal sweep rate value could be expected. The final report, therefore, is that the nominal sweep rate must be set at 250 Hz/s.

Appendix IV to this report is a set of viewgraphs which define the problem, indicate the nature of the problem solution, show the solution as a function of transponder operating conditions and tolerances, and present recommended sweep rate limits. The approach employed to obtain the critical sweep rate values is a modified method of phase-plane analysis that appears in Appendix V. Since the calculations are based on an "ideal" second-order PLL transfer function, a 20% backoff has been made to allow for the mechanization imperfections of the DS transponder.

5.3 Two-Way Phase Noise Performance for PI and Coherent Payload Transponders

In order to obtain a realistic characterization of system performance, it is essential to analyze all of the many error sources, including phase noise. Phase noise is generated in the transmitter reference oscillators and the receiver local oscillators. Other sources which are not as obvious are in the mixer (multiplier) logic noise, AM-to-PM conversion due to link nonlinearities, and possible vibration effects.

The result of this phase noise is degradation of the carrier tracking loop performance, and this contributes to the overall system error probability performance.

Appendix VI contains a detailed discussion of the effects of phase noise using mathematical models of the carrier tracking loops and introducing the appropriate power spectral densities of the various phase noise instabilities. Section 2.0 of this appendix outlines the system model of a two-way coherent communication system and describes the basic system configurations. Section 3.0 calculates the mean-square phase noise for a one-way coherent link, while Section 4.0 extends this elaborate analysis to the two-way link, incorporating both in-band and out-of-band phase noise sources. For the special situation of a close range communication link, Section 5.0 deals with the essentially coherent case of a common transmitter and receiver reference oscillator, where the correlation time of the phase noise is short compared to the round-trip delay times. The conclusion, as might be expected, is a slight modification of the noncoherent two-way link. Section 6.0 expands the analysis to include other internal frequency synthesizer oscillator sources by modeling and incorporating these synthesizer phase noises. Section 7.0 extends the study to the three- and four-way mean-square phase noise situations.

The next appendix, Appendix VII, describes a method of characterizing the phase noise spectra by a mean-square error approximation using measured laboratory results. Two examples of phase noise modeling for specific actual phase noise measurements are outlined, and comparisons are included in both cases which show the derived and expected results.

Finally, Appendix VIII calculates the expected phase noise RMS deviation upper bound of 9° for both the SGLS and STDN modes using the mean-square phase noise relationships of Appendix VI and the mean-square error approximation of Appendix VII.

REFERENCES

1. Nilsen, P., "Preliminary Thoughts on Processing STDN/Shuttle Telecommunications Link Data for Orbiter Antenna Calibration," Axiomatix Report No. R7902-1, February 9, 1979.
2. Loh, Y.C., and Porter, J.A., "RF Coverage Analysis and Performance for Shuttle Communication Links," IEEE Trans. on Communications, Vol. COM-26, No. 11, November 1978, pp. 1745-1757.
3. Weber, C.L., "Construction for Shuttle Antenna Measurements--Problem Statement," Axiomatix Report No. R7904-5, May 1979.
4. Anderson, B.D.O., and Moore, J.B., Optimal Filtering, Prentice-Hall, 1979.
5. Childers, D. (ed), "Modern Spectrum Analysis, IEEE Press Book, 1978.
6. Wood, M.D., and Green, D.N., "Fixed Pointing Errors After SA and SGL Antenna Calibrations," TRW IOC #TDRSS-79-212.D-005, 27 June 1979.
7. Wood, M.D., "Error Analysis of the KSA Autotrack On-Orbit Calibration Procedure," TRW IOC #TDRSS-79-2.3.D-001, 24 January 1979.
8. Simon, M.K., and Smith, J.G., Alternate Symbol Inversion for Improved Symbol Synchronization in Convolutionally Coded Systems, to be published.
9. Peterson, W.W., Error Correcting Codes, MIT Press, 1961.
10. Huth, G.K., Nessibou, T., Nilsen, P.W., Simon, M.K., and Weber, C.L., "Shuttle Ku-Band and S-Band Communications Implementation Study, (Contract No. NAS 9-15240C), Axiomatix Report No. R7902-3, February 28, 1979.
11. Cager, R.H., Jr., LaFlame, D.T., and Parode, L.C., "Orbiter Ku-Band Integrated Radar and Communications Subsystem," IEEE Transactions on Communications, November 1978, pp. 1604-1619.
12. Simon, M.K., "Power Allocation and Costas Loop Subcarrier Tracking Performance Associated with a Digital Phase Shift Implementation of the Three-Channel Orbiter Ku-Band Modulator," Axiomatix Report No. R7709-4, September 29, 1977.
13. Weber, C.L., "Candidate Receivers for Unbalanced QPSK," 1976 ITC Proceedings, Vol. XII, pp. 455-464.
14. Braun, W.R., and Lindsey, W.C., "Carrier Synchronization Techniques for Unbalanced QPSK Signals" (parts I and II), IEEE Transactions on Communications, September 1978, pp. 1325-1341.

15. Simon, M.K., "Error Probability Performance of Unbalanced QPSK Receivers," IEEE Transactions on Communications, September 1978, pp. 1390-1397.
16. Osborne, H.C., "Effect of Noisy Phase Reference on Coherent Detection of Unbalanced QPSK Signals," NTC '78 Proceedings, December 1978, pp. 2.2.1-2.2.6.
17. Divsalar, D., and Yuen, J.H., "Performance of Unbalanced QPSK in the Presence of Noisy Reference and Cross Talk," NTC '79 Proceedings, November 1979.
18. Simon, M.K., Tu, K., and Batson, B.H., "Effects of Data Asymmetry on Shuttle Ku-Band Communications Link Performance," IEEE Trans. on Communications, November 1978, pp. 1639-1651.
19. Orr, R.S., "The Impact of Data Asymmetry on Bit Error Performance," Technical Report, Stanford Telecommunications, Inc., McLean, Virginia, July 21, 1977.
20. Simon, M.K., and Alem, W.K., "Tracking Performance of Unbalanced QPSK Demodulators: Part I - Biphase Costas Loop with Passive Arm Filters," IEEE Trans. on Communications, August 1978, pp. 1147-1156.
21. Simon, M.K., "Tracking Performance of Unbalanced QPSK Modulators: Part II - Biphase Costas Loop with Active Arm Filters," IEEE Trans. on Communications, August 1978, pp. 1157-1166.

APPENDIX I

**KU-BAND BIT SYNCHRONIZER BER DEGRADATION
DUE TO DATA BIT CLOCK JITTER**

By

Jack K. Holmes

1.0 SUMMARY

This report determines the timing error variance and resulting bit error rate degradation in a Ku-band Shuttle-compatible second-order bit synchronizer due to input data clock jitter modeled as either a sinusoidal signal or a spectrally flat random process. Both NRZ and Manchester data are considered.

Results are obtained for the bit synchronizer tracking error for both the sinusoidal and random jitter cases. Next, the bit error probability for both sinusoidal and Gaussian data clock jitter is derived and plotted. Using the timing variance, it is then possible to compute the bit error probability and the associated degradation from the jitter-free case.

Finally, the three bit synchronizer types used with Ku-band data are evaluated to determine their respective bit error rate degradation. Depending on which specification, modulation format and synchronizer are considered, bit error rate degradations vary from less than 0.1 dB to over 10 dB. The degradations tend to be small (0.1 dB) when the frequency deviation and deviation rate are specified at 0.01% R_s but quite large when specified at 0.1% R_s , where R_s is the symbol rate.

2.0 PROBLEM STATEMENT

The problem this report addresses is the determination of the bit error rate degradation caused by data clock timing errors that are either sinusoidal or a random process. This specification appears in basically similar forms in numerous documents. From the Ku-band specification [1] (Appendix VII, p. 456), we have:

"70.3.3.2.2 Data and Clock Jitter. Data and clock jitter shall be taken as the time-varying component of data and/or clock transitions compared to a jitter-free data stream or clock. The definition contains both a jitter magnitude and a rate in the following form:

(a) Jitter magnitude shall be taken as a percentage of the data symbol clock rate. The resulting magnitude shall be the peak magnitude for sinusoidal jitter or the 3-sigma value for random jitter.

(b) Jitter rate shall be taken as a percentage of the data symbol clock rate. The resulting jitter rate shall be the peak rate for sinusoidal jitter or the 3-sigma value when the jitter is random.

When the data are coded, bit jitter shall refer to symbol jitter. Also when a clock accompanies the data, the jitter shall refer to clock jitter as well as data jitter."

Also from [1] (p. 147), the high data rate (HDR) input to the SPA has a jitter specification:

"HDR Payload Digital Data Input to SPA

h. Frequency jitter: plus or minus a frequency deviation of 0.01% rms of the data rate at a rate of 0.01% rms of the data rate."

Other specifications on this topic indicate a 0.1% of the data rate deviation and a 0.1% of the data rate deviation rate.

We will address the sinusoidal jitter case first, then consider the "random" case.

3.0 JITTER MODEL DEDUCED FROM SINE WAVE SPECIFICATION REQUIREMENTS

Consider a phase-modulated sine wave clock modeled by

$$y(t) = \sqrt{2}A \sin(\omega_0 t + \theta(t)) \quad (1)$$

where A is the rms signal amplitude, ω_0 is the angular clock frequency (rad/sec) and $\theta(t)$ is the phase modulation process which causes the jitter. In Figure 1, a typical NRZ data stream and the associated (unmodulated) sinusoidal clock are illustrated. Since the phase modulation process, $\theta(t)$, is assumed to be sinusoidal, we obtain

$$\theta(t) = \theta_0 \sin(\omega_m t) \quad (2)$$

where θ_0 is the peak phase modulation of the clock and ω_m is the frequency of the phase deviation. Now, since the jitter magnitude is specified as a percentage of the data symbol clock rate (frequency amplitude), we have

$$\dot{\theta}(t) = \theta_0 \omega_m \cos(\omega_m t) \quad (3)$$

and the peak is some percentage of the data symbol clock rate, i.e.,

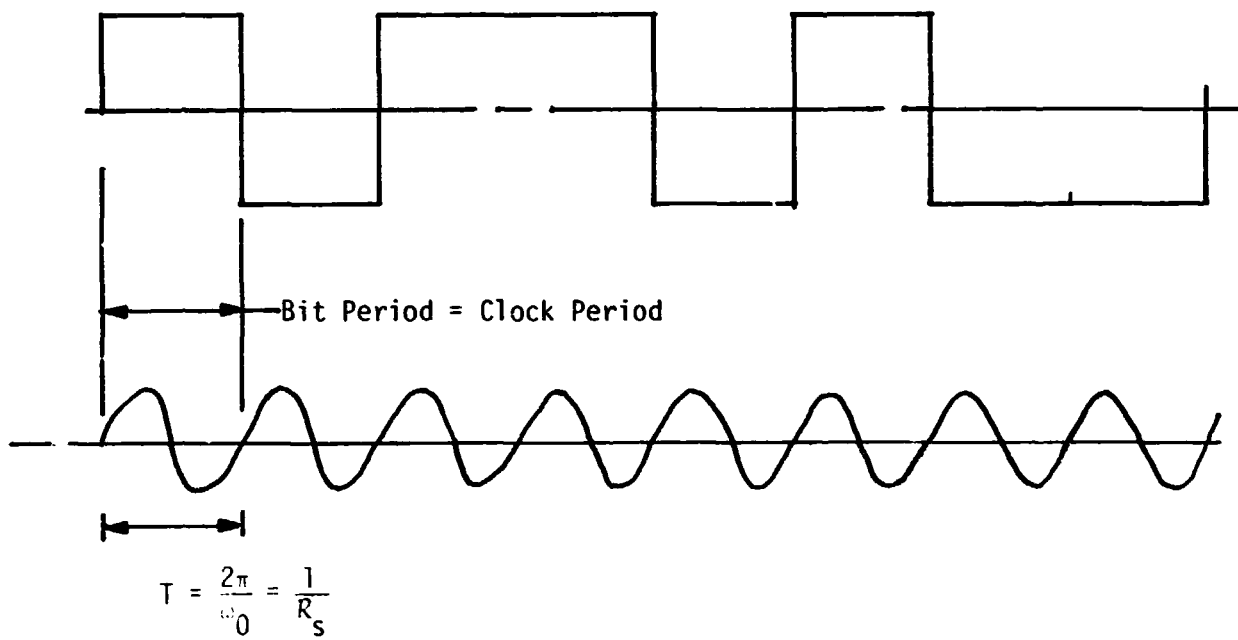


Figure 1. NRZ Bit Sequence and the Associated Clock

$$\theta_0 \omega_m = 2\pi \Delta f = 2\pi D R_s \quad \left(R_s = \frac{2\pi}{\omega_0} \right) \quad (4)$$

where D is the relative frequency deviation relative to the data rate, R_s . From the HDR specification [1] (Section II), we deduce that $D = 0.0001$ (0.01%). The jitter rate specification implies that

$$\omega_m = 2\pi F_m R_s \quad (5)$$

where F_m is such that $\omega_m/2\pi = F_m R_s$ and is the relative modulating frequency (relative to R_s). The jitter rate specification specifies the rate of the sinusoidal jitter. Now, using (4) and (5) in (2) yields

$$\theta(t) = \frac{\Delta f}{f_m} \sin(\omega_m t) = \frac{D}{F_m} \sin(2\pi F_m R_s t) \quad (6)$$

When the relative jitter magnitude (D) and relative jitter rate (F_m) are equal, we obtain

$$\theta(t) = \sin(2\pi f_m t) \quad (7)$$

which indicates a peak one radian phase deviation or $1/2\pi = 16\%$ of a bit period timing jitter (see Figure 2). Other values of D and F_m yield different phase deviations. In the derivation of (6) and (7), the peak jitter magnitude (frequency deviation) was used but, for the jitter rate, only one frequency exists so that the meaning of peak rate is not clear. It is felt that (2) is the only meaningful model of sinusoidal jitter. The clock is therefore modeled as

$$y(t) = \sqrt{2} A \sin \left(\omega_0 t + \frac{\Delta f}{f_m} \sin(2\pi f_m t) \right). \quad (8)$$

If the jitter frequency, $F_m R_s$, is very low compared to the bit synchronizer natural frequency, f_n , all the "jitter" will be tracked out. On the other hand, if the jitter frequency is high compared to the natural frequency of the bit synchronizer, then all the "jitter" will be passed through, with a resulting high BER degradation.

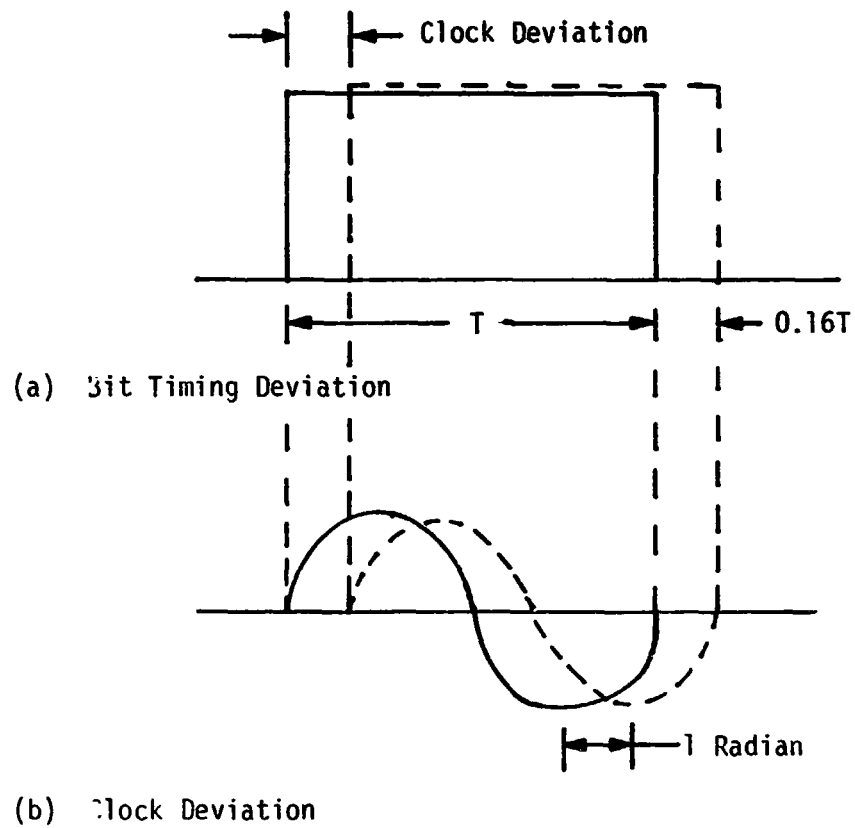


Figure 2. Illustration of One-Radian Clock Deviation and the 16% Bit Time Deviation

We now determine the response of a second-order bit synchronizer with a one radian peak phase modulation on the input. In general, $H(S)$, the closed-loop transfer function, is given by

$$H(S) = \frac{2\zeta\omega_n S + \omega_n^2}{S^2 + 2\zeta\omega_n S + \omega_n^2} \quad (9)$$

where ω_n is the loop natural frequency (rad/sec) and ζ is the damping factor. We wish to evaluate the peak squared tracking error expressed by

$$\phi_p^2 = \phi_i^2 |H(f)|^2 \Big|_{f = f_m} \quad (10)$$

where $S = 2\pi if$, ϕ_i is the input peak phase error and ϕ_p is the residual peak phase out of the bit synchronization loop. If we select $\zeta = 1/\sqrt{2}$, a commonly used value, then it is easy to show that

$$|H(f)|^2 = \frac{f^4}{f^4 + f_n^4} \quad (11)$$

where $f_n = \omega_n/2\pi$ is the natural loop frequency expressed in Hz. From (10), using the input phase modulation process of (6), we have

$$\phi_p^2 = \frac{D^2}{F_m^2} \frac{f^4}{f^4 + f_n^4} \Big|_{f = F_m R_s} \quad (12)$$

or

$$\phi_p^2 = \frac{D^2}{F_m^2} \left[\frac{F_m^4 R_s^4}{F_m^4 R_s^4 + f_n^4} \right] \quad (13)$$

or

$$\phi_p^2 = R_s^2 D^2 \left[\frac{F_m^2 R_s^2}{F_m^4 R_s^4 + f_n^4} \right] \quad (14)$$

Now we fix f_n , R_s and D , and let F_m vary* so that using $F_m R_s = f_m$

$$\frac{\phi_p^2}{R_s^2 D^2} = \frac{f_m^2}{f_m^4 + f_n^4} \quad (15)$$

If we differentiate the right-hand side of (14) and set it equal to zero, we obtain the solution, $f_m = f_n$. It therefore follows that the maximum error occurs at $f_m = f_n$ when the deviation $\Delta f = R_s D$ is fixed and the error at that frequency is given by [using (2), (4) and (15)]

$$\phi_p^2 \Big|_{f_m = f_n} = \frac{R_s^2 D^2}{2 f_m^2} = \frac{\theta_0^2}{2} \quad (16)$$

where

$$\theta_0 = \frac{R_s D}{f_m} \quad (17)$$

It therefore follows that

$$\phi_p = \frac{1}{\sqrt{2}} \theta_0 \text{ at } f_m = f_n; \Delta f \text{ fixed} \quad (18)$$

Whenever $f_m \neq f_n$, the peak value is less for fixed Δf . Figure 3 illustrates the response $\phi_p^2 / \Delta f^2$ as a function of f_m for fixed Δf . This curve is related to BER degradation since a large value of peak phase error, ϕ_p , causes a large BER degradation. Blyth and Carpenter [2] have summarized

* We are fixing the frequency deviation and clock nominal frequency and varying the phase-modulating frequency.

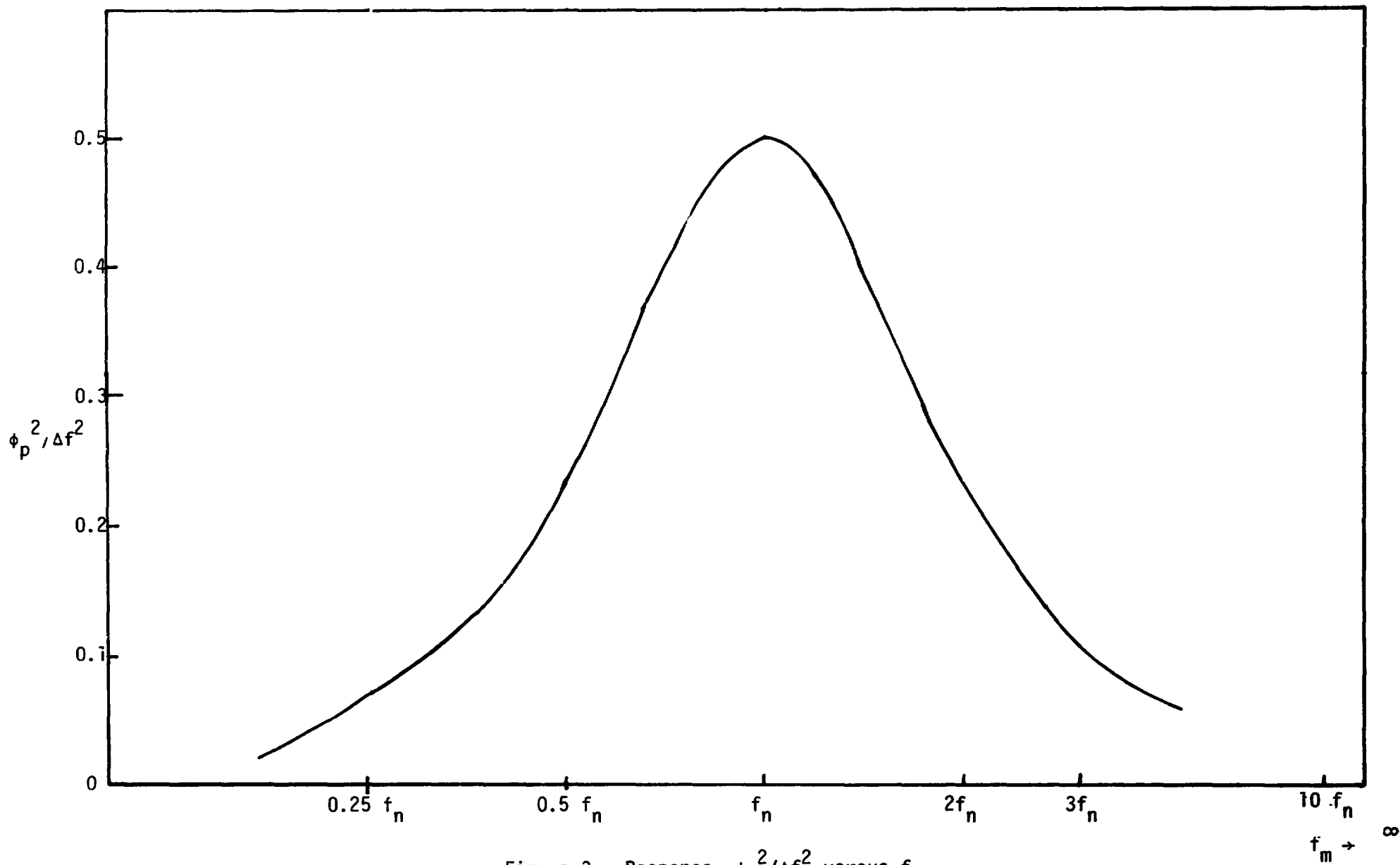


Figure 3. Response $\phi_p^2 / \Delta f^2$ versus f_m

measured BER degradation performance of a bit synchronizer* due to jitter and pointed out under a constant value of Δf the degradation peaks very near $f_m = f_n$!

It should be further pointed out that the peak phase error, ϕ_p , for a fixed input phase modulation deviation, θ_0 , is maximum for frequencies much greater than $f_m = f_n$. This fact is easily demonstrated by starting with (14) and letting $f_m = Kf_n$, so that we have

$$\phi_p^2 = R_s^2 D^2 \frac{f_m^2}{f_m^4 + \left(\frac{f_m}{K}\right)^4} \quad (19)$$

so that we obtain

$$\phi_p^2 = \frac{R_s^2 D^2}{f_m^2} \frac{K^4}{K^4 + 1} = \theta_0^2 \frac{K^4}{K^4 + 1} \quad (20)$$

Hence, as $K = f_m/f_n \rightarrow \infty$, $\phi_p^2 = \theta_0^2$.

In Figure 4, the peak output phase error is plotted versus f_m/f_n for a second-order (high gain) bit synchronizer loop with $\zeta = 0.707$ which has a unit input peak phase deviation.

In conclusion, the phase modulation of the tone having a period equal to the duration of the bit time that satisfies the jitter magnitude and jitter rate specifications is given by

$$\theta(t) = \frac{\Delta f}{f_m} \sin(\omega_m t) \quad (21)$$

where $\Delta f = DR_s$ is the peak jitter magnitude and $f_m = \omega_m/2\pi = F_m R_s$ is the jitter rate, with R_s the symbol rate, D the ratio of frequency deviation to data rate and F_m the ratio of modulation frequency to data rate. Hence, when D and F_m are obtained from the specification's $\theta_0 = D/F_m$ is the peak phase modulation, and Figure 4 allows one to compute ϕ_p^2/θ_0^2 (the ratio

*Based on the available literature, a common test procedure is to vary Δf for fixed f_m and measure the BER degradation.

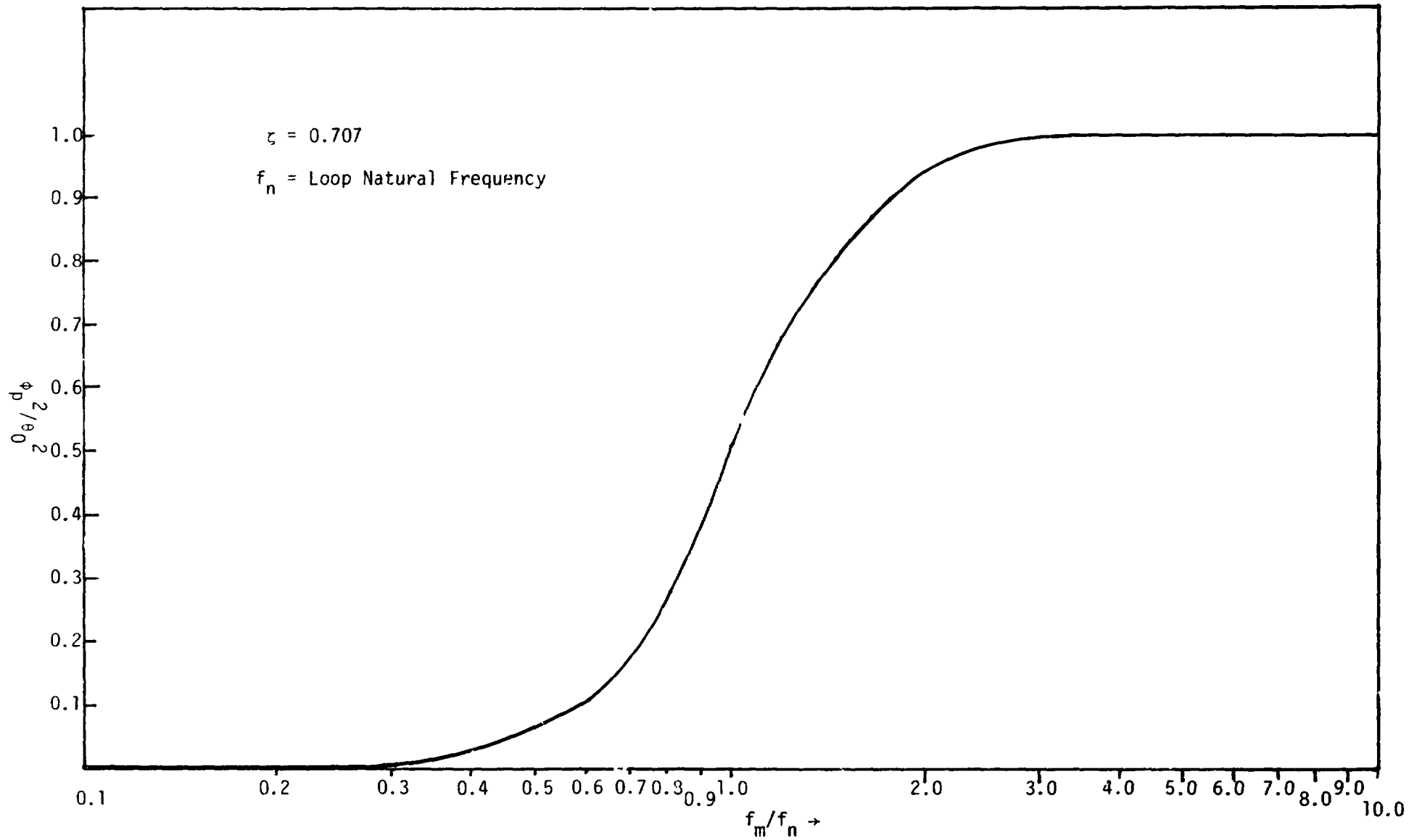


Figure 4. Error Response of Second-Order Bit Synchronizer Loop to Sinusoidal Phase Deviation

of bit synchronizer loop error squared to input phase squared) when f_m/f_n is specified. Recall that f_n is the bit synchronizer loop natural frequency (rad/sec).

4.0 PROBABILITY OF ERROR FOR NRZ AND MANCHESTER DATA VERSUS SINUSOIDAL PEAK TIMING ERROR

We now determine the probability of error versus E_b/N_0 for several values of peak timing error based on a sinusoidal timing error variation with time. The motivation for developing the following results is based on appraising the effects of the jitter magnitude and jitter rate when the jitter is sinusoidal, as specified in the Ku-band specifications.

It will be assumed that the bit clock jitter rate is slow compared to the data rate so that the average bit error rate can be described as

$$PE = \int_{-\infty}^{\infty} P(E/\tau) p(\tau) d\tau \quad (22)$$

where $P(E/\tau)$ is the bit error rate conditioned on the value of the timing error, τ , and $p(\tau)$ is the probability density function of the error timing error τ . First consider $P(E/\tau)$ the conditional probability of bit error given a particular value of timing error τ for NRZ data. For uncoded NRZ signals, there are two cases for the bit error probability. In the first case, when no transition in the bit stream occurs, the probability of error is simply

$$PE_1 = Q\left(\sqrt{\frac{2E_b}{N_0}}\right) \quad (23)$$

where

$$Q(x) = \int_x^{\infty} \frac{1}{\sqrt{2\pi}} e^{-t^2/2} dt \quad (24)$$

When a transition does occur, the bit error probability is no longer expressed by (23) but, rather, is modified to

$$PE_2 = Q\left(\sqrt{\frac{2E_b}{N_0}} (1 - 2|\tau|)\right) \quad (25)$$

The reason for the factor $(1 - 2|\tau|)$ is due to the previous bit (or following bit) being of the opposite sign and being included in the integration of the current bit duration of T seconds (see Figure 5). The matched filter integrates over T seconds. As the bit timing error increases, the integration includes the present bit plus the adjacent bit. When there is no transition, this error produces no decrease in the integrated signal voltage. However, when there is a transition, there is a decrease in the integrated voltage during one bit time. In fact, with a little reflection, it is clear that the decrease in integrated voltage is linear and goes to zero when $\tau = \pm T/2$. It follows that the integrated voltage contains the factor $(1 - 2|\tau|)$ for $|\tau| \leq 1$.

In conclusion, if we denote by P_T the transition probability, the conditional probability of error conditioned on τ is given by

$$\text{NRZ: } P(E/\tau) = P_T Q\left(\sqrt{\frac{2E_b}{N_0}} [1 - 2|\tau|]\right) + (1 - P_T) Q\left(\sqrt{\frac{2E_b}{N_0}}\right) \quad (26a)$$

and

$$\text{Manchester: } P(E/\tau) = (1 - P_T) Q\left(\sqrt{\frac{2E_b}{N_0}} (1 - 4|\tau|)\right) + P_T Q\left(\sqrt{\frac{2E_b}{N_0}} (1 - 2|\tau|)\right) \quad (26b)$$

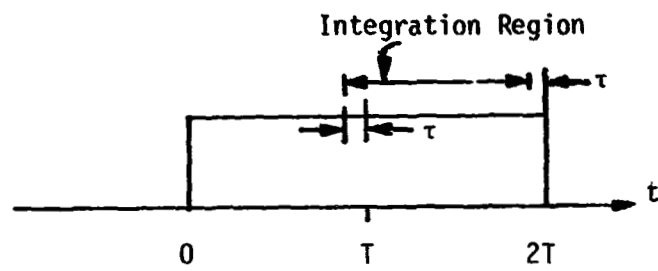
$|\tau| \leq 0.5$

where the Manchester case can be derived in a manner similar to the NRZ case.

Next, we obtain the probability density function of the timing error, $p(\tau)$. We describe the equivalent phase modulation by

$$\phi(t) = \phi_p \sin(\omega_m t + \theta_0) \quad (27)$$

(a) No Transition



(b) Transition

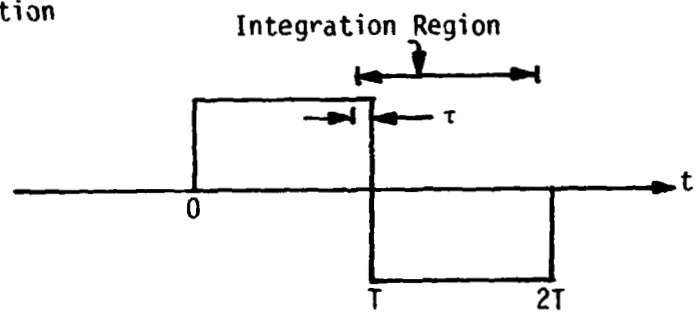


Figure 5. The Bit Integration Region in the Case of No Transition and a Transition with Timing Error τ

where (denoting the data rate by R), ϕ_p is the peak phase error (rad), ω_m is the modulation frequency ($\omega_m \ll 2\pi R_s$) and θ_0 is a random variable uniform over $(-\pi, \pi)$.

Since, for any t , $\omega_m t + \theta_0$ is uniformly distributed over $(-\pi, \pi)$, we model $\phi(t)$ as far as the distribution of $\phi(t)$ goes by

$$\phi(t) = \phi_p \sin \theta_0. \quad (28)$$

where θ_0 is a uniform random variable, uniform on $(-\pi, \pi)$. To obtain the density function of ϕ , we have [3],

$$p(\phi) = \frac{1}{2\pi \sqrt{\phi_p^2 - \phi^2}} + \frac{1}{2\pi \sqrt{\phi_p^2 - \phi^2}} \quad (29)$$

so that

$$p(\phi) = \frac{1}{\pi \sqrt{\phi_p^2 - \phi^2}} \quad -\phi_p \leq \phi \leq \phi_p \quad (30)$$

Now since $\phi_p/2\pi = \tau_p$, the peak timing error, we have, with another change of variables,

$$p(\tau) = \frac{1}{\pi \sqrt{\tau_p^2 - \tau^2}} \quad -\tau_p \leq \tau \leq \tau_p \quad (31)$$

Hence, the average probability of error is given by

$$\text{NRZ: PE} = \frac{1}{2} Q\left(\sqrt{\frac{2E_b}{N_0}}\right) + \frac{1}{2} \int_{-\tau_p}^{\tau_p} Q\left(\sqrt{\frac{2E_b}{N_0}} (1 - 2|\tau|)\right) \frac{1}{\pi \sqrt{\tau_p^2 - \tau^2}} d\tau \quad (32a)$$

and

$$\text{MANCHESTER: PE} = \frac{1}{2} \int_{-\tau_p}^{\tau_p} \frac{1}{\pi \sqrt{\tau_p^2 - \tau^2}} \left\{ Q \left(\sqrt{\frac{2E_b}{N_0}} (1 - 4|\tau|) \right) + Q \left(\sqrt{\frac{2E_b}{N_0}} (1 - 2|\tau|) \right) \right\} d\tau \quad (32b)$$

Equations (32a) and (32b) were programmed on a digital computer, with the results illustrated in Figures 6 and 7. Notice that a 5% (0.05) peak sine wave timing error causes about 0.5 dB degradation at $PE = 10^{-6}$ for NRZ data. For Manchester data, a 5% peak causes about 1 dB degradation.

Although it is not obvious from the curves, there is no irreducible error in this sinusoidal timing error case as there exists in the Gaussian error case.

A comparison of the Manchester case can be made with some experimental measurements of J. Rivers [5] of the NASA Johnson Space Center. In Figure 8, Rivers-measured BER degradation and the theoretical values obtained from Figure 7 are compared for Manchester data at $PE = 10^{-4}$. As can be seen from Figure 8, the theory is quite accurate, having at most a 0.3 dB error.

5.0 JITTER MODEL DEDUCED FROM THE GAUSSIAN SPECIFICATION REQUIREMENTS

Now we consider the Gaussian modulation case and attempt to determine a model of the jitter process. Again consider the sinusoidal clock having a period equal to the bit duration. We have for the clock signal

$$y(t) = \sqrt{2} A \sin(\omega_0 t + \theta(t)) \quad (33)$$

where $\theta(t)$ is assumed to be a stationary Gaussian random process. Since the 3-sigma jitter is specified to be a percentage of the data rate, we have that

$$3^2 \int_{-\infty}^{\infty} \mathcal{L} \dot{\theta}(f) df = (DR_s)^2 (2\pi)^2 \quad (34)$$

Unless the phase process has a specified spectral density, it is impossible to find the 3-sigma modulation frequency. In order to proceed, we will

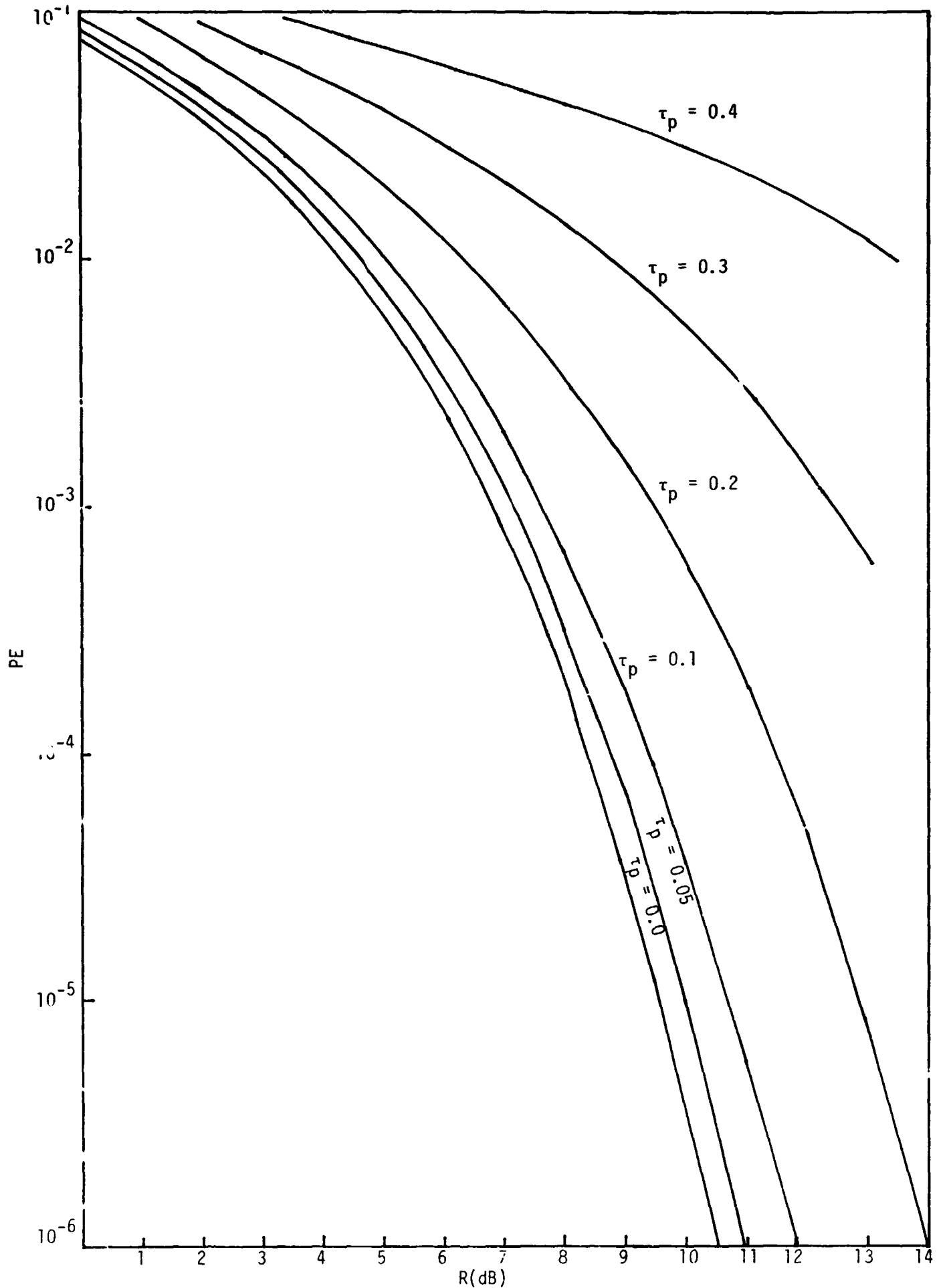


Figure 6. PE versus Peak Sine Wave Timing Error--Sinusoidal NRZ Data, Bit Synchronizer Tracking

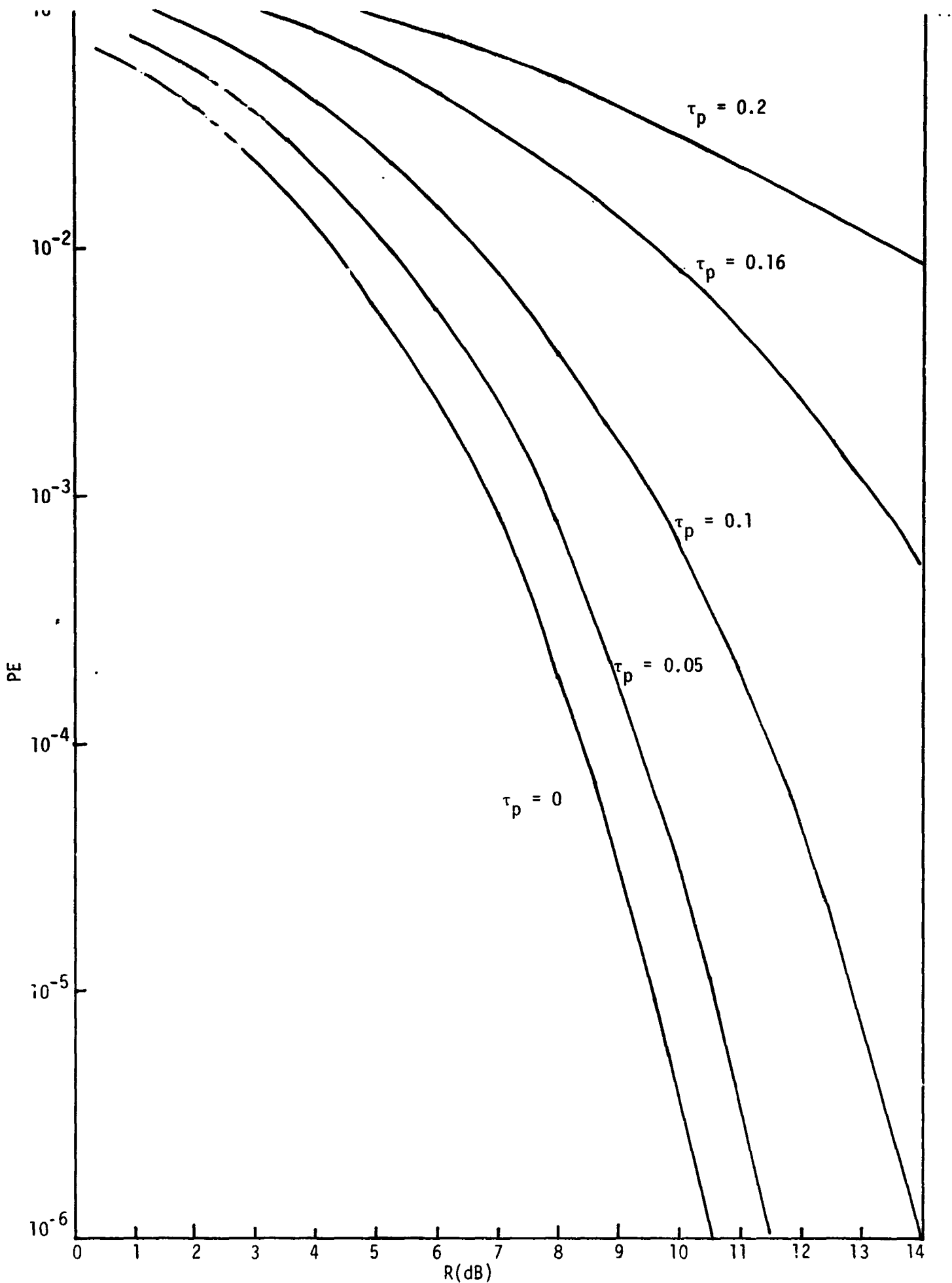


Figure 7. PE versus Peak Sine Wave Timing Error--Sinusoidal Bi- ϕ -L Data, Bit Synchronizer Tracking

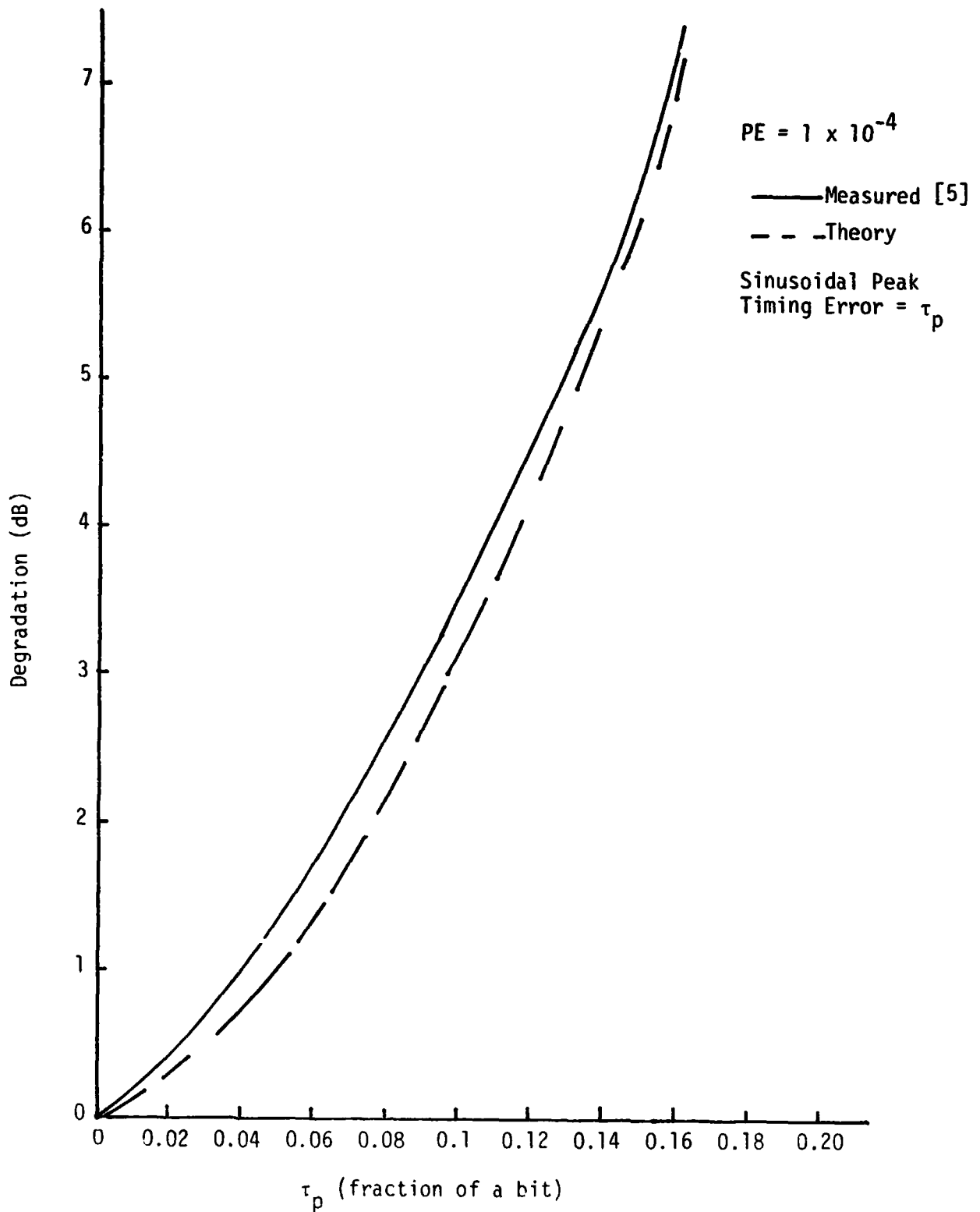


Figure 8. BER Degradation versus τ_p
Manchester Data, Sinusoidal Jitter

assume a phase process spectral shape that is flat in frequency. It should be pointed out that this is a "reasonable" assumption, but is not based on measurements. Figure 9 illustrates the phase process spectral density. We have assumed that all the phase spectra is contained in $2F_m R$ Hz. Since $\omega^2 \mathcal{L}(f)$ is the spectra of the phase rate or frequency (i.e., jitter), we have

$$(2\pi)^2 \sigma_{\Delta f}^2 = \int_{-\infty}^{\infty} \mathcal{L}(f) df = \int_{-\infty}^{\infty} \omega^2 \mathcal{L}(f) df \quad (35)$$

where $\sigma_{\Delta f}$ is the rms frequency deviation (Hz). Evaluating (34) and (35) with the phase process model of Figure 9 yields

$$9 \cdot (2\pi)^2 \sigma_{\Delta f}^2 = 9 \cdot \int_{-F_m R_s}^{F_m R_s} (2\pi)^2 f^2 N_{\theta} df = (2\pi)^2 (DR_s)^2 \quad (36)$$

or

$$2 (2\pi)^2 9 N_{\theta} \frac{(F_m R_s)^3}{3} = (2\pi)^2 (DR_s)^2 \quad (37)$$

Solving for N_{θ} yields

$$N_{\theta} = \frac{1}{6(F_m R_s)} \cdot \frac{D^2}{F_m^2}, \quad -DR_s \leq f \leq DR_s \quad (38)$$

Now that N_{θ} , the spectral density of the phase process, is determined, we can compute rms phase deviation:

$$\sigma_{\theta}^2 = \int_{-DR_s}^{DR_s} \frac{1}{5(F_m R_s)} \left(\frac{D^2}{F_m^2} \right) df \quad (39)$$

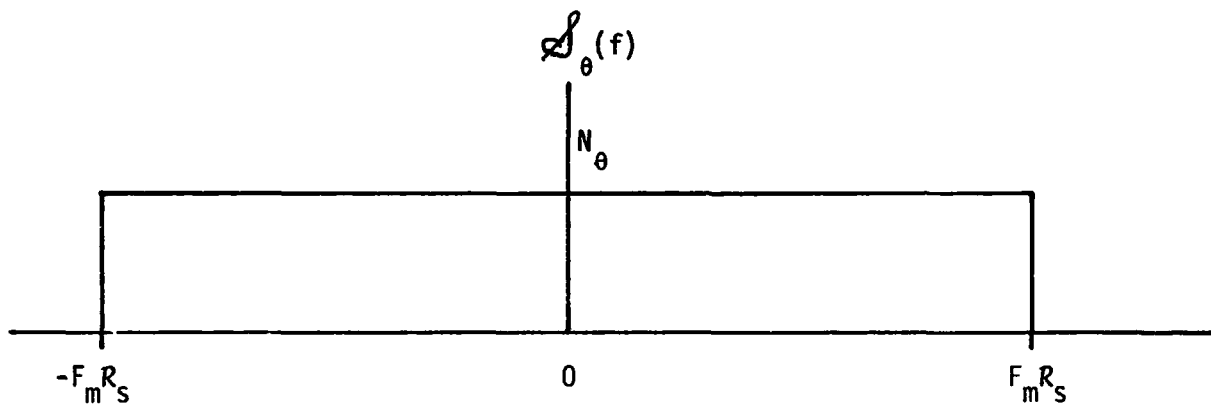


Figure 9. Model of the Phase Process

or

$$\sigma_{\theta}^2 = \frac{1}{3} \left(\frac{D^3}{F_m^3} \right) \text{ rads}^2 \quad (40)$$

Notice again, when $\zeta = F_m$, $\sigma_s = \sqrt{1/3}$ radians. However, the input phase deviation is not nearly as important as the phase error variance of the bit synchronizer given by

$$\int_{-\infty}^{\infty} |1 - H(f)|^2 \mathcal{S}_{\theta}(f) df = \sigma_{\phi}^2 \quad (41)$$

where $H(f)$ is the closed-loop transfer function of the bit synchronizer. Evaluating (39) for a second-order bit synchronizer with $\zeta = 0.707$, we have

$$\sigma_{\phi}^2 = \int_{-F_m R_s}^{F_m R_s} \left[\frac{f^4}{f_n^4 + f^4} \right] \frac{1}{6(F_m R_s)} \left(\frac{D^2}{F_m^2} \right) df \quad (42)$$

Note that

$$\int_{-f_m}^{f_m} \frac{f^4}{f^4 + f_n^4} df = 2f_m - 2f_n \int_0^{f_m/f_n} \frac{1}{1+x^4} dx \quad (43)$$

So from (42), using (43), we arrive at

$$\sigma_{\phi}^2 = \frac{1}{3} \left(\frac{D^2}{F_m^2} \right) \left[1 - \frac{f_n}{f_m} \int_0^{f_m/f_n} \frac{dx}{1+x^4} \right] \quad (44)$$

The integral of (44) was evaluated by computer since the tables appeared to give an incorrect result for values of f_m/f_n larger than one. The curve is shown in Figure 10.

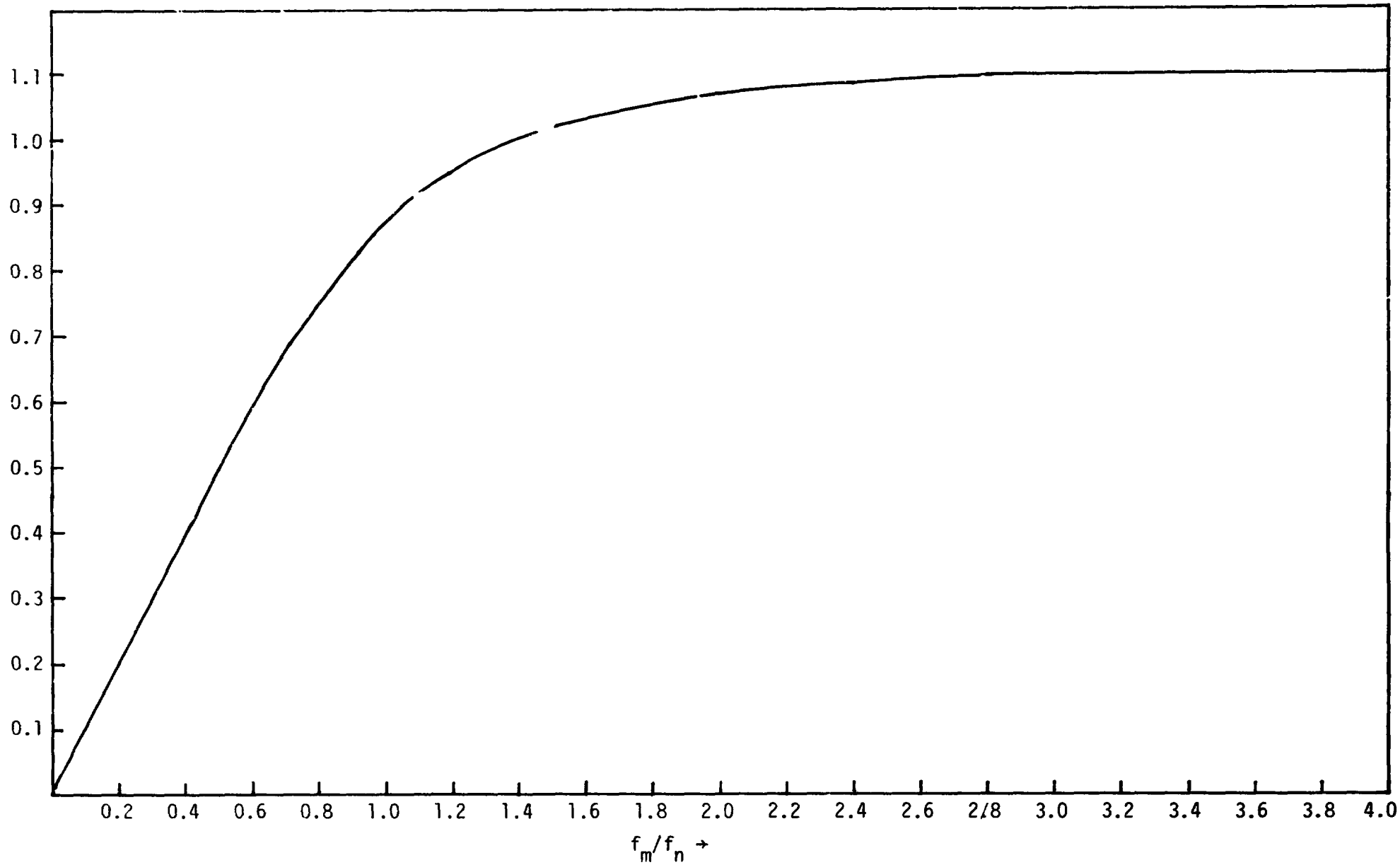


Figure 10. Plot of $\int_0^{f_m/f_n} dx/(1+x^4)$

For values of $f_m/f_n < 0.5$, (44) can be well approximated by

$$\sigma_\phi^2 = \frac{1}{15} \left(\frac{D}{F_m} \right)^2 \left(\frac{f_m}{f_n} \right)^4 \quad (45)$$

Hence, when $F_m R = f_m$, f_n and D are known, σ_ϕ^2 can be evaluated from (45) or (44) along with Figure 10. Note, to convert σ_ϕ to σ_τ (timing error), we have the simple relationship

$$\sigma_\tau = \frac{\sigma_\phi}{2\pi} \quad (\text{fractions of a bit}). \quad (46)$$

6.0 PROBABILITY OF ERROR FOR NRZ AND MANCHESTER DATA VERSUS THE RMS TIMING ERROR FOR A GAUSSIAN PHASE PROCESS

Since the rms timing error has been computed in (44) and (45) using (46), we can now determine the probability of error assuming that the phase process maximum modulating frequency is much less than the data rate, i.e.,

$$f_m = F_m R_s \ll R_s \quad (47)$$

Just as in Section 4.0, it can be shown that the conditional error probability $P(E/\tau)$ is given by

$$\begin{aligned} \text{NRZ: } P(E/\tau) &= (1 - P_T) Q \left(\sqrt{\frac{2E_b}{N_0}} \right) + P_T Q \left(\sqrt{\frac{2E_b}{N_0}} (1 - 2|\tau|) \right) \quad |\tau| \leq 1 \\ \text{MANCHESTER: } P(E/\tau) &= (1 - P_T) Q \left(\sqrt{\frac{2E_b}{N_0}} (1 - 4|\tau|) \right) + P_T Q \left(\sqrt{\frac{2E_b}{N_0}} (1 - 2|\tau|) \right) \\ &\quad |\tau| \leq 1/2 \quad (48) \end{aligned}$$

where τ is the timing error, P_T is the transition probability and $Q(x)$ is defined by

$$Q(x) = \int_x^{\infty} \frac{1}{\sqrt{2\pi}} e^{-t^2/2} dt \quad (49)$$

The probability density function of the timing error is given by

$$p(\tau) = \frac{1}{\sqrt{2\pi\sigma_\tau}} \exp\left[-\frac{\tau^2}{2\sigma_\tau^2}\right] \quad (50)$$

It follows from (48) and (50) that, when $P_T = 1/2$;

$$\text{NRZ: PE} = \frac{1}{2} Q\left(\sqrt{\frac{2E_b}{N_0}}\right) + \int_0^{\infty} \frac{1}{\sqrt{2\pi\sigma_\tau}} e^{-\frac{\tau^2}{2\sigma_\tau^2}} Q\left(\sqrt{\frac{2E_b}{N_0}} (1 - 2|\tau|)\right) d\tau \quad (51)$$

$$\text{MANCHESTER: PE} = \int_0^{\infty} \frac{1}{\sqrt{2\pi\sigma_\tau}} e^{-\frac{\tau^2}{2\sigma_\tau^2}} \left\{ Q\left(\sqrt{\frac{2E_b}{N_0}} (1 - 4\tau)\right) + Q\left(\sqrt{\frac{2E_b}{N_0}} (1 - 2\tau)\right) \right\} d\tau \quad (52)$$

These functions are plotted in Figures 11 and 12 for the NRZ and Manchester (Biphase-L) symbol format case. Note that a 2.5% (0.025) Gaussian timing error produces 0.4 dB degradation for NRZ and about 1 dB degradation for Manchester data. It can be shown that irreducible error probabilities occur in the Gaussian timing error case, causing very high degradations at larger timing errors.

7.0 EVALUATION OF THE BER DEGRADATION FOR THE SHUTTLE KU-BAND RETURN LINK BIT SYNCHRONIZER

In this section, we apply the results of previous sections in order to estimate the bit error rate (BER) degradation due to either sinusoidal or a flat Gaussian phase modulation process. To evaluate the BER degradation, it is necessary to know the bit synchronizer loop bandwidths.

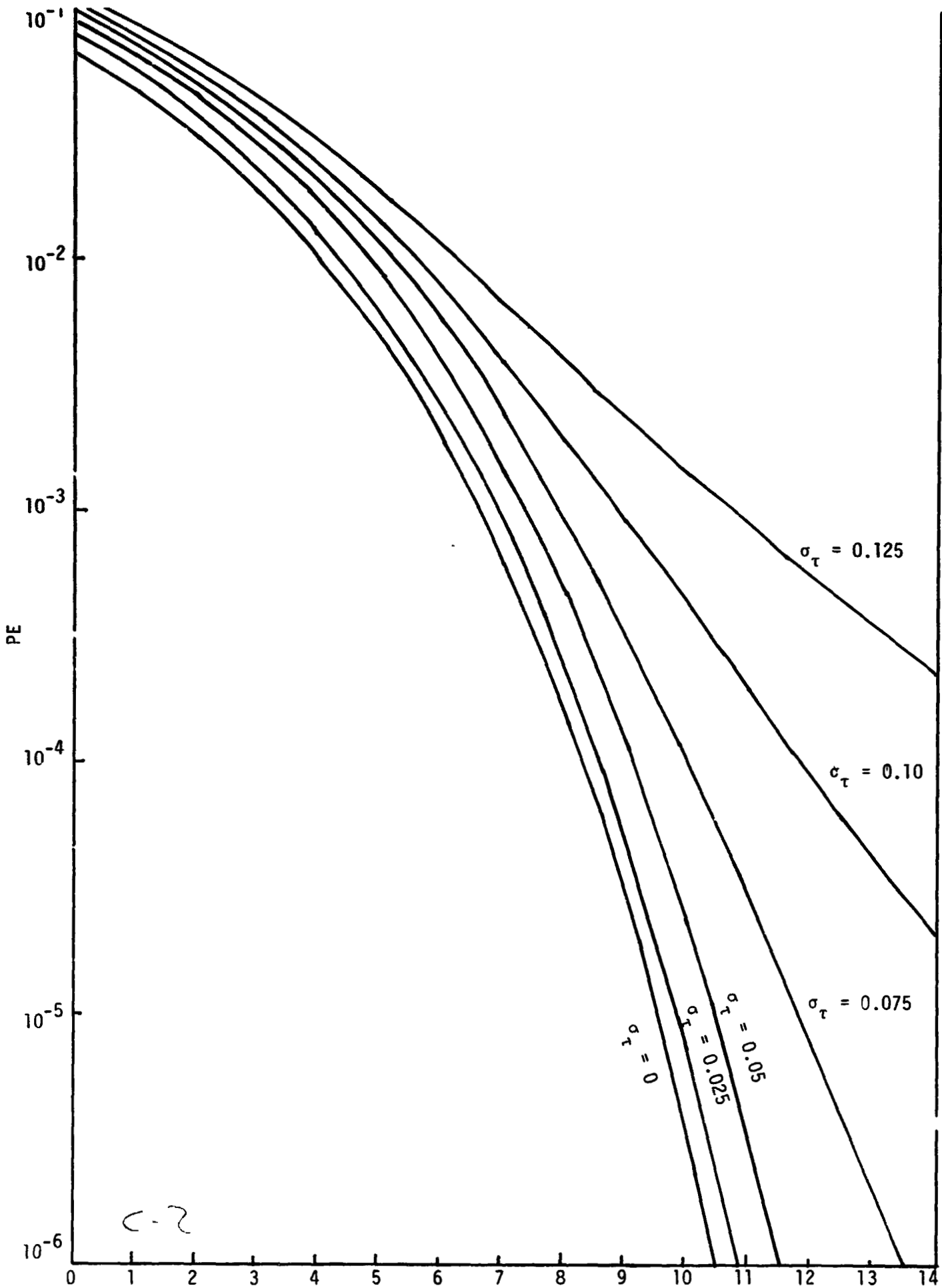


Figure 11. PE versus RMS Timing Error--Gaussian Error NRZ Data, Bit Synchronizer Tracking

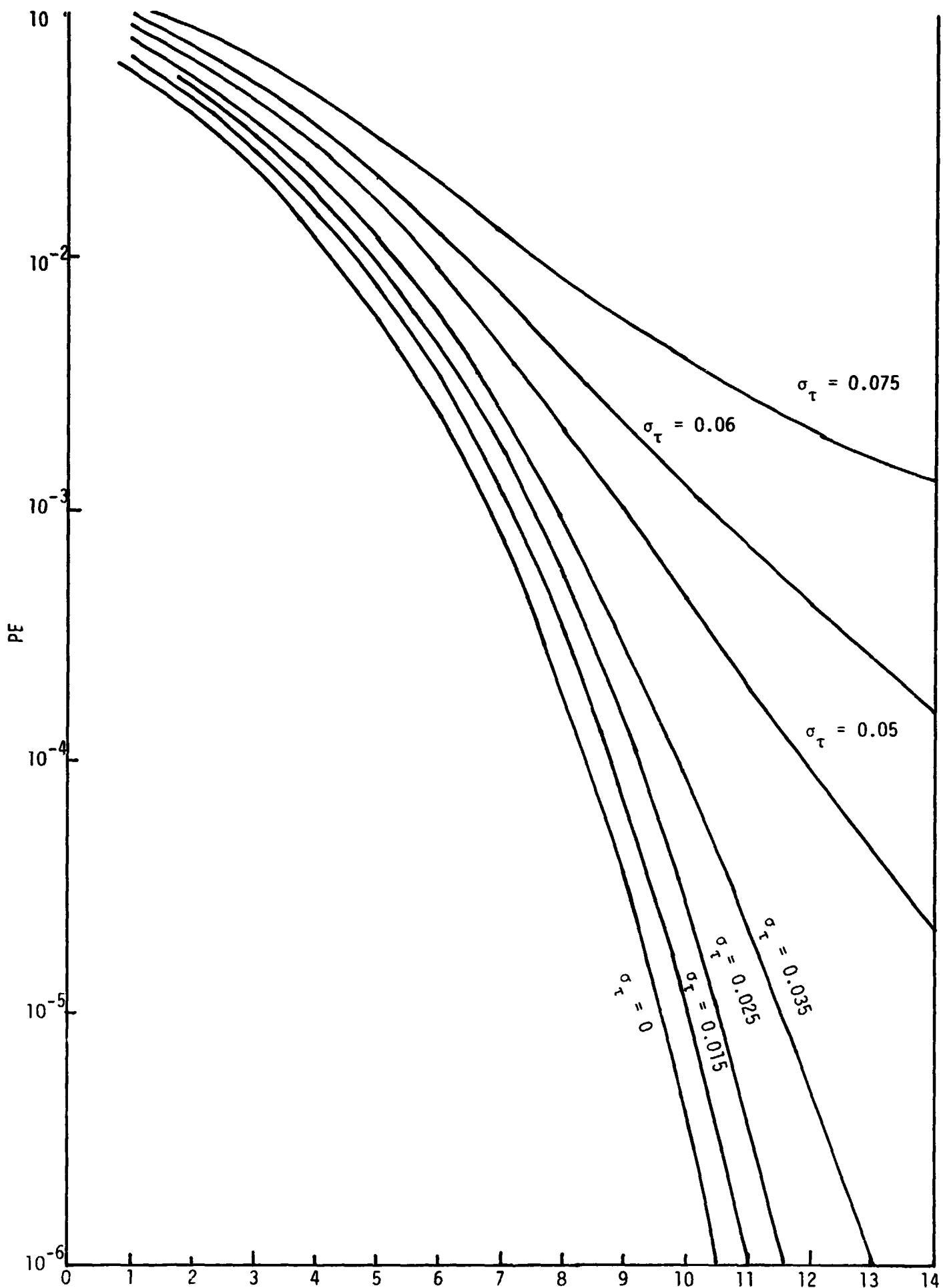


Figure 12. PE versus RMS Timing Error--Gaussian Error
Bi- ϕ -L Data, Bit Synchronizer Tracking

Based on a telephone conversation with John Roach of Harris Corporation (Melbourne, Florida), the following bit synchronizer specifications were obtained:

1. Ultra-High Data Rate Bit Synchronizer (UHDR)

$$R_s = 75-150 \text{ Msps}$$

$$f_n = 60 \text{ kHz} \quad (B_L = 200 \text{ Hz})$$

Manufacturer: Motorola

Jitter problems comments: Yes, since they could not make the loop bandwidth narrow enough due to internal delays

2. High Rate Bit Synchronizer (HDR)

$$R_s = 10-75 \text{ Msps (will operate down to 4 Msps)}$$

$$f_n = 0.08\% R_s \quad (B_L = 0.267\% R_s)$$

Manufacturer: Harris Corporation

Jitter Problem: No

3. Low-Medium Data Bit Synchronizer (LMDR)

$$R_s = 1 \text{ ksps to } 10 \text{ Msps}$$

$$f_n = 0.1\% R_s, 0.3\% R_s, 1\% R_s, 2\% R_s$$

Manufacturer: Aydin Monitor

Jitter Problem: No.

First we consider the sinusoidal jitter case. We consider two subcases; the first is for $\Delta f = 0.01\% R_s$ and $f_m = 0.01\% R_s$, we call this case (a). The second is for $\Delta f = 0.1\% R_s$ and $f_m = 0.1\% R_s$, which we call case (b). The BER degradations are shown in Table 1.

For the random case using the same two subcases, we obtain the results for BER degradation which are shown in Table 2.

In conclusion, we see that, when the frequency deviation and the deviation rate are specified at $0.01\% R_s$, the degradation does not exceed 0.2 dB but, with the specifications at $0.1\% R_s$, the degradation can be over 10 dB. Also from Tables 1 and 2, it can be seen that Manchester

Table 1. Degradation for the Three Bit Synchronizer Classes and the Two Jitter Specifications [(a) and (b)] for Sine Wave Jitter (Uncoded Data)

Bit Synchronizer Class	Degradation		f_m/f_n
	NRZ Data	Bi- ϕ -L Data	
UHDR (a)	0.1 dB	0.2 dB	0.25
UHDR (b)	2.5 dB	= 10 dB	2.5
HDR (a)	≤ 0.1 dB	≤ 0.1 dB	0.125
HDR (b)	2.0 dB	= 8.0 dB	1.25
LMDR (a)	≤ 0.1 dB	≤ 0.1 dB	0.1
LMDR (b)	1.7 dB	4.5 dB	1.0

Table 2. Degradation for the Three Bit Synchronizer Classes and the Two Jitter Specifications [(a) and (b)] Random Noise Jitter (Uncoded Data)

Bit Synchronizer Class	Degradation		f_m/f_n
	NRZ Data	Bi- ϕ -L Data	
UHDR (a)	0.03 dB	0.08 dB	0.25
UHDR (b)	2.6 dB	≥ 10 dB	2.5
HDR (a)	≤ 0.1 dB	≤ 0.1 dB	0.125
HDR (b)	1.6 dB	9.0 dB	1.25
LMDR (a)	≤ 0.1 dB	≤ 0.1 dB	0.1
LMDR (b)	0.7 dB	2.3 dB	1.0

data causes more degradation than NRZ data, as is well-known. Finally, sine wave jitter and flat random noise jitter cause roughly the same level of degradation based on the Ku-band Shuttle jitter specification.

REFERENCES

1. "Shuttle Integrated Communications and Radar Equipment, Ku-Band", Amendment to Specification MC 409-0025 (Rev. B), Rockwell International, Space Division, July 12, 1978.
2. Blyth, R. A., and Carpenter, D. D., "Jitter Effects on Convolutionally Encoded Viterbi Decoded Communication Link", TRW Memo dated September 10, 1979.
3. Papoulis, A., Probability, Random Variables, and Stochastic Processes, McGraw-Hill, 1965..
4. Gradshteyn, I. S., and Ryzhik, I. M., Table of Integrals, Series, and Products, Academic Press, 1965.
5. Rivers, J. W., "AFSCF Dejitter Circuit Test Bit Jitter Calculations", NASA JSC, August 1979.

APPENDIX II

**EFFECT OF DATA ASYMMETRY ON UNBALANCED QPSK
SIGNALS WITH NOISY PHASE REFERENCE**

By

Andreas Polydoros

EFFECT OF DATA ASYMMETRY ON UNBALANCED QPSK SIGNALS WITH NOISY PHASE REFERENCE

By

Andreas Polydoros

1.0 INTRODUCTION

In this report, an analysis is attempted of the impact of data asymmetry on the bit error rate performance of a QPSK signaling scheme used to transmit two data streams with different rates and different powers. Such a model arises, for example, in the QDSB system employed in the Shuttle Ku-band Mode 1 return link [1], which is essentially a cascade of two such unbalanced QPSK systems. Of primary interest here will be the subcarrier QPSK system and, in particular, the version implemented via a digital phase-shift-modulated square-wave subcarrier [2].

The performance of the recently popular unbalanced QPSK (UQPSK) systems in the presence of reference phase noise has been examined by a number of authors (see [3] - [7] and references therein). The general approach is to evaluate the bit error probability conditioned on the data and the value ϕ of the phase error, and then average over these variables. The marginal probability density function (p.d.f.) of ϕ strongly depends on the employed tracking loop and is, in general, difficult to accurately evaluate for sophisticated receivers. Here we follow a truncated Taylor series expansion approach, indicated in [5], which provides credible results, assuming high loop signal-to-noise ratio (SNR). Regardless of the particular method used, the bit error probability (BEP) depends on the powers and data rates of the individual channels.

The ϕ -conditioned BEP (which is a reasonable estimate of BEP for very high SNR) is an increasing function of ϕ , the reason being that an imperfect phase lock loop attenuates the demodulated signal power and at the same time increases interchannel cross talk.

Data asymmetry is a potential source of performance degradation in any digital transmission system. It arises whenever the modulator spends more time at one amplitude state than the other, as a result of the misalignment of a threshold device. It is usually defined as the

difference between the elongated pulse length and the shortened pulse length, normalized by the nominal length. References [8] and [9] pertain to previous work on the issue of determining the effect of data asymmetry on the BEP of BPSK signaling ([8], for a variety of coded and uncoded data) and UQPSK with equal data rates [9]. Since no cross talk was considered in [9], the two QPSK channels are essentially two independent identical BPSK channels with different power allocation.

The present work addresses the problem of evaluating the performance degradation of a UQPSK system due to both data asymmetry and noisy reference. As we shall see, the degradation of each channel can qualitatively be perceived as consisting of a "self-degradation" term plus a "cross-degradation" term. The former is the superposition of a power attenuation (due to noisy reference) along with the impairment caused by asymmetry. The latter (which is actually the interchannel interference) exists because of the presence of noisy reference and also depends on the asymmetry of the companion channel data stream. Hence, the results to be derived here should coincide with those in [8] and [9], if the phase error is assumed zero.

Section 2.0 summarizes the results of this current research and emphasizes the assumptions involved in deriving them, since these assumptions weigh heavily on the validity of the conclusions. In Section 3.0, we elaborate on the system model assumed by the analysis and, in Section 4.0, we proceed to evaluate the BEP for Channels 2 and 3.

2.0 SUMMARY

The parameter of interest here is the additional signal-to-noise ratio ΔSNR (dB) required to compensate for the losses due to asymmetry and phase noise for each channel. It is defined as the difference between the SNR required to achieve a BEP of 10^{-5} under the aforementioned conditions and the nominal value of 9.6 dB for an ideal BPSK system without impairments other than Gaussian noise.

We have assumed a power ratio of 4 and a data rate ratio of 10 for the two channels. These are typical values for the I and Q components of the subcarrier QPSK system of the Orbiter's Ku-band, which operate at 2 Mbps and 0.2 Mbps, respectively.

According to the approach taken in this report, the phase error impact is sufficiently characterized by the mean m_ϕ and the variance σ_ϕ^2 of the tracking jitter ϕ . When a biphasic Costas tracking loop is employed at the receiver, references [10] and [11] provide some (although complicated) analytic results for σ_ϕ . We feel that an extension of these results in the presence of asymmetry is a prohibitively complicated task; therefore, we can only postulate some values for m_ϕ and σ_ϕ . However, it is intuitively appealing to assume that, in the presence of small asymmetry, typical values for σ_ϕ will be slightly higher than what appears in the figures of [10] and [11]. As such, we have selected to examine the cases of $m_\phi = 0^\circ, 3^\circ, 5^\circ$ and $\sigma_\phi^2 = 0, 4, 9$ (degrees)². The analytic results are summarized in (27a), (32), (39), and (48) for the high data rate channel 2 and in (27b), (32), (43), (58), (62), and (63) for the low data rate channel 3. Before commenting on the computer results, let us focus on the assumptions made in the course of the analysis.

First we considered NRZ-L data for both channels. An analysis for biphasic-L data would follow on the same lines. Second, we have assumed perfect symbol synchronization for each individual channel. Third, we have assumed that the data rate ratio N is much greater than one, in general (for the specific application where $N = 10$, such an assumption is well justified). The above assumptions suffice in order to derive a good estimate of the bit error probability of the high data rate channel. For the low data rate channel, two more assumptions are involved: first, that N is an integer, and second, that the two channels are aligned, i.e., no epoch difference exists. Although the second assumption is perhaps rarely met in practice (since there are two different data clocks for the two channels, they most likely are independent, therefore not aligned), one can argue that the significance of the epoch difference diminishes as N increases. Similarly, if N is not an integer, one can consider the integer part of it and still get credible results. In summary, the cardinal assumptions for the analysis to be reasonably precise are that (1) each channel is perfectly synchronized, and (2) N is sufficiently greater than one.

Figures 7(a-c) and 8(a-c) show the plots of ΔSNR as a function of the percent asymmetry A , with m_ϕ and $\text{var } \phi$ as parameters. To gain some confidence about their correctness, let us notice that, for $\text{var } \phi = 0$ and $A = 0$ (m_ϕ is the single parameter then), the results coincide with the results of Figures 9 and 10 of [6] for both channels. Also, for the high data rate channel with $m_\phi = 0$, $\sigma_\phi = 0$, and different degrees of asymmetry, the results coincide with Table 1 of [8].

A study of Figures 7 and 8 shows that the low data rate channel (Q) is more sensitive to parameter variation than the high data rate channel (I). In general, the SNR losses increase exponentially with the amount of asymmetry present for both channels. For the values considered, they range from 0 dB to 1.4 dB for the I channel and from 0 dB to 1.9 dB for the Q channel. We also notice that the plots are virtually parallel (for a fixed σ_ϕ), which means that the presence of a mean phase error shifts the curves upwards. In other words, the effects of phase mean and phase variance are effectively decoupled. However, as expected, as σ_ϕ increases, the effect of phase offset becomes more and more drastic.

3.0 ANALYTIC MODEL

We adopt in this report the following modulation and demodulation schemes.

3.1 Modulator

In Figure 1, the three-channel interplex modulator (Hughes Aircraft Company version) is shown. The waveform $C(t)$ is given by

$$C(t) = \sqrt{P_s} \sin [\omega_{sc}t + \theta(t)], \quad (1)$$

where

$$\theta(t) = m_2(t)m_3(t)\theta_0 - \left(\frac{m_2(t)-1}{2}\right)\pi. \quad (2)$$

The angle $\theta(t)$ is shown in Figure 2. The functions $m_2(t)$ and m_3 represent the digital data streams for the two channels, respectively.

The total three-channel signal is

$$s(t) = \sqrt{2} \{C(t) \cos \omega_0 t + S(t) \sin \omega_0 t\} \quad (3)$$

where ω_0 is the carrier radian frequency and

$$S(t) = \sqrt{P_1} m_1(t) \quad (4)$$

Assuming that $m_2(t)$, $m_3(t)$ are perfectly $\pm 1 \forall t$, then further analysis of (1) shows that [2]:

$$C(t) = \sqrt{P_s} m_2(t) \mathbf{S}^+(\omega_{sc} t; \theta_0) + \sqrt{P_s} m_3(t) \mathbf{S}^-(\omega_{sc} t; \theta_0) \quad (5)$$

where

$$\mathbf{S}^+(\omega_{sc} t; \theta_0) \triangleq \frac{1}{2} \mathbf{S}_{in}(\omega_{sc} t + \theta_0) + \frac{1}{2} \mathbf{S}_{in}(\omega_{sc} t - \theta_0) \quad (6)$$

and $\mathbf{S}^-(\omega_{sc} t; \theta_0) \triangleq \frac{1}{2} \mathbf{S}_{in}(\omega_{sc} t + \theta_0) - \frac{1}{2} \mathbf{S}_{in}(\omega_{sc} t - \theta_0)$

Waveforms $\mathbf{S}^+(\omega_{sc} t; \theta_0)$ and $\mathbf{S}^-(\omega_{sc} t; \theta_0)$ are shown in Figure 3.

The power ratio

$$\left(\frac{P_2}{P_3} \right)_{\text{transmitter}} = \frac{1 - \frac{2\theta_0}{\pi}}{\frac{2}{\pi} \theta_0} \quad (7)$$

It can be further shown (always assuming that $m_1(t)$, $m_2(t)$ take on only values ± 1) that, for this implementation in Mode 1, the bandpass hard limiter has no effect on $s(t)$, so that $z(t) = s(t)$. This is because

$$V(t) = \sqrt{P_1 m_1^2(t) + P_s \mathbf{S}_{in}^2(\omega_{sc} t + \theta(t))} = \text{constant}$$

Note that, in the presence of disturbances affecting the amplitude of either $m_1(t)$ or $\mathbf{S}_{in}(\cdot)$ or both, this will no longer be true and the redistribution of power and the triple cross-modulation term appearance will have to be more closely examined.

3.2 Demodulator/Detector

Figure 4 shows the assumed form of the demodulator/detector for channels 2 and 3. A similar loop is employed for tracking the carrier and demodulating the high data rate channel 1. We assume that this loop has no effect on the subcarrier demodulation loop, i.e., there is no phase-tracking error in the carrier demodulation loop. We will have to relax this assumption later, when we will examine the effect of parameter variations in the high data rate channel 1 since these variations introduce a phase error ϕ_c in the carrier loop. For the time being, we concentrate on the effect of parameter variations in channels 2 and 3 only.

Note the presence of the bandpass filter before the subcarrier loop. The output $x(t)$ of the bandpass filter can be written as

$$x(t) = C_1(t) + n_{BP}(t) \quad (8)$$

where $C_1(t)$ is the bandpass filtered version of $C(t)$ (where only the fundamental is retained) and $n_{BP}(t)$ is bandpass noise represented by

$$n_{BP}(t) = \sqrt{2} \left\{ N_c(t) \cos \omega_{SC} t \cdot N_s(t) \sin \omega_{SC} t \right\} \quad (9)$$

In (9), $N_c(t)$ and $N_s(t)$ are approximately statistically independent white (compared to the data bandwidth) Gaussian noise processes with single-sided spectral density N_0 W/Hz and single-sided bandwidth $B_H < \omega_{SC}/2\pi$ Hz. In the absence of the bandpass filter, such a representation would be of questionable validity.

If we expand $\sin(\cdot)$ into a Fourier series and retain only the first harmonic, (1) gives [2]:

$$\begin{aligned} C_1(t) &= \frac{4}{\pi} \sqrt{P_S} \sin(\omega_{SC} t + \theta(t)) \\ &= \frac{4}{\pi} \sqrt{P_S} \cos \theta(t) \sin \omega_{SC} t + \frac{4}{\pi} \sqrt{P_S} \sin \theta(t) \cos \omega_{SC} t \end{aligned} \quad (10)$$

or, using (2) (always with the assumption that $m_i(t) = \pm 1$, $i = 2, 3$), we get

$$c_1(t) = \frac{4}{\pi} \sqrt{P_s} m_2(t) \cos \theta_0 \sin \omega_{sc} t + \frac{4}{\pi} \sqrt{P_s} m_3(t) \sin \theta_0 \cos \omega_{sc} t \quad (11)$$

The power ratio at the receiver is

$$\left(\frac{P_2}{P_3} \right)_{\text{receiver}} = \frac{\cos^2 \theta_0}{\sin^2 \theta_0} = \cot^2 \theta_0 \quad (12)$$

as can be seen from (11). Comparing (12) with (7), we observe that the BPF rearranges the power allocation. Define

$$P_{2r} = \left[\frac{1}{2} \left(\frac{4}{\pi} \right)^2 \cos^2 \theta_0 \right] P_s \quad (13)$$

$$P_{3r} = \left[\frac{1}{2} \left(\frac{4}{\pi} \right)^2 \sin^2 \theta_0 \right] P_s \quad (14)$$

so that $P_{2r} + P_{3r} = (8/\pi^2) P_s$ (the loss $8/\pi^2$ is due to the BPF). Then (10) is written as

$$c_1(t) = \sqrt{2P_{2r}} m_2(t) \sin \omega_{sc} t + \sqrt{2P_{3r}} m_3(t) \cos \omega_{sc} t \quad (15)$$

We assume switching type phase detectors (i.e., square wave reference signals) for the coherent demodulation of the signal. Let us assume that

$$r_s(t) = \sum \sin [\omega_{sc} t - \phi] \quad (16a)$$

$$r_c(t) = \sum \cos [\omega_{sc} t - \phi] \quad (16b)$$

where $\phi(t)$ is the phase error process. In (16), we have assumed, for simplicity, unit reference gains.

Expanding (16) into a Fourier series and noticing that only the first harmonics $4/\pi \sin(\omega_{sc} t - \phi)$ and $4/\pi \cos(\omega_{sc} t - \phi)$ correlate with the quadrature signals, respectively, we get

$$\begin{aligned}
e_s(t) &= \left[C_1(t) + n_{BP}(t) \right] \cdot \frac{4}{\pi} \sin(\omega_{sc} t - \phi) \Big|_{LP} \\
&= \frac{2\sqrt{2}}{\pi} \left[\sqrt{P_{2r}} m_2(t) - N_s(t) \right] \cos\phi - \frac{2\sqrt{2}}{\pi} \left[\sqrt{P_{3r}} m_3(t) + N_c(t) \right] \sin\phi \quad (17a)
\end{aligned}$$

$$\begin{aligned}
e_c(t) &= \left[C_1(t) + n_{BP}(t) \right] \cdot \frac{4}{\pi} \cos(\omega_{sc} t - \phi) \Big|_{LP} \\
&= \frac{2\sqrt{2}}{\pi} \left[\sqrt{P_{3r}} m_3(t) + N_c(t) \right] \cos\phi - \frac{2\sqrt{2}}{\pi} \left[\sqrt{P_{2r}} m_2(t) - N_s(t) \right] \sin\phi \quad (17b)
\end{aligned}$$

Waveforms $e_s(t)$ and $e_c(t)$ are the inputs to the channel data detectors which we assume to be matched filters. The outputs of these integrate-and-dump circuits at the end of the k th and l th signaling interval of each channel are given by

$$D_2 = \frac{1}{T_2} \int_{(k-1)T_2 + \epsilon_2}^{kT_2 + \epsilon_2} e_s(t) P_2(t - (k-1)T_2 - \epsilon_2) dt \quad (18a)$$

$$D_3 = \frac{1}{T_3} \int_{(l-1)T_3 + \epsilon_3}^{lT_3 + \epsilon_3} e_c(t) P_3(t - (l-1)T_3 - \epsilon_3) dt \quad (18b)$$

where $P_i(t)$; $i=2,3$ is the basic unit power symbol pulse in the i th data stream $m_i(t)$ and is defined to be nonzero only in the interval $(0, T_i)$. Hence, we have assumed that the data stream is ideally of the form

$$m_i(t) = \sum_{n=-\infty}^{\infty} a_{n_i} P_i(t - nT_i - \epsilon_i); \quad i = 2,3 \quad (19)$$

where

(1) $\{a_{n_i}\}$; $i=2,3$ are independent ± 1 sequences with the properties

$$E \left\{ a_{n_i} a_{m_i} \right\} = \delta_{m_n} \begin{cases} 1 & m = n \\ 0 & m \neq n \end{cases} \quad (20)$$

$$E \left\{ a_{n_i} a_{m_j} \right\} = 0, \text{ all } n, m \text{ and } i \neq j$$

(2) ϵ_i ; $i=2,3$ is the arbitrary pulse epoch in these same modulations.

As we shall later see, due to different asymmetries, the series representation of the $m_i(t)$ as a function of a_{n_i} in (19) is no longer correct. In the following, we shall derive an expression for the probability of error as a function of $m_i(t)$ rather than $a_{n_i}(t)$. We shall also assume that $\phi(t)$ is constant over the baud of either channel. Substituting (17) into (18) and dropping the factor $2\sqrt{2}/\pi$, we get

$$D_2 = \sqrt{P_{2r}} \bar{m}_{22} \cos\phi - \sqrt{P_{3r}} \bar{m}_{32} \sin\phi + \tilde{N}_2(t) \quad (21a)$$

$$D_3 = \sqrt{P_{3r}} \bar{m}_{33} \cos\phi + \sqrt{P_{2r}} \bar{m}_{23} \sin\phi + \tilde{N}_3(t) \quad (21b)$$

where

$$\bar{m}_{22} = \frac{1}{T_2} \int_{(k-1)T_2+\epsilon_2}^{kT_2+\epsilon_2} m_2(t) P_2(t - (k-1)T_2 - \epsilon_2) dt \quad (22a)$$

$$\bar{m}_{32} = \frac{1}{T_2} \int_{(k-1)T_2+\epsilon_2}^{kT_2+\epsilon_2} m_3(t) P_2(t - (k-1)T_2 - \epsilon_2) dt \quad (22b)$$

$$\bar{m}_{33} = \frac{1}{T_3} \int_{(\ell-1)T_3+\epsilon_3}^{\ell T_3+\epsilon_3} m_3(t) P_3(t - (\ell-1)T_3 - \epsilon_3) dt \quad (22c)$$

$$\bar{m}_{23} = \frac{1}{T_3} \int_{(\ell-1)T_3+\epsilon_3}^{\ell T_3+\epsilon_3} m_2(t) P_3(t - (\ell-1)T_3 - \epsilon_3) dt \quad (22d)$$

$$\tilde{N}_2(t) = -\frac{1}{T_2} \left[\cos\phi \int_{(k-1)T_2+\epsilon_2}^{kT_2+\epsilon_2} N_s(t) P_2(t - (k-1)T_2 - \epsilon_2) dt \right. \\ \left. + \sin\phi \int_{(k-1)T_2+\epsilon_2}^{kT_2+\epsilon_2} N_c(t) P_2(t - (k-1)T_2 - \epsilon_2) dt \right] \quad (22e)$$

$$\tilde{N}_3(t) = -\frac{1}{T_3} \left[-\cos\phi \int_{(\ell-1)T_3+\epsilon_3}^{\ell T_3+\epsilon_3} N_c(t) P_3(t - (\ell-1)T_3 - \epsilon_3) dt \right. \\ \left. + \sin\phi \int_{(\ell-1)T_3+\epsilon_3}^{\ell T_3+\epsilon_3} N_s(t) P_3(t - (\ell-1)T_3 - \epsilon_3) dt \right] \quad (22f)$$

Notice that, in the absence of any distortion, (22a) and (22c) yield $a_{(k-1),2}$ and $a_{(k-1),3}$, respectively.

From (22e) and (22f), it is easy to show that

$$\tilde{N}_i(t) \sim G\left(0; \frac{N_0}{2T_i}\right); \quad i = 2,3 \quad (23)$$

The decision scheme (a zero-level threshold device) outputs

$$\hat{a}_{\xi,i} = \text{sgn}\{D_i\} \quad ; \quad i = 2,3 \quad (24)$$

at the ξ th signaling interval of either channel.

Conditioned on $\tilde{m}_{22}, \tilde{m}_{32}, \tilde{m}_{33}, \tilde{m}_{23}, \phi$, the random variables D_2 and D_3 are Gaussian, with mean

$$E\{D_2 / (\tilde{m}_{i2}; i=2,3), \phi\} = \sqrt{P_{2r}} \tilde{m}_{22} \cos\phi - \sqrt{P_{3r}} \tilde{m}_{32} \sin\phi \quad (25a)$$

$$E\{D_3 / (\tilde{m}_{i3}; i=3,2), \phi\} = \sqrt{P_{3r}} \tilde{m}_{33} \cos\phi + \sqrt{P_{2r}} \tilde{m}_{23} \sin\phi \quad (25b)$$

and variance $\sigma_i^2 = N_0/2T_i; i = 2,3$.

Hence, the conditional probability of error for each channel is

$$P(e_2 / (\tilde{m}_{i2}; i=2,3), \phi) = Q\left[\text{sgn}\{\tilde{m}_{22}\} \cdot \left(\sqrt{R_2} \tilde{m}_{22} \cos\phi - \sqrt{\frac{R_3}{N_T}} \tilde{m}_{33} \sin\phi\right)\right]$$

$$P(e_3 / (\tilde{m}_{i3}; i=3,2), \phi) = Q\left[\text{sgn}\{\tilde{m}_{33}\} \cdot \left(\sqrt{R_3} \tilde{m}_{33} \cos\phi + \sqrt{\frac{R_2}{N_T}} \tilde{m}_{23} \sin\phi\right)\right]$$

where $R_i = 2P_{ir}T_i/N_0$ (SNR for the i th channel) (27)

and

$$N_T = T_3/T_2 (>>1) \quad (28)$$

is the data rates ratio. (We have arbitrarily assumed that Channel 2 has a higher data rate than channel 3)

and

$$Q(x) = \frac{1}{2\pi} \int_x^\infty \exp\left\{-\frac{x^2}{2}\right\} dx \quad (29)$$

Finally, $\text{sgn}(\cdot)$ stands for the sign function.

4.0 AVERAGE ERROR PROBABILITY

To obtain the average error probability, one has to remove the conditioning on the random variables \tilde{m}_{ij} and ϕ . It is clear that both random variables are data dependent in the sense that any parameter variations in the data stream affect the performance of the Costas loop and hence the p.d.f. of ϕ . Unfortunately, we cannot easily obtain the p.d.f. $P_\phi(\phi)$; hence, we are facing two possible alternatives:

(1) Evaluate the ϕ -conditioned $P(e_i/\phi)$ of either channel just by removing the conditioning on \tilde{m}_{ij} . In the case where the variance σ_ϕ^2 is very small (which implies high SNR in the loop), then $P(e_i/\phi)$ stands as a reasonable estimate of $P(e_i)$. The result of such an analysis will be a set of curves of $P(e_i/\phi)$ as a function of SNR, parameterized by the mean value of ϕ and the degree of asymmetry.

(2) Expand $P(e_i/\tilde{m}_{ij},\phi)$ into a Taylor series in ϕ around m_ϕ and retain only the first three terms (a similar approach has been taken in [5]). The results are credible if one again assumes small σ_ϕ . Then,

$$P(e_i/\underline{\tilde{m}},\phi) \cong P(e_i/\underline{\tilde{m}},m_\phi) + \frac{dP(e_i/\underline{\tilde{m}},m_\phi)}{d\phi} \cdot (\phi - m_\phi) + \frac{d^2P(e_i/\underline{\tilde{m}},m_\phi)}{d\phi^2} \cdot (\phi - m_\phi)^2 \quad (30)$$

so that, if $P_\phi(\phi)$ is the marginal p.d.f. of ϕ , we get

$$P(e_i/\underline{\tilde{m}}) = \int P(e_i/\underline{\tilde{m}},\phi) P_\phi(\phi) d\phi \quad (31) \\ \cong P(e_i/\underline{\tilde{m}},m_\phi) + \frac{d^2P(e_i/\underline{\tilde{m}},m_\phi)}{d\phi^2} \cdot \sigma_\phi^2$$

where $\underline{\tilde{m}} = (\tilde{m}_{i1}, \tilde{m}_{ij})$; $i, j = 2, 3; (i \neq j)$.

Equation (31) is parameterized by m_ϕ and σ_ϕ . Removing the $\underline{\tilde{m}}$ -conditioning from each of the three terms in (31) will yield $P(e_i)$.

The second approach takes us one step further in approximating $P(e_i)$ closer because of the presence of the correcting second term. From (26a) and (26b), we have

$$\frac{dP(e_i/\bar{m}, \phi)}{d\phi} = -\frac{1}{\sqrt{2\pi}} \exp\left\{-\frac{z_i^2}{2}\right\} \frac{dz_i}{d\phi} \quad (32)$$

where $z_i(\phi)$; $i=2,3$ is the argument of $Q(\cdot)$. But

$$\frac{dz_2}{d\phi} = -\operatorname{sgn}\{\bar{m}_{22}\} \cdot \left(\sqrt{R_2} \bar{m}_{22} \sin\phi + \sqrt{\frac{R_3}{N_T}} \bar{m}_{32} \cos\phi \right) \quad (33a)$$

$$\frac{dz_3}{d\phi} = -\operatorname{sgn}\{\bar{m}_{33}\} \cdot \left(\sqrt{R_3} \bar{m}_{33} \sin\phi - \sqrt{R_2 N_T} \bar{m}_{23} \cos\phi \right) \quad (33b)$$

so that

$$\begin{aligned} \frac{d}{d\phi} P(e_2/\bar{m}, \phi) &= \frac{1}{\sqrt{2\pi}} \left(\sqrt{R_2} \bar{m}_{22} \sin\phi + \sqrt{\frac{R_3}{N_T}} \bar{m}_{32} \cos\phi \right) \\ &\cdot \exp\left\{-\frac{\left(\sqrt{R_2} \bar{m}_{22} \cos\phi - \sqrt{\frac{R_3}{N_T}} \bar{m}_{32} \sin\phi \right)^2}{2}\right\} \cdot \operatorname{sgn}\{\bar{m}_{22}\} \quad (34a) \end{aligned}$$

and

$$\begin{aligned} \frac{d}{d\phi} P(e_3/\bar{m}, \phi) &= \frac{1}{\sqrt{2\pi}} \left(\sqrt{R_3} \bar{m}_{33} \sin\phi - \sqrt{R_2 N_T} \bar{m}_{23} \cos\phi \right) \\ &\cdot \exp\left\{-\frac{\left(\sqrt{R_3} \bar{m}_{33} \cos\phi + \sqrt{R_2 N_T} \bar{m}_{23} \sin\phi \right)^2}{2}\right\} \cdot \operatorname{sgn}\{\bar{m}_{33}\} \quad (34b) \end{aligned}$$

then

$$\frac{d^2 P(e_2/\bar{m}, \phi)}{d\phi^2} = \frac{\operatorname{sgn}\{\bar{m}_{22}\}}{\sqrt{2\pi}} \cdot \frac{d}{d\phi} \left(z_2^* \exp\left\{-\frac{z_2^2}{2}\right\} \right) \quad (35)$$

where

$$z_2^* = \sqrt{R_2} \bar{m}_{22} \sin\phi + \sqrt{\frac{R_3}{N_T}} \bar{m}_{32} \cos\phi = -\frac{dz_2}{d\phi} \cdot \operatorname{sgn}\{\bar{m}_{22}\} \quad (36)$$

and

$$\frac{dz_2^*}{d\phi} = z_2^* \operatorname{sgn}\{\bar{m}_{22}\} \quad (37)$$

From (35), (36) and (37), it follows that

$$\begin{aligned} \frac{d^2 P(e_2/\tilde{m}, \phi)}{d\phi^2} &= \frac{\text{sgn}\{\tilde{m}_{22}\}}{\sqrt{2\pi}} \left[z_2 \cdot \text{sgn}\{\tilde{m}_{22}\} \cdot \exp\left\{-\frac{z_2^2}{2}\right\} \right. \\ &\quad \left. + z_2^* \cdot (-z_2) \left(-z_2^* \text{sgn}\{\tilde{m}_{22}\}\right) \cdot \exp\left\{-\frac{z_2^2}{2}\right\} \right] \\ &= \frac{z_2}{\sqrt{2\pi}} \cdot \exp\left\{-\frac{z_2^2}{2}\right\} \cdot \left[1 + (z_2^*)^2\right] \end{aligned}$$

or

$$\begin{aligned} \frac{d^2 P(e_2/\tilde{m}, \phi)}{d\phi^2} &= \frac{\text{sgn}\{\tilde{m}_{22}\}}{\sqrt{2\pi}} \cdot \left(\sqrt{R_2} \tilde{m}_{22} \cos\phi - \sqrt{\frac{R_3}{N_T}} \tilde{m}_{32} \sin\phi\right) \\ &\quad \cdot \left[1 + \left(\sqrt{R_2} \tilde{m}_{22} \sin\phi + \sqrt{\frac{R_3}{N_T}} \tilde{m}_{32} \cos\phi\right)^2\right] \cdot \exp\left\{-\frac{\left(\sqrt{R_2} \tilde{m}_{22} \cos\phi - \sqrt{\frac{R_3}{N_T}} \tilde{m}_{32} \sin\phi\right)^2}{2}\right\} \end{aligned} \quad (38)$$

Similarly, from (34a),

$$\frac{d^2 P(e_3/\tilde{m}, \phi)}{d\phi^2} = \frac{\text{sgn}\{\tilde{m}_{33}\}}{\sqrt{2\pi}} \cdot \frac{d}{d\phi} \left(z_3^* \exp\left\{-\frac{z_3^2}{2}\right\} \right) \quad (39)$$

where

$$z_3^* = \sqrt{R_3} \tilde{m}_{33} \sin\phi - \sqrt{\frac{R_2 N_T}{N_T}} \tilde{m}_{23} \cos\phi = -\frac{dz_3}{d\phi} \text{sgn}\{\tilde{m}_{33}\} \quad (40)$$

and

$$\frac{dz_3^*}{d\phi} = z_3 \text{sgn}\{\tilde{m}_{33}\} \quad (41)$$

The result is

$$\begin{aligned} \frac{d^2 P(e_3/\tilde{m}, \phi)}{d\phi^2} &= \frac{\text{sgn}\{\tilde{m}_{33}\}}{\sqrt{2\pi}} \cdot \left(\sqrt{R_3} \tilde{m}_{33} \cos\phi + \sqrt{\frac{R_2 N_T}{N_T}} \tilde{m}_{23} \sin\phi\right) \\ &\quad \cdot \left[1 + \left(\sqrt{R_3} \tilde{m}_{33} \sin\phi - \sqrt{\frac{R_2 N_T}{N_T}} \tilde{m}_{23} \cos\phi\right)^2\right] \cdot \exp\left\{-\frac{\left(\sqrt{R_3} \tilde{m}_{33} \cos\phi + \sqrt{\frac{R_2 N_T}{N_T}} \tilde{m}_{23} \sin\phi\right)^2}{2}\right\} \end{aligned} \quad (42)$$

Equations (38) and (42) are explicit functions of \tilde{m} and ϕ . Once these are determined (see next section for \tilde{m}), the second derivatives can be evaluated. Note the presence of the factor $\text{sgn}(\cdot)$, as a consequence of (26a) and (26b).

We proceed now to evaluate \tilde{m}_{ij} in (23). Several assumptions will be imposed, and the analysis will advance from the simplest case to more complicated cases by relaxing some of the assumptions.

The parameter variation to be examined is data asymmetry. We shall assume that both channels suffer from data asymmetry of degree A , which is presumably the worst case. Define

$$A = \frac{1}{2} (\text{length of long pulse} - \text{length of short pulse}) \div (\text{nominal pulse length}) \quad (43)$$

See Figure 5. Let us first assume NRZ-L format for both data streams. Parameter a of Figure 5, pertaining to the amount of asymmetry occurring at each transition, relates to A as $a = A/2$. Let us also first calculate \tilde{m}_{22} and \tilde{m}_{33} . We note that these quantities measure the "self-degradation" of each channel due to asymmetry; hence, the epochs ϵ_i play no role (we assume perfect synchronization for each individual channel although the QPSK scheme will most likely be staggered because of the different data rates between the two channels), so that no assumption for the ϵ_i 's is necessary up to this point.

The values of \tilde{m}_{22} and \tilde{m}_{33} pertaining to an individual symbol depend on the adjacent symbols. Table 1 summarizes the results.

Table 1. (\tilde{m}_{22} or \tilde{m}_{33}) (NRZ/NRZ)

	$(1) \overset{\downarrow}{(1)} (1)$	$(1) \overset{\downarrow}{(1)} (-1)$	$(-1) \overset{\downarrow}{(1)} (1)$	$(-1) \overset{\downarrow}{(1)} (-1)$
Prob	1/8	1/8	1/8	1/8
\tilde{m}_{22}	1	1	1	1
\tilde{m}_{33}	1	1	1	1
	$(1) \overset{\downarrow}{(-1)} (1)$	$(1) \overset{\downarrow}{(-1)} (-1)$	$(-1) \overset{\downarrow}{(-1)} (1)$	$(-1) \overset{\downarrow}{(-1)} (-1)$
Prob	1/8	1/8	1/8	1/8
\tilde{m}_{22}	$-1 + 2A$	$-1 + A$	$-1 + A$	-1
\tilde{m}_{33}	$-1 + 2A$	$-1 + A$	$-1 + A$	-1

4.1 High Data Rate Channel

Having assumed $T_3 > T_2$, we now proceed to evaluate \tilde{m}_{32} . Because $T_3 > T_2$, within an interval of length T_2 one of the following exclusive events can happen:

E_{+1}^3 = the event of having Channel 3 at the state $a_{l3} = +1$ in the interval $[(k-1)T_2, kT_2]$

E_{-1}^3 = the event of having Channel 3 at the state $a_{l3} = -1$ in the interval $[(k-1)T_2, kT_2]$

E_{sw}^3 = the event in which Channel 3 switches state in $[(k-1)T_2, kT_2]$

with corresponding probabilities $P(E_{+1}^3)$, $P(E_{-1}^3)$, and $P(E_{sw}^3)$ such that $P(E_{+1}^3) + P(E_{-1}^3) + P(E_{sw}^3) = 1$.

Assigning probabilities to the aforementioned events is a rather difficult task, since these events depend on the ratio T_2/T_3 , the amount of asymmetry present, the epochs statistics, etc. However, things are simplified completely if we make the assumption that $T_3/T_2 \gg 1$. This assumption is justified in our case, where $T_3/T_2 \geq 10$ (see [1]). Then, as $T_3/T_2 \rightarrow \infty$, event E_{sw}^3 is of probability measure zero, so that

$$P(E_{+1}^3) + P(E_{-1}^3) \cong 1 \quad (44)$$

In the absence of asymmetry, it would be $P(E_{+1}^3) = P(E_{-1}^3) = 1/2$. However, because of the asymmetry A present, each of the two probabilities equals the average percentage of time allotted to each symbol correspondingly, i.e.,

$$P(E_{+1}^3) = \frac{1}{8} \cdot 1 + \frac{2}{8} \cdot \left(1 + \frac{A}{2}\right) + \frac{1}{8} (1 + A) = \frac{1}{2} \left(1 + \frac{A}{2}\right) \quad (45)$$

$$P(E_{-1}^3) = \frac{1}{8} \cdot 1 + \frac{2}{8} \left(1 - \frac{A}{2}\right) + \frac{1}{8} (1 - A) = \frac{1}{2} \left(1 - \frac{A}{2}\right) \quad (46)$$

(See Table 1 also.)

Combining (23b) and (45) and the fact that both $p_1(t)$ and $p_2(t)$ are NRZ-L data, we form Table 2:

Table 2. (\tilde{m}_{32})

a_{k3}	+1	-1
Prob	$\frac{1}{2}(1 + \frac{A}{2})$	$\frac{1}{2}(1 - \frac{A}{2})$
\tilde{m}_{32}	1	-1

We are now in a position to write an expression for the average error probability in the high data rate Channel 2:

$$\begin{aligned}
 P(e_2) = & \frac{1}{2} \left[\frac{1}{2} \left(1 + \frac{A}{2}\right) P(e_2/(1,1)) + \frac{1}{2} \left(1 - \frac{A}{2}\right) P(e_2/(1,-1)) \right] \\
 & + \frac{1}{4} \left[\frac{1}{2} \left(1 + \frac{A}{2}\right) P(e_2/(-1+A,1)) + \frac{1}{2} \left(1 - \frac{A}{2}\right) P(e_2/(-1+A,-1)) \right] \\
 & + \frac{1}{8} \left[\frac{1}{2} \left(1 + \frac{A}{2}\right) P(e_2/(-1+2A,1)) + \frac{1}{2} \left(1 - \frac{A}{2}\right) P(e_2/(-1+2A,-1)) \right] \\
 & + \frac{1}{8} \left[\frac{1}{2} \left(1 + \frac{A}{2}\right) P(e_2/(-1,-1)) + \frac{1}{2} \left(1 - \frac{A}{2}\right) P(e_2/(-1,-1)) \right] \quad (47)
 \end{aligned}$$

where the notation

$$P(e_2/a, \beta) \triangleq P(e_2/\tilde{m}_{22} = a, \tilde{m}_{32} = \beta) \quad (48)$$

and the corresponding expression for $P(e_2/(\tilde{m}_{22}, \tilde{m}_{32}))$ is given by (31) in conjunction with (38). (Case I is a special case of II when $\sigma_\phi^2 = 0$.)

We now summarize the conclusion of this section as follows.

Equation (47) yields the average bit error rate for the high data rate Channel 2. Assumptions used to derive (47) are summarized below.

(1) Phase-error variance is small, so that the truncated Taylor series (30) gives reasonably good results.

(2) Both channels suffer from the same degree of asymmetry A as defined in (43). The case of different degrees of asymmetry for

each channel is a trivial modification of the above results. Indeed, assume that each channel is subjected to asymmetry A_i ; $i = 2, 3$ and $A_2 \neq A_3$. Then each parameter A appearing as an argument of $P(e_2/\tilde{m})$ in (47) should be replaced by A_2 , and each parameter A appearing in the multiplicative factors of the form $(1 + A/2)$ or $(1 - A/2)$ should be replaced by A_3 .

(3) Data are NRZ-L for both channels. Cases where one or both channels have biphas-L data can be handled similarly.

(4) Perfect synchronization is assumed for each individual channel.

(5) The ratio $T_3/T_2 \gg 1$. This enabled us to induce assumption (44) which led to forming Table 2.

(6) No assumption about the epoch statistics is necessary.

4.2 Low Data Rate Channel

We now proceed to evaluate \tilde{m}_{23} , and subsequently $P(e_3)$. If E_x means "expectation with respect to x ," then

$$P(e_3) = E_{\tilde{m}_{33}} \left\{ E_{\tilde{m}_{23}} \left\{ P(e_3/\tilde{m}_{33}, \tilde{m}_{23}) \right\} \right\} \quad (49)$$

We shall first evaluate $P(e_3/(m_{33}, m_{23}))$. The analysis will be carried out under the assumption that the two channels are synchronized, i.e., the epoch difference is identically zero [18]. This means that, within a pulse $P_3(t)$, there exists exactly $N(N \in \mathbb{Z}^+)$ pulses $p_2(t)$ (nominally, i.e., in the absence of asymmetry). It is intuitive, however, to conclude that, for large rate ratios N , the presence or absence of epoch difference is not of great practical import.

In Figure 6, we have shown a possible sequence of N (channel 2) pulses (in the absence of asymmetry) within a T_3 -sec time interval. The pulses have been indexed by k_i ($i = 0, 1, \dots, N+1$) according to their position within the interval. Note that, because of the existing asymmetry, two more pulses (k_0 and k_{N+1}) must be taken into account since their presence affects the results. We shall argue later that

* \mathbb{Z}^+ denotes the set of positive integers.

for N large, their contribution is insignificant, which will result in certain simplifications of the final expression. It is the multiplicity of the possible patterns of the N successive pulses, combined with the presence of asymmetry, that necessitates the following analysis. We make the following assumptions:

- E_{γ}^i ; $i = +, -$
 $\gamma \in [0, N+1]$ = the event that a pulse occupying the γ th position has a +1 or -1 value
- $E_{\gamma, \delta}^{i, j}$; $i, j = +, -$
 $\gamma, \delta \in [0, N+1]$ = the joint event that the γ th pulse has an i sign and the δ th pulse has a j sign
- k = number of positive pulses in the interval $[1, N]$ (i.e., excluding pulses k_0 and k_{N+1})
- ℓ = number of transitions from a positive to a negative pulse or vice versa in the interval $[1, N]$ (i.e., excluding the transitions between the boundary pairs $(0, 1)$ and $(N, N+1)$)
- ℓ_{eff} = number of effective transitions in the interval $[1, N]$ (i.e., with the boundary transitions included, whenever they occur).

With the above definitions available, it is a question of exhaustive search to show that the following conditional relationships hold:

$$\ell_{\text{eff}} \begin{cases} \ell & \text{if} \\ \ell + 1 & \text{if} \\ \ell + 2 & \text{if} \end{cases} \left\{ \begin{array}{l} \text{or } E_{0, N+1}^{-, -} \\ \text{or } E_{0, N+1}^{+, -} \cap E_1^- \\ \text{or } E_{0, N+1}^{-, +} \cap E_N^+ \\ \text{or } E_{0, N+1}^{+, -} \cap E_{1, N}^{+, +} \\ \text{or } E_{0, N+1}^{+, -} \cap E_1^- \\ \text{or } E_{0, N-1}^{-, +} \cap E_N^- \\ \text{or } E_{0, N+1}^{+, +} \cap E_{1, N}^{+, -} \\ \text{or } E_{0, N+1}^{+, +} \cap E_{1, N}^{-, +} \\ \text{or } E_{0, N+1}^{+, +} \cap E_{1, N}^{-, -} \end{array} \right. \quad 3.1$$

Note that $\min k = 0$ and $\max k = N$. We now examine the limits ℓ_{\min} and ℓ_{\max} of ℓ as functions of k and E_{1N}^{ij} .

$$\ell_{\min} = \left\{ \begin{array}{l} 0 \dots \dots \dots \text{if} \\ 1 \dots \dots \dots \text{if} \\ 2 \dots \dots \dots \text{if} \end{array} \right\} \left\{ \begin{array}{l} \text{or} \\ \text{or} \\ \text{or} \\ \text{or} \end{array} \right\} \left\{ \begin{array}{l} k = 0 \\ k = N \\ E_{1,N}^{+,-} \cap (1 \leq k \leq N-1) \\ E_{1,N}^{-,+} \cap (1 \leq k \leq N-1) \\ E_{1,N}^{+,+} \cap (2 \leq k \leq N-1) \\ E_{1,N}^{+,-} \cap (N/2 \leq k \leq N-2) \end{array} \right. \quad 3.2$$

For ℓ_{\max} , we have to distinguish between the cases N_{even} and N_{odd} .

(a) N_{even} :

$$\ell_{\max} = \left\{ \begin{array}{l} 2k - 2 \dots \dots \dots \text{if} \\ 2(N-k) \dots \dots \dots \text{if} \\ 2k - 1 \dots \dots \dots \text{if} \\ 2(N-k) - 1 \dots \dots \dots \text{if} \\ 2k \dots \dots \dots \text{if} \\ 2(N-k) - 2 \dots \dots \dots \text{if} \\ N-2 \dots \dots \dots \text{if} \end{array} \right\} \left\{ \begin{array}{l} \text{or} \\ \text{or} \\ \text{or} \\ \text{or} \\ \text{or} \\ \text{or} \\ \text{or} \end{array} \right\} \left\{ \begin{array}{l} E_{1,N}^{+,+} \cap (2 \leq k \leq N/2) \\ E_{1,N}^{+,+} \cap (N/2 < k \leq N) \\ E_{1,N}^{+,-} \cap (1 \leq k \leq N/2) \\ E_{1,N}^{-,+} \cap (1 \leq k \leq N/2) \\ E_{1,N}^{+,-} \cap (N/2 < k \leq N-1) \\ E_{1,N}^{-,+} \cap (N/2 < k \leq N-1) \\ E_{1,N}^{-,-} \cap (0 \leq k < N/2) \\ E_{1,N}^{-,-} \cap (N/2 < k \leq N-2) \\ E_{1,N}^{-,-} \cap (k = N/2) \end{array} \right. \quad 3.3$$

(b) N_{odd} :

$$\ell_{\text{max}} \left\{ \begin{array}{ll} 2k - 2 & \text{if } E_{1,N}^{+,+} \cap 2 \leq k \leq (N-1)/2 \\ 2(N-k) & \text{if } E_{1,N}^{+,+} \cap (N-1)/2 < k \leq N \\ 2(k-1) & \text{if } \left\{ \begin{array}{l} E_{1,N}^{+,-} \cap 1 \leq k \leq (N-1)/2 \\ E_{1,N}^{-,+} \cap 1 \leq k \leq (N-1)/2 \end{array} \right. \\ 2(N-k) - 1 & \text{if } \left\{ \begin{array}{l} E_{1,N}^{+,-} \cap (N-1)/2 < k \leq N-1 \\ E_{1,N}^{-,+} \cap (N-1)/2 < k \leq N-1 \end{array} \right. \\ 2k & \text{if } E_{1,N}^{-,-} \cap 0 \leq k \leq (N-1)/2 \\ 2(N-k) - 2 & \text{if } E_{1,N}^{-,-} \cap (N-1)/2 < k \leq N-2 \end{array} \right. \quad 3.3b$$

We now proceed to evaluate $F = P(e_3/\bar{m}_{33})$. If we define $F(\cdot)$ to mean "F given (\cdot) ," we can apply the law of total probability to get

$$\begin{aligned}
 F &= \sum_{k=0}^N P_N(k) F(k) = \sum_{k=0}^N P_N(k) \sum_{i,j=+,-}^{E_{1,N}^{i,j}} P_N(E_{1,N}^{i,j}/k) F(E_{1,N}^{i,j};k) \\
 &= \sum_{k=0}^N P_N(k) \sum_{i,j=+,-}^{E_{1,N}^{i,j}} P_N(E_{1,N}^{i,j}/k) \cdot \sum_{\ell=\ell_{\min}}^{\ell_{\max}} P_N(\ell/E_{1,N}^{i,j};k) F(E_{1,N}^{i,j};k;\ell) \\
 &= \sum_{k=0}^N P_N(k) \sum_{i,j=+,-}^{E_{1,N}^{i,j}} P_N(E_{1,N}^{i,j}/k) \cdot \sum_{\ell=\ell_{m/n}}^{\ell_{\max}} P_N(\ell/E_{1,N}^{i,j};k) \\
 &\quad \cdot \sum_{p,q=+,-}^{E_{0,N+1}^{p,q}} P_N(E_{0,N+1}^{p,q}/E_{1,N}^{i,j};k;\ell) \cdot F(E_{0,N+1}^{p,q};E_{1,N}^{i,j};k;\ell) \quad (50)
 \end{aligned}$$

where $P_N(A/B)$ denotes the probability of the event A or that random variable A takes the value A, given the event B or that the random variable B assumes the value B, in the presence of N Channel 2 pulses in T_3 seconds.

The quantities involved in (50) can be evaluated as follows. Obviously, the random variable k follows a binomial distribution with parameters $p = q = 1/2$, so that

$$P_N(k) = \binom{N}{k} \cdot \left(\frac{1}{2}\right)^k \left(\frac{1}{2}\right)^{N-k} = \frac{1}{2^N} \cdot \binom{N}{k} \quad (51)$$

Because of the independence of the k_i and k_j pulses ($k_i \neq k_j$), we have that

$$P_N(E_{0,N+1}^{p,q} / E_{1,N}^{i,j}; k; \ell) = P_N(E_{0,N+1}^{p,q}) = \frac{1}{4}, \quad \forall(p,q) \quad (52)$$

The quantity $P_N(\ell / (E_{1,N}^{i,j}), k)$ has been evaluated in Appendix A and is given by (A-24), (A-25), and (A-34).

Observe that the limits ℓ_{\min} and ℓ_{\max} depend on both k and $(E_{1,N}^{i,j})$ through Tables 3.2 and 3.3. The quantities $P_N(E_{1,N}^{i,j}/k)$ have been evaluated in Appendix B and are given by (B-2) through (B-4) and (B-5) through (B-11).

Finally, we have to evaluate $F(E_{0,N+1}^{p,q}; E_{1,N}^{i,j}; k; \ell)$. Note that the triple $[(E_{0,N+1}^{p,q}); (E_{1,N}^{i,j}); \ell]$ virtually defines ℓ_{eff} through Table 3.1. With k and ℓ_{eff} as parameters, it is easy to check from (22d) that

$$\tilde{m}_{23}(N, A, k, \ell_{\text{eff}}) = \frac{1}{T_3} \left[(k - (N-k)) T_2 + A \cdot \ell_{\text{eff}} \cdot T_2 \right] \quad (53a)$$

or

$$\tilde{m}_{23}(N, A, k, \ell_{\text{eff}}) = \frac{2k - N + A \cdot \ell_{\text{eff}}}{N} \quad (53b)$$

since $T_2/T_c = 1/N$. So, simplifying the notation, we have that

$$F(E_{0,N+1}^{p,q}; E_{1,N}^{i,j}; k; \ell) \triangleq F((p,q); (i,j); k; \ell) = P\left(\cdot / \tilde{m}_{33}, \tilde{m}_{23} = \frac{2k - N + A \cdot \ell_{\text{eff}}}{N} \right) \quad (54)$$

where ℓ_{eff} is determined as a function of $(E_{0,N+1}^{p,q})$, $(E_{1,N}^{i,j})$, ℓ from Table 3.1

In principle, the problem has been solved. In the following, we shall first try to perform certain simplifications that result from the formulas and, at a second stage, we shall try to proceed to some approximations which make the final result look more tractable without sacrificing significant accuracy.

First, let us consider only the conditioning on k and write

$$F = P_N(0) \cdot F(0) + P_N(N) \cdot F(N) + P_N(1) \cdot F(1) + P_N(N-1) \cdot F(N-1) + \sum_{k=2}^{N-2} P_N(k) F_k$$

and, applying (50), (51), (52) and (54), Appendices A and B, and Tables 3.2 and 3.3, we find that

$$F = \frac{1}{2^{N+2}} \left\{ \sum_{p,q}^{E_{0,N+1}^{p,q}} \left[F((p,q);(-1,-1);0;0) + F((p,q);(1,1),N;0) \right. \right. \\ + F((p,q);(1,-1);1;1) + F((p,q);(-1,1);1;1) \\ + F((p,q);(1,-1);N-1;1) + F((p,q);(-1,1);N-1;1) \\ + (N-2) \cdot F((p,q);(-1,-1);1;2) + (N-2) \cdot F((p,q);(1,1);N-1;2) \\ + \sum_{k=2}^{N-2} \left[\sum_{\ell=2;\text{even}}^{\ell_{\max}(k, E_{1,N}^{+,+})} \binom{k-1}{\ell/2} \binom{N-1-k}{(\ell-2)/2} \cdot F((p,q);(1,1);k;\ell) \right. \\ + \sum_{\ell=1;\text{odd}}^{\ell_{\max}(k, E_{1,N}^{+,-})} \binom{k-1}{(\ell-1)/2} \binom{N-1-k}{(\ell-1)/2} \cdot F((p,q);(1,-1);k;\ell) \\ + \sum_{\ell=1;\text{odd}}^{\ell_{\max}(k, E_{1,N}^{-,+})} \binom{k-1}{(\ell-1)/2} \binom{N-1-k}{(\ell-1)/2} \cdot F((p,q);(-1,1);k;\ell) \\ \left. \left. + \sum_{\ell=2;\text{even}}^{\ell_{\max}(k, E_{1,N}^{-,-})} \binom{k-1}{(\ell-2)/2} \binom{N-1-k}{\ell/2} \cdot F((p,q);(-1,-1);k;\ell) \right] \right\} \quad (55)$$

Note that (55) is accurate, i.e., only some rearrangement of terms has taken place.

Equation (55) can be programmed as it is to yield an exact result, if Tables 3.0 (for ℓ_{eff}) and 3.3 (for ℓ_{max}) along with (53) are taken into account.

4.3 Approximations to F-Equation

(1) We first note that the coefficients of the first eight terms within the $p_{\Sigma, q}$ expression are either $1/(2^{N+2})$ or $(N-2)/(2^{N+2})$. For $N = 10$, these coefficients are of the order 10^{-3} and can therefore be neglected.

(2) We assume that the "edge effects" are negligible, i.e., the contribution of $E_{0, N+1}^{p, q}$ in F is not significant. Indeed, these factors will contribute some amount of asymmetry in $(0, T_3)$ during $\tau = (1/4 \cdot 3/4 + 2/4 \cdot 1/2 + 1/4 \cdot 0) \cdot 100\% \cong 50\%$ of the time, and the contributions will, on the average, be minimal. In other words, ℓ_{eff} is

$$\ell_{\text{eff}} = \begin{cases} \ell, & \text{for } \frac{9}{16} \cdot 100\% \text{ of the time} \\ \ell + 1, & \text{for } \frac{6}{16} \cdot 100\% \text{ of the time} \\ \ell + 2, & \text{for } \frac{1}{16} \cdot 100\% \text{ of the time} \end{cases}$$

We can then say that $(\ell_{\text{eff}})_{\text{av}} = (9 \cdot \ell + (\ell+1) \cdot 6 + (\ell+2) \cdot 1) / 16 = \ell + 1/2$, and we can use this value independently of Table 3.1. The combination of (1) and (2) greatly simplifies F , which now takes the form (also removing the factor $1/4$ since the conditioning on $E_{0, N+1}^{p/q}$ is removed):

$$F = \frac{1}{2^N} \sum_{k=2}^{N-2} \left[\sum_{\ell=2; \text{ even}}^{\ell_{\text{max}}(k, E_{1, N}^{+, +})} \binom{k-1}{\ell/2} \binom{N-1-k}{(\ell-2)/2} \cdot F_{k, \ell}^* + 2 \sum_{\ell=1; \text{ odd}}^{\ell_{\text{max}}(k, E_{1, N}^{+, -})} \binom{k-1}{(\ell-1)/2} \cdot \binom{N-1-k}{(\ell-1)/2} \cdot F_{k, \ell}^* + \sum_{\ell=2; \text{ even}}^{\ell_{\text{max}}(k, E_{1, N}^{-, -})} \binom{k-1}{(\ell-2)/2} \binom{N-1-k}{\ell/2} \cdot F_{k, \ell}^* \right] \quad (56)$$

where we have defined

$$F_{k,\ell}^* = P\left(e_3 / \bar{m}_{33}, \bar{m}_{23} = \frac{2k - N + A \cdot \left(\ell + \frac{1}{2}\right)}{N}\right) \quad (57)$$

and we have also exploited the symmetry between $E_{1,N}^{+,-}$ and $E_{1,N}^{-,+}$. (We always assume N even.) Furthermore, we can break the summation in (57) into three disjoint sums ($2 \leq k < N/2$), ($k = N/2$), ($N/2 < k \leq N-2$) to get from (57) and Table 3.3a:

$$F = \frac{1}{2^N} \left\{ \begin{aligned} & \sum_{k=2}^{N/2-1} \left[\sum_{\ell=2; \text{even}}^{2k-2} F_{k,\ell}^* \cdot \left[\binom{k-1}{\ell/2} \binom{N-1-k}{(\ell-2)/2} + \binom{k-1}{(\ell-2)/2} \binom{N-1-k}{\ell/2} \right] \right. \\ & \quad \left. + \binom{N-1-k}{k} \cdot F_{k,\ell=2k}^* + 2 \sum_{\ell=1; \text{odd}}^{2k-1} F_{k,\ell}^* \binom{k-1}{(\ell-1)/2} \binom{N-1-k}{(\ell-1)/2} \right] \\ & \quad + \sum_{k=N/2+1}^{N-2} \left[\sum_{\ell=2; \text{even}}^{2(N-k)-2} F_{k,\ell}^* \left[\binom{k-1}{\ell/2} \binom{N-1-k}{(\ell-2)/2} + \binom{k-1}{(\ell-2)/2} \binom{N-1-k}{\ell/2} \right] \right. \\ & \quad \left. + \binom{k-1}{N-k} \cdot F_{k,\ell=2(N-k)}^* + 2 \sum_{\ell=1; \text{odd}}^{2(N-k)-1} F_{k,\ell}^* \binom{k-1}{(\ell-1)/2} \binom{N-1-k}{(\ell-1)/2} \right] \\ & \quad + 2 \sum_{\ell=2; \text{even}}^{N-2} \binom{N/2-1}{\ell/2} \binom{N/2-1}{(\ell-2)/2} F_{k=N/2,\ell}^* + 2 \sum_{\ell=1; \text{odd}}^{N-1} \left[\binom{N/2-1}{(\ell-1)/2} \right]^2 F_{k=N/2,\ell}^* \end{aligned} \right\} \quad (58)$$

Observing certain symmetries, (58) is reduced to

$$\begin{aligned}
F = & \frac{1}{2^N} \left\{ \sum_{k=2}^{N/2-1} \sum_{\ell=2; \text{even}}^{2k-2} \left[F_{k,\ell}^* + F_{N-k,\ell}^* \right] \cdot \left[\binom{k-1}{\ell/2} \binom{N-1-k}{(\ell-2)/2} + \binom{k-1}{(\ell-2)/2} \binom{N-1-k}{\ell/2} \right] \right. \\
& + 2 \sum_{k=2}^{N/2-1} \sum_{\ell=1; \text{odd}}^{2k-1} \left[F_{k,\ell}^* + F_{N-k,\ell}^* \right] \binom{k-1}{(\ell-1)/2} \binom{N-1-k}{(\ell-1)/2} \\
& + \sum_{k=2}^{N/2-1} \left[F_{k,\ell=2k}^* + F_{N-k,\ell=2k}^* \right] \binom{N-1-k}{k} \\
& \left. + 2 \sum_{\ell=2; \text{even}}^{N-2} \left[\binom{N/2-1}{\ell/2} \binom{N/2-1}{(\ell-2)/2} \right] F_{k=N/2,\ell}^* + 2 \sum_{\ell=1; \text{odd}}^{N-1} \left[\binom{N/2-1}{(\ell-1)/2} \right]^2 F_{k=N/2,\ell}^* \right\} \quad (59)
\end{aligned}$$

Finally, if we use the identity

$$\binom{\alpha}{x} \binom{\beta}{x-1} + \binom{\alpha}{x-1} \binom{\beta}{x} = \binom{\alpha}{x} \binom{\beta}{x} \frac{x(\alpha + \beta - 2x + 2)}{(\alpha - x + 1)(\beta - x + 1)} \quad (60)$$

setting $a = k-1$, $b = N-k-1$ and $x = \ell/2$, we get

$$\begin{aligned}
F = & \frac{1}{2^{N-1}} \left\{ \sum_{k=2}^{N/2-1} \left[\sum_{\ell=2; \text{even}}^{2k-2} \left[F_{k,\ell}^* + F_{N-k,\ell}^* \right] \binom{k-1}{\ell/2} \binom{N-k-1}{\ell/2} \cdot \frac{\ell \cdot (N-\ell)}{4(k-\ell/2)(N-k)} \right. \right. \\
& + \sum_{\ell=1; \text{odd}}^{2k-1} \left[F_{k,\ell}^* + F_{N-k,\ell}^* \right] \binom{k-1}{(\ell-1)/2} \binom{N-1-k}{(\ell-1)/2} \left. \right] \\
& + \frac{\left[F_{k,\ell=2k}^* + F_{N-k,\ell=2k}^* \right]}{2} \binom{N-1-k}{k} + \sum_{\ell=2; \text{even}}^{N-2} \binom{N/2-1}{\ell/2} \binom{N/2-1}{(\ell-2)/2} \\
& \left. \cdot F_{k=N/2,\ell}^* + \sum_{\ell=1; \text{odd}}^{N-1} \left[\binom{N/2-1}{(\ell-1)/2} \right]^2 F_{k=N/2,\ell}^* \right\} \quad (61)
\end{aligned}$$

Equation (61) is the final expression for $F = P(e_3/\tilde{m}_{33})$, where $F_{k,l}^*$ is given by (57) and $P(e_3/\tilde{m}_{33}, \tilde{m}_{23})$ is given by the combination of (26a), (31), and (42). The unconditional $P_e(e_3)$ will be derived by averaging F over \tilde{m}_{33} according to Table 1, i.e.,

$$\begin{aligned}
 P(e_3) &= \frac{1}{2} P(e_3/\tilde{m}_{33} = 1) + \frac{1}{4} P(e_3/\tilde{m}_{33} = -1+A) \\
 &\quad + \frac{1}{8} P(e_3/\tilde{m}_{33} = -1) + \frac{1}{8} P(e_3/\tilde{m}_{33} = -1+2A)
 \end{aligned}
 \tag{62}$$

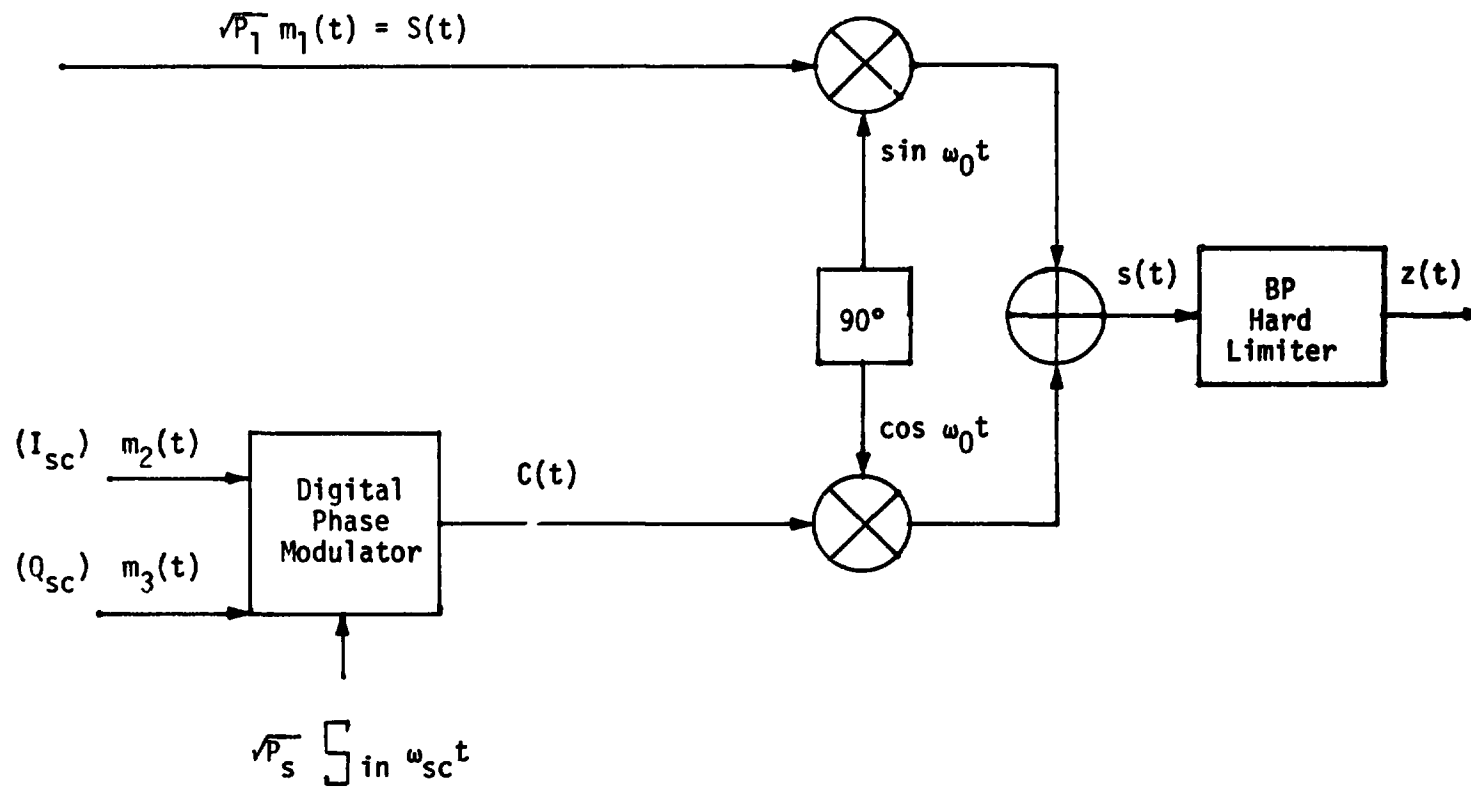


Figure 1. Three-Channel Interplex Modulator

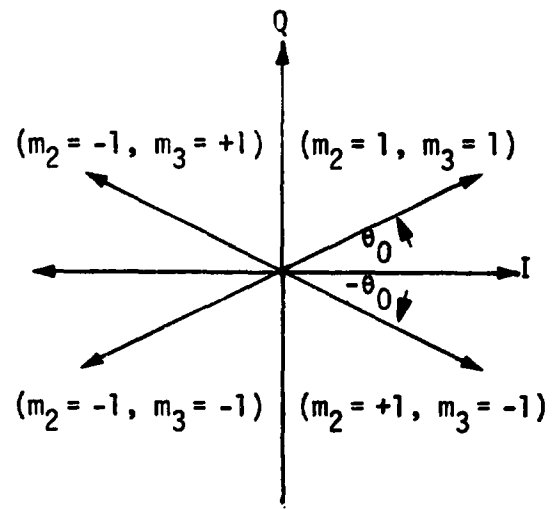


Figure 2. QPSK Signal Set

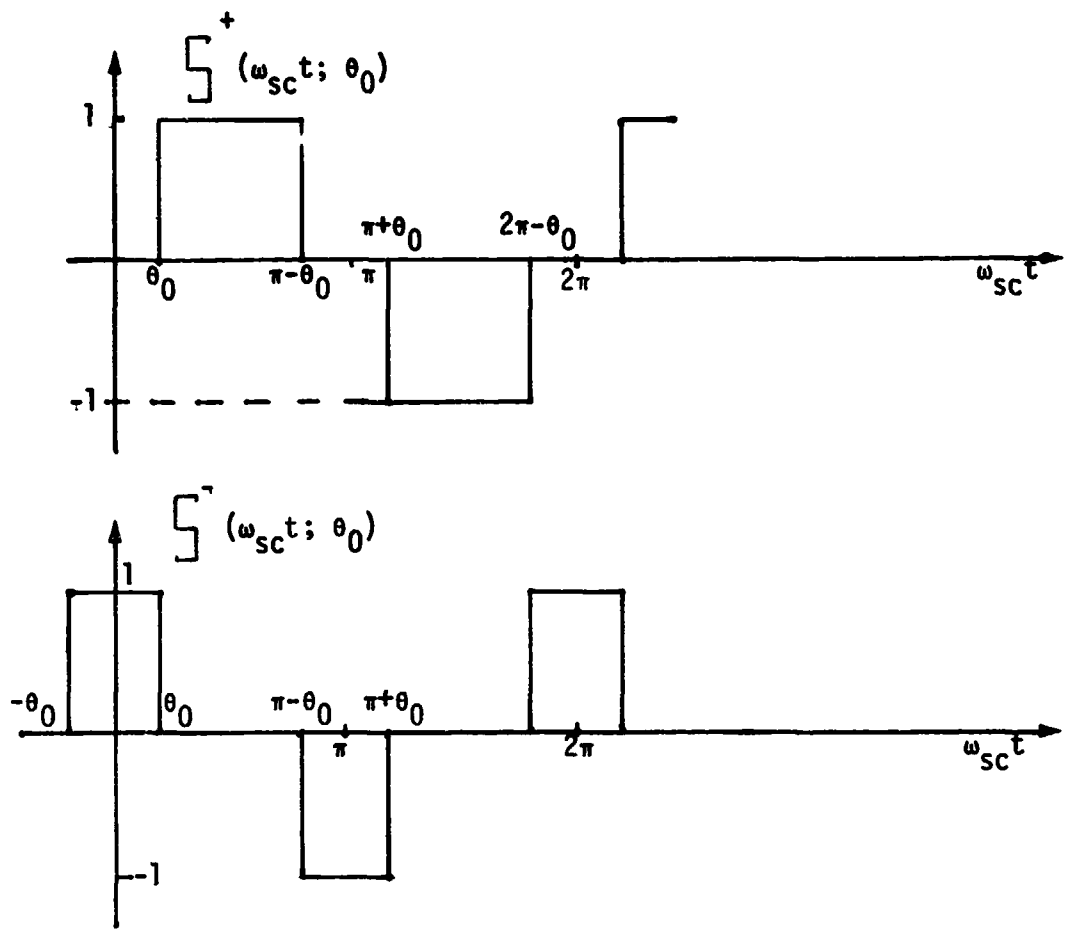


Figure 3. Waveforms $S^+(\omega_{sc}t; \theta_0)$ and $S^-(\omega_{sc}t; \theta_0)$

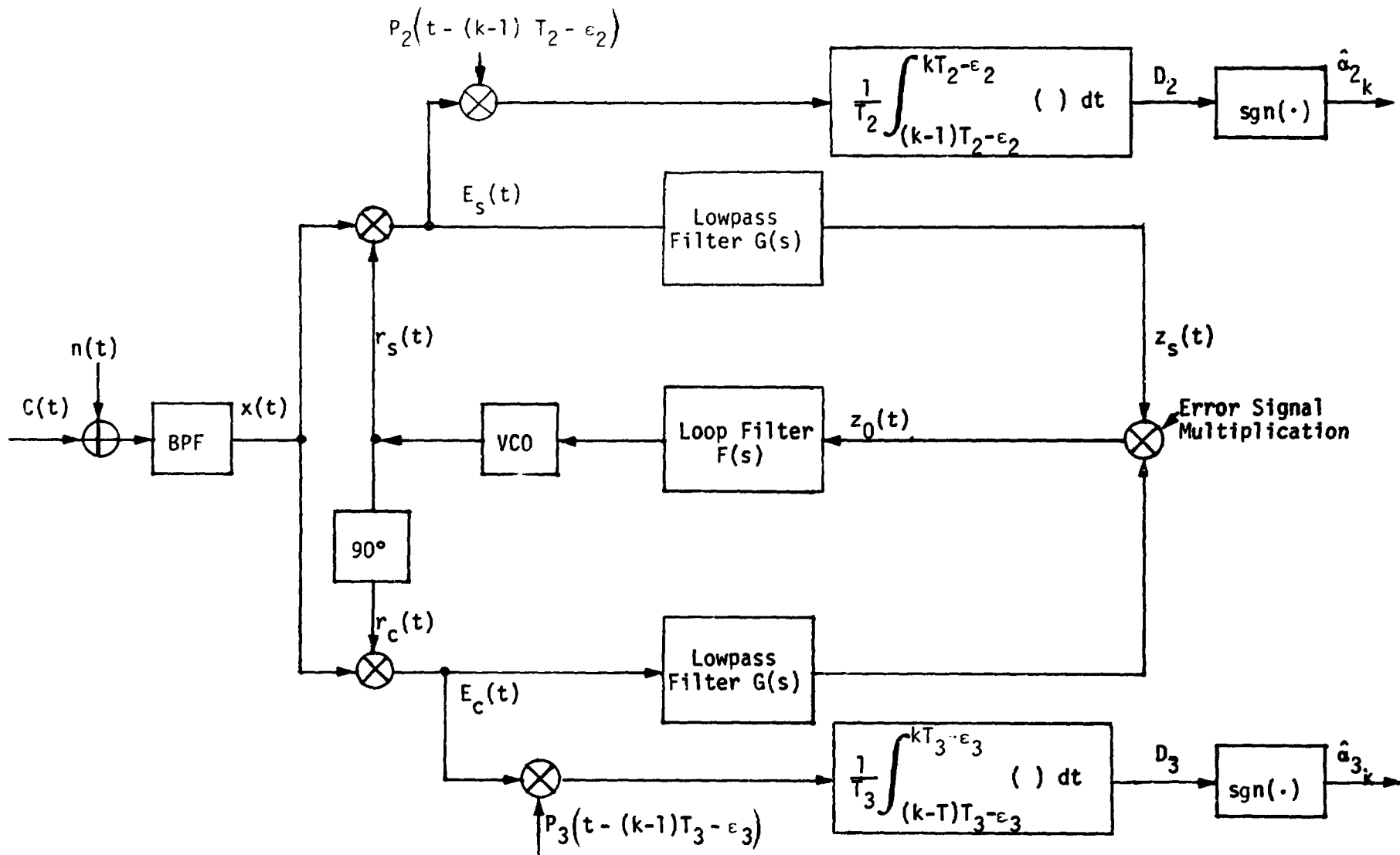
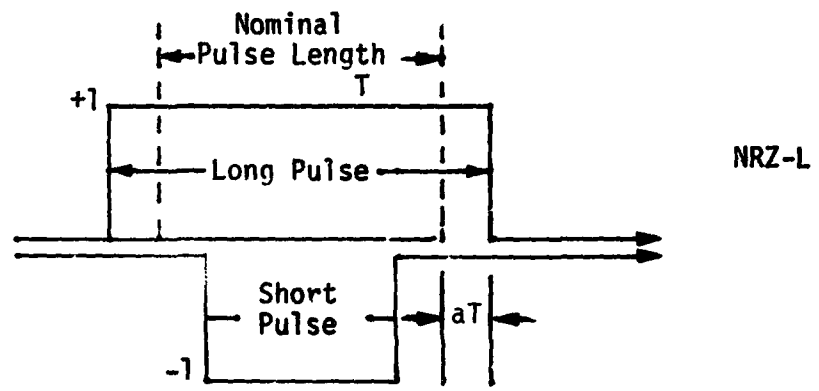
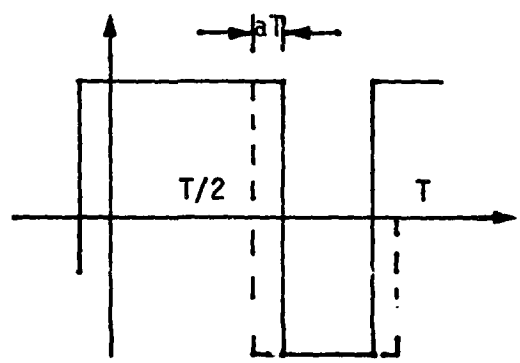


Figure 4. Subcarrier Demodulator/Detector



NRZ-L



Biphase-L

Figure 5. Data Asymmetry Model

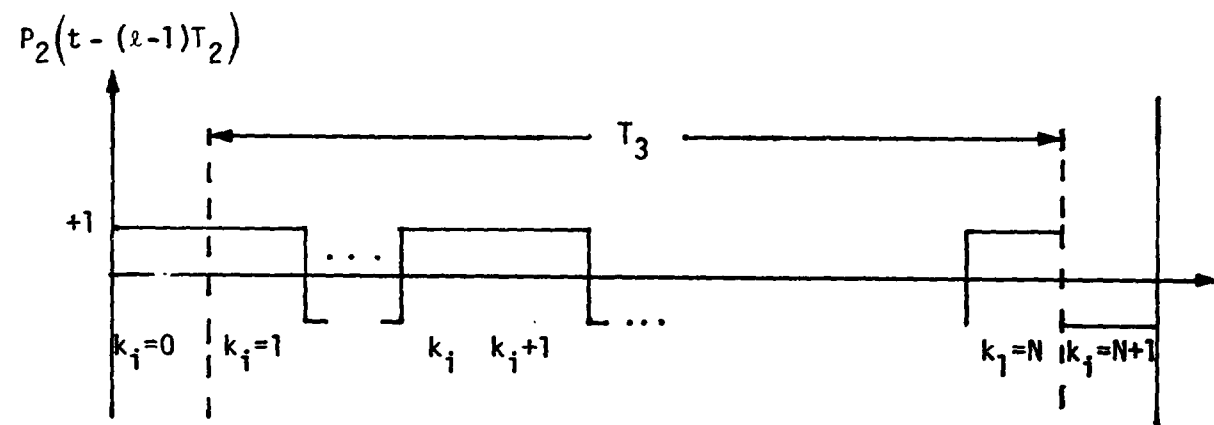


Figure 6. A Possible Sequence of N Channel-2 Pulses Within One Channel-3 Pulse

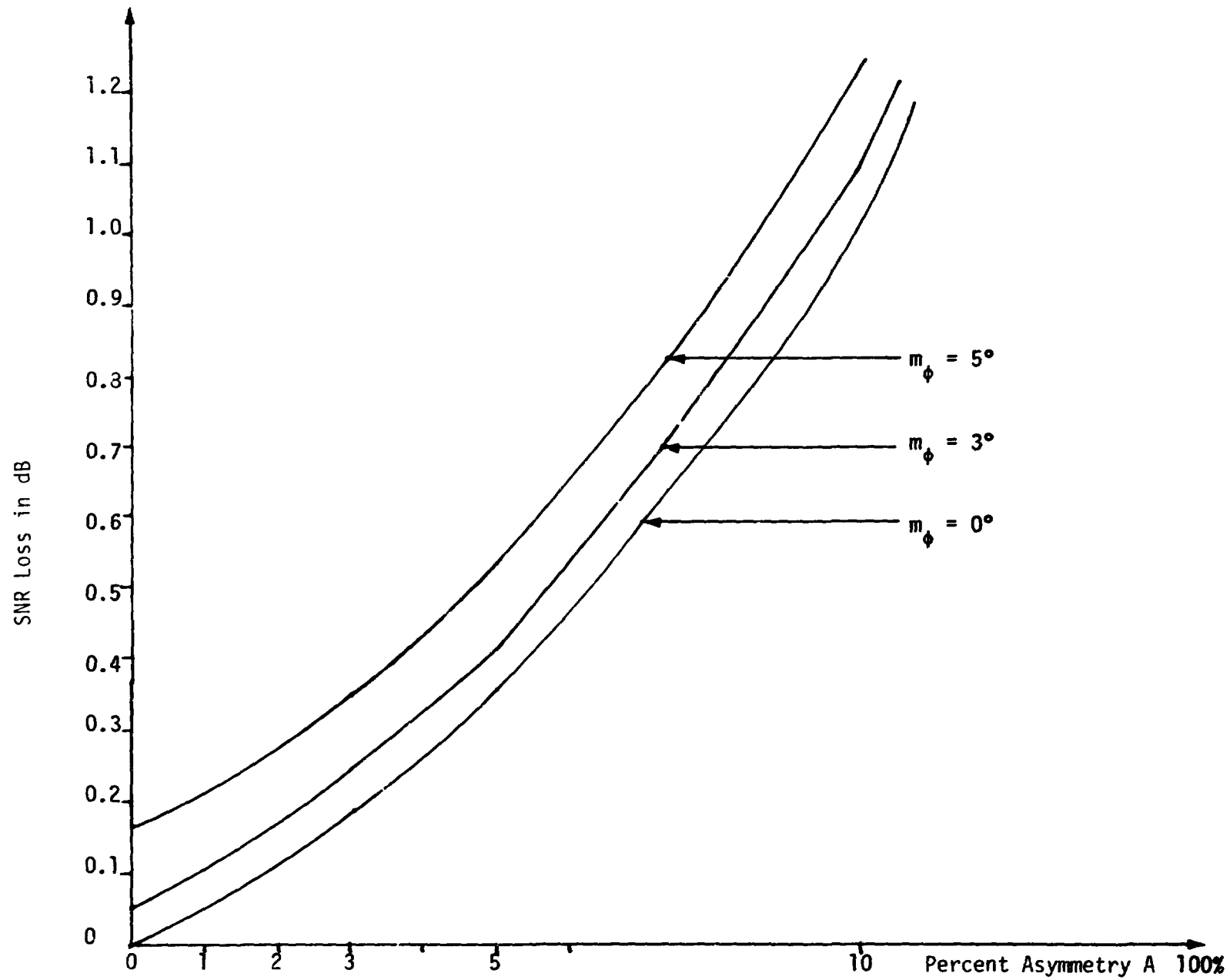


Figure 7a. High Data Rate Channel, $\text{var } \phi = 0$

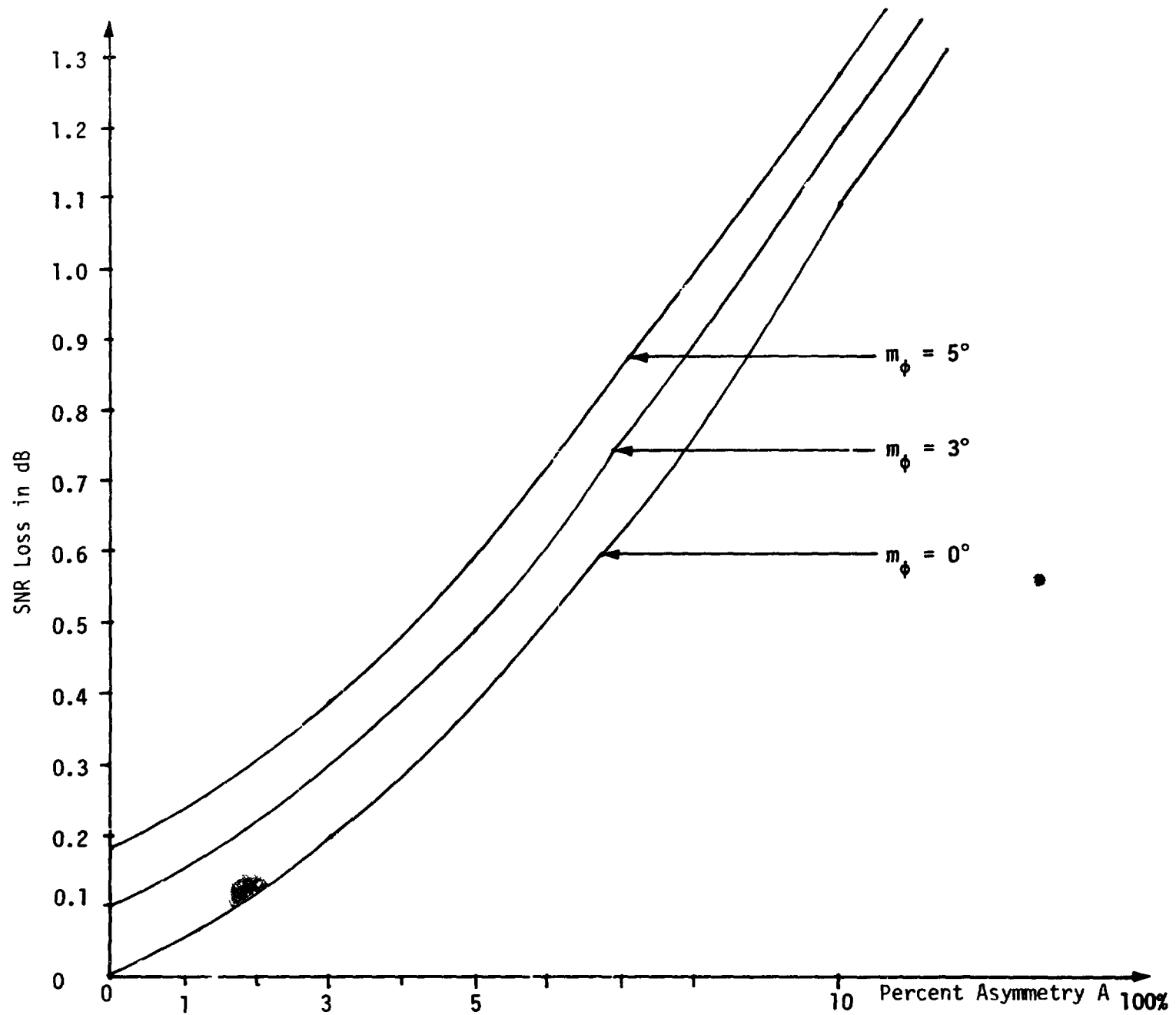


Figure 7b. High Data Rate Channel, $\text{var } \phi = 4$

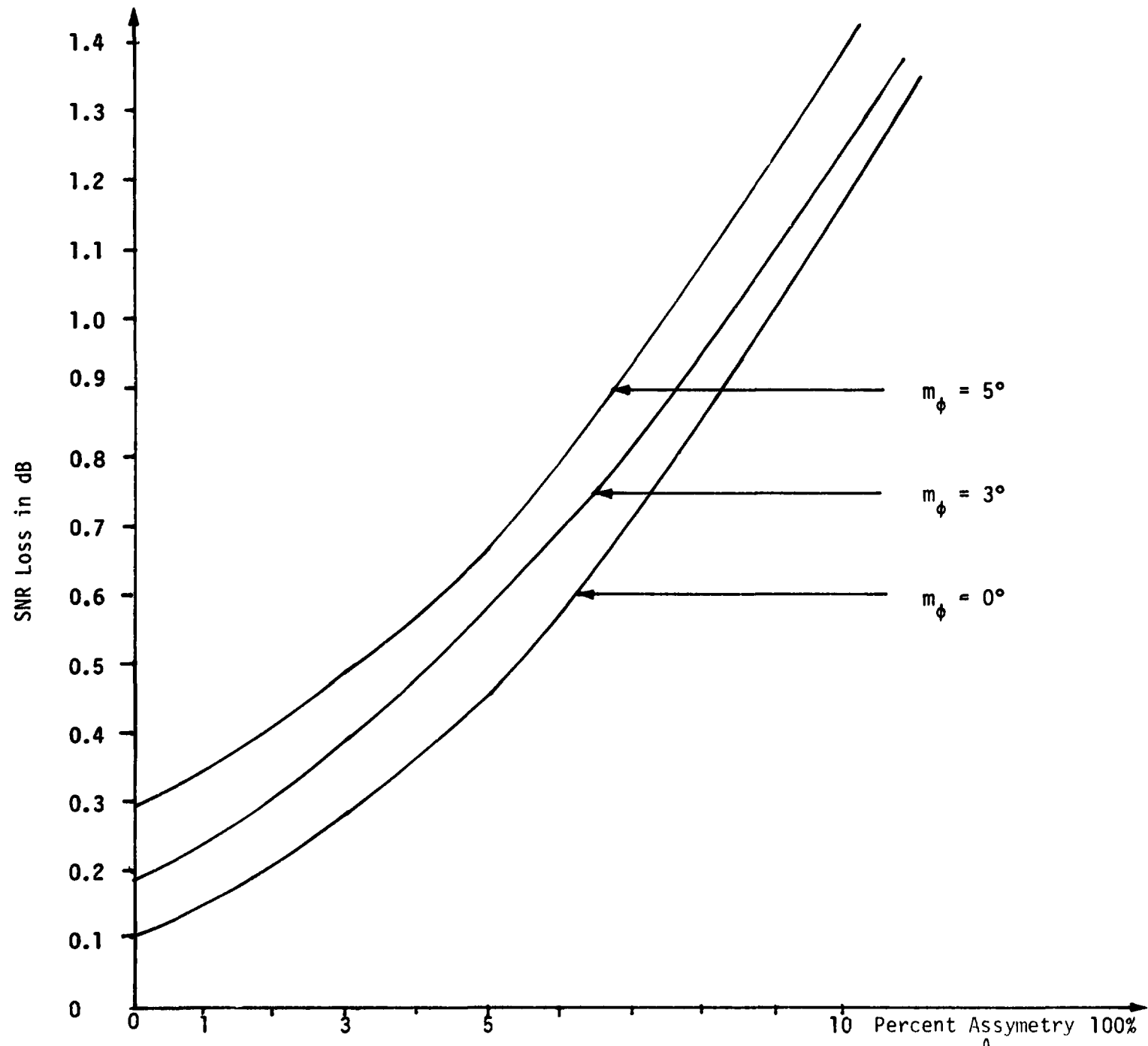


Figure 7c. High Data Rate Channel, $\text{var } \hat{\tau} = 9$

Figure 8a. Low Data Rate Channel,
 $\text{var } \phi = 0$

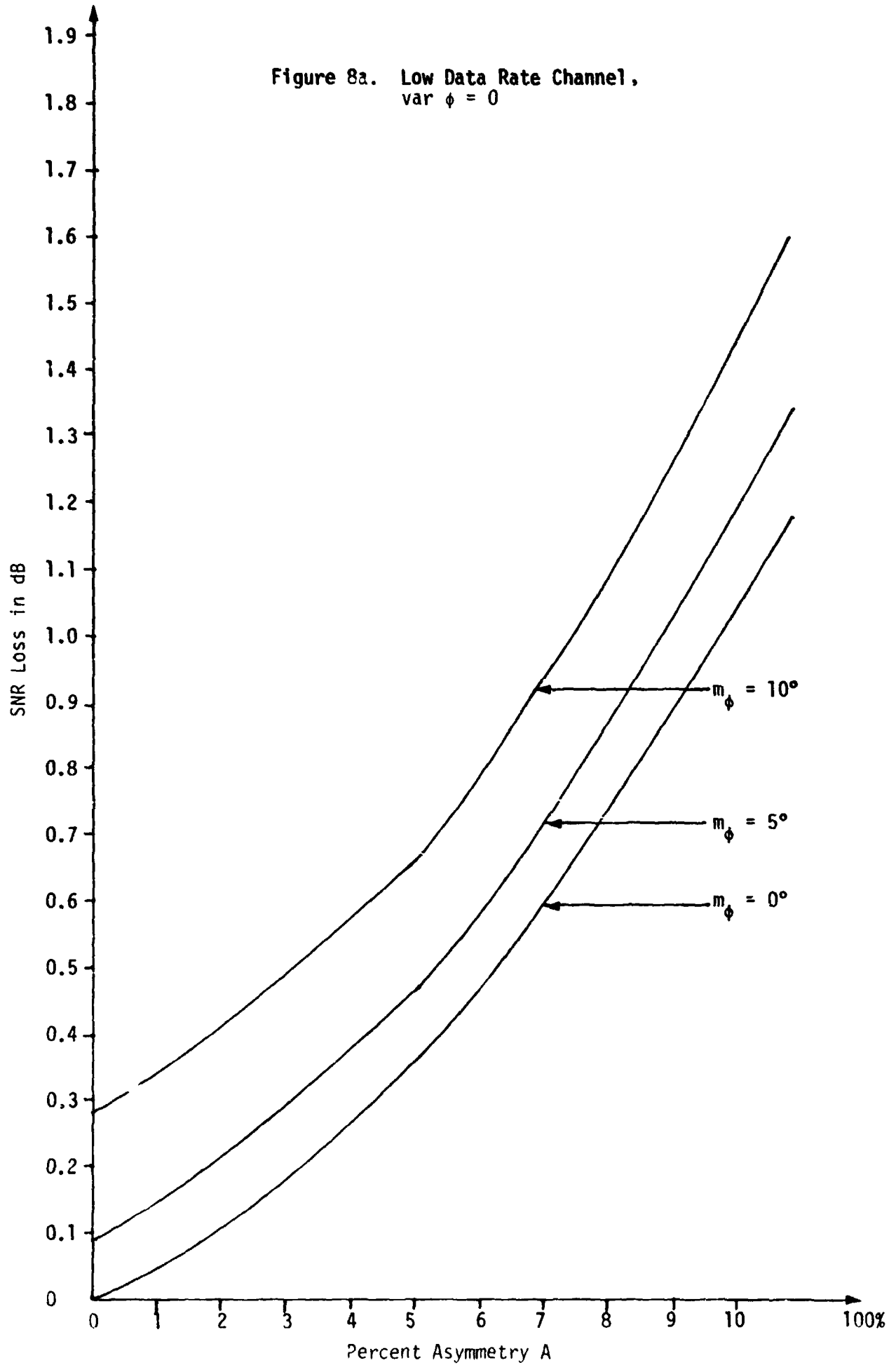


Figure 8b. Low Data Rate Channel,
 $\text{var } \phi = 4$

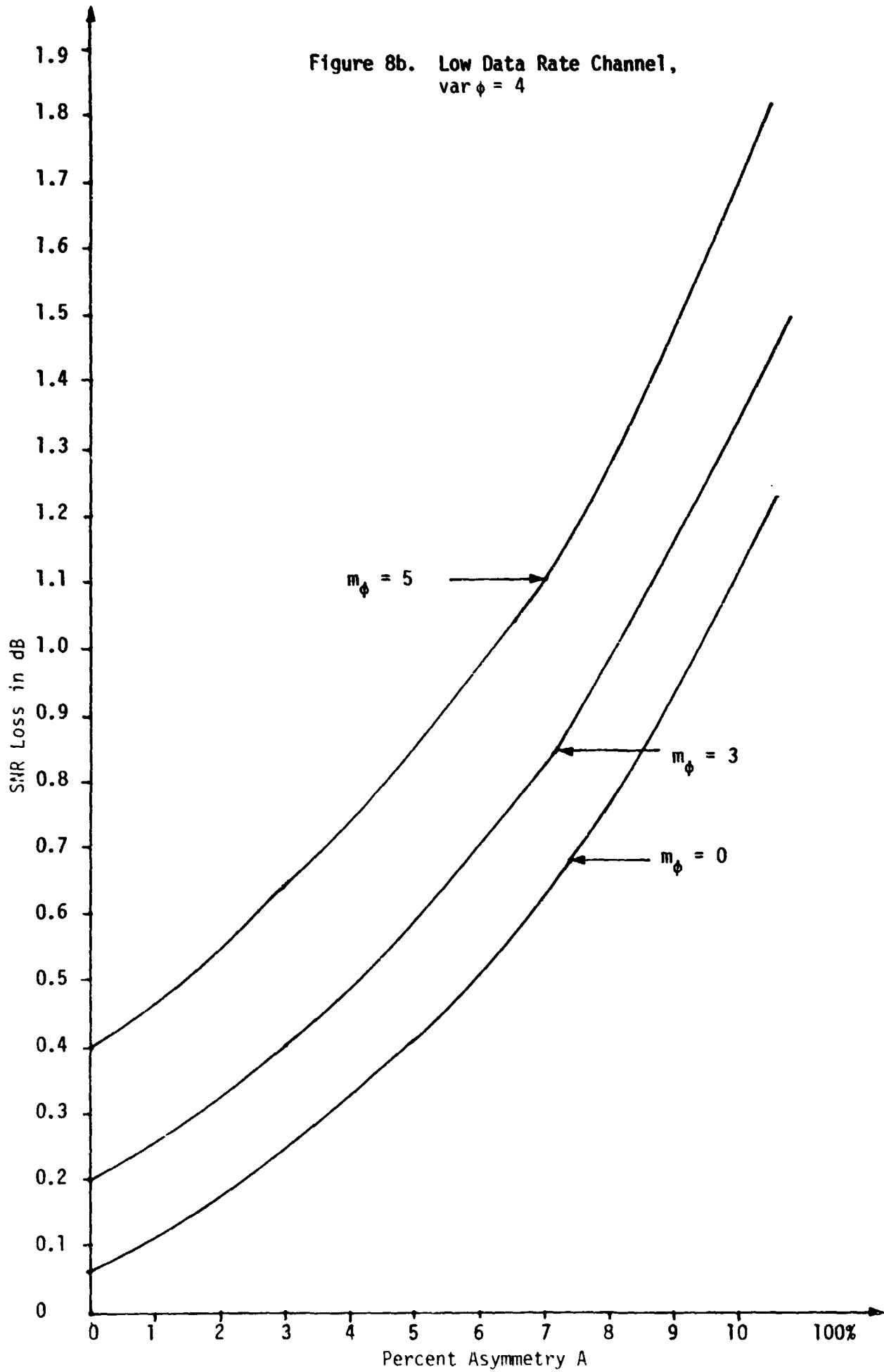
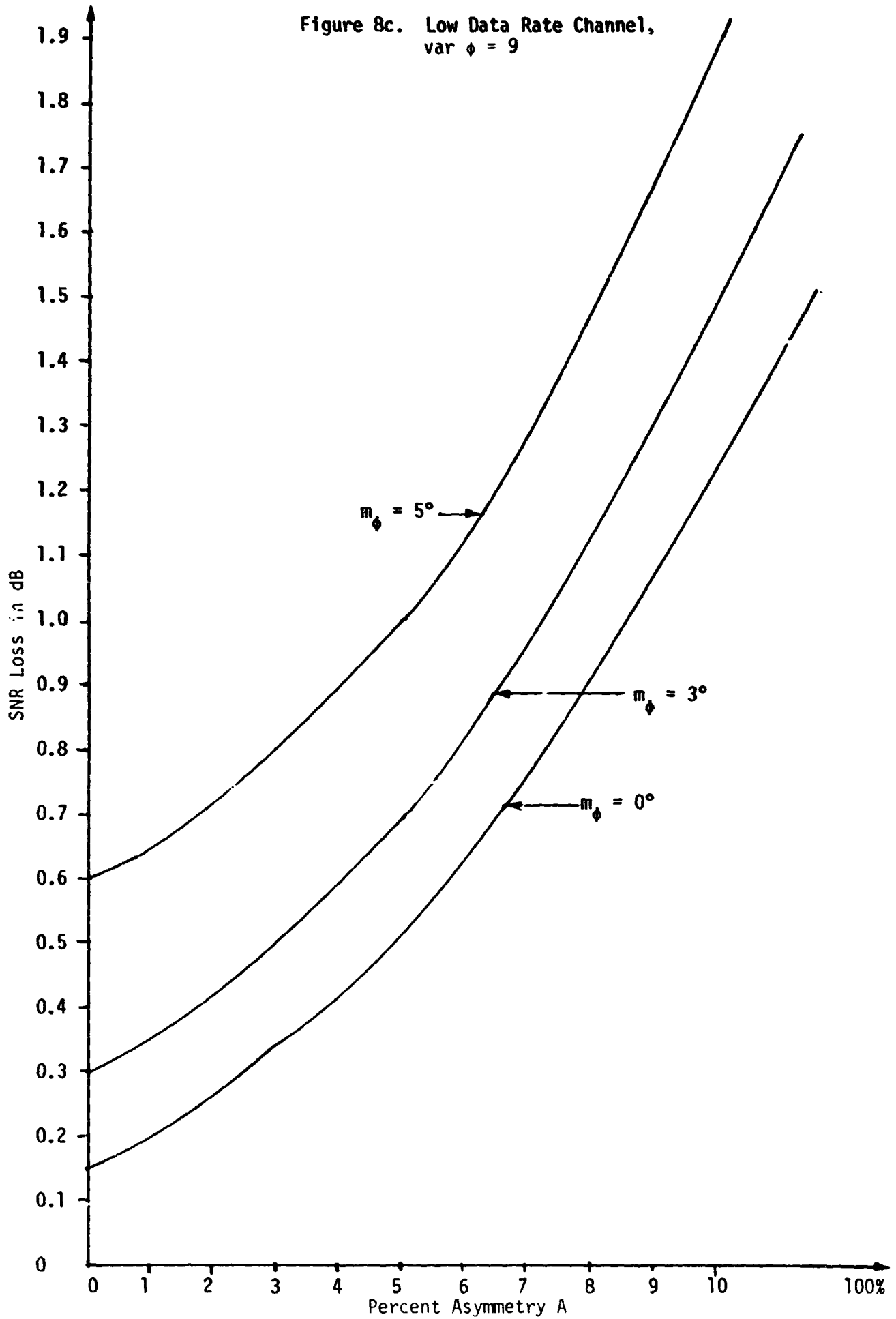


Figure 8c. Low Data Rate Channel,
var $\phi = 9$



GLOSSARY OF SYMBOLS

$\phi(t)$ = Tracking phase error process

m_ϕ = Mean of ϕ

G_ϕ^2 = Variance of ϕ

N = Data rates ratio

$P(e_i / (\tilde{m}_{ij}, \tilde{m}_{ij}));$
 $i, j = 2, 3$ = Error probability of channel i conditioned on $\tilde{m}_{ij}, \tilde{m}_{ij}$

$E_Y^i \{ i = 1, -1 \}$
 $\{ \gamma \in [0, N+1] \}$ = The event that the γ th pulse equals i

$E_{Y, \delta}^{i, j} \{ i, j = 1, -1 \}$
 $\{ \gamma, \delta \in [0, n+1] \}$ = The joint event that the γ th and δ th pulses equal i and j , respectively. Note: Whenever there is a possibility of misunderstanding, it is replaced by (i, j) .

k = Number of positive pulses in $[1, N]$

ℓ = Number of transitions from $+1$ to -1 or vice versa, within the interval $[1, N]$, with the boundary transition excluded.

ℓ_{eft} = Number of effective transitions in $[1, N]$, with the boundary transitions included, whenever they occur.

$\ell_{\text{min}}, \ell_{\text{max}}$ = Limits of ℓ

$F(x) \triangleq P(e_3 / \tilde{m}_{33}, x)$ = Probability of error for Channel 3 conditioned on \tilde{m}_{33} and other events k .

τ = Number of pairs of adjacent positive pulses in $[1, N]$, given in $E_{1, N}^{i, j}$ and k .

$\binom{m}{n}$ = Number of combinations of m objects taken every n

REFERENCES

1. Cager, R. H., Jr., LaFlame, D. T., and Parode, L. C., "Orbiter Ku-Band Integrated Radar and Communications Subsystem," IEEE Transactions on Communications, November 1978, pp 1604-1619.
2. Simon, M. K., "Power Allocation and Costas Loop Subcarrier Tracking Performance Associated with a Digital Phase Shift Implementation of the Three-Channel Orbiter Ku-Band Modulator," Axiomatix Report No. R7709-4, September 29, 1977.
3. Weber, C. L., "Candidate Receivers for Unbalanced QFSK," 1976 ITC Proceedings, Vol. XII, pp 455-464.
4. Braun, W. R., and Lindsey, W. C., "Carrier Synchronization Techniques for Unbalanced QPSK Signals" (parts I and II), IEEE Transactions on Communications, September 1978, pp 1325-1341.
5. Simon, M. K., "Error Probability Performance of Unbalanced QPSK Receivers," IEEE Transactions on Communications, September 1978, pp 1390-1397.
6. Osborne, H. C., "Effect of Noisy Phase Reference on Coherent Detection of Unbalanced QPSK Signals," NTC '78 Proceedings, December 1978, pp 2.2.1-2.2.6.
7. Divsalar, D., and Yuen, J. H., "Performance of Unbalanced QPSK in the Presence of Noisy Reference and Cross Talk," NTC '79 Proceedings, November 1979.
8. Simon, M. K., Tu, K, and Batson, B. H., "Effects of Data Asymmetry on Shuttle Ku-Band Communications Link Performance," IEEE Transactions on Communications, November 1978, pp 1639-1651.
9. Orr, R. S., "The Impact of Data Asymmetry on Bit Error Performance," Technical Report, Stanford Telecommunications, Inc., McLean, Virginia, July 21, 1977.
10. Simon, M. K., and Alem, W. K., "Tracking Performance of Unbalanced QPSK Demodulators: Part I - Biphase Costas Loop with Passive Arm Filters," IEEE Transactions on Communications, August 1978, pp 1147-1156.
11. Simon, M. K., "Tracking Performance of Unbalanced QPSK Modulators: Part II - Biphase Costas Loop with Active Arm Filters," IEEE Transactions on Communications, August 1978, pp 1157-1166.
12. Liu, C. L., Introduction To Combinatorial Mathematics, New York, McGraw-Hill, 1968.

ADDENDUM A

EVALUATION OF THE CONDITIONAL PROBABILITY DISTRIBUTION
OF THE RANDOM VARIABLE ℓ GIVEN THE EVENT $E_{1,N}^{i,j}$ AND k

In this appendix, we evaluate the probability distribution of the random variable ℓ , conditioned on k and $(E_{1,N}^{i,j})$. Let us first define $P_N(\ell/(L_{1,N}^{i,j}), k) \triangleq P(\ell/(i,j), k)$:

$$(1) \text{ If } k=0, \text{ then } P(0/(-1,-1), 0) = 1 \quad (\text{A-1})$$

and every other cond. prob. is zero.

$$(2) \text{ If } k=N, \text{ then } P(0/(1,1), N) = 1 \quad (\text{A-2})$$

and every other cond. prob. is zero.

$$(3) \text{ If } k=1, \text{ then } P(1/(1,-1), 1) = P(1/(-1,1), 1) = 1 \quad (\text{A-3})$$

$$\text{and } P(2/(-1,-1), 1) = 1, P(\ell/(1,1), 1) = 0 \quad (\text{A-4})$$

$$(4) \text{ If } k=N-1, \text{ then } P(1/(1,-1), N-1) = P(1/(-1,1), N-1) = 1 \quad (\text{A-5})$$

$$\text{and } P(2/(1,1), N-1) = 1, P(\ell/(-1,-1), N-1) = 0 \quad (\text{A-6})$$

Let us assume $2 \leq k \leq N-2$, and let us define the random variable τ as the number of pairs of adjacent positive pulses (k_p, k_{p+1}) , given $(E_{1,N}^{i,j})$ and k . Then it is easy to verify that

$$\ell = \begin{cases} 2(k-\tau) - 2 \\ 2(k-\tau) - 1 \\ 2(k-\tau) - 1 \\ 2(k-\tau) \end{cases} \iff \tau = \begin{cases} k - \frac{\ell+2}{2} & \text{if } E_{1,N}^{+,+} \\ k - \frac{\ell+1}{2} & \text{if } E_{1,N}^{+,-} \\ k - \frac{\ell+1}{2} & \text{if } E_{1,N}^{-,+} \\ k - \frac{\ell}{2} & \text{if } E_{1,N}^{-,-} \end{cases} \quad (\text{A-7})$$

Let us now consider the set S of all possible pairs of adjacent (positive) pulses. Then,

$$S = \left\{ (k_1, k_2), (k_2, k_3), \dots, (k_{k-1}, k_k) / E_{1,N}^{i,j} \right\}$$

of cardinality $k-1$. The way we select τ of these pairs does depend on $E_{1,N}^{i,j}$; hence, we distinguish the following cases.

A.1 ($E_{1,N}^{-,-}$)

In this case, $k_1 \neq 1$, $k_k \neq N$. The k pulses lie in an interval of $N' = N-2$ slots. Then, τ of the pairs in S can be selected in $\binom{k-1}{\tau}$ ways, and the possible selections are all equiprobable. Hence, we can write

$$P(\tau/(-1,-1),k) = \binom{k-1}{\tau} P(E_S/(-1,-1),k) \quad (\text{A-8})$$

where the event E_S in (A-8) stands for any particular selection of the τ pairs. We shall select the following particular pattern:

$$E_S = \{(k_1, k_2), (k_2, k_3) \dots (k_\tau, k_{\tau+1})\} / E_{1,N}^{-,-}; k \quad (\text{A-9})$$

i.e., E_S stands for the collection of all patterns having the first $(\tau+1)$ positive pulses adjacent, and the rest $P = k - (\tau+1)$ nonadjacent. The above hold for $\tau > 0$. If $\tau = 0$, then

$$P(\tau=0/(-1,-1),k) = P(\text{no adjacent pulses}/(-1,-1),k) \quad (\text{A-10})$$

and will be derived later in this appendix.

We shall try now to find the probability of the event E_S in (A-9). We write

$$P\{E_S/(-1,-1),k\} = \Xi(\tau, N', k) \cdot P\{\text{any individual pattern}/N', k\} \quad (\text{A-11})$$

where $\Xi(\tau, N', k)$ is the number of patterns within the set E_S , and

$$P\{\text{any individual pattern}/N', k\} = \frac{1}{\binom{N'}{k}} \quad (\text{A-12})$$

Next, we evaluate $\Xi(\tau, N', k)$. We note that

$$\Xi(\tau, N', k) = \Xi(\tau, N', k; k_1) + \Xi(\tau, N', k; k_2) + \dots + \Xi(\tau, N', k; k_m) \quad (\text{A-13})$$

where $\Xi(\tau, N', k; k_i)$, ($i = 1, \dots, k_m$) stands for the number of patterns belonging to E_S whose first positive pulse occurs at the position k_i . The upper limit k_m is easily shown to obey the equation

$$\text{or} \quad 2[k - (\tau+1)] + (\tau+1) + k_m = N$$

$$k_m = N' - 2k + \tau + 3 \quad (\text{A-14})$$

We can then combine (A-13) and (A-14) into

$$\Xi(\tau, N', k) = \sum_{k_i=2}^{N'-2k+\tau+3} \Xi(\tau, N', k; k_i) \quad (\text{A-15})$$

In the following, we proceed to evaluate $\Xi(\tau, N', k; k_i)$. From the setup of the problem, it follows that this number equals the number ε_p^π of all the possible patterns containing $P = k - (\tau+1)$ positive nonadjacent pulses within an interval of $\pi_i = N' - [k_i - 2 + (\tau+1)] = N' - (k_i + \tau) + 1$ slots. From (A-14), it follows that π_i takes on the values $\pi_i \in [(2k - 2\tau - 2), (N' - \tau - 1)]$. An additional constraint should be added here, namely, that the first slot within the π_i places should not contain a positive pulse (since, otherwise, we would have $\tau+2$ pairs of adjacent positive pulses, contradicting the problem formulation). An additional constraint is that $\tau \geq \tau_{\min} = 2k - 1 - N'$, in the case $k > N/2$.

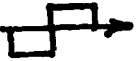
One of the following two ways could be used for solving this combinatorial problem. The first is to formulate a difference equation which the variable ε_p^π should satisfy. Such an equation arises by splitting all these patterns enumerated by ε_p^π into the ones containing a positive pulse at the second slot within the π -interval,


plus the ones which do not. Hence, we can write

$$\left. \begin{aligned} \xi_p^\pi &= \xi_p^{\pi-1} + \xi_{p-1}^{\pi-2} \quad ; \quad \pi \geq 3 \\ \text{with initial conditions} \\ \xi_0^1 &= 1, \quad \xi_{p \neq 0}^1 = 0, \quad \xi_0^2 = 0 \\ \xi_1^2 &= 1, \quad \xi_{p \neq 0,1}^2 = 0, \quad \xi_\pi^\pi = 0 \end{aligned} \right\} \quad (\text{A-16})$$

and try to solve (A-16).

The other approach is to consider that we have a collection of objects of two kinds:

First kind:  i.e., a negative pulse followed by a positive pulse. This assumes that no two positive pulses will be adjacent. There are p of these objects.

Second kind:  i.e., a negative pulse which does not accompany a positive pulse. There are $\pi - 2p$ of these objects.

Hence, the number of all distinguishable permutations containing these two objects is

$$\xi_p^\pi = \binom{(\pi - 2p) + p}{p} = \binom{\pi - p}{p} \quad (\text{A-17})$$

If we substitute (A-17) into (A-16) and use the identity $\binom{N}{n} = \binom{N-1}{n} + \binom{N-1}{n-1}$ we indeed verify that (A-17) is the solution of (A-16).

Combining (A-8), (A-11), (A-12), (A-15), and (A-17), we conclude that

$$P(\tau / (-1, -1), k) = \frac{\binom{k-1}{\tau}}{\binom{N-2}{k}} \sum_{\pi_i = 2(k-\tau-1)}^{N-\tau-3} \binom{\pi_i - k + \tau + 1}{k - \tau - 1}$$

or, changing variables ($\phi = \pi_i - k + \tau + 1$), we have that

$$P(\tau/(-1,-1),k) = \frac{\binom{k-1}{\tau}}{\binom{N-2}{k}} \sum_{\phi=k-1-\tau}^{N-2-k} \binom{\phi}{k-1-\tau} \quad (\text{A-18})$$

The constraints for (A-18) are as in Table 3.3a. Also, we agree that $\binom{0}{0} = 1$.

Finally, the desired quantity $P(\ell/(-1,-1),k)$ is obtained from (A-18) and (A-7):

$$P(\ell/(-1,-1),k) = \frac{\binom{k-1}{k-\ell/2}}{\binom{N-2}{k}} \sum_{\phi=\ell/2-1}^{N-2-k} \binom{\phi}{\ell/2-1}; \ell=\text{even} \geq 2 \quad (\text{A-19})$$

with constraints

$$\left(\begin{array}{l} 2 \leq k < N/2 \\ 2 \leq \ell < 2k \end{array} \right) \text{ or } \left(\begin{array}{l} N/2 < k \leq N-2 \\ 2 \leq \ell \leq 2(N-k)-2 \end{array} \right) \text{ or } \left(\begin{array}{l} k = N/2 \\ 2 \leq \ell \leq N-2 \end{array} \right)$$

For example, $P_N(\ell=2/(-1,-1),N-2) = 1/1 \cdot \binom{0}{0} = 1$, which is correct.

We now examine $P(\tau=0/(-1,-1),k)$. Obviously, $P(\tau=0/(-1,-1),k) = 0$ if $k \geq N/2$. Hence, we examine only the $P(\tau=0/(-1,-1),k)$ with $k < N/2$. Observe that, if $k = N/2$, $\tau \geq 1$, and (A-19) is applicable as it is.

After some thought, we can see that

$$P(\tau=0/(-1,-1),k; 2 \leq k < N/2) = \frac{\xi_k^{N'+1}}{\binom{N-2}{k}}; \text{ where } \xi_k^{N'+1} = \binom{N'+1-k}{k} \quad (\text{A-20})$$

However, we can show that (A-20) is virtually incorporated in (A-19). Indeed, for $\ell = 2k$ (which is equivalent to $\tau = 0$), (A-19) gives

$$P(\ell=2k/(-1,-1); k; 2 \leq k \leq N-2) = \frac{\sum_{\phi=k-1}^{N-2-k} \binom{\phi}{k-1}}{\binom{N-2}{k}} \quad (\text{A-21})$$

and to verify the claim, we have to show [combining (A-20), (A-21)] that

$$\binom{N'+1-k}{k} = \binom{N-1-k}{k} = \sum_{\phi=k-1}^{N-k-2} \binom{\phi}{k-1} \quad (\text{A-22})$$

To prove this, we use the identity ([12], problem 2-2):

$$\sum_{\xi=0}^n \binom{r+\xi}{r} = \binom{r+1+n}{r+1} \quad (\text{A-23})$$

Putting $r=k-1$, $r+n=N-k-2$ in (A-23), we verify (A-22) directly.

The final result for the $(E_{1,N}^{-,-})$ case is summarized in the following (after minor manipulations and using (A-22) again):

$$\left\{ \begin{array}{l} P(0/(-1,-1);0) = 1 \\ P(\ell=2/(-1,-1);1) = 1 \\ P(\ell/(-1,-1);k) = \frac{\binom{k-1}{\ell/2-1} \binom{N-k-1}{\ell/2}}{\binom{N-2}{k}} \end{array} \right. \quad (\text{A-24})$$

where

$\ell = \text{even} \geq 2$; $2 \leq k \leq N-2$; ℓ obeys restrictions of Table 3.3.a.
Finally, $P(\ell/(-1,-1);k) = 0$, elsewhere.

A.2 $(E_{1,N}^{+,+})$

This case is exactly symmetrical to A.1, if one substitutes the k positive pulses with $N-k$ negative ones. Hence, the result can be directly derived from (A-24):

$$\left\{ \begin{array}{l} P(0/(1,1);N) = 1, \quad P(\ell=2/(1,1);N-1) = 1 \\ P(\ell/(1,1);k) = \frac{\binom{k-1}{\ell/2} \binom{N-k-1}{\ell/2-1}}{\binom{N-2}{k-2}} \end{array} \right. \quad (\text{A-25})$$

where $\ell = \text{even} \geq 2$; $2 \leq k \leq N-2$; ℓ obeys restrictions of Table 3.3a.
Finally, $P(\ell/(1,1);k) = 0$, elsewhere

Note that, in order to derive (A-25) from (A-24), we have used the identities

$$\binom{N-2}{N-k} = \binom{N-2}{k-2}; \quad \binom{N-k-1}{N-k-\frac{k}{2}} = \binom{N-k-1}{\frac{k}{2}-1}$$

$$A.3 \quad (E_{1,N}^+, \bar{-}); \quad (E_{1,N}^-, +)$$

These two cases are identical, so we treat the first of them. To find $P(\ell/(1,-1), k)$, we use total probability to write

$$\begin{aligned} P(\ell/(1,-1), k) &= P(\ell/(1,-1); k; k_2=2) \cdot P(k_2=2/(1,-1), k) \\ &\quad + P(\ell/(1,-1); k; k_2 > 2) \cdot P(k_2 > 2/(1,-1), k) \end{aligned} \quad (A-26)$$

We first find $P_N(k_2=2/(1,-1), k)$ and $P_N(k_2 > 2/(1,-1), k)$ as follows

$$\begin{aligned} P(k_2=2/(1,-1), k) &= \frac{P[k_2=2; (k-1) \text{ positive pulses in } [2, N-1]/(1,-1)]}{P[(k-1) \text{ positive pulses in } [2, N-1]/(1,-1)]} \\ &= \frac{\frac{1}{2} \cdot \binom{N-3}{k-2} \cdot \frac{1}{2^{N-3}}}{\frac{1}{2^{N-2}} \cdot \binom{N-2}{k-1}} = \frac{\binom{N-3}{k-2}}{\binom{N-2}{k-1}} \end{aligned} \quad (A-27)$$

Then

$$P[k_2 > 2/(1,-1); k] = 1 - P[k_2=2/(1,-1); k] = \frac{\binom{N-3}{k-1}}{\binom{N-2}{k-1}} \quad (A-28)$$

Second, we note that

$$P\left[\ell/(1,-1); k; k_2=2\right] = P\left[\ell/E_{1,N-1}^{+,-}; (k-1) \text{ positive pulses in } [2, N-1]\right] \quad (\text{A-29})$$

and

$$P\left[\ell/(1,-1); k; k_2 > 2\right] = P\left[\ell-1/E_{1,N-1}^{+,-}; (k-1) \text{ positive pulses in } [2, N-1]\right] \quad (\text{A-30})$$

If we substitute (A-27) through (A-30) into (A-26), a recursive relationship appears for evaluating $P(\ell/(1,-1); k)$, since the quantity in (A-30) is of the form (A-24) for the $(E_{1,N}^{+,-})$ case. To proceed further, we split again the expression in (A-29) in the same format as the original (A-26), replacing $N \rightarrow N-1$ and $k \rightarrow k-1$. This can be repeated n steps, and the result will be of the form (after some manipulation):

$$P[\ell/(1,-1); k] = \frac{1}{\binom{N-2}{k-1}} \sum_{n=1}^{n_{\max}} P\left(\ell-1/E_{1,N-n}^{+,-}; (k-n)\right) \cdot \binom{N-2-n}{k-n} \quad (\text{A-31})$$

The r.v. n accounts for the number of recursions needed to bring the quantity $P_N[\ell/(E_{1,N-n}^{+,-}); (k-n)]$ to zero. A question that arises now regards the value of n_{\max} . From Table 3-3a, we see that

$$n_{\max} = \begin{cases} 2k & \text{if } 1 \leq k \leq N/2 \\ 2(N-k) - 2 & \text{if } N/2 \leq k \leq N-2 \end{cases}$$

[we are referring to the $(E_{1,N}^{+,-})$ case]

Since both N and k are reduced by n at each step, the second limitation is always satisfied. Hence, n_{\max} (i.e., the maximum number of permissible steps) will be determined by forcing

$$\ell_{\max} = \ell - 1 = 2(k - n_{\max})$$

or

$$n_{\max} = \frac{\ell-1}{2} - k \quad (\text{A-32})$$

From (A-24), we have that

$$P\left(\ell / (E_{1, N-n}^{-, -}); (k-n, j)\right) = \frac{\binom{k-n-1}{\frac{\ell-1}{2} - 1} \binom{N-k-1}{\frac{\ell-1}{2}}}{\binom{N-n-2}{k-n}} \quad (\text{A-33})$$

so that (A-31) combined with (A-33) yields

$$P(\ell / (1, -1); k) = \frac{\binom{N-k-1}{\frac{\ell-1}{2}}}{\binom{N-2}{k-1}} \cdot \sum_{n=1}^{k - \frac{\ell-1}{2}} \binom{k-n-1}{\frac{\ell-1}{2} - 1}$$

or, using identity (A-23), we finally arrive at

$$P(\ell=1 / (1, -1); 1) = 1, \quad P(\ell=1 / (1, -1); N-1) = 1$$

$$P(\ell / (1, -1); k) = \frac{\binom{k-1}{\frac{\ell-1}{2}} \binom{N-k-1}{\frac{\ell-1}{2}}}{\binom{N-2}{k-1}} \quad (\text{A-34})$$

where $\ell = \text{odd} \geq 1$; $2 \leq k \leq N-2$ and ℓ obeys the restrictions of Table 3.3.a. Finally, $P(\ell / (1, -1); k) = 0$, elsewhere. An identical result holds for the case $E_{1, N}^{-, +}$.

ADDENDUM B

EVALUATION OF THE CONDITIONAL PROBABILITIES OF THE EVENTS $E_{1,N}^{i,j}$ GIVEN k POSITIVE PULSES IN N SLOTS

In this appendix, we evaluate the probabilities $P_N(E_{1,N}^{k,j}/k) \triangleq P((i,j)/k)$ as follows:

$$P((1,i)/k) = \frac{P((1,1);k)}{P(k)} = \frac{P((1,1);(k-2) \text{ positive pulses in } [2,N-1])}{P(k)} \quad (\text{B-1})$$

and, since the two events in the numerator are independent, we get

$$P((1,i)/k) = \frac{1}{4} \cdot \frac{P((k-2) \text{ positive pulses in } [2,N-1])}{P(k)} = \frac{\frac{1}{4} \binom{N-2}{k-2} \cdot \frac{1}{2^{N-2}}}{\frac{1}{2^N} \binom{N}{k}}$$

or, finally,

$$P((1,1)/k) = \frac{\binom{N-2}{k-2}}{\binom{N}{k}} \quad (\text{B-2})$$

and similarly,

$$P((1,-1)/k) = P((-1,1)/k) = \frac{\binom{N-2}{k-1}}{\binom{N}{k}} \quad (\text{B-3})$$

and

$$P((-1,-1)/k) = \frac{\binom{N-2}{k}}{\binom{N}{k}} \quad (\text{B-4})$$

The above were derived assuming $2 \leq k \leq N-2$. Obviously,

$$P((1,1)/0) = P((1,-1)/0) = P((-1,1)/0) = 0 \quad (\text{B-5})$$

$$P((-1,-1)/N) = P((1,-1)/N) = P((-1,1)/N) = 0 \quad (\text{B-6})$$

$$P((1,1)/1) = 0 \quad (\text{B-7})$$

$$P((-1,-1)/N-1) = 0 \quad (\text{B-8})$$

$$P((-1,-1)/0) = P((1,1)/N) = 1 \quad (\text{B-9})$$

$$P((1,-1)/1) = P((-1,1)/1) = P((1,-1)/N-1) = P((-1,1)/N-1) = \frac{1}{N} \quad (\text{B-10})$$

$$P((-1,-1)/1) = P((1,1)/N-1) = \frac{N-2}{N} \quad (\text{B-11})$$

APPENDIX III

PEAK REGULATOR DESIGN AND BREADBOARD EVALUATION

APPENDIX A

PEAK REGULATOR DESIGN AND BREADBOARD EVALUATION

1.0 INTRODUCTION

As a part of the development and specification of the PI/KuSP bent-pipe interface, Axiomatix undertook to design and evaluate a signal waveform peak regulator. Such a regulator permits the largest possible peak frequency deviation of the FM transmitter for any waveform shape, thus maximizing the mean-square deviation and FM link SNR.

The purpose for this activity was twofold:

- (1) To demonstrate the simplicity of implementation using readily available integrated circuits
- (2) To show that the loop will be stable and perform to expectations for all input waveforms.

2.0 FUNCTIONAL DESIGN

Figure 1 is a functional diagram for the peak regulator loop. The input, V_i , is first passed through a two-pole LPF having a 3 dB frequency of 4.5 MHz. This LPF is really not a part of the loop proper but is necessary to simulate the output bandwidth characteristics of the PI receiver. Following the LPF is a gain-controllable amplifier (GCA) whose gain, K , is voltage controllable by a reference voltage, V_R . The nominal open-loop gain of this amplifier is +16 dB and is variable by the reference from about +36 dB to -34 dB. Prior to the GCA is a 21 dB attenuator and following the GCA is a +20 dB fixed gain amplifier, so that the overall nominal input/output gain is +15 dB (a voltage gain of 5.6). Since the regulated output voltage is specified to be $\pm 2V$ p-p, the nominal input voltage is 357 mV p-p.

Output of the regulator, V_o , is input to an absolute value circuit which is mechanized in the form of a half-wave linear rectifier. (Note: The earlier functional design showed a full-wave linear rectifier but, because of waveform symmetry, the half-wave circuit was judged to be sufficient and simpler to implement.) A gated reset peak detector following

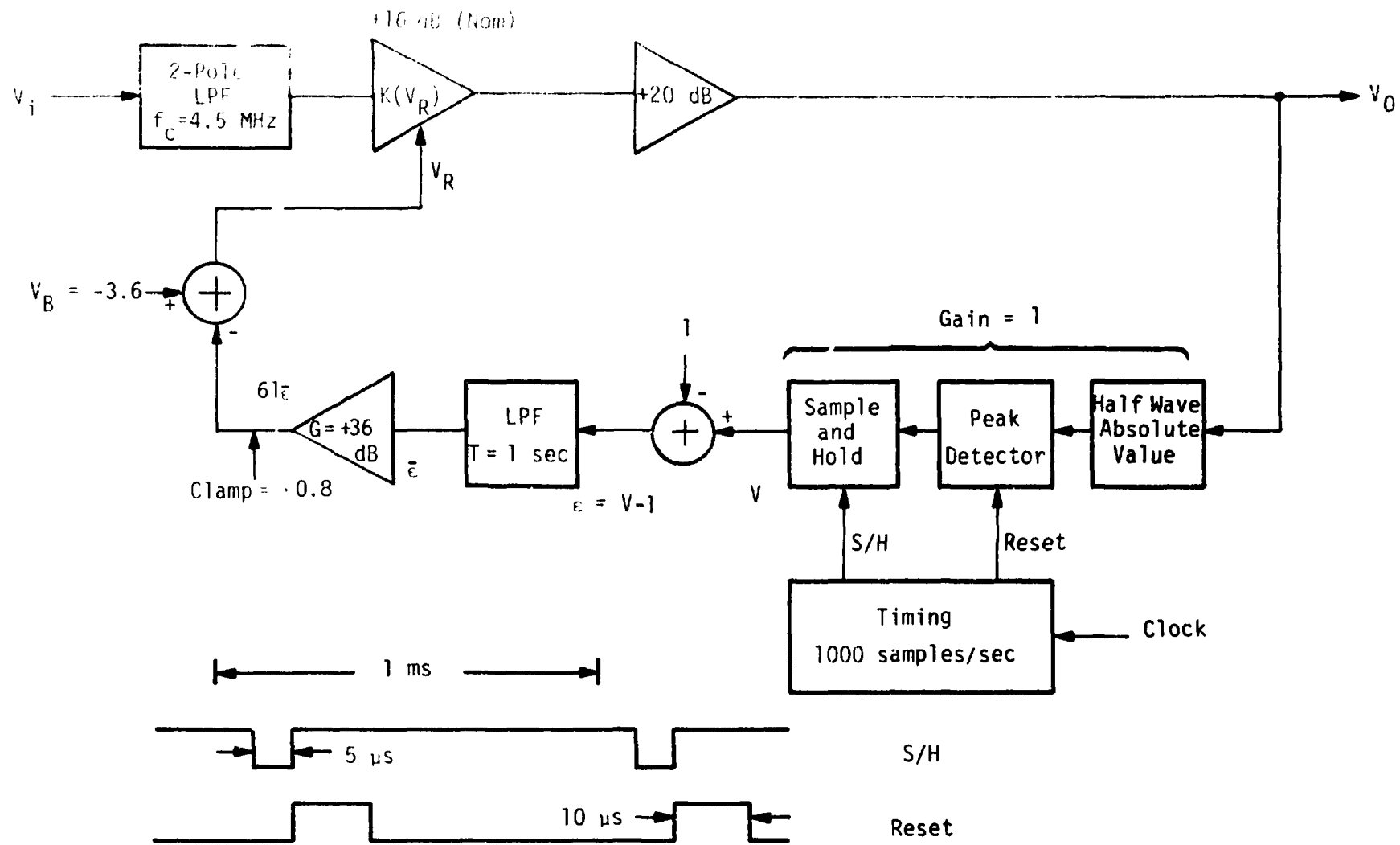


Figure 1. Peak Regulator Loop Functional Diagram

the rectifier functions to store or hold the largest voltage peak observed over a 0.99 ms time period. At the end of each 1 ms sample period, the peak value is transferred to a sample-and-hold amplifier where it is retained while the peak detector memory (capacitor) is reset and the next peak detection operation takes place.

Designating the sample-and-hold output by the symbol V , the loop instantaneous error, ϵ , is formed by subtracting a 1V reference from V . Thus, $\epsilon = V - 1$. An LPF follows (time constant = 1 sec) which averages over a large number of the peak detected error values that may change each 1 ms. The LPF output is denoted by $\bar{\epsilon}$. Following the LPF is a 36 dB gain amplifier which produces at its output $61\bar{\epsilon}$ subject to a maximum constraint of $\pm 0.8V$. This constraint is imposed to keep the reference voltage to the gain-controllable amplifier within a linear operating range, precluding the possibility of an unstable loop condition. The amplifier voltage reference, V_R , is formed by offsetting the error $61\bar{\epsilon}$ by $-3.6V$.

The original specification of the loop regulation performance was to be $\pm 1\%$ on the output for a ± 20 dB input variation. Thus, the equation of regulation would be

$$V_{op} = 5.6 V_{ip} \times 10^{\frac{100(V_{op} - 1)}{20}}$$

where V_{op} and V_{ip} are, respectively, the regulator waveform peak output and input voltages. As will be seen from the actual circuit performance discussed in the following section, this capability was achieved over only a 16.5 dB range.

The peak error sampling rate was chosen as 1 kHz, and the peak detector averaging time per sample is 0.99 ms. Thus, for any of the various waveform shapes considered, where the lowest subcarrier (sinusoid) frequency is expected to be about 30 kHz and random noise occupies the full 4.5 MHz bandwidth, each peak sample should be very close to the true peak value of the waveform. Averaging over a thousand or so error samples also provides the loop with a reasonably rapid response to dynamic input level changes, but is sufficiently long to obviate response to very short signal transients or the possibility of an occasional impulse noise burst due to EMI or other sources.

3.0 REGULATOR CIRCUIT DESIGN AND PERFORMANCE

Figure 2 is a circuit diagram for the Axiomatix peak regulator breadboard, and Figure 3 shows the companion timing logic circuits. As most of the regulator design is based upon operational amplifier configurations, a correspondence between the circuit diagram and the functional diagram of Figure 1 may be easily established. The amplifiers having the AD prefix are Analog Device types, and AD583 is the sample/hold amplifier. Block AH0152 is a FET switch used to discharge the peak detector capacitor (100 pf). Clamp for the error voltage amplifier output is provided by the pair of reversed IN457 duo-diode groups. Timing waveforms are produced by monostable multivibrators.

The RCA CA3002 was originally selected because of its large gain control capability--up to 70 dB for a 1.5V control voltage differential range. When the amplifier was tested to ascertain all of its operating characteristics, it was discovered that the maximum input voltage had to be limited to 150 mv p-p. Above this value, virtually independent of the gain control bias, the amplifier output exhibited a voltage saturation (compression) condition. The result was that the amplifier could not be driven to the levels intended in the original design. This, therefore, necessitated an adjustment of the intended operating point and resulted in a regulating range of 10 dB below the nominal input and 6.5 dB above the nominal input (rather than ± 20 dB). It was decided, however, that this would not compromise the prime reason for the breadboard evaluation of demonstrating excellent peak-to-peak regulation as a function of a variety of complex waveforms plus 4.5 MHz lowpass noise.

The initial regulator breadboard was constructed with a full-wave linear rectifier (see Figure 34 of the Final Report for 1978 Contract NAS 9-15240D for the circuit). This circuit performed very well as a function of input frequencies up to 2.5 MHz. Above 2.5 MHz, however, unsymmetrical phase shifts appeared between the waveforms produced by the individual half-wave rectifier outputs. Further, the overall frequency response was limited to about 3 MHz due to the inability of the AD507 amplifiers to preserve the harmonic structure of the full-wave waveform above this frequency. Rather than redesign the full-wave rectifier using different (wider bandwidth) amplifiers, it was decided to

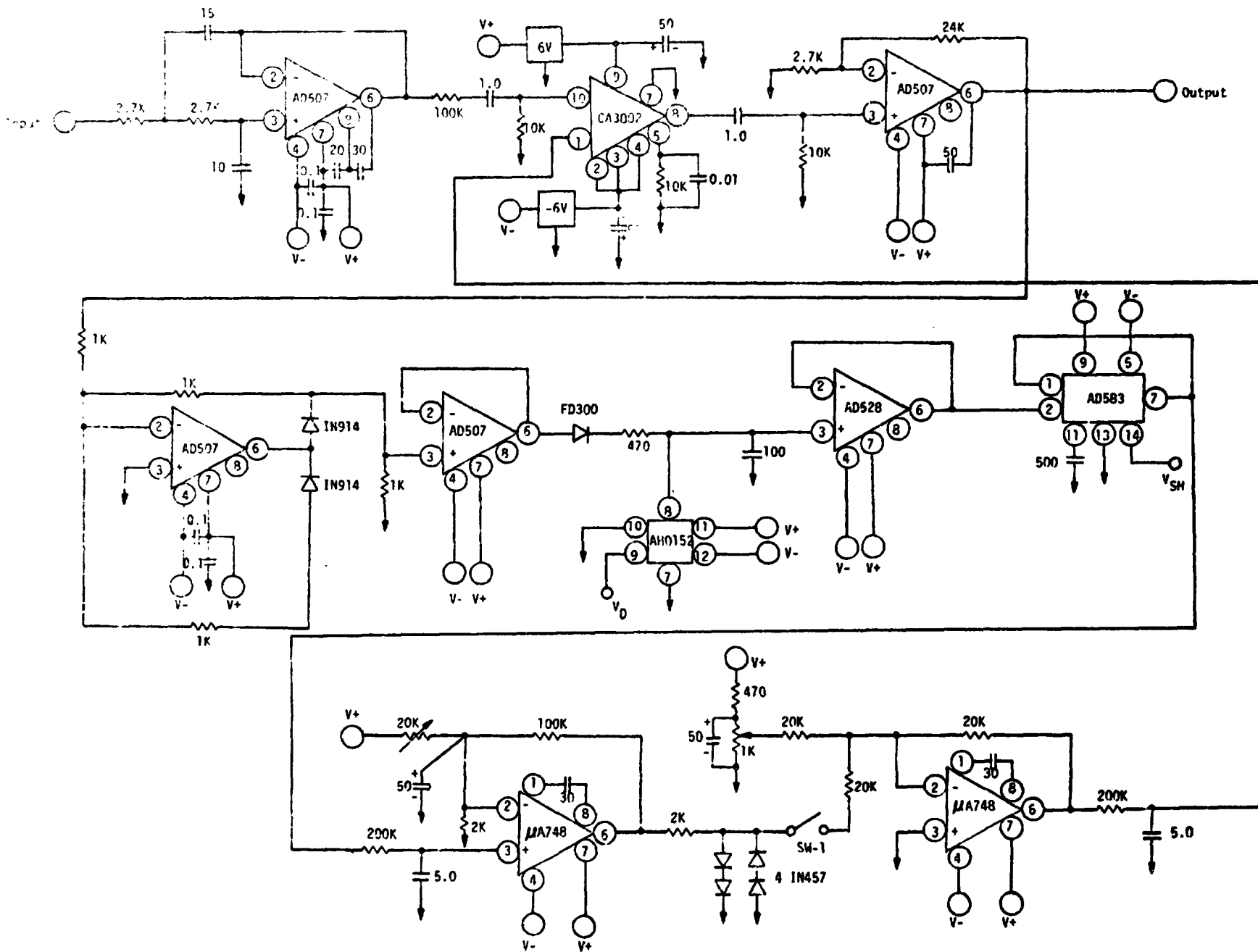


Figure 2. Peak Regulator Circuit Diagram

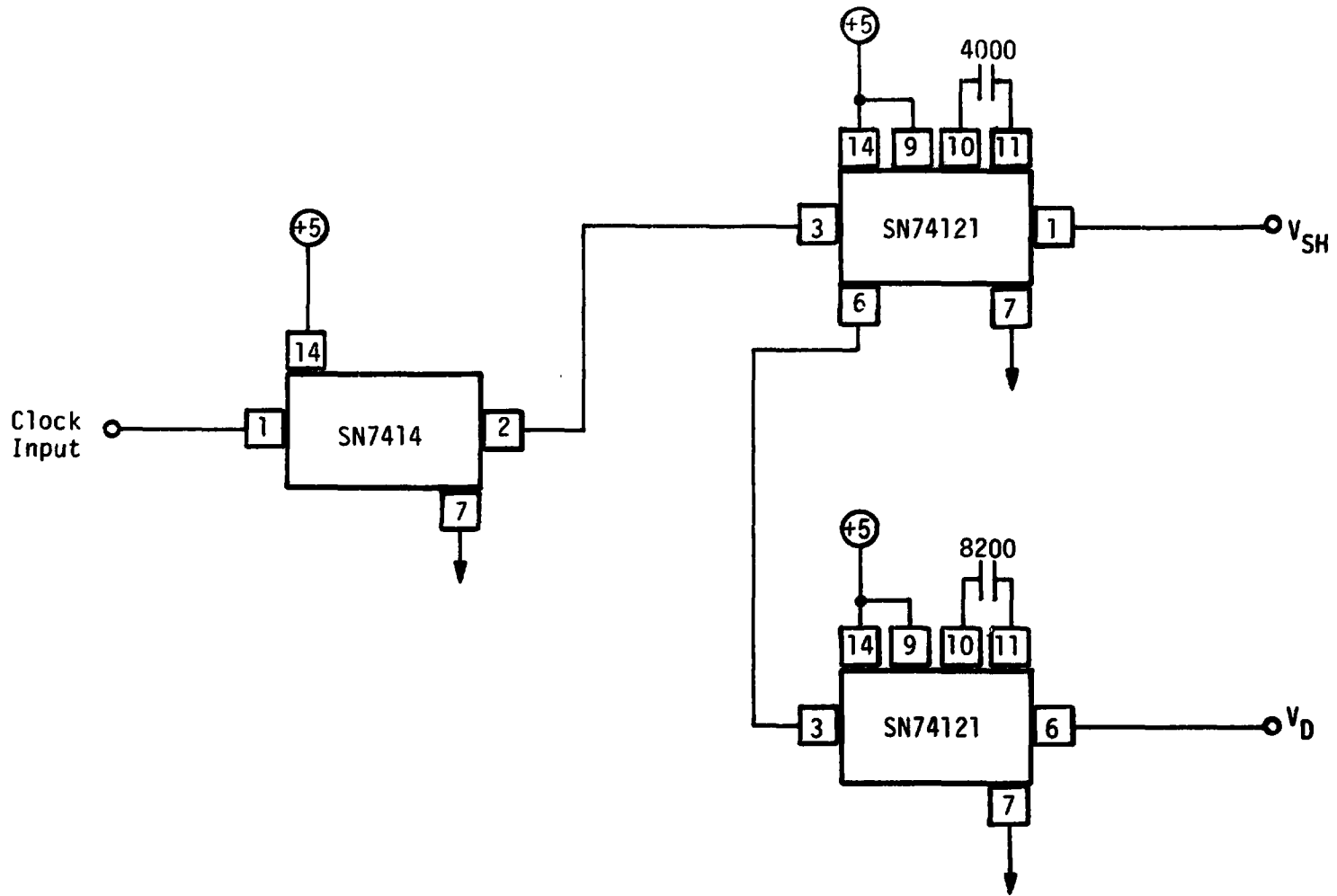


Figure 3. Peak Regulator Timing Logic Diagram

use a linear half-wave circuit instead, as all the contemplated input waveforms are amplitude symmetrical. This change eliminated two AD507 amplifiers, with the result that the half-wave rectifier response was found to be adequate up to 4.2 MHz utilizing IN914 diodes.

All the remaining circuits performed essentially as expected. A 470 Ω resistor had to be installed between the FD300 diode and 100 pf capacitor in the peak detector circuit in order to suppress an undesirable switch-off transient from the AH0152 FET discharge switch.

4.0 DEMONSTRATION AND TEST RESULTS

A measurement of the loop regulation capability was made in the following manner. Figure 4 shows the configuration used to obtain the necessary data. The approach taken was necessitated because of limited equipment but proved to work reasonably well.

The regulation error was measured in a differential fashion. As shown in Figure 4, an oscilloscope was employed to measure the ΔV_0 as a function of V_i . The measurement was calibrated for $V_i = 178$ mV-p and $V_0 = 1$ V-p at a frequency of 500 kHz. (A 500 kHz frequency was selected for this measurement so as to minimize any possible phase shift through the regulating circuits. Some perceptible phase shift at $f = 2$ MHz had been observed through the CA3002 amplifier as a function of its gain.) The scope, operating in its differential input mode ($Y_1 - Y_2$), was calibrated on the Y_2 input, while the Y_1 variable attenuator was adjusted to produce an amplitude null on the scope screen. Voltage, V , was held constant while V_i was changed using the operational adjustable attenuator and measured using a high-frequency RMS-to-DC converter in conjunction with a DVM. The result is that regulation error, ΔV_0 , as a function of V_i , could be read directly on the scope. The only problem encountered was that the wideband noise generated in the regulation loop amplifier circuits made it difficult to measure error voltages below 5 mV.

Table 1 summarizes the regulation measurements. As can be seen, the regulation range of -10 dB to +6.5 dB about the nominal (calibration) point was achieved.

The throughput frequency response of the regulator was measured exclusive of the LPF, and the 3 dB frequency was found to be about 5.2 MHz, the main contributor to the roll-off being attributed to the +20 dB output

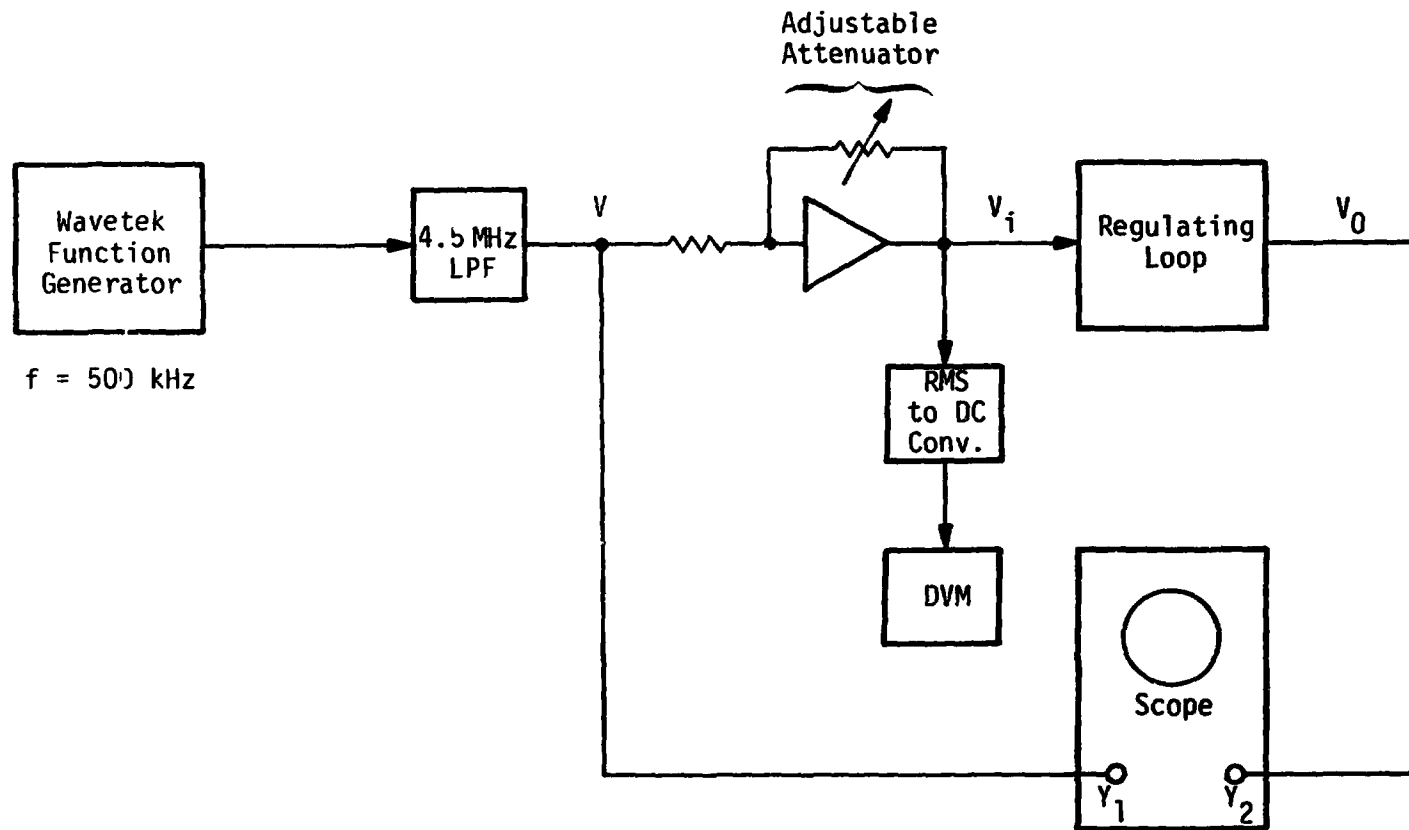


Figure 4. Loop Regulation Measurement Configuration

Table 1. Measured Regulator Performance

V_i	V_o	% Error	
25	860	4.0	} Exceeds Regulator Specification
50	970	3.0	
75	992	0.8	
100	996	0.4	} Calibration
178	1000	0.0	
300	1002	0.2	
400	1006	0.6	
500	1009	0.9	
600	1011	1.1	} Exceeds Regulator Specification
700	1018	1.8	
800	1028	2.8	
900	1050	5.0	} CA3002 Amplifier in Compression
1000	1100	10.0	

All voltages are in mV-peak

amplifier. With the input LPF connected, the throughput 3 dB frequency was 3.9 MHz.

The remainder of the measurements made on the regulator were rather qualitative and consisted of mixtures of signal waveforms and noise. A 1.024 MHz sinewave (representative of a subcarrier), a 200 kHz square wave (representative of NRZ data), and random noise were combined at varying levels and the regulator input and output observed on the scope. The performance was judged to be as expected. It was estimated that the regulator was able to hold regulation on the 4.5 MHz noise peaks at about 2.75σ .

The regulator was never observed to exhibit instability, and was able to accommodate input on/off step transients.

5.0 CONCLUSIONS

Except for the somewhat limited regulator dynamic range of 16.5 dB, all other aspects of the peak regulator design and breadboard evaluation met the objectives set for the effort. If, in the future, it is desired to increase the dynamic range to the original design goal of 40 dB, this may be done by replacing the CA3002 amplifier by a FET or diode current controlled attenuator configuration.

APPENDIX IV

ACQUISITION SWEEP RATE VIEWGRAPHS

DETERMINATION OF DSN TRANSPONDER ACQUISITION SWEEP RATE

CORRECTION NOTICE: THE LAST PAGE HAS BEEN CORRECTED AND REVISED

ORIGINAL: 6/26/79

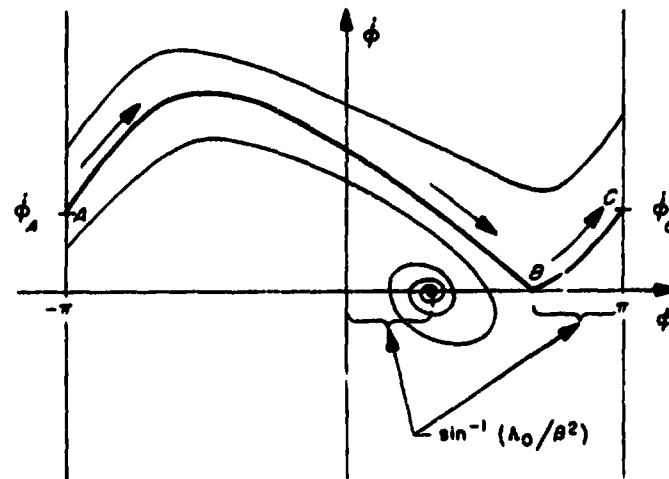
CORRECTED: 7/17/79

- DSN TRANSPONDERS WILL BE SWEEP ACQUIRED BY THE PI UNDER CONDITIONS OF MODERATELY STRONG SIGNAL LEVEL
- AT MODERATELY STRONG SIGNAL LEVELS, THE DSN TRANSPONDER PLL IS CHARACTERIZED BY A TRACKING BANDWIDTH ($2B_L$) BETWEEN 150-225 Hz AND A DAMPING FACTOR (ζ) AS LARGE AS THREE
- THE SWEPT PLL MAXIMUM SWEEP RATE LIMIT FOUND IN THE LITERATURE (VITERBI, ET AL) IS FOR A DAMPING FACTOR OF $\sqrt{2}/2 = 0.707$. THIS RESULT IS THEREFORE NOT APPLICABLE TO THE DSN TRANSPONDER

PROBLEM SOLUTION



- OBTAIN THE ABSOLUTE MAXIMUM SWEEP RATE FOR THE DSN TRANSPONDER PLL TRANSFER FUNCTION
- THE PROCEDURE FOR A SPECIFIC TRANSFER FUNCTION IS TO FIND THE VALUE OF SWEEP FREQUENCY $f_s = \Delta_0/2\pi$ THAT RESULTS IN A SADDLE-POINT B AND $\dot{\phi}_A = \dot{\phi}_C$. (β = PLL NATURAL FREQUENCY, RAD/SEC)



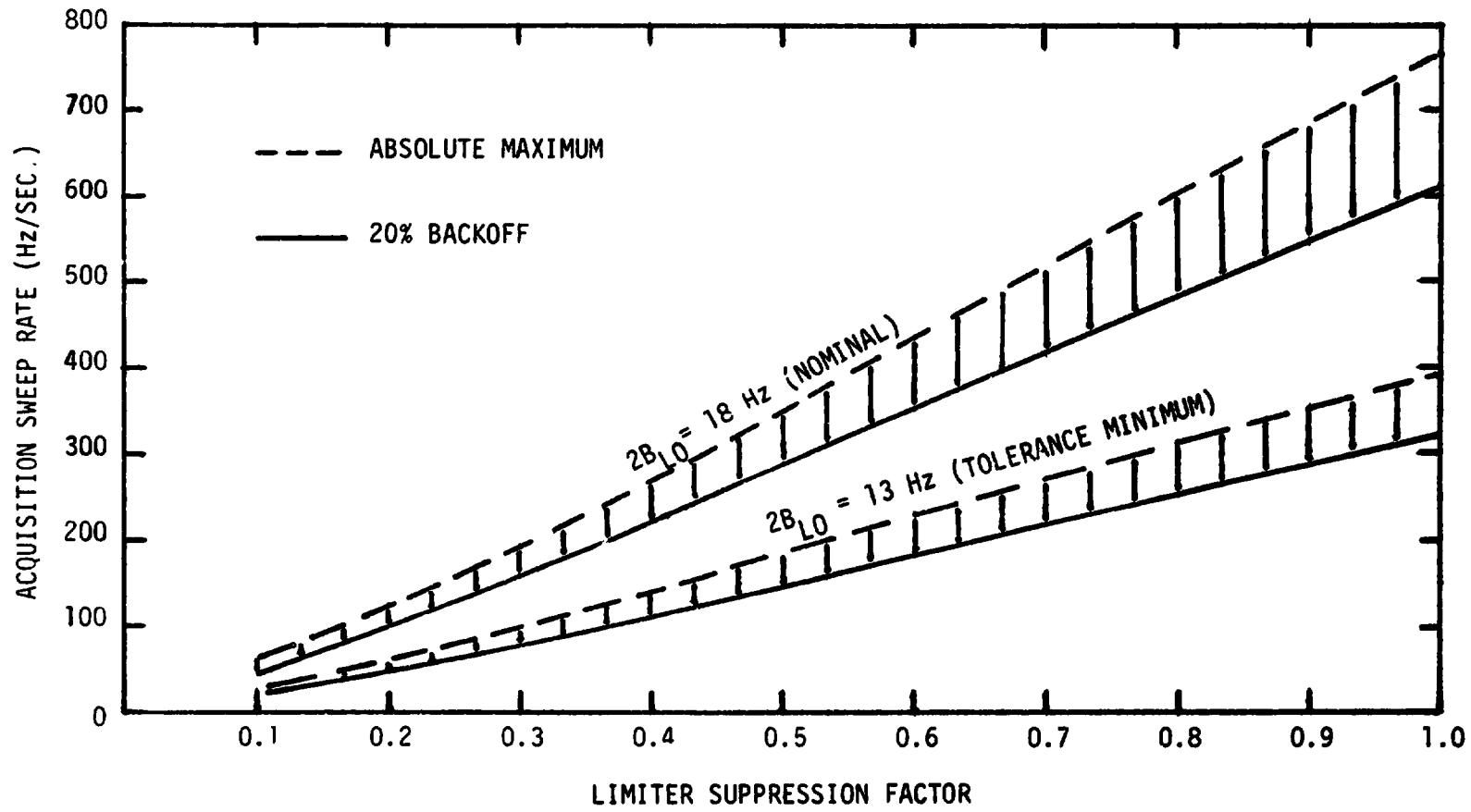
DSN TRANSPONDER CHARACTERISTICS



71

	<u>NOMINAL</u>	<u>TOLERANCE MINIMUM</u>
PLL TWO-SIDED THRESHOLD BW ($2B_{L0}$)	18 Hz	13 Hz
PLL THRESHOLD DAMPING FACTOR (ζ_0)	0.707	-
MAXIMUM SUPPRESSION FACTOR (α_0)	0.0547	-
PLL STRONG SIGNAL BW ($2B_{L(max)}$)	225 Hz	163 Hz
PLL STRONG SIGNAL DAMPING FACTOR (ζ_{max})	3.03	3.03 (By Definition)
STRONG SIGNAL SUPPRESSION FACTOR	1.0	1.0

DSN TRANSPONDER ACQUISITION SWEEP RATE
VERSUS
LIMITER SUPPRESSION



MINIMUM DSN PAYLOAD AND ORBITER LINK CONDITIONS
FOR 10 NMI RANGE



	<u>PI TRANSMITTER POWER</u>		
	<u>37 dBm</u>	<u>27 dBm</u>	<u>4 dBm</u>
PAYLOAD RECEIVED SIGNAL LEVEL	-92 dBm	-102 dBm	-125 dBm
DSN TRANSPONDER NEGATIVE TOLERANCE ALLOWANCE	-4 dB	-4 dB	-4 dB
LIMITER SUPPRESSION FACTOR	1.0	1.0	0.79

- FOR VERY NEAR-RANGE, THE LIMITER SUPPRESSION FACTOR IS 1.0 FOR ALL PI TRANSMITTER POWER LEVELS

PI TRANSMITTER MAXIMUM NOMINAL SWEEP RATES



- 20% BACKOFF FROM ABSOLUTE MAXIMUM PHASE PLANE LIMIT IS ASSUMED
- $\pm 30\%$ SWEEP RATE TOLERANCE ON PI ASSUMED

	<u>PI TRANSMITTER POWER</u>		
	<u>37 dBm</u>	<u>27 dBm</u>	<u>4 dBm</u>
$W_{LO} = 18 \text{ Hz}$ (NOMINAL)	470 Hz/s	470 Hz/s	365 Hz/s
$W_{LO} = 13 \text{ Hz}$ (TOLERANCE MINIMUM)	250 Hz/s	250 Hz/s	190 Hz/s

SWEEP RATE

NOTE: THIS PAGE HAS BEEN CORRECTED AND REVISED FROM THE ORIGINAL OF 6/26/79.

APPENDIX V

**MAXIMUM SWEEP FREQUENCY FOR PHASE-LOCKED LOOPS
WITH LARGE DAMPING FACTORS**

By

Marvin K. Simon

1.0 INTRODUCTION

The classic paper by Viterbi [1] investigates the swept acquisition capability of a phase lock loop (PLL) using the phase plane approach. Therein it was shown that, in the absence of noise, a second-order loop with damping factor $\zeta = 0.707$ could always* be brought to a locked condition as long as the sweep rate Λ_0 (rad/sec) was less than half the square of the loop natural frequency β . For values of $\beta^2/2 < \Lambda_0 < \beta^2$, the loop could not be guaranteed to lock. This is equivalent to saying that some of the phase plane trajectories corresponding to initial conditions in certain regions of the plane would not approach the equilibrium (lock) point in the steady state but, rather, go on to a stable limit cycle. If the initial conditions were such as to bring the loop into lock, however, it would continue to track. For $\Lambda_0 > \beta^2$, the loop would not lock at all. Moreover, if it ever reached the lock point, it would not continue to track.

Extension of these results to other values of loop damping was considered by Dye [2] and Tauseworthe [3]. In particular, Dye showed that, for $\zeta = 0.5$, lock-on is guaranteed for $\Lambda_0 < 0.387 \beta^2$, marginal for $0.387 \beta^2 < \Lambda_0 < \beta^2$, and not possible for $\Lambda_0 > \beta^2$. Tauseworthe verified these results and generalized them by investigating the maximum guaranteed lock-on capability for a range of damping factors between 0.25 and 1.6.

The purpose of this report is twofold. First, we wish to extend Tauseworthe's results to larger damping factors. Second, we shall consider the situation where the PLL is preceded by a narrowband bandpass limiter (BPL) which is typical of the deep-space network (DSN) transponder receiver. Actually, these two generalizations will not be performed independently. Rather, the increase in damping factor will come about because of the increase in SNR in the BPL input bandwidth, thus raising the limiter suppression α from its threshold value α_0 toward its strong signal value. The damping factor (relative to its threshold value ζ_0 , assumed here to be 0.707) is directly proportional to the square root of the ratio of α to α_0 .

The approach taken in this report will once again make use of the phase plane. A simple method for obtaining phase plane trajectories on a digital computer was discussed by the author in [4]. The approach used there will prove useful in obtaining the desired results described above.

*The word "always" as used herein implies an initial frequency offset between the input and loop's VCO reference of any magnitude and a sign in the direction of the sweep.

2.0 THE LOOP EQUATION

A second-order PLL with perfect integrating loop filter

$$F(s) = \frac{1 + \tau_2 s}{\tau_1 s} \quad (1)$$

is governed by the differential equation of operation [3]

$$\Lambda_0 = \frac{d^2 \phi}{dt^2} + \beta^2 \left(\sin \phi + \tau_2 \frac{d\phi}{dt} \cos \phi \right) \quad (2)$$

where ϕ is the loop phase error. The loop damping ζ can be related to β and τ_2 by

$$\zeta = \frac{\beta \tau_2}{2}$$

Thus, defining the normalized time variable $\tau = 2\zeta\beta t$, (2) can be rewritten in the form

$$\frac{d^2 \phi}{d\tau^2} + \frac{d\phi}{d\tau} \cos \phi + \frac{1}{4\zeta^2} \sin \phi = \frac{1}{4\zeta^2} \left(\frac{\Lambda_0}{\beta^2} \right) \quad (3)$$

Further, letting $v = d\phi/d\tau$, and equivalently, $d^2\phi/d\tau^2 = v dv/d\phi$, (3) can be put in a form desirable for using the phase plane approach of [4], namely,

$$\frac{dv}{d\phi} + \cos \phi = \frac{1}{4\zeta^2 v} \left[\frac{\Lambda_0}{\beta^2} - \sin \phi \right] \quad (4)$$

3.0 THE PHASE PLANE TRAJECTORY APPROACH

In [4], it was shown that the parameter arc length defined by

$$ds^2 = dv^2 + d\dot{\phi}^2 \quad (5)$$

was a desirable independent parameter for constructing a plot of ϕ versus v (a phase plane) on a digital computer. Thus, our goal (as in [4]) is to

find a pair of coupled first-order differential equations for ϕ and v , i.e.,

$$\begin{aligned}\frac{d\phi}{ds} &= f_1(\phi, v) \\ \frac{dv}{ds} &= f_2(\phi, v)\end{aligned}\quad (6)$$

and solve these iteratively. To see how this is done, we first observe from (5) that

$$\frac{ds}{d\phi} = \sqrt{1 + \left(\frac{dv}{d\phi}\right)^2}; \quad \frac{d\phi}{ds} = \frac{1}{\sqrt{1 + \left(\frac{dv}{d\phi}\right)^2}} \quad (7)$$

$$\frac{dv}{ds} = \frac{dv}{d\phi} \frac{d\phi}{ds} = \frac{\frac{dv}{d\phi}}{\sqrt{1 + \left(\frac{dv}{d\phi}\right)^2}} \quad (8)$$

Substituting (4) into (7) and (8) gives the desired set of differential equations in the form of (6), namely,

$$\begin{aligned}\frac{d\phi}{ds} &= \frac{v}{\sqrt{v^2 + \left\{ \frac{1}{4\zeta^2} \left(\frac{\Lambda_0}{\beta^2} - \sin \phi - 4\zeta^2 v \cos \phi \right) \right\}^2}} \\ \frac{dv}{ds} &= \frac{\frac{1}{4\zeta^2} \left[\frac{\Lambda_0}{\beta^2} - \sin \phi - 4\zeta^2 v \cos \phi \right]}{\sqrt{v^2 + \left\{ \frac{1}{4\zeta^2} \left(\frac{\Lambda_0}{\beta^2} - \sin \phi - 4\zeta^2 v \cos \phi \right) \right\}^2}}\end{aligned}\quad (9)$$

4.0 DETERMINATION OF THE SADDLE POINT PHASE PLANE TRAJECTORY

The phase planes originally determined by Viterbi [1] contained a trajectory (herein referred to as the saddle point trajectory) which passed through the saddle point $\dot{\phi} = 0$, $\phi = \pi - \sin^{-1} (\Lambda_0/\beta^2)$. The significance of this trajectory depends on the value of loop damping relative to the normalized sweep rate Λ_0/β^2 . For example, Figure 1 illustrates a phase plane plot for $\zeta = 0.707$ and $0 < \Lambda_0 < \beta^2/2$. The saddle point is denoted by point B and the saddle point trajectory corresponds to the trajectory passing through points A, B and C. In particular, we note that the value of $\dot{\phi}$ at point A ($\phi = -\pi$) herein denoted by $\dot{\phi}_A$ is greater than the value of $\dot{\phi}$ at point C ($\phi = \pi$) herein denoted by $\dot{\phi}_C$. Thus, any phase plane trajectory with $\dot{\phi}(0) < 0$ ($\dot{\phi}(0)$ denotes the initial condition on $\dot{\phi}(t)$) will stay below this saddle point trajectory and eventually reach the equilibrium point D ($\phi_D = \sin^{-1} (\Lambda_0/\beta^2)$, $\dot{\phi}_D = 0$). This is consistent with our previous statement that the loop will "always" reach lock when $\Lambda_0 < \beta^2/2$.

If $\zeta = 0.707$ and $\beta^2/2 < \Lambda_0 < \beta^2$, the saddle point trajectory will be such that either $\dot{\phi}_C > \dot{\phi}_A$ or point A disappears entirely. In the latter case (see Figure 2), for example, we observe that there exists a corridor in the phase plane bounded by the trajectories E - E' and F - F' or G - G' and F - F', for which any trajectory originating in this band will be whipped past the equilibrium point and on to a stable limit cycle. Thus, despite the fact that $\Lambda_0 > 0$ and $\dot{\phi}(0) < 0$, the loop will not come to lock if $\dot{\phi}(0)$ is of such a magnitude as to fall into this critical corridor.

From these examples, it is easy to conclude that the critical value of Λ_0 , namely, $\beta^2/2$, for which all trajectories with $\dot{\phi}(0) < 0$ reach the equilibrium point, corresponds to a saddle point trajectory for which $\dot{\phi}_A = \dot{\phi}_C$ (see Figure 3). This, then, is our task, namely, for each value of loop damping ζ , we search for the largest value of Λ_0/β^2 which gives a saddle point trajectory with $\dot{\phi}_A = \dot{\phi}_C$. This value of Λ_0 , namely, $\Lambda_{0\max}$, is then the maximum sweep rate (in rad/sec) for which the loop is guaranteed to acquire.

Using the pair of coupled differential equations of (9), we start at (in the neighborhood of) point B (whose coordinates are known, namely, $v = 0$, $\phi = \pi - \sin^{-1} (\Lambda_0/\beta^2)$) and numerically integrate forward (ds

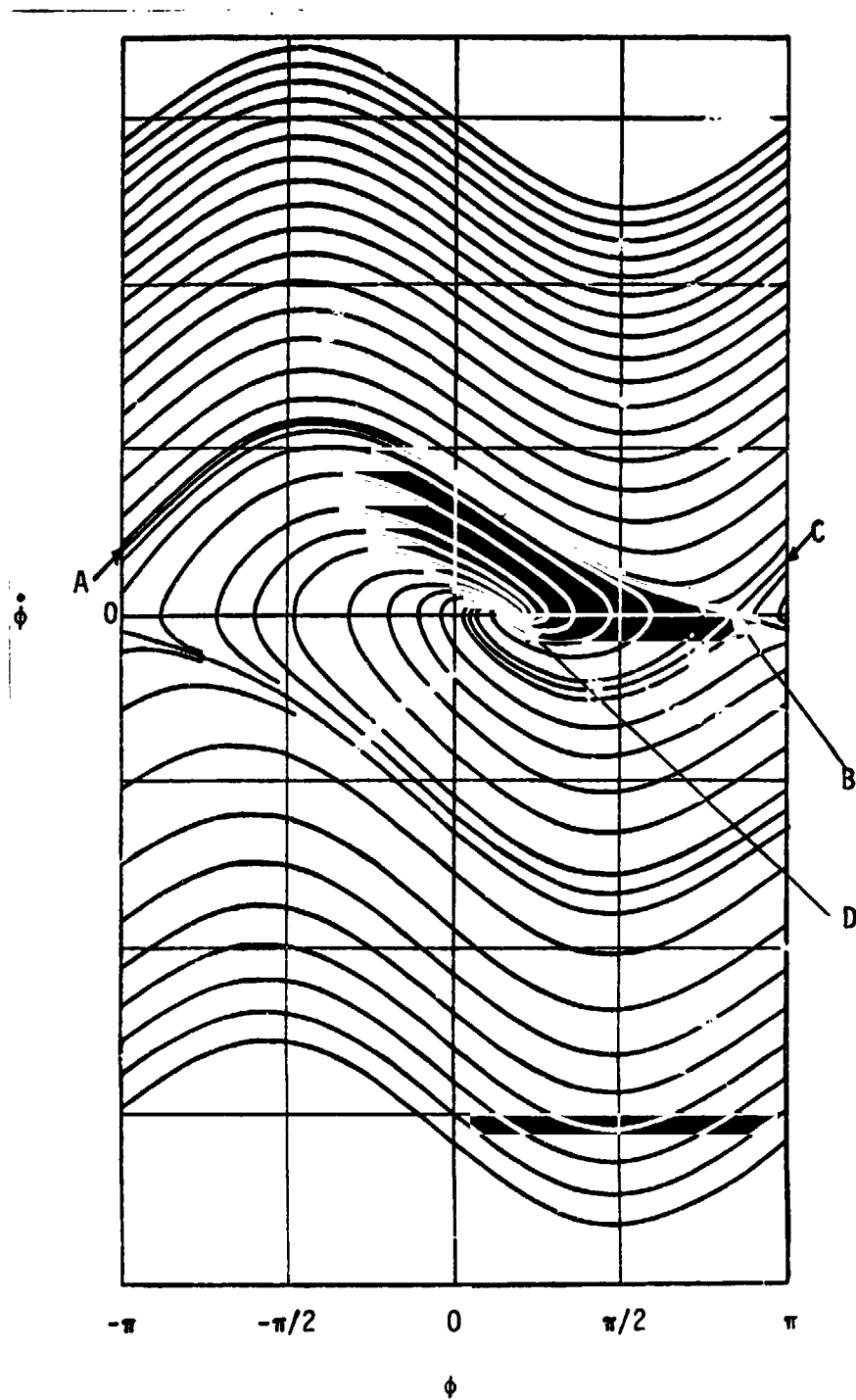


Figure 1. A Typical Phase Plane Trajectory Showing Solutions to the Loop Equation; $\zeta = 0.707$, $\Lambda_0 < \beta^2/2$

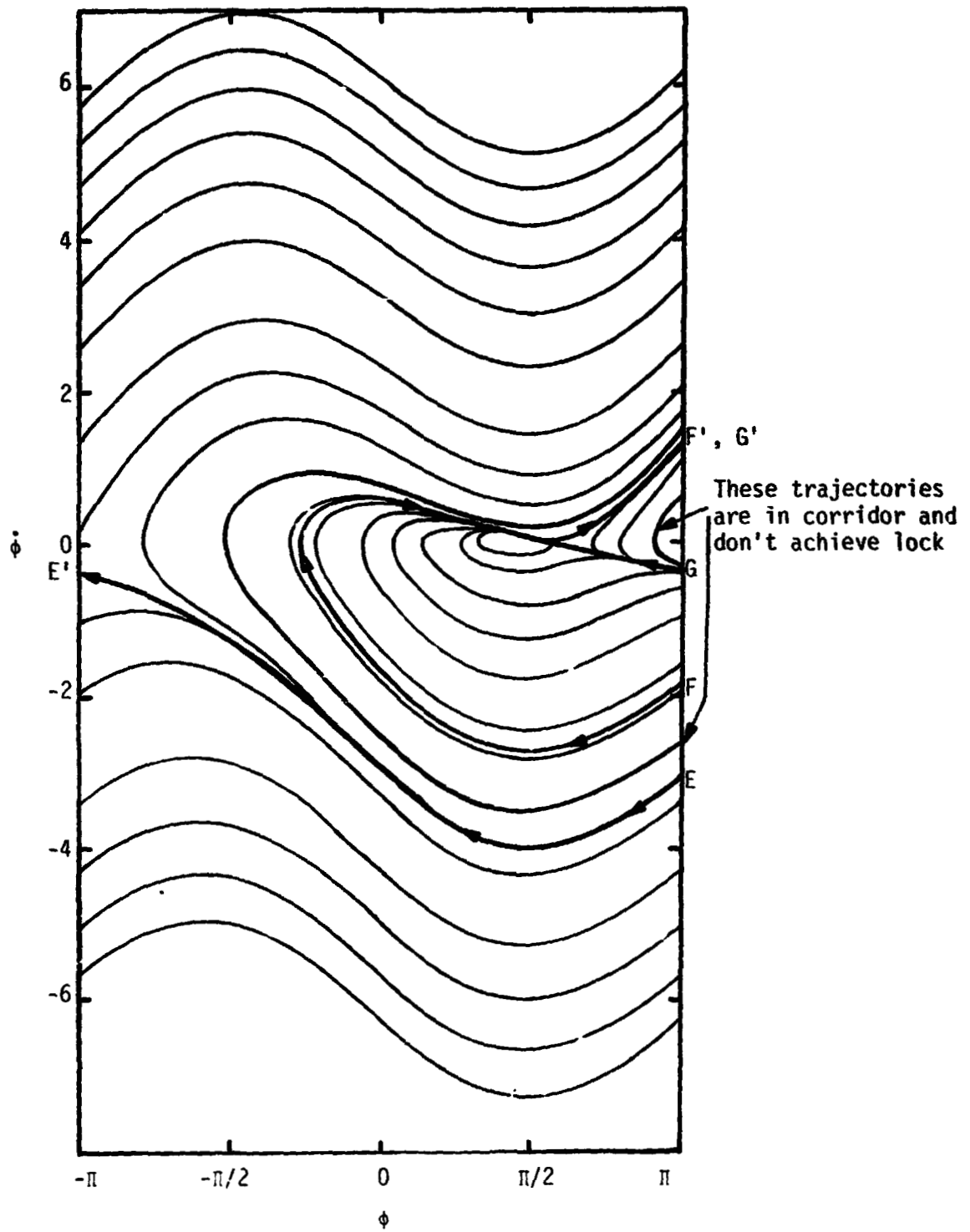


Figure 2. A Typical Phase Plane Trajectory Showing Solution to the Loop Equation

$$\zeta = 0.07, \Lambda_0/\beta^2 = 0.95$$

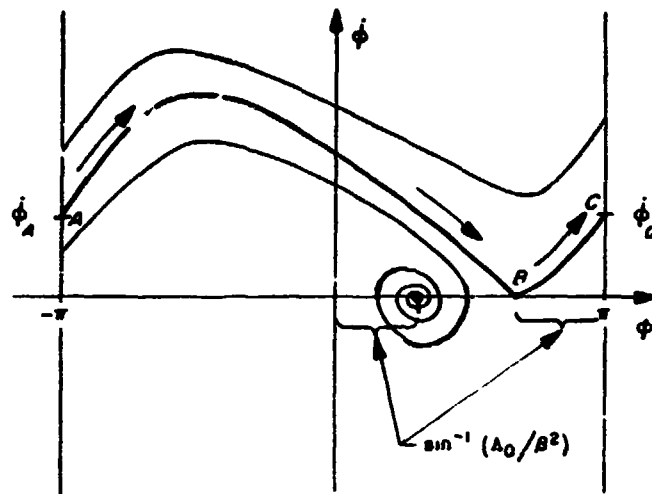


Figure 3. Limiting Trajectory for which Loci with $\dot{\phi}(-\pi) < \dot{\phi}_A$ Converge and $\dot{\phi}(-\pi) > \dot{\phi}_A$ Diverge

positive) to point C ($\phi = \pi$) and backward (ds negative) to point A ($\phi = -\pi$). The value of Λ_0/β^2 at which $v_A = v_C$ is then the desired result.

5.0 DETERMINATION OF THE MAXIMUM SWEEP RATE IN TERMS OF THE DESIGN POINT LOOP PARAMETERS

Letting ζ_0 and β_0 , respectively, denote the design point (threshold) values of loop damping and natural frequency, then, for any operating point SNR in the BPL input bandwidth, the corresponding values are given by

$$\beta = \beta_0 \sqrt{\frac{\alpha}{\alpha_0}} ; \zeta = \zeta_0 \sqrt{\frac{\alpha}{\alpha_0}} \quad (10)$$

In (10), α_0 is the threshold limiter suppression factor and α is the corresponding suppression factor at the operating SNR. Substituting (10) into (9) enables one to determine the critical saddle point trajectory as a function of α for fixed values of α_0 , β_0 and ζ_0 . In particular, for $\alpha_0 = 0.0547$ and $\zeta_0 = 0.707$, Figure 4 is a plot of $f_{\max}/\beta^2 = \Lambda_{0\max}/2\pi\beta^2$ versus α for values of β_0 corresponding to two-sided threshold loop bandwidths W_{LO} of 13 and 18 Hz. The relationship between β_0 and W_{LO} is given by

$$\beta_0 = \left(\frac{4\zeta_0}{1 + 4\zeta_0^2} \right) W_{LO} \quad (11)$$

Table 1 tabulates some of these values along with the corresponding values of β and ζ as computed from (10).

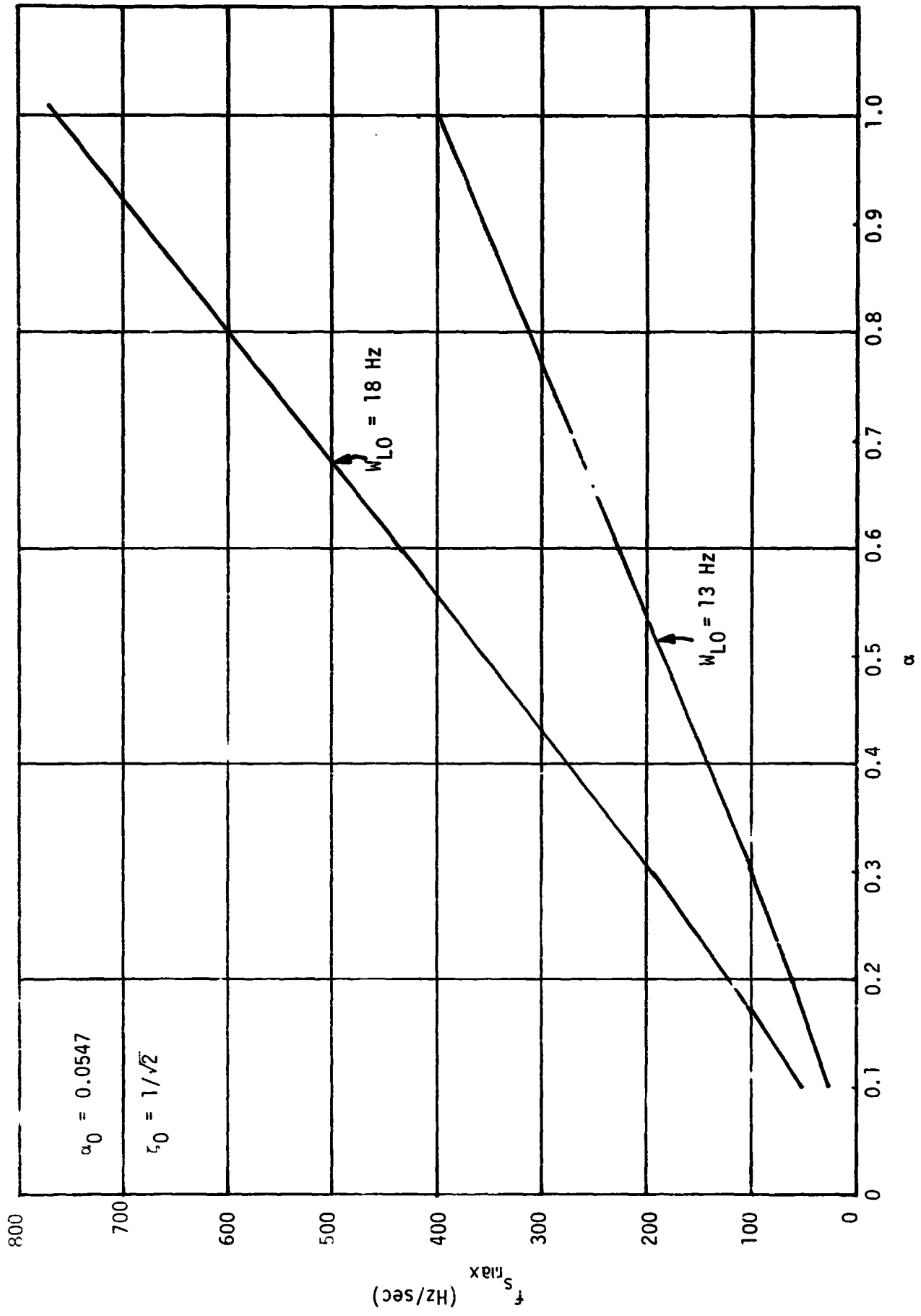


Table 1. PLL Parameters as a Function of Limiter Suppression

α	β	ζ	W_L	$\frac{\Lambda_0}{\beta^2}$	$f_{s_{max}}$
0.1000	16.5719	0.9559	20.1773	0.6140	26.8371
0.2000	23.4363	1.3519	36.0213	0.7320	63.9894
0.3000	28.7034	1.6557	51.8653	0.7890	103.4583
0.4000	33.1439	1.9119	67.7093	0.8260	144.4132
0.5000	37.0560	2.1375	83.5533	0.8510	185.9801
0.6000	40.5928	2.3415	99.3973	0.8690	227.8967
0.7000	43.8452	2.5292	115.2413	0.8840	270.4689
0.8000	46.8725	2.7038	131.0853	0.8890	310.8556
0.9000	49.7158	2.8678	146.9293	0.9040	355.6132
1.0000	52.4051	3.0229	162.7733	0.9120	398.6225

$$\zeta_0 = 0.707$$

$$W_{L0} = 13.0000$$

$$\beta_0 = 12.2565$$

$$\alpha_0 = 0.0547$$

REFERENCES

1. Viterbi, A.J., "Acquisition and Tracking Behavior of Phase-Locked Loops," Symposium on Active Networks and Feedback Systems, Polytechnic Institute of Brooklyn, April 19-21, 1960.
2. Dye, R, "Phase-Locked Loop Swept-Frequency Synchronization Analysis," Record of the 1965 International Space Electronics Symposium, Miami, Florida, November 1965.
3. Tausworthe, R.C., "Maximum Sweep and Doppler Rates in Phase-Locked Loops," JPL Space Programs Summary No. 37-38, Vol. IV, pp 261-264.
4. Simon, M.K., "A Note on the Generation of Phase Plane Plots on a Digital Computer," submitted for publication in the IEEE Transactions on Communications.

APPENDIX VI

**THE THEORY OF MEAN-SQUARE PHASE NOISE PERFORMANCE
OF ONE/TWO-WAY COHERENT COMMUNICATION LINKS**

By

Marvin K. Simon

APPENDIX VI

THE THEORY OF MEAN-SQUARE PHASE NOISE PERFORMANCE OF ONE/TWO-WAY COHERENT COMMUNICATION LINKS

1.0 INTRODUCTION

In assessing the performance of one/two way coherent communication links, one must consider the many sources of random fluctuations present in the overall system and their individual degrading effects. While it is most common to consider only those degradations due to the additive thermal noise on the link(s), a complete characterization of system performance should also include the effects of such phase noise sources as transmitter and receiver local and reference oscillators, mixer (multiplier) logic noise, AM-to-PM conversion due to link nonlinearities, and possible vibration effects. All of these phase noise components degrade carrier tracking loop performance and those which are not tracked by the loop(s) have an additional harmful effect on overall system error probability performance.

Regardless of the analysis technique employed, the first step in assessing tracking loop and bit error performance degradations due to phase noise effects is to introduce appropriate mathematical models for the carrier (discrete or suppressed) tracking loop(s) which include the various sources of phase noise referred to above. These models ordinarily take the form of equivalent linear loop block diagrams with phase noise sources described by power spectral densities characterized by inverse power law behavior as a function of frequency away from some nominal value. A complete discussion of the various phase and frequency instabilities present in precision frequency sources, along with their characterization, is given in [1]. For our purposes, it is convenient (as was done in [2]) to represent the equivalent two-sided lowpass power spectral density $S_{\psi}(\omega)$ of the various phase noise instabilities by the (inverse) power series*

* We shall ignore any discrete frequency components in the spectrum such as those caused by spurs or vibration effects.

$$S_{\psi}(\omega) = \sum_{k=0}^3 \frac{h_k}{|\omega|^k} \quad (1)$$

The $|\omega|^0$ term corresponds to white phase noise, $|\omega|^{-1}$ corresponds to flicker phase noise, $|\omega|^{-2}$ corresponds to white frequency noise, while $|\omega|^{-3}$ corresponds to flicker frequency noise.

In the past, the calculation of mean-square phase error in the presence of phase noise has been based on an equivalent linear loop model for a one-way link, with specific closed-form results obtained only for the case of 0.707 loop damping (Eq. (11) of [2]). While the abstract and introduction of [2] imply that these theoretical results can be applied to assess the tracking loop and bit error probability performances of various Shuttle S-band links (e.g., payload/Shuttle and TDRSS/Shuttle), in reality, this is not true since these links are indeed two-way coherent communication systems. In fact, the theory developed in the first part of [2] is never used in assessing the performance of these links; rather, estimates of the actual power spectral densities of the many phase noise sources combined with piecewise linear approximations of the various loop transfer functions allow for numerical integration computation of mean-square phase error.

In this report, we begin by generalizing the specific one-way results given in [2] to the case of arbitrary loop damping. Following this, we present a theory for computing mean-square phase error due to phase noise sources in two-way coherent communication links. Here again, the two loops are allowed to have arbitrary damping factors and natural frequencies. Several different two-way transfer functions characteristic of payload/Shuttle links (e.g., Inertial Upper Stage (IUS)/Payload Interrogator (PI)), are considered and, in each case, expressions for the mean-square phase error components corresponding to each term in the power spectral density of (1) are derived. These results, when combined with similar results available for mean-square phase error due to additive thermal noise [3], then allow for assessment of total mean-square phase error performance and the corresponding degradation in bit error probability performance.

2.0 SYSTEM MODEL

Consider the simple model of a two-way coherent communication system illustrated in Figure 1. As such, the reference system might represent the PI aboard the Shuttle while the vehicle transponder might represent the IUS/SGLS transponder.* When the switch is in position 1, the system of Figure 1 operates in a two-way coherent mode, i.e., the uplink signal to the vehicle is coherently demodulated and a frequency-translated version of it is retransmitted on the downlink, which is then tracked by the reference tracking loop. When the switch is in position 2, a free-running auxiliary oscillator aboard the vehicle provides the downlink carrier and, as such, the system operates as two independent one-way links.

An equivalent linear baseband model of the system, including various phase noise sources, is illustrated in Figure 2. Using simple control system theory, the block diagram of Figure 2 can be further simplified to Figure 3. From Figure 3, we immediately observe that the phase error ϕ_e in the reference system is given in terms of the various phase noise sources by **

$$\begin{aligned}
 \phi_e = & G_f H_V(s) [1 - H_R'(s)] G_1(s) G_2(s) \psi_{TX}(s) \\
 & + G_f [1 - H_V(s)] [1 - H_R'(s)] G_1(s) G_2(s) \psi_V(s) \\
 & - [1 - H_R'(s)] G_1(s) G_2(s) \psi_{RX}(s) \\
 & - [1 - H_R'(s)] G_2(s) \psi_R(s) \\
 & - [1 - H_R'(s)] \psi_r(s)
 \end{aligned} \tag{2}$$

Assuming for simplicity that the IF amplifiers in the reference system are identical ideal "brickwall" bandpass filters, with $G_1(s)$ and $G_2(s)$ their equivalent lowpass transfer functions, i.e.,

* In reality, the TCXO-linear phase modulator combination is only a part of a more general-purpose frequency synthesizer aboard the Shuttle PI which contains other internal loops and phase noise sources. For the purpose of Sections 2.0 through 5.0, we consider only the direct feedthrough paths of the TCXO to the transmit and receive output terminals of the synthesizer. Later on, we generalize the model to include the other internal frequency synthesizer oscillator sources and other TCXO paths.

** We assume here that the switch in the vehicle system is in position 1.

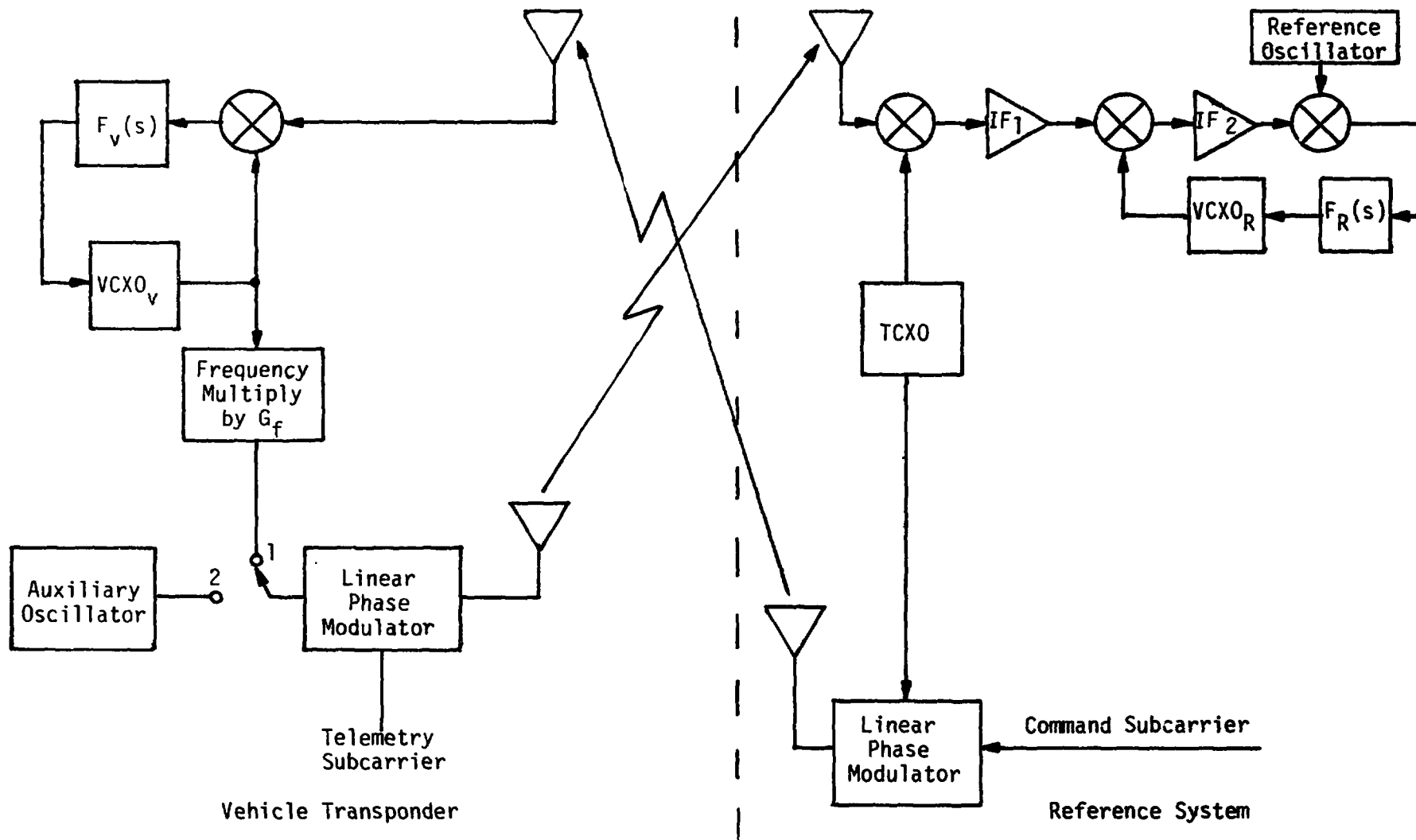


Figure 1. A Simple Block Diagram of a Two-Way Coherent Communication System

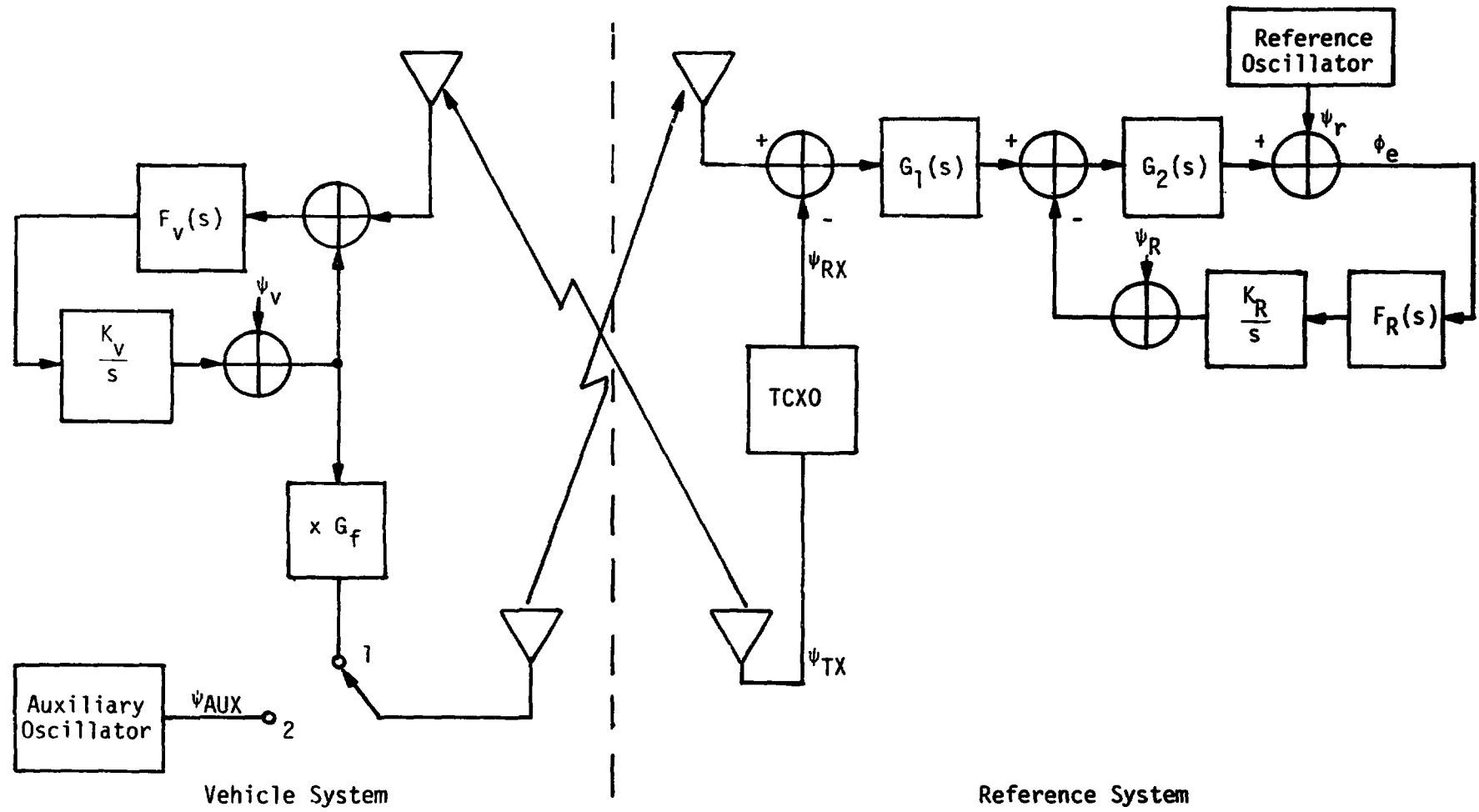


Figure 2. An Equivalent Linear Baseband Model of the System Including Oscillator Phase Noise Sources

$$H_V(s) = \frac{K_V F_V(s)}{s + K_V F_V(s)}$$

$$H'_R(s) = \frac{K_R F_R(s) G_2(s)}{s + K_R F_R(s) G_2(s)}$$

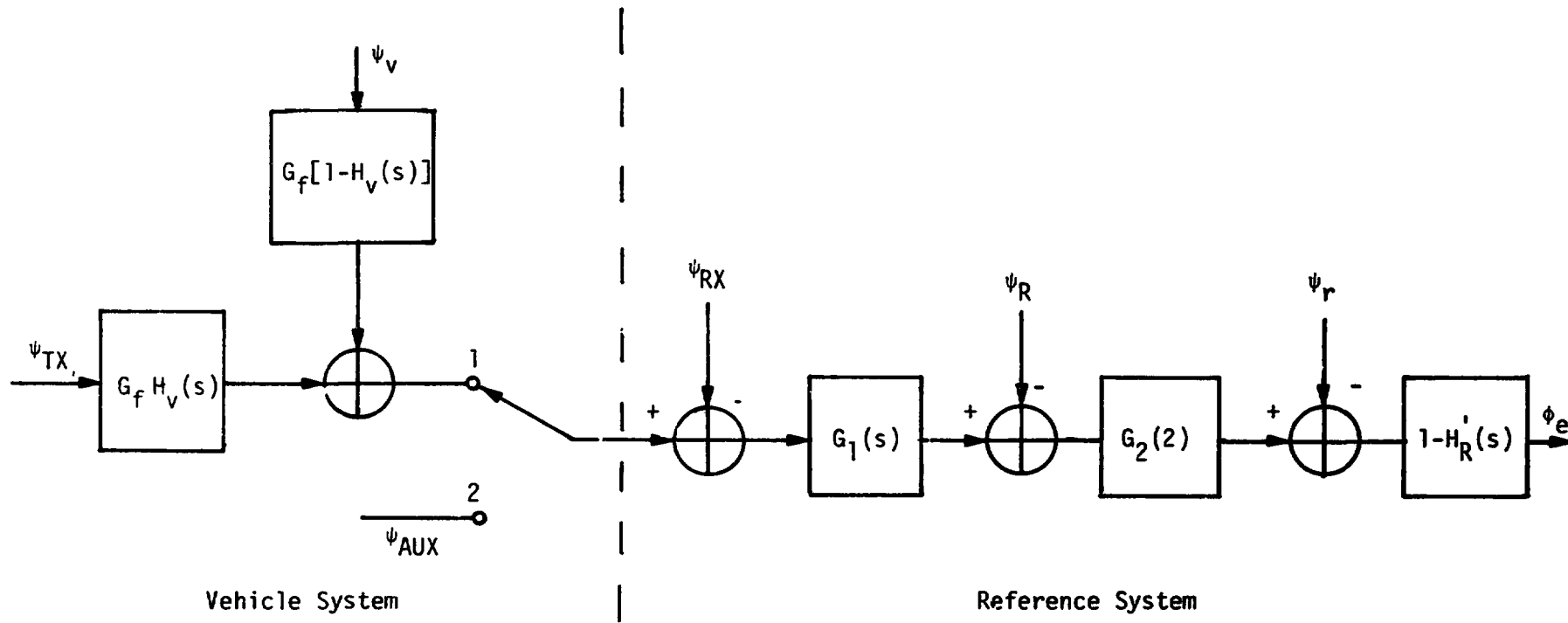


Figure 3. A Simple Block Diagram Representation of the System in Figure 1

$$G_1 = G_2(s) = \begin{cases} 1 & |\omega| \leq \omega_H \\ 0 & \text{elsewhere} \end{cases} \quad (3)$$

then, using the notation

$$\hat{\psi}(s) = G(s) \psi(s), \quad (4)$$

Equation (3) simplifies* to

$$\begin{aligned} \phi_e(s) &= G_f H_V(s) [1 - H_R(s)] \hat{\psi}_{TX}(s) \\ &+ G_f [1 - H_V(s)] [1 - H_R(s)] \hat{\psi}_V(s) \\ &- [1 - H_R(s)] [\hat{\psi}_{RX}(s) + \hat{\psi}_R(s) + \psi_r(s)] \end{aligned} \quad (5)$$

The corresponding mean-square phase noise is obtained from

$$\sigma_\phi^2 = \frac{1}{2\pi j} \int_{-j\infty}^{j\infty} \overline{\phi_e(s) \phi_e(-s)} ds \quad (6)$$

where the overbar denotes statistical expectation. Letting

$$S_\psi(s) \triangleq \overline{\psi(s) \psi(-s)} \quad (7)$$

denote the power spectral density (in Laplace transform notation) of the phase noise process ψ , then (6) is evaluated as

$$\begin{aligned} \sigma_\phi^2 &= \frac{1}{2\pi j} \int_{-j\infty}^{j\infty} G_f^2 H_V(s) H_V(-s) [1 - H_R(s)] [1 - H_R(-s)] S_{\hat{\psi}_{TX}}(s) ds \\ &+ \frac{1}{2\pi j} \int_{-j\infty}^{j\infty} G_f^2 [1 - H_V(s)] [1 - H_V(-s)] [1 - H_R(s)] [1 - H_R(-s)] S_{\hat{\psi}_V}(s) ds \\ &+ \frac{1}{2\pi j} \int_{-j\infty}^{j\infty} [1 - H_R(s)] [1 - H_R(-s)] [S_{\hat{\psi}_{RX}}(s) + S_{\hat{\psi}_R}(s) + S_{\psi_r}(s)] ds \end{aligned} \quad (8)$$

* We further assume that $1 - H_R'(s) \approx 1 - H_R(s)$, where $H_R(s) \triangleq \frac{K_R F_R(s)}{s + K_R F_R(s)}$; i.e., $G_2(s)$ is wideband with respect to $F_R(s)$.

or letting $s = j\omega$,

$$\begin{aligned} \sigma_\phi^2 &= \frac{1}{2\pi} \int_{-\infty}^{\infty} G_f^2 |H_V(j\omega)|^2 |1-H_R(j\omega)|^2 S_{\hat{\phi}_{TX}}(\omega) d\omega \\ &+ \frac{1}{2\pi} \int_{-\infty}^{\infty} G_f^2 |1-H_V(j\omega)|^2 |1-H_R(j\omega)|^2 S_{\hat{\phi}_V}(\omega) d\omega \\ &+ \frac{1}{2\pi} \int_{-\infty}^{\infty} |1-H_R(j\omega)|^2 \left[S_{\hat{\phi}_{RX}}(\omega) + S_{\hat{\phi}_R}(\omega) + S_{\phi_r}(\omega) \right] d\omega \end{aligned} \quad (9)$$

From (9), we observe that three different types of integrals occur; the first two involve two-way communication (i.e., two loops in cascade) and the third, one-way communication (i.e., a single loop). In the following section, we derive closed-form results for these terms when $S_\psi(\omega)$ is given by (1) and the loop transfer functions correspond to second-order loops with arbitrary loop dampings and natural frequencies.

3.0 CALCULATION OF MEAN-SQUARE PHASE NOISE FOR ONE-WAY COHERENT COMMUNICATION LINKS

A second-order carrier-tracking loop has the in-band transfer function [4]

$$H(s) = \frac{1 + \frac{\sqrt{r}}{\omega_n} s}{1 + \frac{\sqrt{r}}{\omega_n} s + \frac{1}{r} \left(\frac{\sqrt{r}}{\omega_n} \right)^2 s^2} \quad (10)$$

where $r = 4\zeta$ is the loop damping factor (ζ is the loop damping) and ω_n is the loop natural frequency in rad/s. The corresponding out-of-band transfer function is clearly

$$1 - H(s) = \frac{\frac{1}{r} \left(\frac{\sqrt{r}}{\omega_n} \right)^2 s^2}{1 + \frac{\sqrt{r}}{\omega_n} s + \frac{1}{r} \left(\frac{\sqrt{r}}{\omega_n} \right)^2 s^2} \quad (11)$$

Finally, the magnitude-squared versions of (10) and (11) are respectively given by

< 3

$$|H(j\omega)|^2 = \frac{\omega_n^2 (\omega_n^2 + r\omega^2)}{\omega^4 + \omega^2 [\omega_n^2 (r-2)] + \omega_n^4}$$

$$|1 - H(j\omega)|^2 = \frac{\omega^4}{\omega^4 + \omega^2 [\omega_n^2 (r-2)] + \omega_n^4} \quad (12)$$

Now consider the evaluation of

$$\sigma^2|_{1\text{-way}} = \frac{1}{2\pi} \int_{-\infty}^{\infty} |1 - H(j\omega)|^2 S_{\psi}(\omega) d\omega \quad (13)$$

where $|1 - H(j\omega)|^2$ is given by (12), $S_{\psi}(\omega)$ by (1), and

$$S_{\psi}(\omega) = \begin{cases} S_{\psi}(\omega) & ; \quad |\omega| \leq \omega_H \\ 0 & ; \quad \text{elsewhere} \end{cases} \quad (14)$$

Substituting (1) combined with (14) into (13) yields

$$\sigma^2|_{1\text{-way}} \triangleq \sum_{k=0}^3 \sigma_k^2|_{1\text{-way}} \quad (15)$$

where

$$\sigma_k^2|_{1\text{-way}} = \frac{1}{\pi} \int_0^{\omega_H} \frac{h_k}{\omega^k} |1 - H(j\omega)|^2 d\omega$$

$$= \frac{h_k}{\pi} \int_0^{\omega_H} \frac{\omega^{4-k}}{\omega^4 + \omega^2 [\omega_n^2 (r-2)] + \omega_n^4} d\omega \quad (16)$$

For simplicity of the resulting expressions and with little loss in accuracy, we shall, wherever possible, allow the upper limit of the integral in (16) to be infinity rather than ω_H . Clearly, this is possible (i.e., the integral converges) for $k = 2, 3$ and is justified by

the already assumed fact that $\omega_H \gg \omega_n$. We begin by evaluating (16) for these two values of k before going on to the more complicated cases corresponding to $k = 0, 1$.

Integrals of the form required in (16) can be found in both their definite and indefinite forms in a standard table of integrals [5]. With regard to [5], we shall herein adopt the notation [5, p.xxx, Eq.(yy)] to identify equation (yy) on page xxx of this reference.

a. (k=3)

From [5, p. 67, Eq. (2.161-2)],

$$\int \frac{x}{x^4 + ax^2 + b} dx = \begin{cases} \frac{1}{2h} \ln \left(\frac{x^2+f}{x^2+g} \right); & h^2 > 0 \\ \frac{1}{2q^2 \sin \alpha} \tan^{-1} \left(\frac{x^2 - q^2 \cos \alpha}{q^2 \sin \alpha} \right); & h^2 < 0 \end{cases} \quad (17)$$

where

$$\begin{aligned} h &= \sqrt{a^2 - 4b} ; & f &= \frac{a-h}{2} ; & g &= \frac{a+h}{2} \\ q &= b^{1/4} ; & \cos \alpha &= -\frac{a}{2\sqrt{b}} \end{aligned} \quad (18)$$

Letting

$$a = \omega_n^2(r-2) \triangleq \omega_n^2 R ; \quad b = \omega_n^4 \quad (19)$$

we have

$$\begin{aligned} h &= \omega_n^2 \sqrt{R^2 - 4} ; & f &= \frac{\omega_n^2}{2} \left[R - \sqrt{R^2 - 4} \right] ; & g &= \frac{\omega_n^2}{2} \left[R + \sqrt{R^2 - 4} \right] \\ q &= \omega_n ; & \cos \alpha &= -\frac{R}{2} , & \sin \alpha &= \frac{\sqrt{4-R^2}}{2} \end{aligned} \quad (20)$$

and

$$\int \frac{\omega}{\omega^4 + \omega^2 \left[\omega_n^2 (r-2) \right] + \omega_n^4} d\omega = \begin{cases} \frac{1}{2\omega_n^2 \sqrt{R^2-4}} \ln \left(\frac{\omega^2 + \frac{\omega_n^2}{2} \left[R - \sqrt{R^2-4} \right]}{\omega^2 + \frac{\omega_n^2}{2} \left[R + \sqrt{R^2-4} \right]} \right); & R > 2 \\ \frac{1}{\omega_n^2 \sqrt{4-R^2}} \tan^{-1} \left(\frac{2\omega^2 + \omega_n^2 R}{\omega_n^2 \sqrt{4-R^2}} \right); & R < 2 \end{cases} \quad (21)$$

Evaluating (21) between zero and infinity gives the definite integral

$$\int_0^\infty \frac{\omega}{\omega^4 + \omega^2 \left[\omega_n^2 (r-2) \right] + \omega_n^4} d\omega = \begin{cases} \frac{1}{2\omega_n^2 \sqrt{R^2-4}} \ln \left(\frac{R + \sqrt{R^2-4}}{R - \sqrt{R^2-4}} \right); & R > 2 \\ \frac{1}{\omega_n^2 \sqrt{4-R^2}} \left[\frac{\pi}{2} - \tan^{-1} \left(\frac{R}{\sqrt{4-R^2}} \right) \right]; & R < 2 \end{cases} \quad (22)$$

Finally, letting $\omega_H = \infty$ in (16), as previously agreed upon, we immediately have from (22)

$$\sigma_3^2 \Big|_{1\text{-way}} = \frac{h_3}{\pi} \begin{cases} \frac{1}{2\omega_n^2 \sqrt{R^2-4}} \ln \left(\frac{R + \sqrt{R^2-4}}{R - \sqrt{R^2-4}} \right); & R > 2 \\ \frac{1}{\omega_n^2 \sqrt{4-R^2}} \left[\frac{\pi}{2} - \tan^{-1} \left(\frac{R}{\sqrt{4-R^2}} \right) \right]; & R < 2 \end{cases} \quad (23)$$

b. (k=2)

From [5, p. 67, Eq. (2.161-3)],

$$\int \frac{x^2}{x^4+ax^2+b} dx = \frac{g}{h} \int \frac{dx}{x^2+g} - \frac{f}{h} \int \frac{dx}{x^2+f} ; \quad h^2 > 0 \quad (24)$$

where f , g , and h are defined as in (18). Since $b = \omega_n^4 > 0$ in our case, then $h < a$, and both f and g are positive. Hence

$$\int \frac{x^2}{x^4+ax^2+b} dx = \frac{1}{h} \left\{ \sqrt{g} \tan^{-1}\left(\frac{x}{\sqrt{g}}\right) - \sqrt{f} \tan^{-1}\left(\frac{x}{\sqrt{f}}\right) \right\} ; \quad h^2 > 0 \quad (25)$$

Since (24) results merely from factorization of the denominator of the integrand and a partial-fraction expansion, we can apply a similar factorization for $h^2 < 0$. To obtain a closed-form solution analogous to (25), we proceed as follows:

For $h^2 < 0$, let $h^2 = -h'^2$, or

$$h = jh' = j\sqrt{4b-a^2} \quad (26)$$

and

$$f = \frac{a-jh'}{2} ; \quad g = \frac{a+jh'}{2} \quad (27)$$

Expressing f and g in polar form,

$$f = |f|e^{-j\theta} ; \quad g = |g|e^{j\theta} \quad (28)$$

where

$$\begin{aligned} |f| &= |g| = \frac{1}{2} \sqrt{a^2+h'^2} = \frac{1}{2} \sqrt{a^2+4b-a^2} = \sqrt{b} = q^2 \\ \theta &= \tan^{-1}\left(\frac{h'}{a}\right) = \tan^{-1}\left(\frac{\sqrt{4b-a^2}}{a}\right) = \cos^{-1}\left(\frac{a}{2\sqrt{b}}\right) \\ &= \pi - \alpha \end{aligned} \quad (29)$$

then

$$\begin{aligned}
 x^4+ax^2+b &= (x^2+g)(x^2+f) \\
 &= (x+j\sqrt{|g|}e^{j\theta/2})(x-j\sqrt{|g|}e^{j\theta/2})(x-j\sqrt{|g|}e^{-j\theta/2})(x+j\sqrt{|g|}e^{-j\theta/2}) \\
 &= (x^2-2x\sqrt{|g|}\sin\frac{\theta}{2}+\sqrt{|g|})(x^2+2x\sqrt{|g|}\sin\frac{\theta}{2}+\sqrt{|g|}) \\
 &= (x^2-2xq^2\sin\frac{\theta}{2}+q^2)(x^2+2xq^2\sin\frac{\theta}{2}+q^2) \quad (30)
 \end{aligned}$$

Forming a partial-fraction expansion, namely,

$$\frac{x^2}{x^4+ax^2+b} = \frac{C_1x}{x^2-2xq\sin\frac{\theta}{2}+q^2} + \frac{C_2x}{x^2+2xq\sin\frac{\theta}{2}+q^2} \quad (31)$$

and solving for C_1 and C_2 yields

$$C_1 = -C_2 = \frac{1}{4q\sin\frac{\theta}{2}} \quad (32)$$

Thus,

$$\int \frac{x^2}{x^4+ax^2+b} dx = \frac{1}{4q\sin\frac{\theta}{2}} \left\{ \int \frac{x}{x^2-2xq\sin\frac{\theta}{2}+q^2} dx - \int \frac{x}{x^2+2xq\sin\frac{\theta}{2}+q^2} dx \right\} \quad (33)$$

$h^2 < 0$

The two integrals in (33) can be evaluated using [5, p. 68, Eq. (2.175-1)], namely,

$$\int \frac{xdx}{x^2+\beta x+\gamma} = \frac{1}{2} \ln(x^2+\beta x+\gamma) - \frac{\beta}{\sqrt{\Delta}} \tan^{-1} \left(\frac{\beta+2x}{\sqrt{\Delta}} \right); \quad \Delta > 0 \quad (34)$$

where

$$\begin{aligned} \Delta &= 4\gamma - \beta^2 = 4q^2 - (\pm 2q \sin \frac{\theta}{2})^2 \\ &= 4q^2 \cos^2 \frac{\theta}{2} > 0 \end{aligned} \quad (35)$$

Finally, combining (33) and (34) gives the desired result

$$\begin{aligned} \int \frac{x^2}{x^4 + ax^2 + b} dx &= \frac{1}{4q \sin \frac{\theta}{2}} \left\{ -\frac{1}{2} \ln \left(\frac{x^2 + 2xq \sin \frac{\theta}{2} + q^2}{x^2 - 2xq \sin \frac{\theta}{2} + q^2} \right) \right. \\ &\quad \left. + \tan \frac{\theta}{2} \left[\tan^{-1} \left(\frac{x - q \sin \frac{\theta}{2}}{q \cos \frac{\theta}{2}} \right) + \tan^{-1} \left(\frac{x + q \sin \frac{\theta}{2}}{q \cos \frac{\theta}{2}} \right) \right] \right\}; \\ &\quad h^2 < 0 \quad (36) \end{aligned}$$

or, since from (29)

$$\sin \frac{\theta}{2} = \cos \frac{\alpha}{2}; \quad \cos \frac{\theta}{2} = \sin \frac{\alpha}{2}; \quad \sin \theta = \sin \alpha \quad (37)$$

then

$$\begin{aligned} \int \frac{x^2}{x^4 + ax^2 + b} dx &= \frac{1}{4q \sin \alpha} \left\{ -\left[\sin \frac{\alpha}{2} \right] \ln \left(\frac{x^2 + 2xq \cos \frac{\alpha}{2} + q^2}{x^2 - 2xq \cos \frac{\alpha}{2} + q^2} \right) \right. \\ &\quad \left. + 2 \left[\cos \frac{\alpha}{2} \right] \left[\tan^{-1} \left(\frac{x - q \cos \frac{\alpha}{2}}{q \sin \frac{\alpha}{2}} \right) + \tan^{-1} \left(\frac{x + q \cos \frac{\alpha}{2}}{q \sin \frac{\alpha}{2}} \right) \right] \right\} \\ &\quad h^2 < 0 \quad (38) \end{aligned}$$

Applying (25) and (38) to the specific evaluations of a and b in (19) and f , g , h , and q of (20),

$$\int \frac{\omega^2}{\omega^4 + \omega^2 [\omega_n^2 (r-2)] + \omega_n^4} d\omega = \frac{1}{\omega_n \sqrt{R^2 - 4}} \times \left\{ \sqrt{R^+} \tan^{-1} \left(\frac{\omega}{\omega_n \sqrt{R^+}} \right) - \sqrt{R^-} \tan^{-1} \left(\frac{\omega}{\omega_n \sqrt{R^-}} \right) \right\};$$

$R > 2$ (39a)

and

$$\int \frac{\omega^2}{\omega^4 + \omega^2 [\omega_n^2 (r-2)] + \omega_n^4} d\omega = \frac{1}{4\omega_n \sqrt{4-R^2}} \times \left\{ -\sqrt{2+R} \ln \left(\frac{1 + \left(\frac{\omega}{\omega_n}\right) \sqrt{2+R} + \left(\frac{\omega}{\omega_n}\right)^2}{1 - \left(\frac{\omega}{\omega_n}\right) \sqrt{2+R} + \left(\frac{\omega}{\omega_n}\right)^2} \right) + 2\sqrt{2-R} \left[\tan^{-1} \left(\frac{2\left(\frac{\omega}{\omega_n}\right) - \sqrt{2+R}}{\sqrt{2-R}} \right) + \tan^{-1} \left(\frac{2\left(\frac{\omega}{\omega_n}\right) + \sqrt{2+R}}{\sqrt{2-R}} \right) \right] \right\};$$

$R < 2$ (39b)

where

$$R^+ \triangleq \frac{1}{2} \left[R + \sqrt{R^2 - 4} \right]$$

and

$$R^- \triangleq \frac{1}{2} \left[R - \sqrt{R^2 - 4} \right] \quad (40)$$

The corresponding definite integrals with limits of zero and infinity are identical and are simply given by

$$\int_0^{\infty} \frac{\omega}{\omega^4 + \omega^2 [\omega_n^2 (r-2)] + \omega_n^4} d\omega = \frac{\pi}{2\sqrt{R+2} \omega_n} ; \text{ all } R \quad (41)$$

Finally, substituting (41) into (16) gives the desired result

$$\sigma_2^2 \Big|_{1\text{-way}} = \frac{h_2}{2 \sqrt{R+2} \omega_n} ; \text{ all } R \quad (42)$$

c. (k=1)

The indefinite integral

$$\int \frac{x^3}{x^4 + ax^2 + b} dx$$

is not tabulated in [5] but can be obtained as follows. First note that

$$\int \frac{4x^3 + 2ax}{x^4 + ax^2 + b} dx = \ln(x^4 + ax^2 + b) . \quad (43)$$

Then, since the desired integral can be expressed in the form

$$\int \frac{x^3}{x^4 + ax^2 + b} dx = \frac{1}{4} \int \frac{4x^3 + 2ax}{x^4 + ax^2 + b} dx - \frac{a}{2} \int \frac{x}{x^4 + ax^2 + b} dx \quad (44)$$

and since the latter integral is given by (17), we immediately obtain

$$\int \frac{x^3}{x^4 + ax^2 + b} dx = \frac{1}{4} \ln(x^4 + ax^2 + b) - \frac{a}{2} \begin{cases} \frac{1}{2h} \ln \left(\frac{x^2 + f}{x^2 + g} \right); & h^2 > 0 \\ \frac{1}{2q^2 \sin \alpha} \tan^{-1} \left(\frac{x^2 - q^2 \cos \alpha}{q^2 \sin \alpha} \right); & h^2 < 0 \end{cases} \quad (45)$$

Applying (45) to the case of interest gives

$$\int \frac{\omega^3}{\omega^4 + \omega^2 [\omega_n^2 (r-2)] + \omega_n^4} d\omega = \frac{1}{4} \ln \left[1 + \left(\frac{\omega}{\omega_n} \right)^2 R + \left(\frac{\omega}{\omega_n} \right)^4 \right] \\ - \begin{cases} \frac{R}{4\sqrt{R^2-4}} \ln \left(\frac{2\left(\frac{\omega}{\omega_n}\right)^2 + R^-}{2\left(\frac{\omega}{\omega_n}\right)^2 + R^+} \right); & R > 2 \\ \frac{R}{2\sqrt{4-R^2}} \tan^{-1} \left(\frac{2\left(\frac{\omega}{\omega_n}\right)^2 + R}{\sqrt{4-R^2}} \right); & R < 2 \end{cases} \quad (46)$$

where, as before, R^+ and R^- are defined in (40). Finally, integrating (46) between 0 and ω_H [note the upper limit cannot be infinity since the first term of (46) would become unbounded] and introducing the notation

$$\gamma_H \triangleq \frac{\omega_H}{\omega_n} \quad (47)$$

we obtain the desired result from (16), namely,

$$\sigma_i^2 \Big|_{1\text{-way}} = \frac{h_1}{4\pi} \left[\ln(1 + \gamma_H^2 R + \gamma_H^4) \right. \\ - \begin{cases} \frac{R}{\sqrt{R^2-4}} \left[\ln \left(\frac{2\gamma_H^2 + R^-}{2\gamma_H^2 + R^+} \right) - \ln \left(\frac{R^-}{R^+} \right) \right]; & R > 2 \\ \frac{2R}{\sqrt{4-R^2}} \left[\tan^{-1} \left(\frac{2\gamma_H^2 + R}{\sqrt{4-R^2}} \right) - \tan^{-1} \left(\frac{R}{\sqrt{4-R^2}} \right) \right]; & R < 2 \end{cases} \quad (48)$$

d. (k=0)

Noting that

$$\frac{x^4}{x^4 + ax^2 + b} = 1 - \frac{ax^2 + b}{x^4 + ax^2 + b} \quad (49)$$

then

$$\int \frac{x^4}{x^4 + ax^2 + b} dx = x - \int \frac{ax^2 + b}{x^4 + ax^2 + b} dx \quad (50)$$

The second integral in (50) can be obtained from a generalization of (25) and (38). In particular, multiplying (25) by A and using [5, p. 67, Eq. (2.161-1)], we get

$$\int \frac{Ax^2 + B}{x^4 + ax^2 + b} dx = \frac{1}{h} \left[\frac{(Ag-B)}{\sqrt{g}} \tan^{-1} \left(\frac{x}{\sqrt{g}} \right) + \frac{(B-fA)}{\sqrt{f}} \tan^{-1} \left(\frac{x}{\sqrt{f}} \right) \right]; h^2 < 0 \quad (51)$$

Similarly, following the procedure which produced (38), we get

$$\begin{aligned} \int \frac{Ax^2 + B}{x^4 + ax^2 + b} dx &= \frac{B}{4q^3 \sin \alpha} \\ &\times \left\{ \left(1 - \frac{Aq^2}{B} \right) \left(\sin \frac{\alpha}{2} \right) \ln \left(\frac{x^2 + 2xq \cos \frac{\alpha}{2} + q^2}{x^2 - 2xq \cos \frac{\alpha}{2} + q^2} \right) \right. \\ &\quad \left. + 2 \left(1 + \frac{Aq^2}{B} \right) \left(\cos \frac{\alpha}{2} \right) \left[\tan^{-1} \left(\frac{x - q \cos \frac{\alpha}{2}}{q \sin \frac{\alpha}{2}} \right) \right. \right. \\ &\quad \left. \left. + \tan^{-1} \left(\frac{x + q \cos \frac{\alpha}{2}}{q \sin \frac{\alpha}{2}} \right) \right] \right\}; h^2 > 0 \quad (52) \end{aligned}$$

Letting $A = a$ and $B = b$ and substituting (51) or (52) into (50) gives the desired result.

Since, to evaluate $\sigma_0^2 \Big|_{1\text{-way}}$, we need the definite integral version of (5) with limits 0 and ω_H , letting a and b be as defined in (19), we get, after some simplification

$$\int_0^{\omega_H} \frac{\omega^2 [\omega_n^2 (r-2)] + \omega_n^4}{\omega^4 + \omega^2 [\omega_n^2 (r-2)] + \omega_n^4} d\omega = \frac{\omega_n}{\sqrt{R^2-4}} \left[\frac{RR^+ - 1}{\sqrt{R^+}} \tan^{-1} \left(\frac{\gamma_H}{\sqrt{R^+}} \right) + \frac{1 - RR^-}{\sqrt{R^-}} \tan^{-1} \left(\frac{\gamma_H}{\sqrt{R^-}} \right) \right];$$

$R > 2$ (53a)

and

$$\int_0^{\omega_H} \frac{\omega^2 [\omega_n^2 (r-2)] + \omega_n^4}{\omega^4 + \omega^2 [\omega_n^2 (r-2)] + \omega_n^4} d\omega = \frac{\omega_n}{4} \left\{ \frac{1-R}{\sqrt{2-R}} \ln \left(\frac{1 + \gamma_H \sqrt{2-R} + \gamma_H^2}{1 - \gamma_H \sqrt{2-R} + \gamma_H^2} \right) + \frac{2(1+R)}{\sqrt{2+R}} \right.$$

$$\left. \times \left[\tan^{-1} \left(\frac{2\gamma_H - \sqrt{2+R}}{\sqrt{2+R}} \right) + \tan^{-1} \left(\frac{2\gamma_H - \sqrt{2-R}}{\sqrt{2+R}} \right) \right] \right\};$$

$R < 2$ (53b)

Finally combining (50) and (52) with (16) and recognizing the further simplifications

$$\frac{RR^+ - 1}{\sqrt{R^+}} = (R^+)^{3/2}$$

and

$$\frac{1 - RR^-}{\sqrt{R^-}} = - (R^-)^{3/2} \quad (54)$$

gives the desired result

$$\boxed{\sigma_0^2 \Big|_{1\text{-way}} = \frac{h_0 \omega_n}{\pi} \left[\gamma_H - g(R, \gamma_H) \right]} \quad (55)$$

where

$$g(R, \gamma_H) = \begin{cases} \frac{1}{\sqrt{R^2-4}} \left[(R^+)^{3/2} \tan^{-1} \left(\frac{\gamma_H}{\sqrt{R^+}} \right) - (R^-)^{3/2} \tan^{-1} \left(\frac{\gamma_H}{\sqrt{R^-}} \right) \right]; & R > 2 \\ \frac{1}{4} \left\{ \frac{1-R}{\sqrt{2-R}} \ln \left(\frac{1 + \gamma_H \sqrt{2-R} + \gamma_H^2}{1 - \gamma_H \sqrt{2-R} + \gamma_H^2} \right) \right. \\ \left. + \frac{2(1+R)}{\sqrt{2+R}} \left[\tan^{-1} \left(\frac{2\gamma_H - \sqrt{2-R}}{\sqrt{2+R}} \right) + \tan^{-1} \left(\frac{2\gamma_H + \sqrt{2-R}}{\sqrt{2+R}} \right) \right] \right\}; & R < 2 \end{cases} \quad (56)$$

When the loop has $\zeta = 0.707$ damping (i.e., $r = 2$ or $R = r-2 = 0$), then (23), (42), (48) and (55) simplify immensely. In particular,

$$\begin{aligned} \sigma_3^2 \Big|_{1\text{-way}} &= \frac{h_3}{4\omega_n^2} \\ \sigma_2^2 \Big|_{1\text{-way}} &= \frac{h_2}{2\sqrt{2}\omega_n} \\ \sigma_1^2 \Big|_{1\text{-way}} &= \frac{h_1}{4\pi} \ln(1 + \gamma_H^4) \\ \sigma_0^2 \Big|_{1\text{-way}} &= \frac{h_0 \omega_n}{\pi} \left\{ \gamma_H - \frac{1}{4\sqrt{2}} \ln \left(\frac{1 + \gamma_H \sqrt{2} + \gamma_H^2}{1 - \gamma_H \sqrt{2} + \gamma_H^2} \right) \right. \\ &\quad \left. - \frac{1}{2\sqrt{2}} \left[\tan^{-1}(\gamma_H \sqrt{2} - 1) + \tan^{-1}(\gamma_H \sqrt{2} + 1) \right] \right\} \quad (57) \end{aligned}$$

The first three relations in (57) agree with similar results* obtained in [2].

4.0 CALCULATION OF MEAN-SQUARE PHASE NOISE FOR TWO-WAY COHERENT COMMUNICATION LINKS

Here we consider the evaluation of mean-square phase noise components whose forms resemble the first two terms of (9). Subsection 4.1 of this section treats the evaluation of the first of these two components (i.e., the in-band phase noise in the vehicle system) while subsection 4.2 considers the second term corresponding to the out-of-band vehicle system phase noise.

For simplicity of notation, we shall use the integers 1 and 2 to replace, respectively, the subscripts V and R previously used to denote vehicle and reference systems. Furthermore, it is noted that the vehicle and reference system second-order carrier-tracking loops have in-band and out-of-band transfer functions of the form given by (10) and (11), with arbitrary damping factors r_1 , r_2 and radian natural frequencies ω_{n1} , ω_{n2} .

4.1 In-Band Mean-Square Phase Noise

Consider the evaluation of

$$\sigma_I^2 \Big|_{2\text{-way}} = \frac{1}{2\pi} \int_{-\infty}^{\infty} |H_1(j\omega)|^2 |1 - H_2(j\omega)|^2 S_{\hat{\psi}}(\omega) d\omega \quad (58)$$

where $|H_1(j\omega)|^2$ and $|1 - H_2(j\omega)|^2$ are both given by (12) with the appropriate subscript appendages and $S_{\hat{\psi}}(\omega)$ is defined as before in (14). Substituting (14) combined with (1) into (58) yields

$$\sigma_I^2 \Big|_{2\text{-way}} \triangleq \sum_{k=0}^3 \sigma_{Ik}^2 \Big|_{2\text{-way}} \quad (59)$$

where

* Eq. (11) of [2] (which includes many typographical errors) essentially expresses the sum of the first three results of (57).

$$\begin{aligned}
\sigma_{Ik}^2 \Big|_{2\text{-way}} &= \frac{1}{\pi} \int_0^{\omega_H} \frac{h_k}{\omega^k} |H_1(j\omega)|^2 |1 - H_2(j\omega)|^2 d\omega \\
&= \frac{h_k}{\pi} \int_0^{\omega_H} \left[\frac{\omega_{n1}^2 (\omega_{n1}^2 + r_1 \omega^2)}{\omega^{4+\omega^2} [\omega_{n1}^2 (r_1 - 2)] + \omega_{n1}^4} \right] \left[\frac{\omega^{4-k}}{\omega^{4+\omega^2} [\omega_{n2}^2 (r_2 - 2)] + \omega_{n2}^4} \right] d\omega
\end{aligned} \tag{60}$$

As before, for simplicity of the resulting expressions, we shall allow the upper limit of (60) to be infinity whenever such an integral is bounded. Here again, the justification is based on the fact that $\omega_H \gg \omega_{n1}, \omega_{n2}$.

a. (k=3)

To evaluate $\sigma_{I3}^2 \Big|_{2\text{-way}}$, it is clear from (60) that we must first consider the evaluation of an integral of the form

$$\int \frac{Cx^3 + Dx}{(x^4 + a_1x^2 + b_1)(x^4 + a_2x^2 + b_2)} dx$$

The procedure employed is to expand the integrand into its partial fractions, namely,

$$\frac{Cx^3 + Dx}{(x^4 + a_1x^2 + b_1)(x^4 + a_2x^2 + b_2)} = \frac{A_1x^3 + B_1x}{x^4 + a_1x^2 + b_1} + \frac{A_2x^3 + B_2x}{x^4 + a_2x^2 + b_2} \tag{61}$$

where

$$A_1 = -A_2 = \frac{C(b_2 - b_1) - D(a_2 - a_1)}{\Delta}$$

and

$$B_1 = \frac{D}{b_2} - \frac{b_1 B_2}{b_2} = \frac{Cb_1(a_2 - a_1) + D[b_2 - b_1 - a_1(a_2 - a_1)]}{\Delta} \tag{62}$$

with

$$\Delta \stackrel{\Delta}{=} (b_2 - b_1)^2 + (a_2 - a_1)(a_2 b_1 - a_1 b_2) \quad (63)$$

Then using (17) and (45), we obtain the desired result, which is

$$\begin{aligned} \int \frac{Cx^3 + Dx}{(x^4 + a_1 x^2 + b_1)(x^4 + a_2 x^2 + b_2)} dx &= \frac{A_1}{4} \ln \left(\frac{x^4 + a_1 x^2 + b_1}{x^4 + a_2 x^2 + b_2} \right) \\ &+ \left[B_1 - \frac{a_1 A_1}{2} \right] f(x; h_1^2) \\ &+ \left[\frac{D}{b_1} - \frac{b_2 B_1}{b_1} + \frac{a_2 A_1}{2} \right] f(x; h_2^2), \quad (64) \end{aligned}$$

where

$$f(x; h_i^2) = \begin{cases} \frac{1}{2h_i} \ln \left(\frac{x^2 + f_i}{x^2 + g_i} \right); & h_i^2 > 0 \\ \frac{1}{\sqrt{-h_i^2}} \tan^{-1} \left(\frac{2x^2 + a_i}{\sqrt{-h_i^2}} \right); & h_i^2 < 0 \end{cases} \quad i = 1, 2 \quad (65)$$

The parameters f_i , g_i and h_i are related to a_i and b_i as in (18).

Applying (64) to the evaluation of σ_{I3}^2 |2-way, we first relate a_i , b_i , C , and D to the loop damping and natural frequency parameters, namely,

$$\begin{aligned} a_i &= \omega_{ni}^2 (r_i - 2) \stackrel{\Delta}{=} \omega_{ni}^2 R_i; \quad b_i = \omega_{ni}^4; \quad i = 1, 2 \\ C &= \omega_{n1}^2 r_1 = \omega_{n1}^2 (R_1 + 2); \quad D = \omega_{n1}^4 = b_1 \quad (66) \end{aligned}$$

Finally, then, combining (61-66) and substituting into (60)* with $k = 3$, we obtain, after much simplification,

$$\sigma_{I3}^2 \Big|_{2\text{-way}} = \frac{h_3}{\pi \omega_{n1}} \left\{ -\frac{A_{13}}{4} \ln \gamma^4 + A_{23} f(R_1) - A_{33} f(R_2) \right\} \quad (67)$$

where we have introduced the parameter γ to characterize the ratio of loop natural frequencies, i.e.,

$$\gamma \triangleq \frac{\omega_{n1}}{\omega_{n2}} \quad (68)$$

and

$$f(R) \triangleq \begin{cases} \frac{1}{\sqrt{4-R^2}} \left[\frac{\pi}{2} - \tan^{-1} \left(\frac{R}{\sqrt{4-R^2}} \right) \right]; & R < 2 \\ \frac{1}{2\sqrt{R^2-4}} \ln \left(\frac{R+\sqrt{R^2-4}}{R-\sqrt{R^2-4}} \right); & R > 2 \end{cases} \quad (69)$$

with weighting coefficients

$$A_{13} = \frac{\gamma^4 \left[(1-\gamma^4)(R_1+2) - \gamma^2(R_2 - \gamma^2 R_1) \right]}{\Delta_0},$$

$$A_{23} = \frac{\gamma^4 \left[(1-\gamma^4) \left[1 - \frac{R_1(R_1+2)}{2} \right] + \gamma^2(R_2 - \gamma^2 R_1) \left(2 + \frac{R_1}{2} \right) \right]}{\Delta_0},$$

$$A_{33} = \frac{\gamma^4 \left[(1-\gamma^4) \left[\gamma^2 - \frac{R_2(R_1+2)}{2} \right] + (R_2 - \gamma^2 R_1) \left(R_1+2 - \frac{\gamma^2 R_2}{2} \right) \right]}{\Delta_0}$$

and

*An infinite upper limit is used here.

$$\Delta_0 \triangleq \frac{\Delta}{\omega_{n2}^8} = (1 - \gamma^4)^2 + \gamma^2(R_2 - \gamma^2 R_1) (\gamma^2 R_2 - R_1) \quad (70)$$

b. (k=2)

To evaluate $\sigma_{I2}^2 \Big|_{2\text{-way}}$, we again begin by considering the generic form of the integrand and expanding it into its partial fractions, i.e.,

$$\frac{Cx^4 + Dx^2}{(x^4 + a_1x^2 + b_1)(x^4 + a_2x^2 + b_2)} = \frac{A_1x^2 + B_1}{x^4 + a_1x^2 + b_1} + \frac{A_2x^2 + B_2}{x^4 + a_2x^2 + b_2} \quad (71)$$

where now

$$\begin{aligned} A_1 &= -A_2 = \frac{D(b_2 - b_1) + C(a_2b_1 - a_1b_2)}{\Delta} \\ B_1 &= -\left(\frac{b_1}{b_2}\right) B_2 = \frac{b_1 [D(a_2 - a_1) - C(b_2 - b_1)]}{\Delta} \end{aligned} \quad (72)$$

and Δ is still as in (63). Using (51) and (52) to integrate the two terms on the right side of (71), we immediately get the desired result, namely,

$$\int \frac{Cx^4 + Dx^2}{(x^4 + a_1x^2 + b_1)(x^4 + a_2x^2 + b_2)} dx = f(x; A_1, B_1) + f(x; A_2, B_2)$$

where

$$f(x; A_i, B_i) = \begin{cases} \frac{1}{h_i} \left[\frac{(A_i g_i - B_i)}{\sqrt{g_i}} \tan^{-1} \left(\frac{x}{\sqrt{g_i}} \right) + \frac{(B_i - f_i A_i)}{\sqrt{f_i}} \tan^{-1} \left(\frac{x}{\sqrt{f_i}} \right) \right]; h_i^2 > 0 \\ \frac{B_i}{4q_i^3 \sin \alpha_i} \left\{ \left[1 - \frac{A_i q_i^2}{B_i} \right] \left(\sin \frac{\alpha_i}{2} \right) \ln \left(\frac{x^2 + 2xq_i \sin \frac{\alpha_i}{2} + q_i^2}{x^2 - 2xq_i \sin \frac{\alpha_i}{2} + q_i^2} \right) \right. \\ \quad \left. + 2 \left[1 + \frac{A_i q_i^2}{B_i} \right] \left(\cos \frac{\alpha_i}{2} \right) \right. \\ \quad \left. \times \left[\tan^{-1} \left(\frac{x - q_i \cos \frac{\alpha_i}{2}}{q_i \sin \frac{\alpha_i}{2}} \right) + \tan^{-1} \left(\frac{x + q_i \cos \frac{\alpha_i}{2}}{q_i \sin \frac{\alpha_i}{2}} \right) \right] \right\}; h_i^2 < 0 \end{cases} \quad (73)$$

When (73) is evaluated between zero and infinity and the appropriate substitutions are made for f_i , g_i , h_i , q_i , and α_i in terms of r_i and ω_{ni} ; $i = 1,2$, we get the much simplified result

$$\int_0^{\infty} \frac{Cx^4 + Dx^2}{(x^4 + a_1x^2 + b_1)(x^4 + a_2x^2 + b_2)} dx = \frac{\pi}{2} \left\{ \frac{1}{\sqrt{R_1+2}} \left(\frac{B_1 + \omega_{n1}^2 A_1}{\omega_{n1}^3} \right) + \frac{1}{\sqrt{R_2+2}} \left(\frac{B_2 + \omega_{n2}^2 A_2}{\omega_{n2}^3} \right) \right\};$$

all R_1, R_2 (74)

Finally, substituting (72) into (74) and relating C and D to the appropriate parameters in the integrand of $\sigma_{I2}^2|_{2\text{-way}}$, e.g., (66), we obtain, after much simplification,

$$\sigma_{I2}^2|_{2\text{-way}} = \frac{h_2}{2\omega_{n1}} \left[\frac{1}{\sqrt{R_1+2}} A_{12} + \frac{1}{\sqrt{R_2+2}} A_{22} \right] \quad (75)$$

where

$$A_{12} = - \frac{\gamma^4 \left\{ (1 - \gamma^4)(1 + R_1) - \gamma^2(3 + R_1)R_2 + (\gamma^4 + 2 + R_1)R_1 \right\}}{\Delta_0}$$

$$A_{22} = \frac{\gamma^3 \left\{ (1 - \gamma^4)(R_1 + 2 - \gamma^2) - \gamma^2 \left[1 + \gamma^2(R_1 + 2) \right] R_2 + \gamma^2(\gamma^2 + R_1 + 2)R_1 \right\}}{\Delta_0} \quad (76)$$

and Δ_0 is still given by (70).

c. ($k=1$)

For $k = 1$, we must consider the integral

$$\int \frac{Cx^5 + Dx^3}{(x^4 + a_1x^2 + b_1)(x^4 + a_2x^2 + b_2)} dx$$

whose integrand has the same partial-fraction expansion as in (61), namely,

$$\frac{Cx^5 + Dx^3}{(x^4 + a_1x^2 + b_1)(x^4 + a_2x^2 + b_2)} = \frac{A_1x^3 + B_1x}{x^4 + a_1x^2 + b_1} + \frac{A_2x^3 + B_2x}{x^4 + a_2x^2 + b_2} \quad (77)$$

except that now A_1 , B_1 , A_2 , and B_2 are given by

$$\begin{aligned} A_1 = -A_2 &= \frac{D(b_2 - b_1) + C(a_2b_1 - a_1b_2)}{\Delta} \\ B &= -\left(\frac{b_1}{b_2}\right)B_2 = \frac{b_1 \left[D(a_2 - a_1) - C(b_2 - b_1) \right]}{\Delta} \end{aligned} \quad (78)$$

with Δ as in (63). Since the right-hand sides of (64) and (65) are now also equal to the above integral, then using (66), evaluation of (60) with an infinite upper limit and $k = 1$ yields, upon simplification,

$$\boxed{\sigma_{11}^2 \Big|_{2\text{-way}} = \frac{h_1}{\pi} \left\{ -\frac{A_{11}}{4} \ln \gamma^4 + A_{21} f(R_1) - A_{31} f(R_2) \right\}} \quad (79)$$

where

$$A_{11} = \frac{\gamma^4 \left[1 - \gamma^4 + (R_1 + 2)(R_2\gamma^2 - R_1) \right]}{\Delta_0},$$

$$A_{21} = \frac{\gamma^4 \left[- (1 - \gamma^4) \left(\frac{3R_1}{2} + 2 \right) + \gamma^2 (R_2 - \gamma^2 R_1) - \frac{R_1 (R_1 + 2)}{2} (\gamma^2 R_2 - R_1) \right]}{\Delta_0},$$

and

$$A_{31} = \frac{\gamma^2 \left[- (1 - \gamma^4) \left(R_1 + 2 + \frac{\gamma^2 R_2}{2} \right) + \gamma^2 (R_2 - \gamma^2 R_1) - \frac{\gamma^2 R_2 (R_1 + 2)}{2} (\gamma^2 R_2 - R_1) \right]}{\Delta_0} \quad (80)$$

d. ($k=0$)

For $k = 0$, we must consider the integral

$$\int \frac{Cx^6 + Dx^4}{(x^4 + a_1x^2 + b_1)(x^4 + a_2x^2 + b_2)} dx$$

whose integrand has the same partial-fraction expansion as in (71), namely

$$\frac{Cx^6 + Dx^4}{(x^4 + a_1x^2 + b_1)(x^4 + a_2x^2 + b_2)} = \frac{A_1x^2 + B_1}{x^4 + a_1x^2 + b_1} + \frac{A_2x^2 + B_2}{x^4 + a_2x^2 + b_2} \quad (81)$$

where, now,

$$A_1 = C - A_2 = \frac{-C \left[b_1(b_2 - b_1) + a_1(a_2b_1 - a_1b_2) \right] + D(a_2b_1 - a_1b_2)}{\Delta}$$

$$B_1 = -\left(\frac{b_1}{b_2}\right)B_2 = -\frac{b_1 \left[C(a_2b_1 - a_1b_2) + D(b_2 - b_1) \right]}{\Delta} \quad (82)$$

Since the right-hand side of (74) also applies to the above integral, then, using (66), evaluation of (60) with an infinite upper limit and $k = 0$ yields, upon simplification,

$$\sigma_{I0}^2 \Big|_{2\text{-way}} = \frac{h_0 \omega_{n1}}{2} \left[\frac{A_{10}}{\sqrt{R_1+2}} + \frac{A_{20}}{\sqrt{R_2+2}} \right] \quad (83)$$

where

$$A_{10} = - \frac{\gamma^4 \left\{ (1-\gamma^4)(3+R_1) + (\gamma^2 R_2 - R_1) \left[(R_1+2)(R_1+1) - 1 \right] \right\}}{\Delta_0}$$

$$A_{20} = \frac{\gamma \left\{ (1-\gamma^4)(\gamma^2 + R_1 + 2) + \gamma^2 (\gamma^2 R_2 - R_1) \left[(R_1+2)(R_2+1) - \gamma^2 \right] \right\}}{\Delta_0} \quad (84)$$

Analogous to what was true for the one-way case, the two-way mean-square phase noise expressions for (67), (75), (79) and (83) simplify immensely when $r_1 = r_2 = 2$, i.e., both loops have 0.707 damping. Thus, letting $R_1 = R_2 = 0$ in (67), (75), (79), and (83) yields

$$\sigma_{I3}^2 \Big|_{2\text{-way}} = \frac{h_3 \gamma^4}{4\omega_{n1}^2 (1-\gamma^4)} \left\{ 1 - \gamma^2 - \frac{2}{\pi} \ln \gamma^4 \right\}$$

$$\sigma_{I2}^2 \Big|_{2\text{-way}} = \frac{h_2 \gamma^3 (1-\gamma)(2+\gamma)}{2\sqrt{2} \omega_{n1} (1-\gamma^4)}$$

$$\sigma_{I1}^2 \Big|_{2\text{-way}} = \frac{h_1 \gamma^2}{4(1-\gamma^4)} \left[2(1-\gamma^2) - \frac{\gamma^2}{\pi} \ln \gamma^4 \right]$$

$$\sigma_{I0}^2 \Big|_{2\text{-way}} = \frac{h_0 \gamma \omega_{n1}}{2\sqrt{2} (1-\gamma^4)} \left[2 + \gamma^2 - 3\gamma^3 \right] \quad (85)$$

A simple check on the result in (83) can be had by realizing that this calculation was performed in [3, Chap. 3]. In particular,

$$\sigma_{10}^2 \Big|_{2\text{-way}} = h_0 W_{L1} K_R(r_1, r_2, \xi) \quad (86)$$

where W_{Li} ; $i = 1, 2$ denotes the two-sided loop bandwidth and $K_R(r_1, r_2, \xi)$ is defined in [3, Eq. (3-18)] with

$$\xi \triangleq \frac{W_{L1}(r_2+1)}{W_{L2}(r_1+1)} = \frac{W_{L1}(3+R_2)}{W_{L2}(3+R_1)} \quad (87)$$

Since loop bandwidth and natural frequency are related by

$$W_{Li} = \frac{\omega_{ni}(1+r_i)}{2\sqrt{r_i}} = \frac{\omega_{ni}(3+R_i)}{2\sqrt{2+R_i}} \quad ; \quad i = 1, 2 \quad (88)$$

then using (88), we can rewrite (87) as

$$\xi = \gamma \sqrt{\frac{R_2+2}{R_1+2}} \quad (89)$$

Finally, equating (86) and (83) gives

$$K_R\left(R_1+2, R_2+2, \gamma \sqrt{\frac{R_2+2}{R_1+2}}\right) = \frac{A_{10} + \sqrt{\frac{R_1+2}{R_2+2}} A_{20}}{3+R_1} \quad (90)$$

Substituting (84) into the right-hand side of (90) and executing some routine algebra results in [3, Eq. (3-18)], thus proving the result in (90).

4.2 Out-Of-Band Mean-Square Phase Noise

In this section, we consider the evaluation of

$$\sigma_Q^2 \Big|_{2\text{-way}} = \frac{1}{2\pi} \int_{-\infty}^{\infty} |1 - H_1(j\omega)|^2 |1 - H_2(j\omega)|^2 S_{\hat{\psi}}(\omega) d\omega \quad (91)$$

where once again $|1 - H_i(j\omega)|^2$; $i = 1, 2$ are both given by (12), with the appropriate subscript appendages and $S_{\hat{\psi}}(\omega)$ is defined by (14). Substituting (14) combined with (1) in (91) yields

$$\sigma_Q^2 \Big|_{2\text{-way}} = \sum_{k=0}^3 \sigma_{Qk}^2 \Big|_{2\text{-way}} \quad (92)$$

where

$$\begin{aligned} \sigma_{Qk}^2 \Big|_{2\text{-way}} &= \frac{1}{\pi} \int_0^{\omega_H} \frac{h_k}{\omega^k} |1 - H_1(j\omega)|^2 |1 - H_2(j\omega)|^2 d\omega \\ &= \frac{h_k}{\pi} \int_0^{\omega_H} \frac{\omega^{8-k}}{\left[\omega^4 + \omega^2 \left[\omega_{n1}^2 (r_1 - 2) \right] + \omega_{n1}^4 \right] \left[\omega^4 + \omega^2 \left[\omega_{n2}^2 (r_2 - 2) \right] + \omega_{n2}^4 \right]} d\omega \end{aligned} \quad (93)$$

a. (k=3)

The integrand required to evaluate $\sigma_{Q3}^2 \Big|_{2\text{-way}}$ has the same partial-fraction expansion as (61), namely,

$$\frac{x^5}{(x^4 + a_1 x^2 + b_1)(x^4 + a_2 x^2 + b_2)} = \frac{A_1 x^3 + B_1 x}{x^4 + a_1 x^2 + b_1} + \frac{A_2 x^3 + B_2 x}{x^4 + a_2 x^2 + b_2} \quad (94)$$

with now

$$A_1 = -A_2 = \frac{a_2 b_1 - a_1 b_2}{\Delta} \quad ; \quad B_1 = -\left(\frac{b_1}{b_2}\right) B_2 = \frac{-b_1 (b_2 - b_1)}{\Delta} \quad (95)$$

Thus, letting $D = 0$ in (64), we can apply the right-hand side of this result to (94) which, when combined with (95) and (66), gives an equation identical to (67), namely.

$$\sigma_{Q3}^2 \Big|_{2\text{-way}} = \frac{h_3}{\pi \omega_{n1}} \left\{ -\frac{A_{13}}{4} \ln \gamma^4 + A_{23} f(R_1) - A_{33} f(R_2) \right\} \quad (96)$$

where now

$$\begin{aligned} A_{13} &= \frac{\gamma^4 (\gamma^2 R_2 - R_1)}{\Delta_0} \\ A_{23} &= \frac{-\gamma^4 \left[(1 - \gamma^4) + \frac{R_1}{2} (\gamma^2 R_2 - R_1) \right]}{\Delta_0} \\ A_{33} &= -\frac{\gamma^2 \left[(1 - \gamma^4) + \gamma^2 \frac{R_2}{2} (\gamma^2 R_2 - R_1) \right]}{\Delta_0} \end{aligned} \quad (97)$$

b. (k=2)

Once again for $k = 2$, we can make use of the partial-fraction expansion of (71), namely,

$$\frac{x^6}{(x^4 + a_1 x^2 + b_1)(x^4 + a_2 x^2 + b_2)} = \frac{A_1 x^2 + B_1}{x^4 + a_1 x^2 + b_1} + \frac{A_2 x^2 + B_2}{x^4 + a_2 x^2 + b_2} \quad (98)$$

where now

$$\begin{aligned} A_1 &= 1 - A_2 = \frac{-\left[b_1 (b_2 - b_1) + a_1 (a_2 b_1 - a_1 b_2) \right]}{\Delta} \\ B_1 &= -\left(\frac{b_1}{b_2} \right) B_2 = \frac{-b_1 (a_2 b_1 - a_1 b_2)}{\Delta} \end{aligned} \quad (99)$$

Thus, (73) and (74) apply directly to this case which, when combined with (99) and (66), give an equation identical to (75), namely,

$$\sigma_{Q2}^2 \Big|_{2\text{-way}} = \frac{h_2}{2\omega_{n1}} \left[\frac{1}{\sqrt{R_1+2}} A_{12} + \frac{1}{\sqrt{R_2+2}} A_{22} \right] \quad (100)$$

where now

$$A_{12} = - \frac{\gamma^4 \left[(1 - \gamma^4) + (R_1 + 1)(\gamma^2 R_2 - R_1) \right]}{\Delta_0}$$

$$A_{22} = \frac{\gamma \left[(1 - \gamma^4) + \gamma^2 (R_2 + 1)(\gamma^2 R_2 - R_1) \right]}{\Delta_0} \quad (101)$$

c. (k=1)

For $k = 1$, the upper limit ω_H of (93) cannot be allowed to extend to infinity since the integral would become unbounded. Nevertheless, the partial-fraction expansion of (61) still applies, namely,

$$\frac{x^7}{(x^4 + a_1 x^2 + b_1)(x^4 + a_2 x^2 + b_2)} = \frac{A_1 x^3 + B_1 x}{x^4 + a_1 x^2 + b_1} + \frac{A_2 x^3 + B_2 x}{x^4 + a_2 x^2 + b_2} \quad (102)$$

now with A_1 and B_1 given by (99). Thus, again letting $D = 0$ in the right right-hand side of (64) and evaluating the result between the limits of 0 and ω_H gives

$$\begin{aligned}
& \int_0^{\omega_H} \frac{\omega^7}{\left[\omega^4 + \omega^2(\omega_{n1}^2 R_1) + \omega_{n1}^4\right] \left[\omega^4 + \omega^2(\omega_{n2}^2 R_2) + \omega_{n2}^4\right]} d\omega \\
&= \frac{A_1}{4} \left[\ln \left(\frac{\omega_H^4 + a_1 \omega_H^2 + b_1}{\omega_H^4 + a_2 \omega_H^2 + b_2} \right) - \ln \gamma^4 \right] + \left(B_1 - \frac{a_1 A_1}{2} \right) \left[f(\omega_H; h_1^2) - f(0; h_1^2) \right] \\
&\quad - \left[\left(\frac{b_2}{b_1} \right) B_1 + (1 - A_1) \frac{a_2}{2} \right] \left[f(\omega_H; h_2^2) - f(0; h_2^2) \right] \tag{103}
\end{aligned}$$

where $f(x; h_i^2)$ is defined in (65). Finally, substituting (99) together with (66) into (103) and simplifying enables evaluation of (93) for $k = 1$, namely,

$$\begin{aligned}
\sigma_{Q,2}^2 \Big|_{2\text{-way}} &= \frac{h_1}{\pi} \left\{ \frac{A_{11}}{4} \ln \left(\frac{1 + R_1 \left(\frac{\gamma_H}{\gamma} \right)^2 + \left(\frac{\gamma_H}{\gamma} \right)^4}{1 + R_2 \gamma_H^2 + \gamma_H^4} \right) \right. \\
&\quad + \frac{1}{4} \ln \left(1 + R_2 \gamma_H^2 + \gamma_H^4 \right) \\
&\quad \left. + A_{21} f_2 \left(R_1, \frac{\gamma_H}{\gamma} \right) + A_{31} f_2 \left(R_2, \gamma_H \right) \right\} \tag{104}
\end{aligned}$$

where γ_H is defined analogous to (47) for the one-way case, namely,

$$\gamma_H \triangleq \frac{\omega_H}{\omega_{n2}} \tag{105}$$

and

$$A_{11} = - \frac{\gamma^4 \left[(1 - \gamma^4) + R_1 (\gamma^2 R_2 - R_1) \right]}{\Delta_0}$$

$$A_{21} = \frac{\gamma^4 \left[\frac{R_1}{2} (1 - \gamma^4) + \left(\frac{R_1^2}{2} - 1 \right) (\gamma^2 R_2 - R_1) \right]}{\Delta_0}$$

$$A_{31} = \frac{\frac{R_2}{2} (1 - \gamma^4) + \gamma^2 \left[\frac{R_2^2}{2} - 1 \right] (\gamma^2 R_2 - R_1)}{\Delta_0}$$

$$f_2(R, \Gamma) = \begin{cases} \frac{1}{\sqrt{4-R^2}} \left[\tan^{-1} \left(\frac{2\Gamma^2+R}{\sqrt{4-R^2}} \right) - \tan^{-1} \left(\frac{R}{\sqrt{4-R^2}} \right) \right]; & R < 2 \\ \frac{1}{2\sqrt{R^2-4}} \left[-\ln \left(\frac{2\Gamma^2+R+\sqrt{R^2-4}}{2\Gamma^2+R-\sqrt{R^2-4}} \right) + \ln \left(\frac{R+\sqrt{R^2-4}}{R-\sqrt{R^2-4}} \right) \right]; & R > 2 \end{cases} \quad (106)$$

Also note that

$$\lim_{\Gamma \rightarrow \infty} f_2(R, \Gamma) = f(R) \quad (107)$$

where $f(R)$ is defined in (69).

d. (k=0)

Here again, the upper limit ω_H of (93) cannot be allowed to extend to infinity. In addition, before applying the partial-fraction procedure to the integrand required in (93) for $k = 0$, we must first reduce this integrand to one whose numerator is a lower order polynomial than its denominator, i.e.,

$$\frac{x^8}{(x^4 + a_1 x^2 + b_1)(x^4 + a_2 x^2 + b_2)} = 1 - \frac{Cx^6 + Dx^4 + Ex^2 + F}{(x^4 + a_1 x^2 + b_1)(x^4 + a_2 x^2 + b_2)} \quad (108)$$

where

$$\begin{aligned}
 C &= a_1 + a_2 \\
 D &= b_1 + b_2 + a_1 a_2 \\
 E &= a_1 b_2 + a_2 b_1 \\
 F &= b_1 b_2
 \end{aligned} \tag{109}$$

Applying the partial-fraction expansion technique to the second term in (108) yields

$$\frac{x^8}{(x^4 + a_1 x^2 + b_1)(x^4 + a_2 x^2 + b_2)} = 1 - \frac{A_1 x^2 + B_1}{x^4 + a_1 x^2 + b_1} - \frac{A_2 x^2 + B_2}{x^4 + a_2 x^2 + b_2} \tag{110}$$

where now

$$\begin{aligned}
 A_1 = C - A_2 &= \frac{(b_2 - b_1) \left(E - b_1 C - \frac{a_1}{b_1} F \right) + (a_2 b_1 - a_1 b_2) \left(D - a_1 C - \frac{F}{b_1} \right)}{\Delta} \\
 B_1 = -\left(\frac{L_1}{b_2}\right) B_2 + \frac{F}{b_2} &= \frac{b_1 \left[(a_2 - a_1) \left(E - b_1 C - \frac{a_1}{b_1} F \right) - (b_2 - b_1) \left(D - a_1 C - \frac{F}{b_1} \right) \right]}{\Delta}
 \end{aligned} \tag{111}$$

Evaluating (109) using (66) and substituting into (111) results, upon simplification, in

$$\begin{aligned}
 A_1 &= \frac{\omega_{n1}^2 \gamma^4 \left[-R_1 (1 - \gamma^4) + (1 - R_1^2) (\gamma^2 R_2 - R_1) \right]}{\Delta_0} \\
 B_1 &= -\frac{\omega_{n1}^4 \gamma^4 \left[\gamma^2 R_1 (R_2 - \gamma^2 R_1) + (1 - R_1^2) (1 - \gamma^4) \right]}{\Delta_0} \\
 A_2 &= \frac{\omega_{n2}^2 \left\{ (1 - \gamma^4) \left[\gamma^2 R_1 + (1 - \gamma^4) R_2 \right] + \gamma^2 (R_2^2 - \gamma^4) (\gamma^2 R_2 - R_1) \right\}}{\Delta_0} \\
 B_2 &= \frac{\omega_{n2}^4 \left\{ (1 - \gamma^4) (1 - \gamma^4 R_1^2) + \gamma^2 \left[\gamma^2 R_2 - R_1 (1 - \gamma^4) \right] (R_2 - \gamma^2 R_1) \right\}}{\Delta_0}
 \end{aligned} \tag{112}$$

Using (51) and (52) on (110) with limits of zero and ω_H , we arrive, after much simplification, to the final result, namely,

$$\sigma_{Q0}^2 \Big|_{2\text{-way}} = \frac{h_0 \omega_{n1}}{\pi} \left\{ \frac{\gamma_H}{\gamma} - g(R_1, A_{10}, A_{20}, \frac{\gamma_H}{\gamma}) - \frac{1}{\gamma} g(R_2, A_{30}, A_{40}, \gamma_H) \right\} \quad (113)$$

where

$$g(R, \alpha, \beta, \gamma) = \begin{cases} \frac{1}{\sqrt{R^2-4}} \left[\left(\frac{\alpha R^+ - \beta}{\sqrt{R^+}} \right) \tan^{-1} \left(\frac{\gamma}{\sqrt{R^+}} \right) - \left(\frac{\alpha R^- - \beta}{\sqrt{R^-}} \right) \tan^{-1} \left(\frac{\gamma}{\sqrt{R^-}} \right) \right]; & R > 2 \\ \frac{\beta}{4} \left\{ \frac{(1 - \frac{\alpha}{\beta})}{\sqrt{2-R}} \ln \left(\frac{1 + \gamma \sqrt{2-R} + \gamma^2}{1 - \gamma \sqrt{2-R} + \gamma^2} \right) \right. \\ \left. + \frac{2(1 + \frac{\alpha}{\beta})}{\sqrt{2+R}} \left[\tan^{-1} \left(\frac{2\gamma - \sqrt{2-R}}{\sqrt{2+R}} \right) + \tan^{-1} \left(\frac{2\gamma + \sqrt{2-R}}{\sqrt{2+R}} \right) \right] \right\}; & R < 2 \end{cases}$$

$$A_{10} \triangleq \frac{A_1}{\omega_{n1}^2} = \frac{\gamma^4 \left[-R_1(1 - \gamma^4) + (1 - R_1^2)(\gamma^2 R_2 - R_1) \right]}{\Delta_0}$$

$$A_{20} \triangleq \frac{B_1}{\omega_{n1}^4} = - \frac{\gamma^4 \left[\gamma^2 R_1 (R_2 - \gamma^2 R_1) + (1 - R_1^2)(1 - \gamma^4) \right]}{\Delta_0}$$

$$A_{30} \triangleq \frac{A_2}{\omega_{n2}^2} = \frac{(1 - \gamma^4) \left[\gamma^2 R_1 + (1 - \gamma^4) R_2 \right] + \gamma^2 (R_2 - \gamma^4)(\gamma^2 R_2 - R_1)}{\Delta_0}$$

$$A_{40} \triangleq \frac{B_2}{\omega_{n2}^4} = - \frac{(1 - \gamma^4) (1 - \gamma^4 R_1^2) + \gamma^2 \left[\gamma^2 R_2 - R_1 (1 - \gamma^4) \right] (R_2 - \gamma^2 R_1)}{\Delta_0} \quad (114)$$

and R^+ , R^- are given by (40). Also note that

$$\lim_{\gamma \rightarrow \infty} g(R, \alpha, \beta, \gamma) = \frac{\pi}{2} \frac{(\beta + \alpha)}{\sqrt{2+R}}; \quad \text{all } R \quad (115)$$

5.0 CALCULATION OF MEAN-SQUARE PHASE NOISE FOR TWO-WAY LINKS WITH COHERENT TRANSMIT/RECEIVE OSCILLATOR SOURCES

Until now, we have implicitly assumed that the receive and transmit phase noise sources, ψ_{RX} and ψ_{TX} , which emanate from the reference system TCXO (see Figure 2) can be considered as statistically independent random processes insofar as their effect on the computation of mean-square phase noise in this same system [see (9)]. Since, in reality, ψ_{RX} and ψ_{TX} are derived from the same oscillator source, the above assumption is justified by considering the extreme situation wherein the round-trip delay of ψ_{TX} to the vehicle system and back is long relative to the correlation time of the process itself. As such, a sample of ψ_{TX} which leaves the TCXO arrives back at the reference system essentially uncorrelated with the corresponding sample of ψ_{RX} .

The other extreme is to assume the case where the round-trip delay time to the vehicle system and back is short relative to the correlation time of the phase noise process. Here, the simplest model is to assume $\psi_{RX} = \psi_{TX}$, whereupon (5) is modified to

$$\begin{aligned} \phi_e(s) = & \left[G_f H_v(s) - 1 \right] \left[1 - H_R(s) \right] \hat{\psi}_{TX}(s) \\ & + G_f \left[1 - H_v(s) \right] \left[1 - H_R(s) \right] \hat{\psi}_v(s) \\ & - \left[1 - H_R(s) \right] \left[\hat{\psi}_R(s) + \psi_r(s) \right] \end{aligned} \quad (116)$$

and, correspondingly, (9) becomes

$$\begin{aligned} \sigma_\phi^2 = & \frac{1}{2\pi} \int_{-\infty}^{\infty} |G_f H_v(j\omega) - 1|^2 |1 - H_R(j\omega)|^2 S_{\hat{\psi}_{TX}}(\omega) d\omega \\ & + \frac{1}{2\pi} \int_{-\infty}^{\infty} G_f^2 |1 - H_v(j\omega)|^2 |1 - H_R(j\omega)|^2 S_{\hat{\psi}_v}(\omega) d\omega \\ & + \frac{1}{2\pi} \int_{-\infty}^{\infty} |1 - H_R(j\omega)|^2 \left[S_{\psi_R}(\omega) + S_{\psi_r}(\omega) \right] d\omega \end{aligned} \quad (117)$$

Thus, we must now consider evaluation of a new type of integral whose generic form [see the first term in [117]] is

$$\sigma_G^2 \Big|_{2\text{-way}} = \frac{1}{2\pi} \int_{-\infty}^{\infty} |GH_1(j\omega) - 1|^2 |1 - H_2(j\omega)|^2 S_{\hat{\psi}}(\omega) d\omega \quad (118)$$

where, as before, we use the subscripts "1" and "2" to replace "V" and "R", respectively, and, for further notational simplicity, we drop the "f" subscript on the frequency multiplication ratio (turnaround transponder ratio), G_f .

From the closed-loop transfer function defined in (10), we immediately find that

$$GH_1(s) - 1 = - \frac{s^2 + \omega_{n1} \sqrt{r_1} (1-G)s + \omega_{n1}^2 (1-G)}{s^2 + \omega_{n1} \sqrt{r_1} s + \omega_{n1}^2} \quad (119)$$

Thus, from (11) and (119),

$$\begin{aligned} I(s)I(-s) &\triangleq (GH_1(s) - 1)(1 - H_2(s))(GH_1(-s) - 1)(1 - H_2(-s)) \\ &= \frac{s^4 \left\{ s^4 - (1-G)^2 \omega_{n1}^2 \left[r_1 - \frac{2}{1-G} \right] s^2 + (1-G)^2 \omega_{n1}^4 \right\}}{\prod_{i=1}^2 \left(s^4 - \omega_{ni}^2 (r_i - 2) s^2 + \omega_{ni}^4 \right)} \\ &= \frac{s^8}{\prod_{i=1}^2 \left(s^4 - \omega_{ni}^2 (r_i - 2) s^2 + \omega_{ni}^4 \right)} \\ &\quad + (1-G)^2 \frac{s^4 \left\{ -\omega_{n1}^2 \left[r_1 - \frac{2}{1-G} \right] s^2 + \omega_{n1}^4 \right\}}{\prod_{i=1}^2 \left(s^4 - \omega_{ni}^2 (r_i - 2) s^2 + \omega_{ni}^4 \right)} \end{aligned} \quad (120)$$

Finally, letting $s = j\omega$

$$\begin{aligned}
|I(j\omega)|^2 &= |GH_1(j\omega) - 1|^2 |1 - H_2(j\omega)|^2 \\
&= \frac{\omega^8}{\prod_{i=1}^2 \left(\omega^4 + \omega^2 \left[\omega_{ni}^2 (r_i - 2) \right] + \omega_{ni}^4 \right)} \\
&\quad + (1-G)^2 \frac{\omega^4 \omega_{n1}^2 \left(\omega_{n1}^2 + \left(r_1 - \frac{2}{1-G} \right) \omega^2 \right)}{\prod_{i=1}^2 \left(\omega^4 + \omega^2 \left[\omega_{ni}^2 (r_i - 2) \right] + \omega_{ni}^4 \right)} \quad (121)
\end{aligned}$$

When (121) is substituted in (118) together with the definition of $S_{\hat{\varphi}}(\omega)$ given in (14), then, as before, we can express the two-way mean-square phase noise as a sum of four terms, i.e.,

$$\sigma_G^2 \Big|_{2\text{-way}} = \sum_{k=0}^3 \sigma_{Gk}^2 \Big|_{2\text{-way}} \quad (122)$$

where

$$\begin{aligned}
\sigma_{Gk}^2 \Big|_{2\text{-way}} &= \frac{1}{\pi} \int_0^{\omega_H} \frac{h_k}{\omega^k} |GH_1(j\omega) - 1|^2 |1 - H_2(j\omega)|^2 d\omega \\
&= \frac{h_k}{\pi} \int_0^{\omega_H} \frac{\omega^{8-k}}{\left[\omega^4 + \omega^2 \left[\omega_{n1}^2 (r_1 - 2) \right] + \omega_{n1}^4 \right] \left[\omega^4 + \omega^2 \left[\omega_{n2}^2 (r_2 - 2) \right] + \omega_{n2}^4 \right]} d\omega \\
&\quad + (1-G)^2 \frac{h_k}{\pi} \int_0^{\omega_H} \frac{\omega_{n1}^2 \left(\omega_{n1}^2 + \left(r_1 - \frac{2}{1-G} \right) \omega^2 \right) \omega^{4-k}}{\left[\omega^4 + \omega^2 \left[\omega_{n1}^2 (r_1 - 2) \right] + \omega_{n1}^4 \right] \left[\omega^4 + \omega^2 \left[\omega_{n2}^2 (r_2 - 2) \right] + \omega_{n2}^4 \right]} d\omega \quad (123)
\end{aligned}$$

Note that the first term of (123) is identical to $\sigma_{Qk}^2 \Big|_{2\text{-way}}$ of (93). Aside from the $(1-G)^2$ multiplication factor, the second term of (123) is quite similar to $\sigma_{Ik}^2 \Big|_{2\text{-way}}$ of (60), the difference being that

the coefficient of ω^2 in the numerator of the integrand is $r_1 - 2/(1-G)$ rather than r_1 . Because of this similarity, evaluation of the second term of (123) should yield results identical to (67), (75), (79), and (83), with the only change being the definitions of the coefficients A_{ij} in these expressions. In particular, one can show, after much tedious algebra, that:

(k=3)

$$\begin{aligned}
 A_{13} &= \frac{\gamma^4 \left\{ (1-\gamma^4) \left(R_1 + \frac{2G}{G-1} \right) - \gamma^2 (R_2 - \gamma^2 R_1) \right\}}{\Delta_0} \\
 A_{23} &= \frac{\gamma^4 \left\{ (1-\gamma^4) \left[1 - \frac{R_1}{2} \left(R_1 + \frac{2G}{G-1} \right) \right] + \gamma^2 (R_2 - \gamma^2 R_1) \left(\frac{2G}{G-1} + \frac{R_1}{2} \right) \right\}}{\Delta_0} \\
 A_{33} &= \frac{\gamma^4 \left\{ (1-\gamma^4) \left[\gamma^2 - \frac{R_2}{2} \left(R_1 + \frac{2G}{G-1} \right) \right] + (R_2 - \gamma^2 R_1) \left[R_1 + \frac{2G}{G-1} - \frac{\gamma^2 R_2}{2} \right] \right\}}{\Delta_0} \quad (124)
 \end{aligned}$$

(k=2)

$$\begin{aligned}
 A_{12} &= \frac{\gamma^4 \left\{ (1-\gamma^4) \left(\frac{2G}{G-1} - 1 + R_1 \right) - \gamma^2 \left(\frac{2G}{G-1} + 1 + R_1 \right) R_2 + R_1 \left(\gamma^4 + \frac{2G}{G-1} + R_1 \right) \right\}}{\Delta_0} \\
 A_{22} &= \frac{\gamma^3 \left\{ (1-\gamma^4) \left(R_1 + \frac{2G}{G-1} - \gamma^2 \right) - \gamma^2 R_2 \left(1 + \frac{2\gamma^2 G}{G-1} + \gamma^2 R_1 \right) + \gamma^2 R_1 \left(\frac{2G}{G-1} + \gamma^2 + R_1 \right) \right\}}{\Delta_0} \quad (125)
 \end{aligned}$$

(k=1)

$$\begin{aligned}
A_{11} &= \frac{\gamma^4 \left\{ (1 - \gamma^4) + \left(R_1 + \frac{2G}{G-1} \right) (\gamma^2 R_2 - R_1) \right\}}{\Delta_0} \\
A_{21} &= \frac{\gamma^4 \left\{ -(1 - \gamma^4) \left[\frac{3R_1 + 2G}{2} + \frac{2G}{G-1} \right] + \gamma^2 (R_2 - \gamma^2 R_1) - \frac{R_1 (R_1 + \frac{2G}{G-1})}{2} (\gamma^2 R_2 - R_1) \right\}}{\Delta_0} \\
A_{31} &= \frac{\gamma^2 \left\{ -(1 - \gamma^4) \left(R_1 + \frac{\gamma^2 R_2 + 2G}{2} + \frac{2G}{G-1} \right) + \gamma^2 (R_2 - \gamma^2 R_1) - \frac{\gamma^2 R_2 (R_1 + \frac{2G}{G-1})}{2} (\gamma^2 R_2 - R_1) \right\}}{\Delta_0}
\end{aligned} \tag{126}$$

(k=0)

$$\begin{aligned}
A_{10} &= \frac{\gamma^4 \left\{ (1 - \gamma^4) \left(1 + R_1 + \frac{2G}{G-1} \right) + (\gamma^2 R_2 - R_1) \left[\left(R_1 + \frac{2G}{G-1} \right) (1 + R_1) - 1 \right] \right\}}{\Delta_0} \\
A_{20} &= \frac{\gamma \left\{ (1 - \gamma^4) \left(\gamma^2 + R_1 + \frac{2G}{G-1} \right) + \gamma^2 (\gamma^2 R_2 - R_1) \left[\left(R_1 + \frac{2G}{G-1} \right) (1 + R_2) - \gamma^2 \right] \right\}}{\Delta_0}
\end{aligned} \tag{127}$$

Finally, then,

$$\sigma_{Gk}^2 \Big|_{2\text{-way}} = \sigma_{Qk}^2 \Big|_{2\text{-way}} + (1-G)^2 \sigma_{I'k}^2 \Big|_{2\text{-way}} ; \tag{128}$$

k = 0, 1, 2, 3

where the prime on the "I" subscript denotes the fact that (67), (75), (79), and (83) are evaluated using (124), (125), (126), and (127), respectively.

6.0 SYSTEM MODEL WITH FREQUENCY SYNTHESIZER

In this section, we generalize the simple two-way coherent communication system discussed in Section 2.0 and illustrated in Figure 1 to include the other internal frequency synthesizer oscillator sources and other TCXO paths. In particular, we now consider the two-way system illustrated in Figure 4 whose equivalent linear baseband model is given in Figure 5. As such, Figure 3 also applies as the block diagram representation of Figure 4 and, thus, the reference system phase error, ϕ_e , is still given by (2). However, ψ_{RX} and ψ_{TX} , the equivalent phase noises at the receive and transmit outputs of the frequency synthesizer, must now be expressed in terms of the individual oscillator component phase noise sources within the synthesizer itself. To do this, we must postulate a specific synthesizer structure.

Figure 6 illustrates the frequency synthesizer used in the Payload Interrogator (PI) of the Shuttle orbiter, and Figure 7 is its equivalent linear phase noise model. Using routine control loop analysis methods, it is straightforward to show that

$$\begin{aligned} \psi_{RX}(s) = & 2 \left[8 + \left(\frac{N}{D} + 4 \right) H_{RX}(s) \right] \psi_{TCXO}(s) \\ & + \left[1 - H_{RX}(s) \right] \psi_1(s) \end{aligned} \quad (129)$$

and

$$\begin{aligned} \psi_{TX}(s) = & 2 \left\{ 8 + \frac{FN}{DE} H_{RX}(s) H_{TX}(s) - 4 \frac{F}{E} H_{TX}(s) \left[1 - H_{RX}(s) \right] \right\} \psi_{TCXO}(s) \\ & + \frac{F}{E} \left[1 - H_{RX}(s) \right] H_{TX}(s) \psi_1(s) + G_V H_{TX}(s) \psi_{VCXO}(s) \\ & + \left[1 - H_{TX}(s) \right] \psi_2(s) \end{aligned} \quad (130)$$

where

$$H_{RX}(s) \triangleq \frac{\frac{K_{RX}}{N} F_{RX}(s)}{s + \frac{K_{RX}}{N} F_{RX}(s)} ; \quad H_{TX}(s) \triangleq \frac{\frac{K_{TX}}{N} F_{TX}(s)}{s + \frac{K_{TX}}{N} F_{TX}(s)} \quad (131)$$

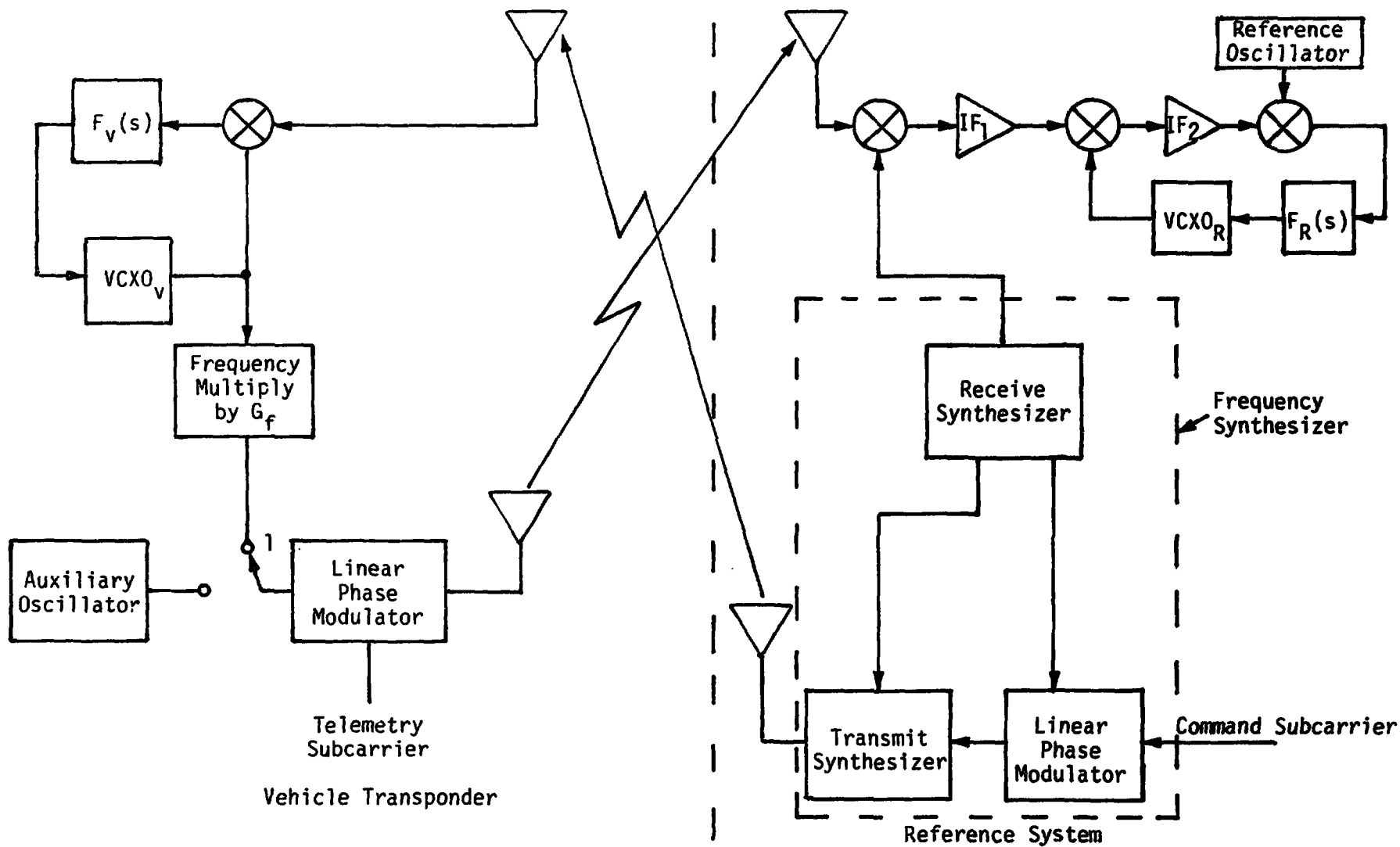


Figure 4. A Simple Block Diagram of a Two-Way Coherent Communication System Employing a Frequency Synthesizer

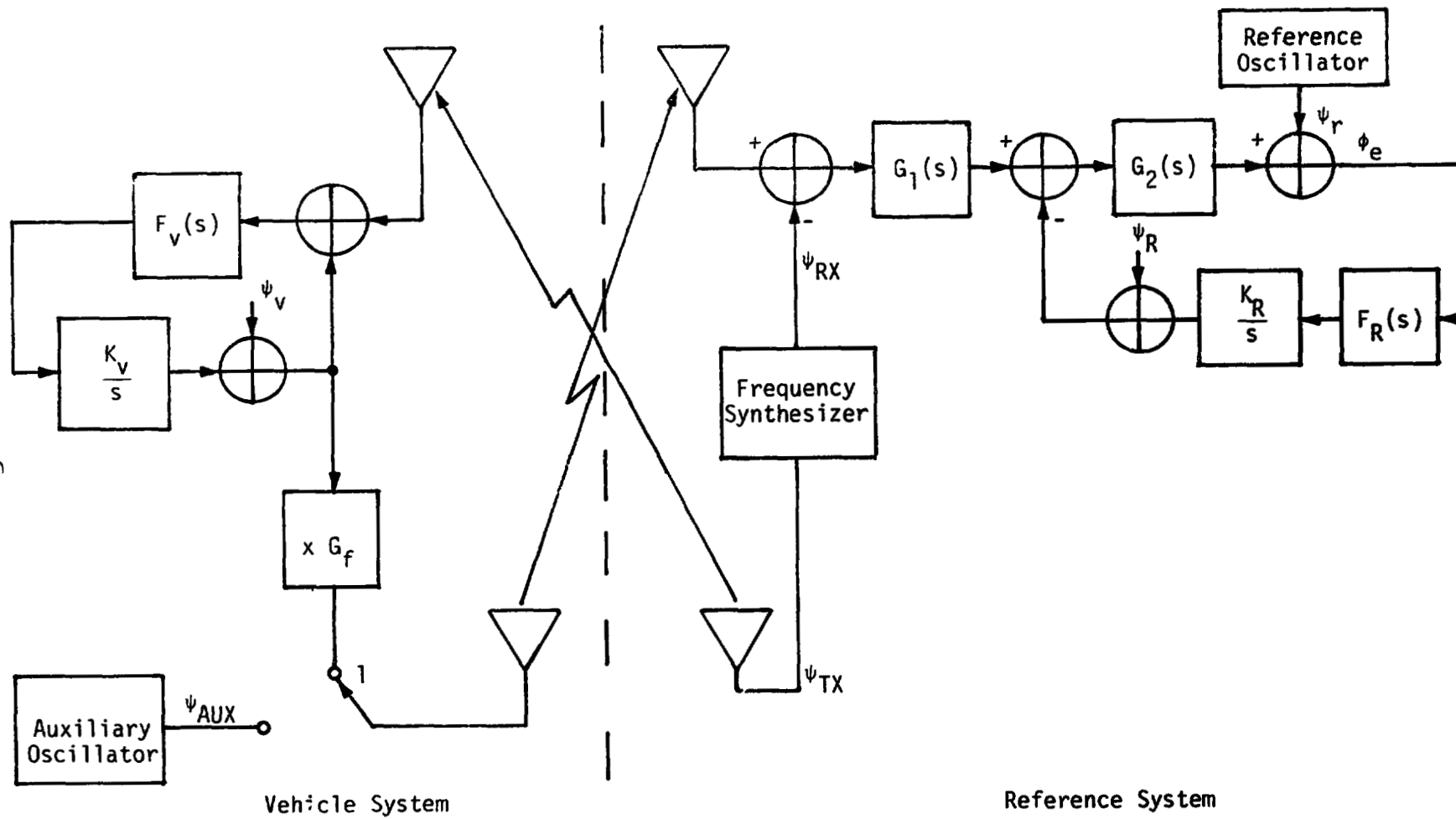


Figure 5. An Equivalent Linear Baseband Model of the System Including Oscillator Phase Noise Sources

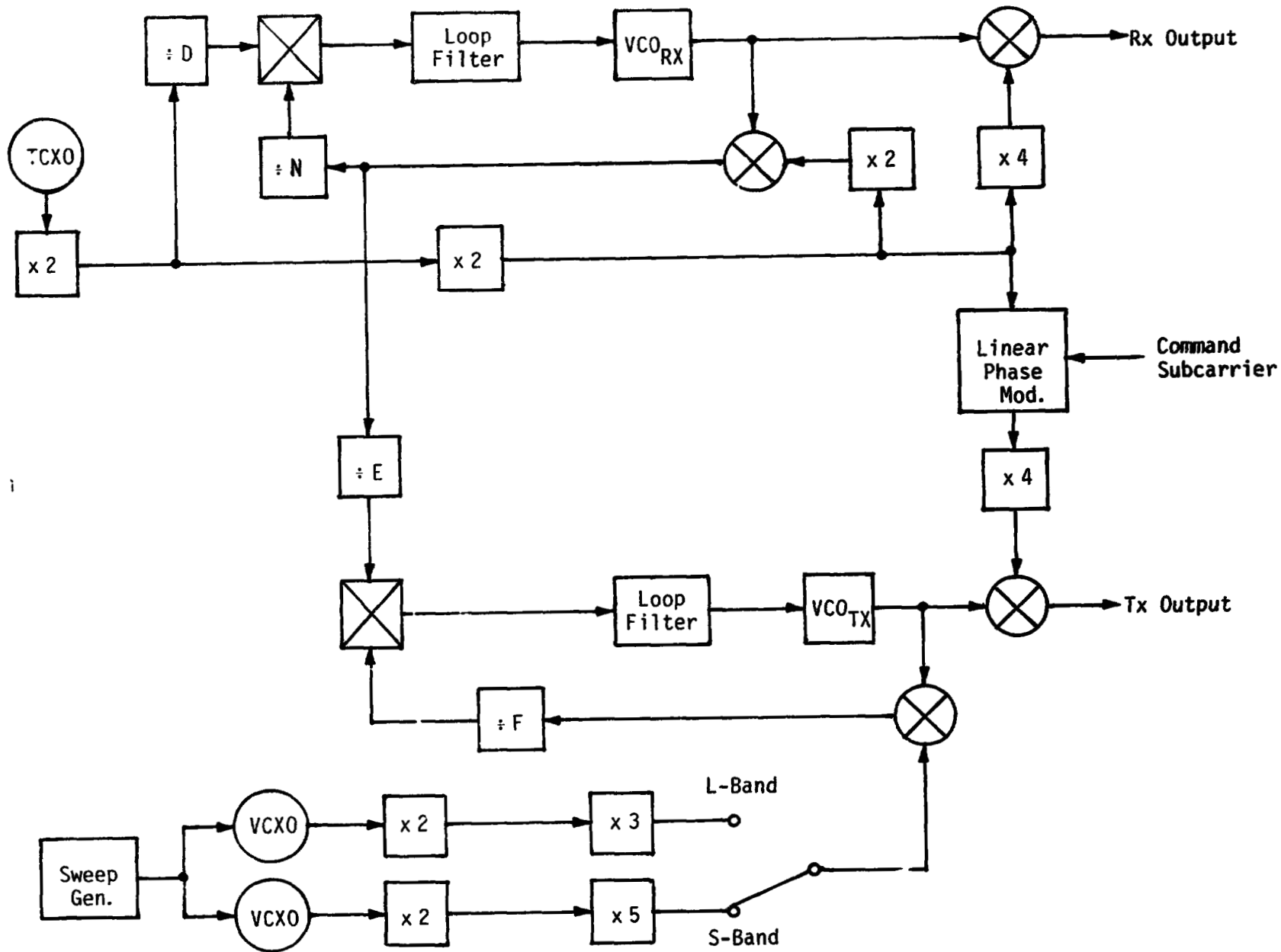


Figure 6. PI Frequency Synthesizer

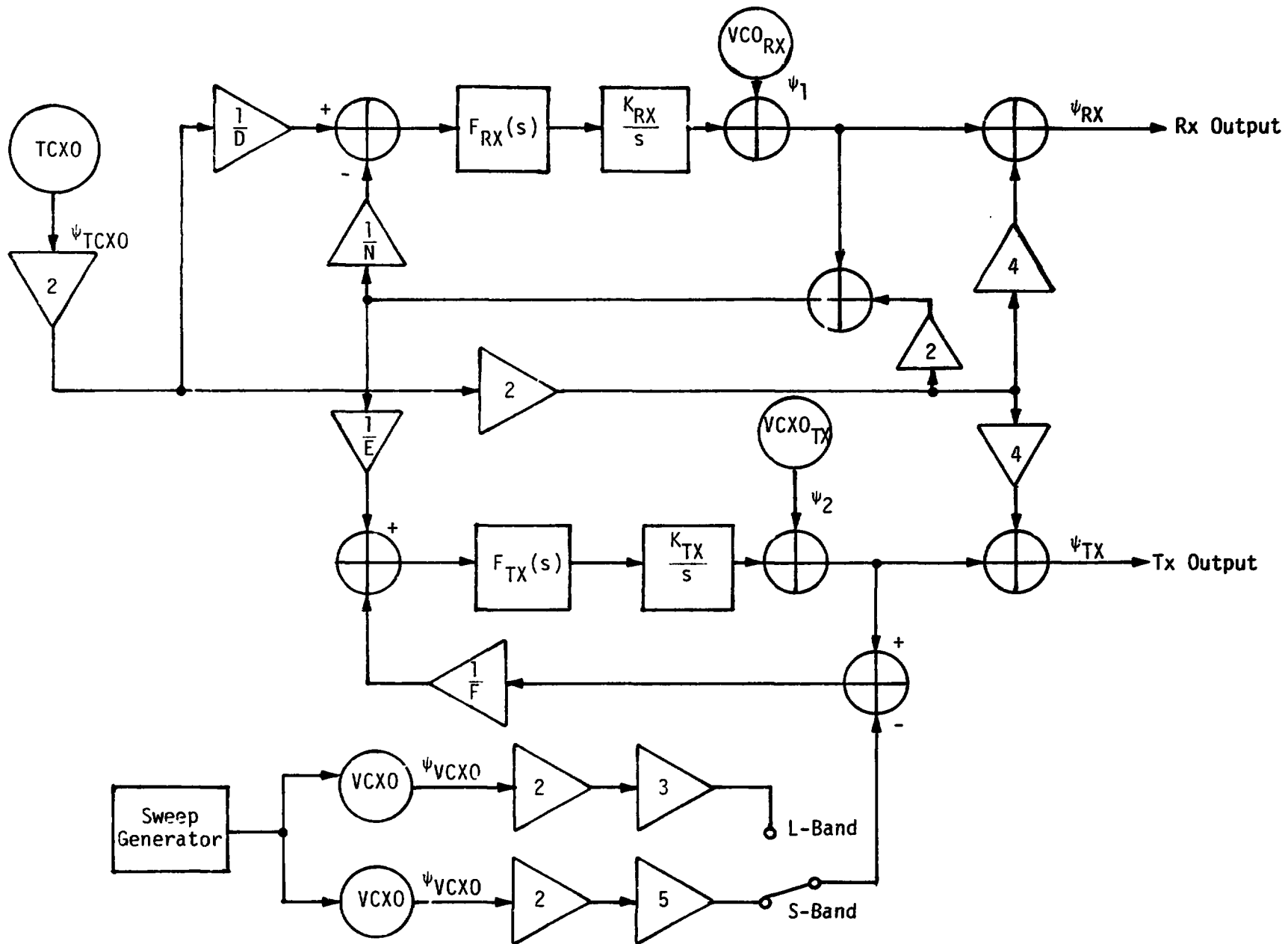


Figure 7. Phase Noise Model for PI Frequency Synthesizer

Also,

$$G_V = \begin{cases} 6 & \text{for L-band} \\ 10 & \text{for S-band} \end{cases} \quad (132)$$

Note from (129) and (130) that the TCXO phase noise ψ_{TCXO} and the transmit VCO phase noise ψ_1 each contribute to both the transmit and receive synthesizer outputs. Furthermore, the first terms of the TCXO contributions, namely, $16\psi_{TCXO}$, represent the direct feedthrough paths of the TCXO previously accounted for in Section 2.0.

Substituting (129) and (130) into (2) and making the notation simplifications and assumptions leading to (5) gives the desired result for the reference system (PI) phase error in terms of all the individual phase noise sources, namely,

$$\begin{aligned} \phi_e(s) = & G_f H_V(s) \left[1 - H_R(s) \right] \left\{ 16 + 2 \frac{FN}{DE} H_{RX}(s) H_{TX}(s) \right. \\ & \left. - 8 \frac{F}{E} H_{TX}(s) \left[1 - H_{RX}(s) \right] \right\} \hat{\psi}_{TCXO}(s) \\ & + G_f \left(\frac{F}{E} \right) H_V(s) \left[1 - H_R(s) \right] \left[1 - H_{RX}(s) \right] H_{TX}(s) \hat{\psi}_1(s) \\ & + G_f G_V H_V(s) \left[1 - H_R(s) \right] H_{TX}(s) \hat{\psi}_{VCXO}(s) \\ & + G_f H_V(s) \left[1 - H_R(s) \right] \left[1 - H_{TX}(s) \right] \hat{\psi}_2(s) \\ & + G_f \left[1 - H_V(s) \right] \left[1 - H_R(s) \right] \hat{\psi}_V(s) \\ & - \left[1 - H_R(s) \right] \left[16 + 2 \left(\frac{N}{D} + 4 \right) H_{RX}(s) \right] \hat{\psi}_{TCXO}(s) \\ & - \left[1 - H_R(s) \right] \left[1 - H_{RX}(s) \right] \hat{\psi}_1(s) \\ & - \left[1 - H_R(s) \right] \left[\hat{\psi}_R(s) + \psi_r(s) \right] \end{aligned} \quad (133)$$

The frequency division constants E, F, N and D of Figure 6 depend on the operating mode of the vehicle transponder (IUS) and the channel number, CN, assigned to the particular frequency selected in the frequency band corresponding to this mode. In particular, the following table applies:

<u>Frequency Division Multiple</u>	<u>STDN</u>	<u>DSN</u>	<u>SGLS</u>
E	240	240	256
F	222	221	205
N	CN + 519	CN - 431	40CN - 35460
D	1280	432	1280
CN	1 - 808	850 - 882	900 - 919
G_f	240/222	240/221	256/205

From the above, we observe that, for all three modes,

$$G_f \left(\frac{F}{E} \right) = 1 \quad (134)$$

Also, from (133), the worst-case (largest) phase error would occur for the maximum value of N which corresponds to the highest channel number. Thus,

$$G_f \left(\frac{FN_{\max}}{DE} \right) = \frac{N_{\max}}{D} = \begin{cases} \left(\frac{1327}{1280} \right) = 1.0367 & \text{STDN} \\ \left(\frac{451}{432} \right) = 1.044 & \text{DSN} \\ \left(\frac{1300}{1280} \right) = 1.0156 & \text{SGLS} \end{cases} \quad (135)$$

Before proceeding with the evaluation of mean-square phase noise corresponding to $\phi_e(s)$ of (133), we point out that we have intentionally written the pair of contributions from $\hat{\psi}_{TCX0}(s)$ and $\hat{\psi}_1(s)$ as separate terms in this equation. The reason for this is to identify the fact that in each case one of the contributions (the first of the pair)

originates at the transmit output of the frequency synthesizer, travels through the vehicle, and returns to the reference system phase error output, while the second contribution of each pair enters the reference system directly from the receive output of the synthesizer without ever passing through the vehicle system. As was done in Section 5.0, we shall assume in what follows that the round-trip to the vehicle system and back is long relative to the correlation time of either phase noise process itself; thus, the two phase noise components in each pair are essentially uncorrelated.

We now turn to deriving expressions for the necessary 3-way and 4-way mean-square phase noise components associated with the phase error process in (133). Furthermore, to simplify matters, in this section, we shall ignore altogether the terms corresponding to the TCXO phase noise since, typically, these contributions are much less dominant than those arising from the other phase noise sources. Thus, analogous to (9), we get

$$\begin{aligned}
\sigma_{\phi}^2 &= \frac{1}{2\pi} \int_{-\infty}^{\infty} |H_V(j\omega)|^2 |1 - H_R(j\omega)|^2 |1 - H_{RX}(j\omega)|^2 |H_{TX}(j\omega)|^2 S_{\hat{\psi}_1}(\omega) d\omega \\
&+ \frac{1}{2\pi} \int_{-\infty}^{\infty} G_f^2 G_v^2 |H_V(j\omega)|^2 |1 - H_R(j\omega)|^2 |H_{TX}(j\omega)|^2 S_{\hat{\psi}_{VCXO}}(\omega) d\omega \\
&+ \frac{1}{2\pi} \int_{-\infty}^{\infty} G_f^2 |H_V(j\omega)|^2 |1 - H_R(j\omega)|^2 |1 - H_{TX}(j\omega)|^2 S_{\hat{\psi}_2}(\omega) d\omega \\
&+ \frac{1}{2\pi} \int_{-\infty}^{\infty} G_f^2 |1 - H_V(j\omega)|^2 |1 - H_R(j\omega)|^2 S_{\hat{\psi}_V}(\omega) d\omega \\
&+ \frac{1}{2\pi} \int_{-\infty}^{\infty} |1 - H_R(j\omega)|^2 |1 - H_{RX}(j\omega)|^2 S_{\hat{\psi}_1}(\omega) d\omega \\
&+ \frac{1}{2\pi} \int_{-\infty}^{\infty} |1 - H_R(j\omega)|^2 \left[S_{\hat{\psi}_R}(\omega) + S_{\psi_r}(\omega) \right] d\omega \tag{136}
\end{aligned}$$

7.0 CALCULATION OF THREE-WAY AND FOUR-WAY MEAN-SQUARE PHASE NOISE COMPONENTS

Here we consider the evaluation of mean-square phase noise components whose forms resemble the first three terms of (136). Subsection 7.1 treats the evaluation of the third term, while subsections 7.2 and 7.3 consider the second and first terms, respectively.

As was done in Section 4.0, we shall, for simplicity of notation, use the integers 1 and 2 to replace, respectively, the subscripts V and R previously used to denote vehicle and reference systems. Furthermore, we shall use the subscripts 3 and 4 to replace, respectively, the subscripts TX and RX previously used to denote transmit and receive synthesizer output terminals. Also, as before, all of the second-order carrier-tracking loops (vehicle system, reference system, transmit synthesizer, receive synthesizer) have in-band and out-of-band transfer functions of the form given by (10) and (11), with arbitrary damping factors r_i ; $i=1,2,3,4$ and radian natural frequencies ω_{ni} ; $i=1,2,3,4$.

7.1 Out-of-Band* Three-Way Mean-Square Phase Noise

Consider the evaluation of

$$\sigma_Q^2 \Big|_{3\text{-way}} = \frac{1}{2\pi} \int_{-\infty}^{\infty} |H_1(j\omega)|^2 |1 - H_2(j\omega)|^2 |1 - H_3(j\omega)|^2 S_{\psi}(\omega) d\omega \quad (137)$$

where $|H_1(j\omega)|^2$ and $|1 - H_i(j\omega)|^2$; $i=2,3$ are given by (12), with the appropriate subscript appendages and $S_{\psi}(\omega)$ is defined as before in (14).

Substituting (14) combined with (1) into (137) yields

$$\sigma_Q^2 \Big|_{3\text{-way}} \triangleq \sum_{k=0}^3 \sigma_{Qk}^2 \Big|_{3\text{-way}} \quad (138)$$

where

*The term "out-of-band" is used here with respect to the third tracking loop.

$$\begin{aligned}
\sigma_{Qk}^2 \Big|_{3\text{-way}} &= \frac{1}{\pi} \int_0^{\infty} \frac{h_k}{\omega^k} |H_1(j\omega)|^2 |1 - H_2(j\omega)|^2 |1 - H_3(j\omega)|^2 d\omega \\
&= \frac{h_k}{\pi} \int_0^{\infty} \frac{[\omega_{n1}^2 (\omega_{n1}^2 + r_1 \omega^2)] \omega^{8-k}}{\prod_{i=1}^3 [\omega^4 + \omega^2 [\omega_{ni}^2 (r_i - 2)] + \omega_{ni}^4]} d\omega \quad (139)
\end{aligned}$$

a. (k=3)

To evaluate $\sigma_{Q3}^2 \Big|_{2\text{-way}}$, it is clear from (60) that we must first consider the evaluation of an integral of the form

$$\int \frac{Cx^7 + Dx^5}{\prod_{i=1}^3 (x^4 + a_i x^2 + b_i)} dx$$

where

$$\begin{aligned}
a_i &= \omega_{ni}^2 (r_i - 2) \triangleq \omega_{ni}^2 R_i ; b_i = \omega_{ni}^4 ; i = 1, 2, 3 \\
C &= \omega_{n1}^2 r_1 = \omega_{n1}^2 (R_1 + 2) ; D = \omega_{n1}^4 = b_1 \quad (140)
\end{aligned}$$

The procedure employed is, as before, to expand the integrand into its partial fractions, namely,

$$\frac{Cx^7 + Dx^5}{\prod_{i=1}^3 (x^4 + a_i x^2 + b_i)} = \sum_{i=1}^3 \frac{A_{i3} x^3 + B_{i3} x}{x^4 + a_i x^2 + b_i} \quad (141)$$

Then, integrating the right-hand side of (141) using (17) and (45) gives the desired result, namely,

$$\int \frac{Cx^7 + Dx^5}{\prod_{i=1}^3 (x^4 + a_i x^2 + b_i)} dx = \sum_{i=1}^3 \left[\frac{A_{i3}}{4} \ln(x^4 + a_i x^2 + b_i) + \left(B_{i3} - \frac{a_i A_{i3}}{2} \right) f(x; h_i^2) \right] \quad (142)$$

where $f(x; h_i^2)$ is given by (65). Before evaluating (142) between the limits of 0 and infinity, we digress to discuss the determination of the six unknown coefficients $A_{i3}, B_{i3}; i=1,2,3$.

Multiplying both sides of (141) by $\prod_{i=1}^3 (x^4 + a_i x^2 + b_i)$ gives the relation

$$\sum_{i=1}^3 (A_{i3} x^3 + B_{i3} x) \prod_{\substack{\ell=1 \\ \ell \neq i}}^3 (x^4 + a_\ell x^2 + b_\ell) = Cx^7 + Dx^5 \quad (143)$$

Equating coefficients of like powers of x on both sides of (143) results in a set of six linear equations whose solution gives the desired unknown coefficients.

Rather than obtain specific closed-form expressions for these coefficients as was done previously in the one-way and two-way results, it is more convenient here to describe the solution in matrix notation. Specifically, let \underline{V}_3 denote the unknown coefficient vector

$$\underline{V}_3 = \begin{bmatrix} A_{13} \\ B_{13} \\ A_{23} \\ B_{23} \\ A_{33} \\ B_{33} \end{bmatrix} \quad (144)$$

and \underline{F}_3 the forcing function vector

$$\underline{F}_3 = \begin{bmatrix} 0 \\ 0 \\ C \\ D \\ 0 \\ 0 \end{bmatrix} = \begin{bmatrix} 0 \\ 0 \\ \omega_{n1}^2 (R_1 + 2) \\ \omega_{n1}^4 \\ 0 \\ 0 \end{bmatrix} \quad (145)$$

then the solution to (143) as described above can be written as

$$[M]\underline{V}_3 = \underline{F}_3 \quad (146)$$

or, equivalently,

$$\underline{V}_3 = [M]^{-1} \underline{F}_3$$

where, making use of (140), the 6x6 matrix [M] is characterized by

$$[M] = \begin{bmatrix} m_{11} & m_{12} & \cdot & \cdot & \cdot & m_{16} \\ m_{21} & m_{22} & \cdot & \cdot & \cdot & m_{26} \\ \cdot & \cdot & \cdot & \cdot & \cdot & \cdot \\ \cdot & \cdot & \cdot & \cdot & \cdot & \cdot \\ \cdot & \cdot & \cdot & \cdot & \cdot & \cdot \\ m_{61} & m_{62} & \cdot & \cdot & \cdot & m_{66} \end{bmatrix} \quad (148)$$

with

$$\begin{aligned}
m_{1i} &= 1 ; i=1,3,5 \\
m_{1i} &= 0 ; i=2,4,6 \\
m_{2i} &= \sum_{\substack{j=1 \\ j \neq i}}^3 \omega_{nj}^2 R_j \\
m_{3i} &= \sum_{\substack{j=1 \\ j \neq i}}^3 \omega_{nj}^4 + \prod_{\substack{j=1 \\ j \neq i}}^3 \omega_{nj}^2 R_j \\
m_{4i} &= \sum_{\substack{j=1 \\ j, k \neq i \\ j \neq k}}^3 \sum_{k=1}^3 \omega_{nj}^2 R_j \omega_{nk}^4 \\
m_{5i} &= \prod_{\substack{j=1 \\ j \neq i}}^3 \omega_{nj}^4 \\
m_{6i} &= 0 \\
m_{ji} &= m_{j-1, i-1}; i=2,4,6; j=2,3,\dots,6
\end{aligned}
\left. \vphantom{\begin{aligned} m_{1i} \\ m_{1i} \\ m_{2i} \\ m_{3i} \\ m_{4i} \\ m_{5i} \\ m_{6i} \\ m_{ji} \end{aligned}} \right\} i=1,3,5 \tag{149}$$

Using the first two relations of (149) in (147), i.e., the elements of the first row of $[M]$, we immediately see that

$$\sum_{i=1}^3 A_{i3} = 0 \tag{150}$$

Furthermore, from the second row of $[M]$, we have that

$$\sum_{i=1}^3 \left[B_{i3} - (\omega_{ni}^2 R_i) A_{i3} \right] = \sum_{i=1}^3 (B_{i3} - a_i A_{i3}) = 0 \tag{151}$$

or, equivalently,

$$\sum_{i=1}^3 \left(B_{i3} - \frac{a_i A_{i3}}{2} \right) = \sum_{i=1}^3 \frac{a_i A_{i3}}{2} \quad (152)$$

Solving for A_{i3} and $B_{i3} - (a_i A_{i3})/2$ from (150) and (152) and substituting into (142) gives the alternate form

$$\int \frac{Cx^7 + Dx^5}{\prod_{i=1}^3 (x^4 + a_i x^2 + b_i)} dx = \sum_{i=1}^2 \left\{ \frac{A_{i3}}{4} \ln \left(\frac{x^4 + a_i x^2 + b_i}{x^4 + a_3 x^2 + b_3} \right) + \left(B_{i3} - \frac{a_i A_{i3}}{2} \right) \left[f(x; h_i^2) - f(x; h_3^2) \right] + \frac{A_{i3}(a_i - a_3)}{2} f(x; h_3^2) \right\} \quad (153)$$

It is now convenient to evaluate (153) between the limits 0 and infinity which, upon algebraic simplification, results in

$$\int_0^{\infty} \frac{Cx^7 + Dx^5}{\prod_{i=1}^3 (x^4 + a_i x^2 + b_i)} dx = \sum_{i=1}^2 \left\{ -\frac{A_{i3}}{4} \ln \gamma_i^4 + \left(B_{i3} - \frac{\omega_{ni}^2 R_i A_{i3}}{2} \right) \left[f(R_i) - f(R_3) \right] + \frac{A_{i3}(\gamma_i^2 R_i - R_3)}{2} f(R_3) \right\} \quad (154)$$

where $f(R)$ is defined in (69) and the parameter γ_i characterizes the ratio of loop natural frequencies relative to that of the third loop, i.e.,

$$\gamma_i \triangleq \frac{\omega_{ni}}{\omega_{n3}}; \quad i=1,2 \quad (155)$$

Finally, then,

$$\sigma_{Q3}^2 \Big|_{3\text{-way}} = \frac{h_3}{\pi} \sum_{i=1}^2 \left\{ -\frac{A_{i3}}{4} \ln \gamma_i^4 + \left(B_{i3} - \frac{\omega_{ni}^2 R_i A_{i3}}{2} \right) [f(R_i) - f(R_3)] + \frac{A_{i3} (\gamma_i^2 R_i - R_3)}{2} f(R_3) \right\} \quad (156)$$

b. (k=2)

To evaluate $\sigma_{Q2}^2 \Big|_{3\text{-way}}$, we again begin by considering the generic form of the integrand and expanding it into its partial fractions, i.e.,

$$\frac{Cx^8 + Dx^6}{\prod_{i=1}^3 (x^4 + a_i x^2 + b_i)} = \sum_{i=1}^3 \frac{A_{i2} x^2 + B_{i2}}{x^4 + a_i x^2 + b_i} \quad (157)$$

where $a_i, b_i; i=1,2,3$ and C, D are as previously given in (140). From (71) and (73), the integral of (157) is easily seen to be

$$\int \frac{Cx^8 + Dx^6}{\prod_{i=1}^3 (x^4 + a_i x^2 + b_i)} dx = \sum_{i=1}^3 f(x; A_{i2}, B_{i2}) \quad (158)$$

where $f(x; A_i, B_i)$ is given in (73). When (158) is evaluated between 0 and infinity and the appropriate substitutions are made for f_i , g_i , h_i , q_i , and α_i in terms of r_i and ω_{ni} ; $i=1,2,3$, we get the much simplified result

$$\int_0^{\infty} \frac{Cx^8 + Dx^6}{\prod_{i=1}^3 (x^4 + a_i x^2 + b_i)} dx = \frac{\pi}{2} \sum_{i=1}^3 \frac{1}{\sqrt{R_i+2}} \left(\frac{B_{i2} + \omega_{ni}^2 A_{i2}}{\omega_{ni}^3} \right) \quad (159)$$

Finally, then,

$$\sigma_{Q2}^2 \Big|_{3\text{-way}} = \frac{h_2}{2} \sum_{i=1}^3 \frac{1}{\sqrt{R_i+2}} \left(\frac{B_{i2} + \omega_{ni}^2 A_{i2}}{\omega_{ni}^3} \right) \quad (160)$$

Evaluation of the coefficients A_{i2} , B_{i2} ; $i=1,2,3$ proceeds as before by multiplying both sides of (157) by

$$\prod_{i=1}^3 (x^4 + a_i x^2 + b_i)$$

and equating coefficients of like powers of x . The resulting set of linear equations has the solution

$$\underline{V}_2 = [M]^{-1} \underline{E}_2 \quad (161)$$

where now

$$\underline{V}_2 = \begin{bmatrix} A_{12} \\ B_{12} \\ A_{22} \\ B_{22} \\ A_{32} \\ B_{32} \end{bmatrix}; \quad \underline{F}_2 = \begin{bmatrix} 0 \\ \omega_{n1}^2(R_1+2) \\ \omega_{n1}^4 \\ 0 \\ 0 \\ 0 \end{bmatrix} \quad (162)$$

and [M] is still described by (148) and (149).

In the interest of brevity, we shall merely present the results for the cases $k=1$ and $k=0$. With only minor changes, the procedure to obtain these results follows that just described for $k=3$ and $k=2$, respectively.

c. ($k=1$ and $k=0$)

$$\sigma_{Q1}^2 \Big|_{3\text{-way}} = \frac{h_1}{\pi} \sum_{i=1}^2 \left\{ -\frac{A_{i1}}{2} \ln \gamma_i^4 + \left(B_{i1} - \frac{\omega_{ni}^2 R_i A_{i1}}{2} \right) [f(R_i) - f(R_3)] + \left[\omega_{n1}^2 (R_1+2) + \frac{A_{i1} (\gamma_i^2 R_i - R_3)}{2} \right] f(R_3) \right\}$$

(163)

$$\sigma_{Q0}^2 \Big|_{3\text{-way}} = \frac{h_0}{2} \sum_{i=1}^3 \frac{1}{\sqrt{R_i+2}} \left(\frac{B_{i0} + \omega_{ni}^2 A_{i0}}{\omega_{ni}^3} \right)$$

(164)

where

$$\underline{V}_k = [M]^{-1} \underline{E}_k; \quad k=0,1 \quad (165)$$

with

$$\underline{V}_k = \begin{bmatrix} A_{1k} \\ B_{1k} \\ A_{2k} \\ B_{2k} \\ A_{3k} \\ B_{3k} \end{bmatrix}; \quad \underline{E}_1 = \underline{E}_2; \quad \underline{E}_0 = \begin{bmatrix} \omega_{n1}^{2(R_1+2)} \\ \omega_{n1}^4 \\ 0 \\ 0 \\ 0 \\ 0 \end{bmatrix} \quad (166)$$

7.2 In-Band Three-Way Mean-Square Phase Noise

In this section we consider the evaluation of

$$\sigma_I^2 \Big|_{3\text{-way}} = \frac{1}{2\pi} \int_{-\infty}^{\infty} |H_1(j\omega)|^2 |1 - H_2(j\omega)|^2 |H_3(j\omega)|^2 S_{\hat{\psi}}(\omega) d\omega \quad (167)$$

where once again $|1 - H_i(j\omega)|^2$; $i=1,2$ are both given by (12), with the appropriate subscript appendages and $S_{\hat{\psi}}(\omega)$ is defined by (14). Substituting (14) combined with (1) in (167) yields

$$\sigma_I^2 \Big|_{3\text{-way}} = \sum_{k=0}^3 \sigma_{Ik}^2 \Big|_{3\text{-way}} \quad (168)$$

where

$$\begin{aligned}
\sigma_{Ik}^2 \Big|_{3\text{-way}} &= \frac{1}{\pi} \int_0^{\infty} \frac{h_k}{\omega^k} |H_1(j\omega)|^2 |1 - H_2(j\omega)|^2 |H_3(j\omega)|^2 d\omega \\
&= \frac{h_k}{\pi} \int_0^{\infty} \frac{[\omega_{n1}^2 (\omega_{n1}^2 + r_1 \omega^2) \omega_{n3}^2 (\omega_{n3}^2 + r_3 \omega^2)] \omega^{4-k}}{\prod_{i=1}^3 [\omega^4 + \omega^2 [\omega_{ni}^2 (r_i - 2)] + \omega_{ni}^4]} d\omega \quad (169)
\end{aligned}$$

From (169), it is clear that we must evaluate integrals of the form

$$\int \frac{Cx^{8-k} + Dx^{6-k} + Ex^{4-k}}{\prod_{i=1}^3 (x^4 + a_i x^2 + b_i)} dx ; k=0,1,2,3$$

where a_i and b_i are defined in (140) and

$$\begin{aligned}
C &= \omega_{n1}^4 r_1 \omega_{n3}^4 r_3 = \omega_{n1}^4 (R_1 + 2) \omega_{n3}^4 (R_3 + 2) \\
D &= \omega_{n1}^2 r_1 + \omega_{n3}^2 r_3 = \omega_{n1}^2 (R_1 + 2) + \omega_{n3}^2 (R_3 + 2) \\
E &= \omega_{n1}^4 \omega_{n3}^4 \quad (170)
\end{aligned}$$

Since the partial fraction approach taken in subsection 7.1 also applies to the above integral, we can essentially write down the desired results by inspection. Thus, rather than go through the development for each value of k , as was done previously, we shall merely present a summary of the results in compact notation. Thus,

For k=1,3

$$\sigma_{Ik}^2 \Big|_{3\text{-way}} = \frac{h_k}{\pi} \sum_{i=1}^2 \left\{ -\frac{A_{ik}}{4} \ln \gamma_i^4 + \left(B_{ik} - \frac{\omega_{ni}^2 R_i A_{ik}}{2} \right) [f(R_i) - f(R_3)] \right. \\ \left. + \frac{A_{ik}(\gamma_i^2 R_i - R_3)}{2} f(R_3) \right\} \quad (171)$$

For k=0,2

$$\sigma_{Ik}^2 \Big|_{3\text{-way}} = \frac{h_k}{2} \sum_{i=1}^3 \frac{1}{\sqrt{R_i+2}} \left(\frac{B_{ik} + \omega_{ni}^2 A_{ik}}{\omega_{ni}^3} \right) \quad (172)$$

where γ_i ; $i=1,2$ is defined in (155) and the unknown coefficient vector defined in (166) has a solution of the form in (165) with, however, forcing vectors given by

$$\underline{F}_0 = \begin{bmatrix} 0 \\ C \\ D \\ E \\ 0 \\ 0 \end{bmatrix}; \quad \underline{F}_1 = \underline{F}_2 = \begin{bmatrix} 0 \\ 0 \\ C \\ D \\ E \\ 0 \end{bmatrix}; \quad \underline{F}_3 = \begin{bmatrix} 0 \\ 0 \\ 0 \\ C \\ D \\ E \end{bmatrix} \quad (173)$$

The parameters C, D and E in (173) are defined in (170), thus completing the solution.

7.3 Four-Way Mean-Square Phase Noise

In this final subsection, we consider the evaluation of the four-way mean-square phase noise component necessary to compute the first term of (136), namely,

$$\begin{aligned}\sigma_k^2 \Big|_{4\text{-way}} &= \frac{1}{2\pi} \int_{-\infty}^{\infty} |H_1(j\omega)|^2 |1 - H_2(j\omega)|^2 |H_3(j\omega)|^2 |1 - H_4(j\omega)|^2 S_{\hat{\psi}}(\omega) d\omega \\ &= \sum_{k=0}^3 \sigma_k^2 \Big|_{4\text{-way}}\end{aligned}\quad (174)$$

where

$$\begin{aligned}\sigma_k^2 \Big|_{4\text{-way}} &= \frac{1}{\pi} \int_0^{\infty} \frac{h_k}{\omega^k} |H_1(j\omega)|^2 |1 - H_2(j\omega)|^2 |H_3(j\omega)|^2 |1 - H_4(j\omega)|^2 d\omega \\ &= \frac{n_k}{\pi} \int_0^{\infty} \frac{\omega_{n1}^2 (\omega_{n1}^2 + r_1 \omega^2) \omega_{n3}^2 (\omega_{n3}^2 + r_3 \omega^2) \omega^{8-k}}{\prod_{i=1}^4 [\omega^4 + \omega^2 [\omega_{ni}^2 (r_i - 2)] + \omega_{ni}^4]} d\omega\end{aligned}\quad (175)$$

Comparing (169) with (175), one would intuitively expect results which are similar in form to those of (171) and (172). Indeed, this is the case. In fact, without belaboring the details, one obtains

For $k=1,3$

$$\begin{aligned}\sigma_k^2 \Big|_{4\text{-way}} &= \frac{h_k}{\pi} \sum_{i=1}^3 \left\{ -\frac{A_{ik}}{4} \ln \gamma_i^4 + \left(B_{ik} - \frac{\omega_{ni}^2 R_i A_{ik}}{2} \right) [f(R_i) - f(R_4)] \right. \\ &\quad \left. + \frac{A_{ik} (\gamma_i^2 R_i - R_4)}{2} f(R_4) \right\}\end{aligned}\quad (176)$$

For k=0,2

$$\sigma_k^2 \Big|_{4\text{-way}} = \frac{h_k}{2} \sum_{i=1}^4 \frac{1}{\sqrt{R_i+2}} \left(\frac{B_{ik} + \omega_{ni}^2 A_{ik}}{\omega_{ni}^3} \right) \quad (177)$$

where the γ_i 's are now defined relative to ω_{n4} , i.e.,

$$\gamma_i \triangleq \frac{\omega_{ni}}{\omega_{n4}}; \quad i=1,2,3 \quad (178)$$

The unknown coefficient vector which now has eight components, i.e.,

$$\underline{V}_k = \begin{bmatrix} A_{1k} \\ B_{1k} \\ A_{2k} \\ B_{2k} \\ A_{3k} \\ B_{3k} \\ A_{4k} \\ B_{4k} \end{bmatrix} \quad (179)$$

still has a solution of the form in (165), where the forcing vectors are the same as those in (173) with the addition of two zeros to the bottom of each and the 8x8 matrix [M] is characterized by

$$[M] = \begin{bmatrix} m_{11} & m_{12} & \cdot & \cdot & \cdot & m_{18} \\ m_{21} & m_{22} & \cdot & \cdot & \cdot & m_{28} \\ \cdot & \cdot & & & & \cdot \\ \cdot & \cdot & & & & \cdot \\ \cdot & \cdot & & & & \cdot \\ m_{81} & m_{82} & & & & m_{88} \end{bmatrix} \quad (180)$$

with

$$m_{1i} = 1 ; i=1,3,5,7$$

$$m_{1i} = 0 ; i=2,4,6,8$$

$$m_{2i} = \sum_{\substack{j=1 \\ j \neq i}}^4 \omega_{nj}^{2R_j}$$

$$m_{3i} = \frac{1}{2} \sum_{\substack{j=1 \\ j, k \neq i \\ j \neq k}}^4 \sum_{k=1}^4 \omega_{nj}^{2R_j} \omega_{nk}^{2R_k} + \sum_{\substack{j=1 \\ j \neq i}}^4 \omega_{nj}^4$$

$$m_{4i} = \sum_{\substack{j=1 \\ j, k \neq i \\ j \neq k}}^4 \sum_{k=1}^4 \omega_{nj}^{2R_j} \omega_{nk}^4 + \prod_{\substack{j=1 \\ j \neq i}}^4 \omega_{nj}^{2R_j}$$

$$m_{5i} = \frac{1}{2} \sum_{\substack{j=1 \\ j, k \neq i \\ j \neq k}}^4 \sum_{k=1}^4 \omega_{nj}^4 \omega_{nk}^4 + \frac{1}{2} \sum_{\substack{j=1 \\ j, k, \ell \neq i \\ j \neq k \neq \ell}}^4 \sum_{k=1}^4 \sum_{\ell=1}^4 \omega_{nj}^{2R_j} \omega_{nk}^{2R_k} \omega_{n\ell}^4 \quad \left. \vphantom{m_{5i}} \right\} i=1,3,5,7$$

$$m_{6i} = \frac{1}{2} \sum_{\substack{j=1 \\ j, k, \ell \neq i \\ j \neq k \neq \ell}}^4 \sum_{k=1}^4 \sum_{\ell=1}^4 \omega_{nj}^{2R_j} \omega_{nk}^4 \omega_{n\ell}^4$$

$$m_{7i} = \prod_{\substack{j=1 \\ j \neq i}}^4 \omega_{nj}^4$$

$$m_{8i} = 0$$

$$m_{ji} = m_{j-1, i-1} \quad i=2,4,6,8; j=2,3,\dots,8$$

(181)

REFERENCES

1. Rutman, J., "Characterization of Phase and Frequency Instabilities in Precision Frequency Sources: Fifteen Years of Progress," Proceedings of the IEEE, Vol. 66, No. 9, September 1978, pp. 1048-1075.
2. Lindsey, W. C., and Tu, K., "Phase Noise Effects on Space Shuttle Communication Link Performance," IEEE Trans. on Communications, Vol. COM-26, November 1978, pp. 1532-1541.
3. Lindsey, W. C., and Simon, M. K., Telecommunication Systems Engineering, Prentice-Hall, Inc., Englewood Cliffs, New Jersey, 1973, Chapter 3.
4. Lindsey, W.C., Synchronization Systems in Communication and Control, Prentice-Hall, Inc., Englewood Cliffs, New Jersey, 1972.
5. Gradshteyn, I. S., and Ryzhik, I. M., Table of Integrals, Series, and Products, Academic Press, New York, New York, 1965.

APPENDIX VII

MEAN-SQUARE ERROR APPROXIMATION TO PHASE NOISE SPECTRA

By

Andreas Polydoros

APPENDIX VII

MEAN-SQUARE ERROR APPROXIMATION TO PHASE NOISE SPECTRA

Here we wish to derive a formula for approximating a given phase noise power spectral density $S(f)$ by a power series in f^{-k} , $k \in \mathbb{N}$, in the least mean-square error sense (LMSE).

$S(f)$ is either directly available from measurements or is given in a piecewise linear form. The approximating function $\hat{S}(f)$ is assumed to be

$$\hat{S}(f) = h_0 + h_1 f^{-1} + h_2 f^{-2} + h_3 f^{-3} \quad (1)$$

where h_i ; $i = 0, 1, 2, 3$ are unknown coefficients to be determined.

The specific form of $\hat{S}(f)$ in (1) is dictated by physical considerations. The f^0 term corresponds to white phase noise, f^{-1} corresponds to white flicker noise, f^{-2} corresponds to white frequency noise, and f^{-3} serves to model flicker frequency noise. The physical significance of (1) then is that it represents the spectral superposition of the aforementioned random components, assumed independent, in the frequency band of interest.

The spectra to be approximated usually exhibit a flat portion for high frequencies. We can then assume that this value, which is directly measurable, determines h_0 . Henceforth, we will deal with the evaluation of h_k , $k \geq 1$.

The frequency band of interest will be denoted by (α, β) . We shall also assume, as is common practice, that $\beta \gg \alpha$. Indeed, customarily, α is on the order of tens of hertz while β is on the order of megahertz.

Since h_0 is known, let us define

$$S'(f) = S(f) - h_0 \quad (2)$$

The function to be minimized is

$$\begin{aligned}
 E &= \int_{\alpha}^{\beta} \left[S(f) - \left(h_0 + \frac{h_1}{f} + \frac{h_2}{f^2} + \frac{h_3}{f^3} \right) \right]^2 df \\
 &= \int_{\alpha}^{\beta} \left[S'(f) - \left(\frac{h_1}{f} + \frac{h_2}{f^2} + \frac{h_3}{f^3} \right) \right]^2 df \quad (3)
 \end{aligned}$$

Since E is a quadratic function of h_n ; $n = 1, 2, 3$, it follows that

$$\lim_{\substack{h_n \rightarrow \pm\infty \\ n=1,2,3}} E = +\infty$$

Therefore, the extremum of E , to be determined from the condition

$$\frac{\partial E}{\partial h_n} = 0, \quad n = 1, 2, 3,$$

clearly corresponds to a minimum.

Differentiating (3), we get

$$\frac{\partial E}{\partial h_n} = -2 \int_{\alpha}^{\beta} \left[S'(f) - \left(\frac{h_1}{f} + \frac{h_2}{f^2} + \frac{h_3}{f^3} \right) \right] \frac{df}{f^n} = 0$$

or

$$\int_{\alpha}^{\beta} \left[\frac{h_1}{f^{n+1}} + \frac{h_2}{f^{n+2}} + \frac{h_3}{f^{n+3}} \right] df = \int_{\alpha}^{\beta} \frac{S'(f)}{f^n} df; \quad n=1, 2, 3 \quad (4)$$

Recalling that, for $n > 1$,

$$\int_{\alpha}^{\beta} \frac{df}{f^n} = \frac{1}{(n-1)} \left[\frac{1}{\alpha^{n-1}} - \frac{1}{\beta^{n-1}} \right]$$

and inserting the assumption $\beta^{-1} \ll \alpha^{-1}$, we eventually derive from (4) the following system of equations:

$$\left. \begin{aligned} \frac{1}{\alpha} h_1 + \frac{1}{2\alpha^2} h_2 + \frac{1}{3\alpha^3} h_3 &= W_1 \\ \frac{1}{2\alpha^2} h_1 + \frac{1}{3\alpha^3} h_2 + \frac{1}{4\alpha^4} h_4 &= W_2 \\ \frac{1}{3\alpha^3} h_1 + \frac{1}{4\alpha^4} h_2 + \frac{1}{5\alpha^5} h_5 &= W_3 \end{aligned} \right\} \quad \text{I}$$

where we have defined

$$W_n \triangleq \int_{\alpha}^{\beta} \frac{S'(f)}{f^n} df ; n=1,2,3 \quad (5)$$

If we further define

$$\left. \begin{aligned} h'_n &\triangleq \frac{h_n}{\alpha^n} \\ W'_n &\triangleq \alpha^{n-1} W_n \end{aligned} \right\} \quad n=1,2,3 \quad (6)$$

the system I is written in matrix notation as

$$\begin{bmatrix} 1 & 1/2 & 1/3 \\ 1/2 & 1/3 & 1/4 \\ 1/3 & 1/4 & 1/5 \end{bmatrix} \begin{bmatrix} h'_1 \\ h'_2 \\ h'_3 \end{bmatrix} = \begin{bmatrix} W'_1 \\ W'_2 \\ W'_3 \end{bmatrix} \quad \text{II}$$

The solution of II is of the form

$$h'_n = \frac{\Delta_n}{\Delta} \quad (7)$$

where

$$\Delta = \frac{1}{2160}$$

and

$$\Delta_1 = \frac{W_1'}{240} - \frac{W_2'}{60} + \frac{W_3'}{72} \quad (8a)$$

$$\Delta_2 = \frac{-W_1'}{60} + \frac{4W_2'}{45} - \frac{W_3'}{12} \quad (8b)$$

$$\Delta_3 = \frac{W_1'}{72} - \frac{W_2'}{12} + \frac{W_3'}{12} \quad (8c)$$

From (6), (7) and (8), it eventually follows that

$$\left. \begin{aligned} h_1 &= \alpha \left[9 W_1' - 36 W_2' + 30 W_3' \right] \\ h_2 &= 12 \alpha^2 \left[-3 W_1' + 16 W_2' - 15 W_3' \right] \\ h_3 &= 30 \alpha^3 \left[W_1' - 6 W_2' + 6 W_3' \right] \end{aligned} \right\} \quad (9)$$

where, from (5) and (6),

$$W_n' = \alpha^{n-1} \int_{\alpha}^{\beta} \left(\frac{S(f) - h_0}{f^n} \right) df; \quad n=1,2,3 \quad (10)$$

Once the W_n' is evaluated as in (10), then the h_n follows directly from (9). However, except for the unlikely case that $S(f)$ is given in a closed form, evaluation of (10) is not apparent. To circumvent this, we propose the following: assume that $S(f)$ is given by a dB-amplitude/log-frequency plot, as measured directly in the laboratory. We approximate the plot by a series of N piecewise linear segments, each valid in the region $F_i \leq f \leq F_{i+1}$; $i=1, \dots, N$, where $F_1 = \alpha$ and $F_{N+1} = \beta$. Let us also denote by S_i the value of the spectrum at F_i , i.e., $S_i = S(F_i)$. Obviously, the quality of approximation to $S(f)$ increases as N increases. The piecewise linear approximation in the log/log scale implies that $S(f)$ is

assumed to have the analytic representation

$$\text{for } \left. \begin{aligned} S(f) &= S_i \left(\frac{f}{F_i} \right)^{-P_i} \\ F_i &\leq f \leq F_{i+1} \end{aligned} \right\} \quad (11)$$

In (11), the exponent $-P_i$ represents the slope of the line, viz.,

$$-P_i = \frac{\text{slope of line in dB/decade}}{10} \quad (12)$$

Direct substitution of (11) into (10) gives

$$W_1' = \int_{F_1}^{F_{N+1}} \frac{S'(f)}{f} df = \sum_{i=1}^N S_i \cdot F_i^{P_i} \int_{F_i}^{F_{i+1}} \frac{df}{f^{P_i+1}} - \int_{F_i}^{F_{N+1}} \frac{h_0 df}{f}$$

or

$$W_1' = \sum_{i=1}^N \frac{S_i}{P_i} \left[1 - \left(\frac{F_i}{F_{i+1}} \right)^{P_i} \right] - h_0 \ln \frac{F_{N+1}}{F_1} \quad (13a)$$

Similarly, we obtain

$$W_2' = \alpha \left\{ \sum_{i=1}^N \frac{S_i}{F_i^{(P_i+1)}} \left[1 - \left(\frac{F_i}{F_{i+1}} \right)^{P_i+1} \right] - h_0 \left[\frac{1}{F_1} - \frac{1}{F_{N+1}} \right] \right\} \quad (13b)$$

and

$$W_3' = \alpha^2 \left\{ \sum_{i=1}^N \frac{S_i}{F_i^{2(P_i+2)}} \left[1 - \left(\frac{F_i}{F_{i+1}} \right)^{P_i+2} \right] - \frac{h_0}{2} \left[\frac{1}{F_1^2} - \frac{1}{F_{N+1}^2} \right] \right\} \quad (13c)$$

Note in the above that, in general, the P_i 's need not be integers.

Comment

The above theory solely derives the LMSE estimate $\hat{S}(f)$ of $S(f)$. However, no care has been taken to account for the fact that $\hat{S}(f)$ should be nonnegative as it represents a spectral density. Indeed, on some occasions, the results provide a negative $\hat{S}(f)$ for some frequency regions. In these cases, the coefficients of the LMSE estimate can serve as good starting values which, after some heuristic small perturbation, produce a good new estimate $\hat{S}^*(f)$. This new $\hat{S}^*(f)$ should also conform with the aforementioned physical constraint of positiveness. The above comments were used in Example 2 following.

Applications

We now apply the previous results to the following two examples.

Example 1

Consider the TCX0 phase noise spectral density of Figure 1. The coefficients of $\hat{S}(f)$ were calculated to be

$$\begin{cases} h_0 = 0.31622776 \times 10^{-15} \\ h_1 = 0.39822958 \times 10^{-9} \\ h_2 = -0.14756626 \times 10^{-7} \\ h_3 = 0.31740942 \times 10^{-4} \end{cases}$$

Table 1 following compares certain values of $S_{\text{TCXO}}(f)$ with the corresponding ones of $\hat{S}(f)$.

Table 1

Frequency $f(\text{Hz})$	10 Hz	100 Hz	1 kHz	10 kHz	100 kHz	1 MHz
$S_{\text{TCXO}}(f)$ (db)	-75	-105	-125	-135	-145	-155
$\hat{S}(f)$ (dB)	-75	-104.7	-123.8	-134	-144	-155

Example 2

Next we consider the VCXO phase noise spectral density, shown in Figure 2. It was approximated by three piecewise linear segments. Table 2 summarizes the characteristic values considered for the implementation of the previous algorithms.

Table 2

n	1	2	3	4
F_n (Hz)	1 Hz	1 kHz	8.1 kHz	1 MHz
S_n (db)	-14	-104	-115	-
$P_n = \frac{\text{dB/decade}}{10}$ (slope)	-3	-1.4	0	-

PRECEDING PAGE BLANK NOT FILMED

The coefficients were found to be

$$\begin{aligned} h_0 &= 0.31622777 \times 10^{-11} \\ h_1 &= -0.3000000 \times 10^{-7} \\ h_2 &= 0.10874600 \times 10^{-3} \\ h_3 &= 0.39684600 \times 10^{-1} \end{aligned}$$

Table 3 provides a comparison between $S(f)$ and $\hat{S}(f)$ at distinct points for this case.

Table 3

Frequency $S(\text{Hz})$	1 Hz	10 Hz	100 Hz	1 kHz	10 kHz	100 kHz	1 MHz
$S(f)$ (db)	-14	-44	-74	-104	-115	-115	-115
$\hat{S}(f)$ (db)	-14	-43.9	-73	-99.2	-118	-115.4	-115

PRECEDING PAGE BLANK NOT FILMED

APPENDIX VIII

**CALCULATIONS AND FINAL RESULTS ON THE PHASE NOISE ERROR VARIANCE
FOR THE S-BAND PI AND TRANSPONDER FOR SGLS AND STDN**

By

Andreas Polydoros

APPENDIX VIII

CALCULATIONS AND FINAL RESULTS ON THE PHASE NOISE ERROR VARIANCE FOR THE S-BAND PI AND TRANSPONDER FOR SGLS AND STDN

The noncoherent result is

$$\begin{aligned}
 \phi_e(s) = & 128 \psi_{IUS} (1 - H_{IUS})(1 - H_{PI}) + \psi_1(1 - H_1)(1 - H_{PI}) \cdot H_2 \cdot H_{IUS} \\
 & - \psi_1'(1 - H_1)(1 - H_{PI}) + \psi_2 G_f (1 - H_2) H_{IUS} (1 - H_{PI}) \\
 & - 10 \psi_{PI} (1 - H_{PI}) - \theta_{r_2} (1 - H_{PI}) \quad (1)
 \end{aligned}$$

where ψ_1' and ψ_1 are two independent processes with the same statistics. Furthermore, the spectra of ψ_{IUS} , ψ_{PI} , θ_{r_2} are the same (VCXO spectrum) as given in Figure 1. Since the spectrum in Figure 1, $S_I(f)$, is measured with respect to a 2211 MHz carrier, the following is true:

$$(a) \quad S_{128\psi_{IUS}}(f) = S_I(f)$$

(b) ψ_{PI} is measured at 1.84 MHz, hence

$$S_{10\psi_{PI}}(f) = \left(\frac{18.4}{2211}\right)^2 S_I(f)$$

(c) θ_{r_2} is measured at 31 MHz, hence,

$$S_{\theta_{r_2}}(f) = \left(\frac{31}{2211}\right)^2 S_I(f).$$

The common spectrum $S_{II}(f)$ (see Figure 2) of the processes ψ_1 , ψ_1' , ψ_2 is measured at 2211 MHz. The method of extracting the shape of $S_{II}(f)$ from the TCXO output spectrum measurement is described elsewhere (see Addendum). Incorporating the above comments in (1) yields

$$\begin{aligned}
 S_\phi(f) = & S_I(f) \left\{ 2.658 \times 10^{-4} \left[|1 - H_{PI}(f)|^2 + |1 - H_{IUS}(f)|^2 |1 - H_{PI}(f)|^2 \right] \right\} \\
 & + S_{II}(f) \left\{ |1 - H_1(f)|^2 |H_2(f)|^2 |1 - H_{IUS}(f)|^2 |1 - H_{PI}(f)|^2 + |1 - H_1(f)|^2 \right. \\
 & \quad \left. \times |1 - H_{PI}(f)|^2 + G_f^2 |1 - H_2(f)|^2 |H_{IUS}(f)|^2 |1 - H_{PI}(f)|^2 \right\} \quad (2)
 \end{aligned}$$

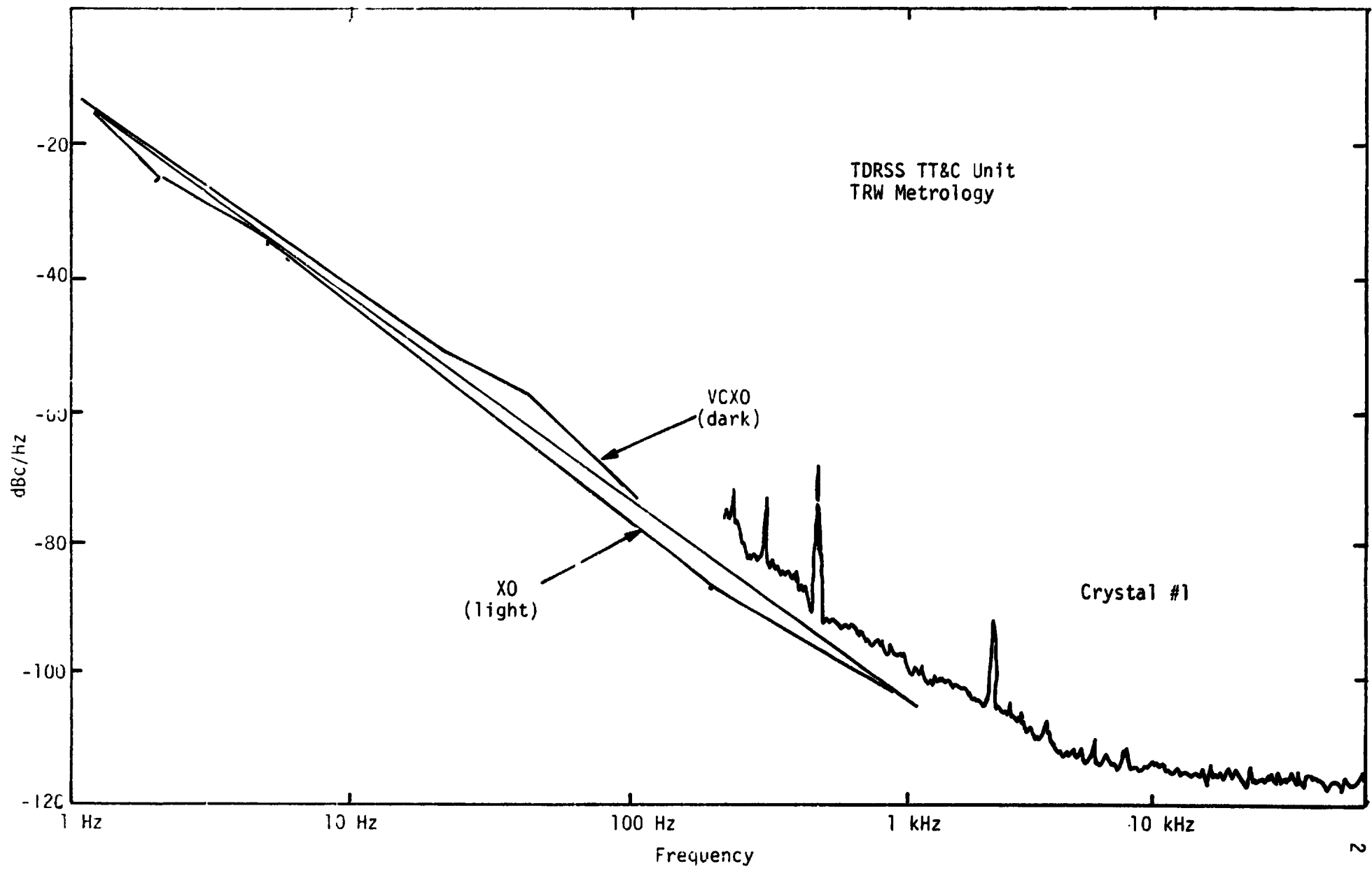


Figure 1. VCXO Measured Phase Noise Sideband Power Spectral Density

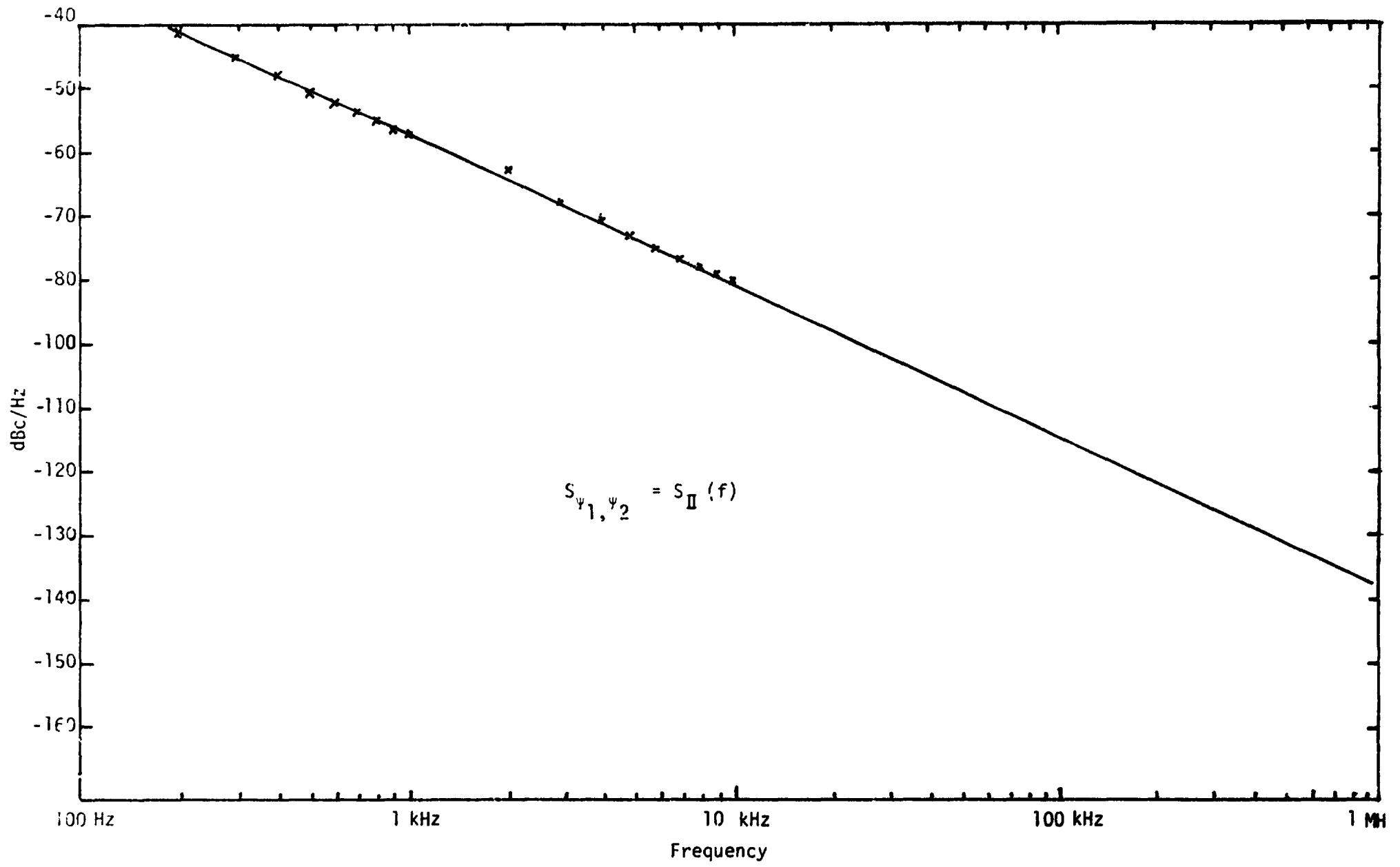


Figure 2. VCO Phase Noise Power Spectra after Filter Extraction

We now make the following simplification. For the SGLS mode, the bandwidth of $H_{IUS}(f)$ is 3774 Hz, while that of $H_2(f)$ is 560 Hz, or about 1/7 of the latter. Hence, we can safely ignore $H_{IUS}(f)$ in the fourth-order products of (2) and use the approximation

$$|1-H_1(f)|^2 |H_2(f)|^2 |H_{IUS}(f)|^2 |1-H_{PI}(f)|^2 \approx |1-H_1(f)|^2 |H_2(f)|^2 |1-H_{PI}(f)|^2$$

The above substitution simplifies matters significantly because we now have to calculate two three-product integrals of the form

$$I_1 = \int_{-\infty}^{\infty} f^{-k} |H_2(f) (1-H_1(f)) (1-H_{PI}(f))|^2 df \quad (3a)$$

and

$$I_2 = \int_{-\infty}^{\infty} f^{-k} |H_{IUS}(f) (1-H_2(f)) (1-H_{PI}(f))|^2 df \quad (k=0,1,2,3) \quad (3b)$$

instead of a three-product and four-product integral.

The evaluation of the variance

$$\sigma_{\phi}^2 = \int_{-\infty}^{\infty} S_{\phi}(f) df$$

requires approximating the spectra $S_I(f)$ and $S_{II}(f)$ by a series of the form

$$\sum_{i=0}^3 c_i f^{-i}.$$

The least square approximation method is described in Appendix VII of this report and gives the following results

$$S_I(f) \approx 0.158 \times 10^{-11} - \frac{0.15 \times 10^{-7}}{f} + \frac{0.544 \times 10^{-4}}{f^2} + \frac{0.1984 \times 10^{-1}}{f^3} \quad (4a)$$

and

$$S_{II}(f) \approx \frac{0.5}{f^2} \quad (4b)$$

Note: The spectra shown in Figures 1 and 2 are one-sided, while $S_I(f)$ and $S_{II}(f)$ are two-sided expressions. Therefore, 3 dB should be subtracted first from the figure plots before approximation is attempted.

The evaluations of the one-product integral

$$\int_{-\infty}^{\infty} f^{-k} |1 - H_{PI}(f)|^2 df$$

and the two two-product integrals

$$\int_{-\infty}^{\infty} f^{-k} |1 - H_{IUS}(f)|^2 |1 - H_{PI}(f)|^2 df$$

and

$$\int_{-\infty}^{\infty} f^{-k} |1 - H_1(f)|^2 |1 - H_{PI}(f)|^2 df; \quad k=0,1,2,3$$

are performed by the program PHNOISE. Next we describe the evaluation of I_1 and I_2 .

1.0 EVALUATION OF I_1 and I_2

According to the theory developed, the evaluation of I_1 and I_2 requires the prior computation of the matrix M , as given by (148) and (149) of Appendix VI of this report. This was done by the program M , and the results are as follows:

$$I_1: \\ M = \begin{bmatrix} 1 & | & 0 & | & 1 & | & 0 & | & 1 & | & 0 \\ 0.4939 \times 10^7 & | & 1 & | & 0.327 \times 10^8 & | & 1 & | & 0.356 \times 10^8 & | & 1 \\ 0.250 \times 10^{14} & | & 0.4939 \times 10^7 & | & 0.625 \times 10^{14} & | & 0.327 \times 10^8 & | & 0.180 \times 10^{21} & | & 0.356 \times 10^8 \\ 0.3923 \times 10^{20} & | & 0.250 \times 10^{14} & | & 0.3092 \times 10^{20} & | & 0.625 \times 10^{14} & | & 0.628 \times 10^{21} & | & 0.180 \times 10^{21} \\ 0.1814 \times 10^{26} & | & 0.3923 \times 10^{20} & | & 0.983 \times 10^{23} & | & 0.3092 \times 10^{20} & | & 0.178 \times 10^{37} & | & 0.628 \times 10^{21} \\ 0 & | & 0.1814 \times 10^{26} & | & 0 & | & 0.983 \times 10^{23} & | & 0 & | & 0.178 \times 10^{37} \end{bmatrix}$$

and

$$I_2: \\ M = \begin{bmatrix} 1 & | & 0 & | & 1 & | & 0 & | & 1 & | & 0 \\ 0.3367 \times 10^8 & | & 1 & | & 0.307 \times 10^8 & | & 1 & | & 0.336 \times 10^8 & | & 1 \\ 0.1086 \times 10^{15} & | & 0.3367 \times 10^8 & | & 0.203 \times 10^{15} & | & 0.307 \times 10^8 & | & 0.22 \times 10^{15} & | & 0.336 \times 10^8 \\ 0.558 \times 10^{21} & | & 0.1086 \times 10^{15} & | & 0.623 \times 10^{22} & | & 0.203 \times 10^{15} & | & 0.739 \times 10^{22} & | & 0.22 \times 10^{15} \\ 0.178 \times 10^{25} & | & 0.558 \times 10^{21} & | & 0.199 \times 10^{26} & | & 0.623 \times 10^{22} & | & 0.362 \times 10^{39} & | & 0.739 \times 10^{22} \\ 0 & | & 0.178 \times 10^{25} & | & 0 & | & 0.199 \times 10^{26} & | & 0 & | & 0.362 \times 10^{39} \end{bmatrix}$$

Since we are interested in the $k=2$ term only (see (4b) in connection with (2)), we have to evaluate the following F_2 column vectors:

$$I_1: F_2 = \begin{bmatrix} 0 & | & 0.313 \times 10^8 & | & 0.983 \times 10^{11} & | & 0 & | & 0 & | & 0 \end{bmatrix}^T$$

and

$$I_2: F_2 = \begin{bmatrix} 0 & | & 0.28486 \times 10^8 & | & 0.202865 \times 10^{15} & | & 0 & | & 0 & | & 0 \end{bmatrix}^T$$

The solution of the system $[M] \cdot [V_2] = [F_2]$ is accomplished through the subroutine SLEQ for the solution of a system of linear equations. Despite the fact that the matrix M is ill-conditioned (i.e., the eigenvalues differ by many orders of magnitude), the program produces results of satisfactory accuracy. They are

$$I_1: \begin{bmatrix} A_{12} \\ B_{12} \\ A_{22} \\ B_{22} \\ A_{32} \\ B_{32} \end{bmatrix} = \begin{bmatrix} -0.1011 \times 10^1 \\ 0.5171 \times 10^7 \\ 0.1011 \times 10^1 \\ -0.1937 \times 10^7 \\ -0.695 \times 10^{-1} \\ -0.521 \times 10^{-4} \end{bmatrix}$$

and

$$I_2: \begin{bmatrix} A_{12} \\ B_{12} \\ A_{22} \\ B_{22} \\ A_{32} \\ B_{32} \end{bmatrix} = \begin{bmatrix} 0.222 \times 10^1 \\ -0.8665 \times 10^8 \\ -0.222 \times 10^1 \\ 0.1085 \times 10^9 \\ -0.1734 \times 10^{-8} \\ -0.554 \times 10^{-5} \end{bmatrix}$$

Applying (160) of Appendix VI for the proper transfer functions and $k=2$, we find that $I_1 = 0.11504 \times 10^{-2}$ and $I_2 = 0.3034 \times 10^{-1}$. These numbers represent the integrals I_1 and I_2 as defined by (3), not the parameter $\sigma_2^2|_{3\text{-way}}$ of (160) of Appendix VI. To evaluate the latter, one should multiply with $h_2 = 0.5$ as given by (4b).

The transfer function parameters (natural frequency f_n , damping factor ζ) which were used in the computation of the integrals are given in the following table:

Parameters \ H	$H_{IUS}(\text{SGLS})$	H_{PI}	$H_{1\text{synthesizer}}$	$H_{2\text{synthesizer}}$
f_n (Hz)	3774	2064	1000	560
ζ	$\frac{1}{\sqrt{2}} = 0.707$	0.82	1.0	5.0

2.0 SUMMARY OF RESULTS AND COMMENTS

With respect to the calculation of the one-product and two-product integrals appearing in (2), we should mention that some of them, notably, the parameters σ_0^2 and σ_1^2 for both of them, are evaluated with the upper limit of integration being some finite f_H instead of $+\infty$. This parameter was chosen to be $f_H = 6$ MHz (i.e., 12 MHz two-sided bandwidth) since that was found as the lowest cutoff frequency of the IF filters. Also, the gain G_f is of the value $256/204 = 1.2488$.

The final deviation found is $\sigma_\phi = 8.93^\circ$ RMS (SGLS mode). In the STDN mode, the bandwidth of H_{IUS} is 755 Hz, i.e., of the same order as the H_2 bandwidth. In this case, the approximation of the four-product integral by a three-product one is not valid anymore, and precise results can be obtained only by using the appropriate formulas. Nevertheless, it is straightforward to see that the STDN variance is going to be slightly less than the SGLS variance found because $|H_{IUS}| \leq 1$; we virtually substituted H_{IUS} with its upper bound in the previous calculations. We can therefore claim that the 8.93° found represent an upper bound for both SGLS and STDN modes.

A final comment pertains to the value of σ_ϕ . By straightforward integration of the phase noise spectrum of the TCXO output (see appropriate memo), one gets a deviation of approximately 3.5° . Adding the same amount at the PI receiver demodulator plus additional contributions from the PI and IUS VCXO's (of considerably lower value, however, see Figure 1), one concludes that the value found indeed lies within the expected range.

ADDENDUM

Let us denote by $S_{\text{TCXO},0}(f)$ the phase noise spectrum measured at the output of the PI TCXO, as plotted in Figure 3. From the PI diagram, it follows that

$$S_{\text{TCXO},0}(f) = S_{\psi_1}(f) |1 - H_1(f)|^2 |H_2(f)|^2 + S_{\psi_2}(f) |1 - H_2(f)|^2 G_f + 256 S_{\theta_T}(f) \quad (5)$$

We now entail the reasonable assumption that $S_{\theta_T}(f) \cong 0$, i.e., its contribution is negligible. This assumption is verified if we plot the product $256 S_{\theta_T}(f)$ against $S_{\text{TCXO},0}(f)$ and realize that it is several decibels below the latter. Furthermore, we assume that the noise processes $\psi_1(t)$ and $\psi_2(t)$ possess the same spectral characteristics.

Denoting this common spectral density by $S_{II}(f)$, we get, from (5), that

$$S_{II}(f) = \frac{S_{\text{TCXO},0}(f)}{|1 - H_1|^2 |H_2|^2 + |1 - H_2|^2 G_f^2} \quad (6)$$

Here,

$$|H_2|^2 = \frac{f_{n_2}^2 (f_{n_2}^2 + r_2 f^2)}{f^4 + R_2 f_{n_2}^2 + f_{n_2}^2}$$

$$|1 - H_i|^2 = \frac{f^4}{f^4 + R_i f_{n_i}^2 + f_{n_i}^4}; \quad i=1,2$$

where R_i equals $4\zeta_i^2 - 2$ and $r_i = 4\zeta_i^2$.

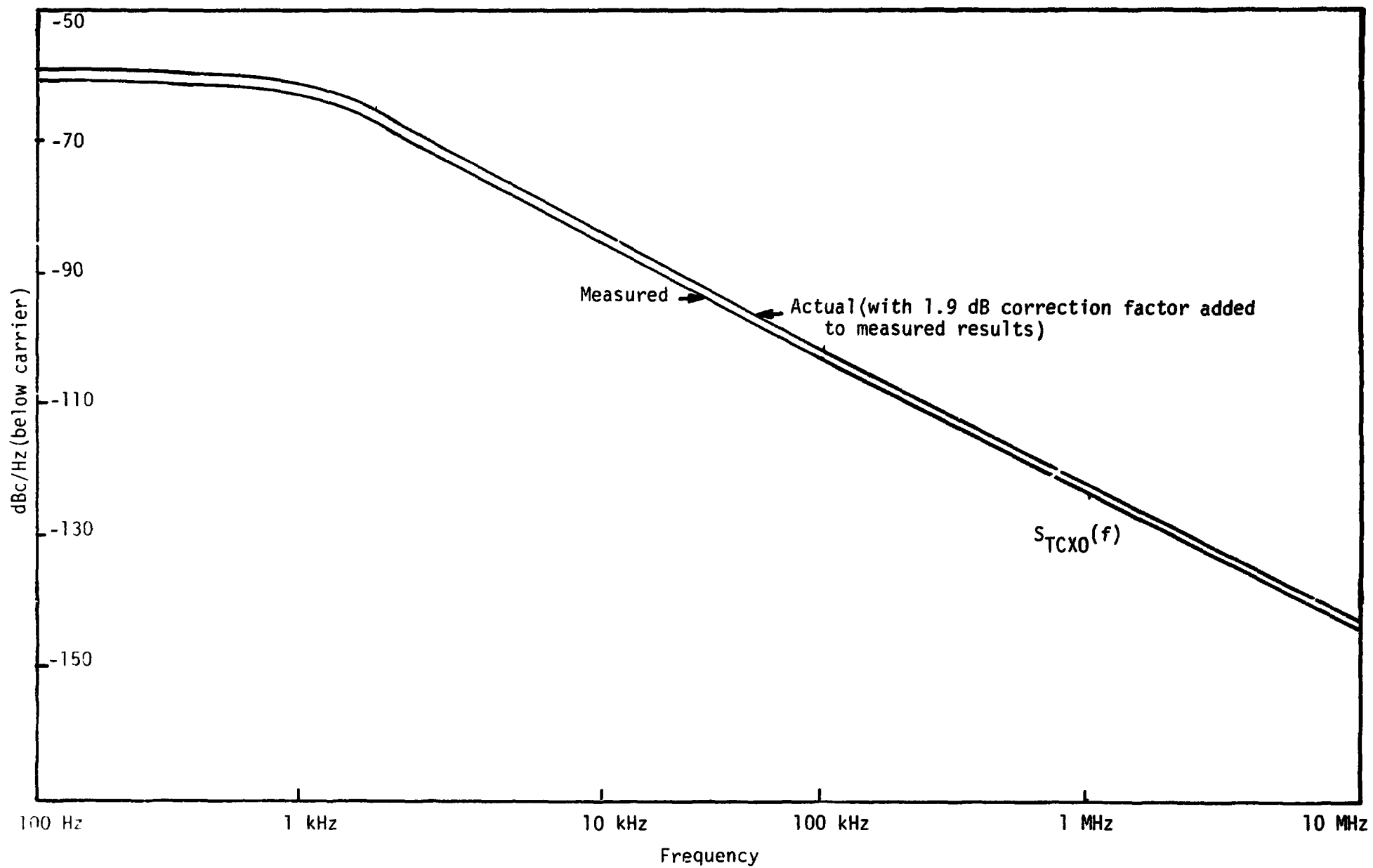


Figure 3. Measured Transmitter Single-Sideband Phase Noise Spectral Density

Substituting the previous expressions in the denominator D of (6), we get

$$\begin{aligned}
 D &= \frac{f^4}{f^4 + R_2 f_{n_2}^2 f^2 + f_{n_2}^4} \left[\frac{f_{n_2}^2 (f_{n_2}^2 + r_2 f^2)}{f^4 + R_1 f_{n_1}^2 f^2 + f_{n_1}^4} + G_f^2 \right] \\
 &= \frac{G_f^2 f^8 + (G_f^2 R_1 f_{n_1}^2 + r_2 f_{n_2}^2) f^6 + (f_{n_2}^4 + G_f^2 f_{n_1}^4) f^4}{f^8 + (R_1 f_{n_1}^2 + R_2 f_{n_2}^2) f^6 + (f_{n_1}^4 + f_{n_2}^4 + R_1 R_2 f_{n_1}^2 f_{n_2}^2) f^4 + f_{n_1}^4 f_{n_2}^4} \quad (7)
 \end{aligned}$$

Through (6), (4) and the $S_{TCX0,0}(f)$ of Figure 3, the spectrum $S_{II}(f)$ of Figure 2 was derived.